

## Durham E-Theses

---

### *Novel Acoustic Methods for Directly Monitoring Seabed Sediment Transport, Geohazards & Scour*

TRACEY, NIALL

#### How to cite:

---

TRACEY, NIALL (2024) *Novel Acoustic Methods for Directly Monitoring Seabed Sediment Transport, Geohazards & Scour*, Durham theses, Durham University. Available at Durham E-Theses Online:  
<http://etheses.dur.ac.uk/15332/>

#### Use policy

---

The full-text may be used and/or reproduced, and given to third parties in any format or medium, without prior permission or charge, for personal research or study, educational, or not-for-profit purposes provided that:

- a full bibliographic reference is made to the original source
- a [link](#) is made to the metadata record in Durham E-Theses
- the full-text is not changed in any way

The full-text must not be sold in any format or medium without the formal permission of the copyright holders.

Please consult the [full Durham E-Theses policy](#) for further details.

# Novel Acoustic Methods for Directly Monitoring Seabed Sediment Transport, Geohazards & Scour

---

*Submitted in accordance with the requirements for the degree of a Doctor of Philosophy*



Niall David Tracey

July 2023

# Declaration

---

No part of the material contained within this thesis has been previously submitted for a degree in this or any other institution. Where appropriate, acknowledgement of data collected outside the duration of this PhD has been clearly indicated. Work for this thesis was conducted from September 2020 to July 2023 under the primary supervision of Prof. Peter Talling at Durham University and secondary supervision from Dr Steve Simmons at the University of Hull and Prof. Dan Parsons at Loughborough University.

Niall Tracey

Durham University

July 2023

# Funding

---

The research presented within this thesis contains work carried out during a PhD study undertaken as part of the Engineering and Physical Sciences Research Council (EPSRC) and Natural Environment Research Council (NERC), Aura Centre for Doctoral Training (Aura) [Grant number: EP/S023763/1], their support is gratefully acknowledged.

I want to thank the support of the Natural Environment Research Council (NERC) [Grant numbers: NER/A/S/2001/00445, NER/B/S/ 2003/00243, NE/E001661/1, NE/C002636/1, NE/E016022/1, NE/I015876/1, NE/R001952/1, NE/S010068/1, NE/K011480/1, NE/M017540/1 and NE/W000601/1]. In addition, I would also like to acknowledge the backing of the Secretary of Science and Technology, Universidad Nacional del Litoral, Santa Fe, Argentina [grant number: CAI+D 2011], U.S. Geological Survey (USGS) Coastal and Marine Program, and Ocean University of China. Their funding allowed for the collection of the various data sets presented within this study.

# Abstract

---

In the natural environment, sediment transport processes can pose significant hazards to marine infrastructure, such as offshore wind turbines or seabed cables that carry both power onshore as well as carrying over 99% of global data. These processes are often extremely challenging to measure directly because sensors can be easily damaged by the processes themselves. It would, therefore, be highly advantageous to remotely sense and quantify sediment transport via sensors that are located outside the region of sediment transport. One way to do this is via sensors higher in the water column that detect acoustic signals emitted by sediment transport processes closer to the bed.

Previous work such as Wren *et al.* (2015), Marineau *et al.* (2016), and Le Guern *et al.* (2021) have started to develop passive acoustic methods to record signals from sediment transport, using tools such as hydrophones and acoustic Doppler current profilers (ADCPs). Normally, ADCPs actively emit their own acoustic pulses, and their reflections are used to monitor flow velocities and concentrations. However, with modification to extend their listening times, ADCP's can also be used to passively record acoustic signals emitted by sediment transport processes. Thus far, the potential of these passive acoustic methods have not been fully developed, and the fundamental controls that determine the type of acoustic signals produced are not yet fully understood.

This PhD sought to understand what controls the nature (frequencies, strength etc) of these signals and, thus, what they can tell us about sediment transport processes (Thorne, 1985,1986,1990,2014; Rigby *et al.* 2016). It aims to do this using a combination of laboratory experiments (Chapter 2) and detailed fieldwork (Chapters 3 and 4) using acoustic signals passively emitted by sediment flows. In addition, the thesis includes work testing the use of active acoustic methods to monitor sediment transport processes within the natural environment, specifically seabed sediment flows (called turbidity currents) (Chapter 5).

Results from this thesis found a general relationship between the strength of self-generated noise and flow speed in some types of sediment flows (Chapters 2, 3 and 4). However, the strength of this relationship changes depending on the frequency and details of the environment investigated. Field data from the Río Paraná (Chapter 3) suggested no relationship between bedload flux and acoustic signal strength, nor between acoustic signal strength and friction

velocity. This is unexpected because previous research by Sime *et al.* (2007), Hossein and Rennie (2009), Hatcher (2017), Hay *et al.* (2021) and Le Guern *et al.* (2021) proposed links between flow speed (and bed shear stress and bedload transport) and passively detected noise strength.

Passive acoustic signals generated by turbidity currents were used to monitor these flows in a set of submarine canyons, which were Bute Inlet (Canada), Monterey Canyon (offshore California), and the Congo Canyon (offshore West Africa) (Chapter 4). Noticeable variations in the level of passively detected noise between these three field sites were observed. These variations are thought to be related to the main sediment grain size present within each canyon, with lower noise being detected with an increasing mud content of the seabed. In addition, differences in noise down submarine canyons suggest that flow processes and concentration could be controlling the level of sediment-generated noise, with implications of flow field dynamics.

Chapter 5 uses one of the most detailed (near-daily) series of multibeam swath bathymetry surveys yet collected, which come from within Bute Inlet, Canada, in September 2022. This unusual set of field observations is used to understand the relationship between flow evolution and the initiation mechanism of turbidity currents. For example, the Bute Inlet study supports the findings from Hizzett *et al.* (2018) that there is no link between the initiation mechanism and runout distance of a turbidity current.

Further research is needed to improve understanding of the controls on acoustic signals in the natural environment, and to also improve our ability to use acoustic signals to monitor sediment transport in a wider range of environments, such as around offshore wind farms.

# Acknowledgements

---

First, I would like to thank my supervisory team and the Aura CDT for their continual support throughout this PhD. I would especially like to thank Pete and Steve for their enormous help in making a hard task that little bit easier, giving me invaluable feedback on each chapter of the PhD, which was desperately needed due to my Dyslexia. I would like to thank Dan for giving his limited time to help at critical stages of the PhD.

Many thanks go out to the Aura CDT for providing me with the skills to undertake this PhD and for facilitating the chance to complete one. I want to thank all those who I can call friends within the Aura CDT and Durham Earth Science Department for providing plenty of support, entertainment and trips to the pub. I am incredibly grateful for the first cohort of the Aura CDT (Jordan, Rachael, Hannah, Sophie), as well as Sean Ruffell for their help, support, and advice during the first year at the CDT, the Covid-19 pandemic and the later stages of the PhD. They have always been the people who I could rely on when in a pinch.

I would like to thank the MOD for allowing me to join the URNU in 2021 and for providing invaluable time aboard HMS Magpie. I am also grateful to Matthieu Cantigny for providing an amazing opportunity during the PhD to help out with his fieldwork expedition to Bute Inlet, Canada, in 2022. The friends and skills developed during these occasions will last a lifetime.

I would also like to thank my loving parents for always believing in me and sparking my interest in science. A special thanks goes out to my mother, Michele (whose name is spelt correctly). She has always strived to help whenever it was needed. In this PhD, she used many of her days off to help proofread my PhD, for which I am eternally grateful. I am grateful to my brother William for sharing his random facts and knowledge as a child, further driving me to love science and discovering the undiscovered. I cannot forget to mention the constant emotional support provided by my two dogs, Walter and Ted.

I would also like to acknowledge the support of my entire extended family, who are too large to mention but know who they are. Sadly, two of which (Pat and Dave) are not able to see me

finish this PhD; I will forever be grateful for their constant loving support throughout my life, and I know they would be proud to see me at this stage.

Thank you to everyone I have listed and those who have not been mentioned. Completing a PhD is an arduous task which one alone would struggle to complete. Therefore, I am extremely grateful for any help that was provided to me in any way, as those actions made this journey that bit easier and enjoyable.

*© The copyright of this thesis rests with the author. No quotation from it should be published without the author's prior written consent and information derived from it should be acknowledged.*

## Table of Contents

---

<b>Declaration</b> .....	<b>ii</b>
<b>Funding</b> .....	<b>ii</b>
<b>Abstract</b> .....	<b>iii</b>
<b>Acknowledgements</b> .....	<b>v</b>
<b>1. Introduction to the thesis</b> .....	<b>1</b>
1.1. Underwater acoustics: an introduction.....	2
1.2. Active acoustic methods .....	4
1.2.1. Types of active acoustic method .....	4
1.1.2.1. Multibeam echo sounder principles and limitations.....	5
1.1.2.2. Acoustic Doppler current profilers (ADCPs).....	7
1.3. Understanding sediment transport using passive acoustic signals.....	10
1.3.1. Sediment transport.....	10
1.3.1.1. Modes of sediment transport .....	10
1.3.1.2. Shear stress variability in tidal and riverine environments.....	11
1.3.1.3. Bedform development .....	11
1.3.2. What is sediment-generated noise?.....	14
1.3.3. Review of laboratory experiments analysing sediment-generated noise .....	15
1.3.3.1. Experiments in rotating drums .....	15
1.3.3.2. Experiments in flume tanks .....	15
1.3.4. Review of past theoretical modelling of sediment-generated noise.....	16
1.3.5. Review of past field studies for sediment-generated noise.....	17
1.3.6. Understanding controls on sound pressure level.....	18
1.3.7. Frequency of acoustic noise from particle-particle collisions.....	21
1.3.7.1. Pebbles, Gravel and Sand .....	22
1.3.7.2. Silt and Clay .....	24

1.3.7.3.	Extracellular polymeric substances (EPS).....	26
1.3.8.	Predicting grain size using acoustic signals .....	26
1.3.9.	Calculating bed shear stress .....	27
1.3.10.	Calculating directionality .....	28
1.3.11.	Uncertainties involved in acoustic monitoring.....	29
1.3.11.1.	Sources of uncertainty in acoustic monitoring .....	29
1.3.11.2.	Ways of mitigating uncertainty in acoustic monitoring .....	32
1.4.	Applications of acoustic monitoring of sediment transport.....	34
1.4.1.	Turbidity currents.....	34
1.4.1.1.	Geohazards due to turbidity currents.....	36
1.4.1.2.	Research on turbidity currents and sediment-generated noise .....	37
1.5.	Knowledge gaps.....	39
1.5.1.	Thesis aims.....	40
<b>2.</b>	<b>Laboratory analysis of passively detected acoustic signals in recirculating flume experiments.....</b>	<b>43</b>
2.1.	Introduction.....	44
2.1.1.	Previous labwork experiments .....	44
2.1.2.	Incentives to test and develop new passive methods .....	45
2.1.2.1.	Research into sediment-generated noise within river environments .....	45
2.1.2.2.	Sediment-generated noise within deep marine environments .....	45
2.1.2.3.	Alternative passive instruments to monitor sediment-generated noise .....	46
2.1.3.	Aims and objectives .....	47
2.2.	Flume experiment methods.....	49
2.2.1.	The first round of experiments procedures .....	52
2.2.2.	The second round of experiments procedures.....	55
2.2.2.1.	Hydrophone experimental setup .....	55
2.2.2.2.	ADCP experimental setup .....	57

2.2.3.	The third round of experiments procedures .....	58
2.2.4.	Data processing procedures.....	60
2.2.4.1.	Hydrophone data analysis.....	60
2.2.4.2.	ADCP data analysis .....	63
2.3.	Results.....	66
2.3.1.	Acoustic signal variation with sediment type (Hydrophone).....	66
2.3.2.	Bedform analysis.....	68
2.3.2.1.	Acoustic variation across a bedform profile.....	68
2.3.2.2.	Relationships between bedform types and acoustic power .....	71
2.3.3.	600 kHz ADCP analysis.....	72
2.3.4.	1.2 MHz ADCP analysis .....	77
2.4.	Discussion.....	81
2.4.1.	Relationships derived from the passively recorded hydrophone data.....	81
2.4.2.	Acoustic output variation across a bedform.....	83
2.4.3.	Acoustic variation in bedform type.....	83
2.4.4.	Relationships between passively detected acoustic noise and flow speed.....	85
2.4.4.1.	Comparisons to Hatcher (2017) and Hay <i>et al.</i> (2021).....	85
2.4.4.2.	The effects of different equipment on the level of detected sediment-generated noise .....	87
2.5.	Conclusion .....	88
2.5.1.	Future work .....	89
2.5.1.1.	Future studies into hydrophones.....	89
2.5.1.2.	Future studies using ADCPs.....	89
<b>3.</b>	<b>Can acoustic signals help to understand sediment transport in a sand-bed river? ...</b> .....	<b>91</b>
3.1.	Introduction.....	92
3.1.1.	The importance of studying sediment-generated noise in rivers.....	92

3.1.2.	Aims and objectives .....	95
3.1.3.	Background .....	97
3.2.	Methods.....	100
3.2.1.	ADCP data processing methods.....	100
3.2.1.1.	Collecting and understading passively detected noise .....	100
3.2.1.2.	WinADCP data conversion .....	103
3.2.1.3.	ADCP data calculations.....	104
3.3.	Results.....	108
3.3.1.	Cross-plots to show the relationships between different variables .....	108
3.3.1.1.	The relationship between flow speed and passively detected noise.....	108
3.3.1.2.	The relationship between friction velocity and passively detected noise.....	109
3.3.1.3.	The relationship between bedload transport rate and passively detected noise .....	110
3.3.1.4.	The relationship between friction velocity and bedload transport rate .....	111
3.3.2.	The relationship between Received Signal Strength Indicator and flow speed ..	111
3.3.3.	Uncertainties within water flow speed (m/s).....	114
3.4.	Discussion.....	115
3.4.1.	Relationships between flow speed and passively detected noise.....	115
3.4.2.	Relationships between friction velocity and passively detected noise within the Río Paraná .....	116
3.4.3.	Relationships between bedload transport rate and passively detected noise within the Río Paraná .....	118
3.4.4.	Variations in passively detected noise across the profile of bedforms .....	118
3.5.	Conclusion .....	120
3.5.1.	Future work .....	121
<b>4.</b>	<b>Passive acoustic monitoring of turbidity currents within submarine channel systems .....</b>	<b>123</b>

4.1.	Introduction.....	124
4.1.1.	Research Aims.....	126
4.1.2.	Background to the field sites.....	127
4.1.2.1.	Bute Inlet, British Columbia, Canada.....	127
4.1.2.2.	Congo Canyon-channel, offshore West Africa.....	128
4.1.2.3.	Monterey Canyon, California, USA.....	129
4.2.	Methods.....	131
4.2.1.	Analysis of ADCP data sets.....	131
4.2.2.	Estimating sediment concentrations using the Chézy Equation.....	133
4.3.	Results.....	135
4.3.1.	Passive acoustic signals from turbidity currents within Bute Inlet.....	135
4.3.2.	Observed turbidity currents within the Congo Canyon.....	139
4.3.3.	Observed turbidity currents within the Monterey Canyon.....	139
4.3.4.	Comparison of the occurrence of passively detected noise between each submarine system.....	143
4.4.	Discussion.....	144
4.4.1.	Variations in acoustic signals between different submarine canyons.....	144
4.4.2.	Acoustic variations within individual turbidity currents.....	146
4.4.3.	Causes of differences in acoustic signals between each field site.....	148
4.5.	Conclusions.....	151
4.5.1.	Future work.....	152
<b>5.</b>	<b>Initiation mechanisms of turbidity currents occurring at Bute Inlet and Squamish Delta .....</b>	<b>153</b>
5.1.	Introduction.....	154
5.1.1.	Previous research.....	155
5.1.1.1.	Initiation mechanisms of turbidity currents.....	155
5.1.1.2.	Evolution of turbidity currents.....	156

5.1.2.	Aims and objectives .....	156
5.1.3.	Regional background.....	157
5.1.3.1.	Bute Inlet .....	157
5.1.3.2.	Squamish Delta.....	160
5.2.	Methods.....	163
5.2.1.	Initial data collection .....	163
5.2.2.	Data processing and analysis .....	163
5.2.2.1.	Data processing within Caris .....	163
5.2.2.2.	Data processing within ArcGIS Pro .....	164
5.2.2.3.	Data processing within MATLAB .....	166
5.3.	Results.....	171
5.3.1.	Identification and logging of all events within Bute Inlet.....	171
5.3.2.	In-depth analysis of event volume and runout distance .....	173
5.3.2.1.	Variations in type of initiation mechanism(s) .....	173
5.3.2.2.	Variations in the location of events along the delta-lip.....	174
5.3.3.	River discharge, tidal height and total volume of events within Bute Inlet .....	176
5.4.	Discussion .....	178
5.4.1.	The initial cause of the sediment transport events in Bute Inlet .....	178
5.4.2.	The most frequent location and form of initiation mechanism for sediment transport events .....	178
5.4.3.	Which initiation mechanism reworks the most sediment in Bute Inlet.....	179
5.4.4.	Links between sediment type, frequency and volume of turbidity currents .....	180
5.4.4.1.	Links regarding the frequency of turbidity currents between both Bute Inlet and Squamish Delta.....	180
5.4.4.2.	Variations in turbidity current volume between both Bute Inlet and Squamish Delta.....	180

5.4.5.	Links between turbidity current runout distance: comparing Bute Inlet and Squamish Delta .....	181
5.5.	Conclusion .....	182
5.5.1	Future work .....	182
<b>6.</b>	<b>Conclusions and future work.....</b>	<b>184</b>
6.1.	Rationale .....	185
6.2.	Conclusions.....	187
6.2.1.	Chapter 2 - Laboratory analysis of passively detected acoustic signals in recirculating flume experiments.....	187
6.2.2.	Chapter 3 - Can acoustic signals help to understand sediment transport in a sand-bed river?.....	188
6.2.3.	Chapter 4 - Passive acoustic monitoring of turbidity currents within submarine channel systems.....	189
6.2.4.	Chapter 5 - Initiation mechanisms of turbidity currents occurring at Bute Inlet and Squamish Delta .....	190
6.3.	Wider implications.....	192
6.3.1.	Wider implications for flume experiments.....	192
6.3.2.	Implications for studying turbidity currents within submarine channel systems and geohazard assessment.....	192
6.4.	Future research.....	193
6.4.1.	Weak relationships in Río Paraná data.....	193
6.4.2.	Passive acoustic monitoring of submarine canyons.....	193
6.4.3.	Sediment transport assessment around offshore windfarms .....	194
6.4.3.1.	Why is it important to monitor windfarms? .....	194
6.4.3.2.	How can sediment-generated noise be used to monitor windfarms? .....	195
<b>7.</b>	<b>Bibliography .....</b>	<b>196</b>
<b>8.</b>	<b>Appendices.....</b>	<b>226</b>
8.1.	Appendix A.....	226

# Chapter One

---

## Introduction to the thesis



*Figure 1.1. Remote passive acoustic instrument deployed on the seabed (NOAA, 2018).*

## 1.1. Underwater acoustics: an introduction

Within the natural environment, underwater acoustics is the study of the propagation of sound within water, and how sound interacts with objects within the water. Underwater acoustics has a long history, with figures such as Aristotle mentioning changes to sound travelling within water (Johnstone, 2013). Since then, scientific understanding has advanced, with the first research paper on underwater acoustics being published in 1919, to where underwater acoustic methods are widely used for many marine site investigations (Lichte, 1919; Duguid, 2017).

The study of acoustic noise generated by sediment is very broad and important. This is because acoustics can be used to monitor bedload transport, geohazards and scour in the natural environment (Pensieri and Bozzano, 2017). Acoustics can generally be split into two forms based on active or passive acoustic signals (Pensieri and Bozzano, 2017; Melo *et al.* 2021).

Active methods emit an acoustic pulse and then listen to its echo (Pensieri and Bozzano, 2017). Active methods predominantly comprise of multibeam echo sounders (MBES), side-scan sonars, sub-bottom profilers and seismic surveys and acoustic Doppler current profilers (ADCPs) (Jobson *et al.* 2016). These active methods are usually used in the exploration of oil and gas, monitoring of the water column and, more recently, for monitoring offshore windfarms (O'Brien, 1983; Mondol and Bjørlykke, 2010; Haught *et al.* 2017; Montereale-Gavazzi *et al.* 2019; Chen and Tian 2021). Recent studies, such as those within both the Congo and Monterey Canyons, have shown that they are also useful for monitoring poorly understood large-scale seabed sediment flows colloquially known as turbidity currents, such as with ADCPs (Smith *et al.* 2005; Talling *et al.* 2022). The benefit of using active acoustic methods is that they can give a spatially high-resolution images of turbidity currents in action (Talling *et al.* 2022). However, two disadvantages of active methods are their cost and manpower, as they are typically deployed using powered surface vessels. They also use high levels of energy, so if they are deployed onto the seabed, they cannot collect data for significant periods of time (Clare *et al.* 2020).

Within recent years promising alternative bedload transport monitoring techniques have been developed (Rigby *et al.* 2015; Gaida *et al.* 2020). These new techniques use passive acoustics in order to remotely monitor sediment transport, geohazards, and scour (Fig. 1.1). The ability to remotely deploy these instruments can, in turn, reduce cost and labour. These passive sensors

do not emit sound and only detect incoming signals. Thus, they have much lower energy requirements than active sensors that emit their own sound pulses. This removes the demand for a high energy source, cutting down costs, increasing battery life and deployment durations. Their relatively low cost allows more passive sensors to be placed over larger areas of the seabed. Such sensors can cover the same area as a survey vessel while also giving a more continuous data set, allowing for a more temporally detailed analysis of processes occurring on the seabed (Bassett *et al.* 2013; Rigby *et al.* 2015).

Within both the marine scientific and offshore wind development communities, there is a need for the development of new equipment and methods to monitor sedimentary processes. This results from the destructive capabilities of geohazards within the deep marine environment and the scale of new offshore developments (Weinert *et al.* 2015; Clare *et al.* 2020). The development of new active and passive acoustic methods for monitoring sediment transport will be able to help further understanding of these deep marine geohazards and, eventually, help to create a listening network to locate and quantify where sediment transport occurs. After this, marine infrastructure can avoid those locations, saving costs. Passive methods could also increase the monitoring capability for offshore wind installations, and such monitoring urgently needs improvement due to the infrequency of marine vessel-based surveys (Arnot *et al.* 2014; Weinert *et al.* 2015). The improvement in monitoring could thus reduce maintenance costs and avoid catastrophic failures of offshore turbines. Any reduction in maintenance costs for offshore wind by passive monitoring could help further reduce the price of renewable energy production. This is highly desirable, as it will help to pivot the world away from fossil fuels.

## 1.2. Active acoustic methods

This section gives an introduction to the active acoustic methods used to monitor changes to the seabed and the water column. This thesis only uses two active methods, multibeam swath bathymetry and ADCPs. Therefore, this section will exclude other active methods, only describing multibeam swath bathymetry and the uses and limitations of ADCPs.

### 1.2.1. Types of active acoustic method

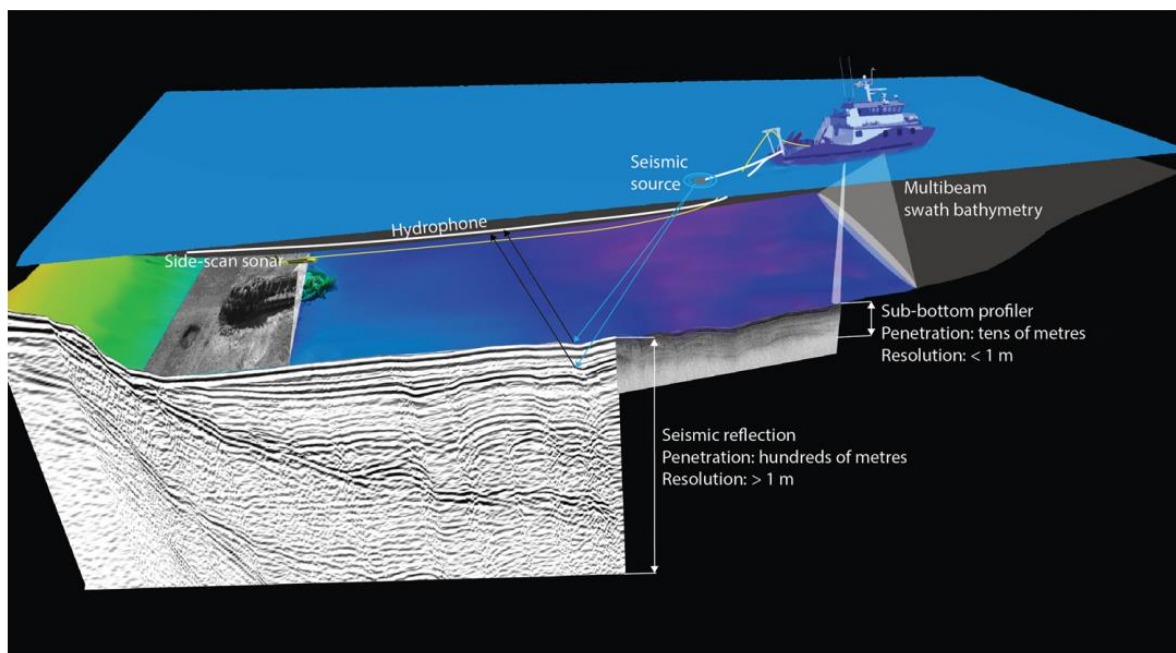


Figure 1.2. Principles of side-scan sonar, seismic, sub-bottom profiler and multibeam echo sounder surveys.

There are multiple forms of active acoustic methods used to monitor the environment (Fig. 1.2). For monitoring the seabed and subsurface, these methods include side-scan sonar, sub-bottom profiler, seismic reflection/refraction surveys and multibeam echo sounders (Sea Beam, 2000).

In addition, ADCPs, which are also an active acoustic method, can be used to measure velocity profiles of the water column. This is commonly performed from either a fixed position (e.g. mooring), or via an ADCP attached to a moving vessel (Yoo *et al.* 2009; Huang, 2019; Clare *et al.* 2020).

### 1.1.2.1. Multibeam echo sounder principles and limitations

Most active methods use broadly similar principles to collect data. Methods such as multibeam swath echo sounders emit sound waves of controlled frequencies, which are then reflected off the seabed, and then returned to a receiver (Sea Beam, 2000).

Multibeam echo sounders use two orthogonally disposed transducers, which are typically mounted to the bottom of a ship's hull or pole mounted over the side of the vessel (Zwolak, 2015; Jakobsson *et al.* 2016). This method uses a transmitting transducer to emit an acoustic beam in a wide plane, which is perpendicular to the receiving transducer, and in a narrow plane parallel to the transducer (Zwolak, 2015). This beam is then reflected off the seabed, and due to the setup of the multibeam system, the receiving transducer only receives a reflected acoustic signal from the bottom within a narrow-angle in a plane that is perpendicular to the survey line (Fig. 1.2; Zwolak, 2015). As the vehicle moves forward, successive reflected returns build up a successive swath corridor (Hughes Clarke, 2018). The maximum footprint of the multibeam is dependent on the water depth, and this footprint increasing as the water depth increases (Hughes Clarke, 2018).

Multibeam swath bathymetry uses the principle that water depth ( $D$ ) can be inferred from knowing the acoustic velocity of water ( $v$ ) and the recorded two-way time ( $TWT$ ), which is the time taken for the emitted signal to be received again (Eq. 1.1):

$$D = v \times \frac{TWT}{2} \quad (1.1)$$

In order to use multibeam systems, there are many corrections and limitations that need to be accounted for; for example, maximum swath angle (maximum beam angle) is affected by three factors. The first factor, which is present in all active systems, is that not all energy is emitted in a single direction, with some being emitted off in alternative directions, such as vertically (IHO, 2005; Liu *et al.* 2019; Desanto and Sandwell, 2022). These secondary lobes of energy are called side lobes and are described as secondary lobes of energy that appear in the response pattern of a beamforming system (IHO, 2005; Liu *et al.* 2019; Desanto and Sandwell, 2022; Nortek, 2022). This vertically emitted sound can reflect off the sea surface and then the seabed. If this occurs, its two-way travel time can become equal to energy emitted at a 60° angle from the multibeam system. As a result, data above 60° swath angle is commonly discarded, as it is difficult to separate real data from erroneous reflections. This effect means that swath angles

are limited to around 3.5 times the vertical ocean depth (IHO, 2005; Liu *et al.* 2019; Desanto and Sandwell, 2022). The second factor which can affect the maximum swath angle is that multibeam systems are easily affected by non-uniform sound velocities in the ocean (Lurton and Jackson, 2004). Therefore, profiles of sound velocity through the water column are commonly taken, particularly in volumes of water with high sound speed stratification and mixing between different water bodies (Lurton and Jackson, 2004). However, this non-uniformity can still cause an emitted sound pulse's ray path to bend outwards. At large swath angles of 90°, this bend can be so severe that the emitted sound may never reach the ocean floor (IHO, 2005; Desanto and Sandwell, 2022). The final factor is attenuation; if there is strong attenuation within the ocean, then the sonar will not be able to detect any returning energy (IHO, 2005; Desanto and Sandwell, 2022).

It is noted that higher frequency waves are more strongly attenuated along acoustic travel paths than lower frequency waves, but higher frequency waves provide higher resolution (Desanto and Sandwell, 2022; Kongsberg, 2023). As a result, swath multibeam system manufacturers such as Kongsberg have created multiple-frequency multibeam systems, thus allowing users to select the best frequency to use for a given location (Kongsberg, 2023).

Depending on the survey area's water depth, different frequencies ranging from 3.5 kHz – 500 kHz (Ainslie and McColm, 1998; Desanto and Sandwell, 2022; Kongsberg, 2023). The highest frequencies (500 kHz) are especially suited for shallow water depths (10's of metres), and lower frequencies (3.5 – 12 kHz) are better suited for deeper water depths of up to 11,000 m (Ainslie and McColm, 1998; Desanto and Sandwell, 2022; Kongsberg, 2023).

As multibeam echo sounders are normally attached to the keel of a floating vessel, multibeam systems are affected by the vessel's roll, pitch, yaw and heave. As the vessel moves around, the multibeam system constantly changes its grazing angle, meaning that any bathymetric image is not commonly created in one single continuous line (IHO, 2005). Also, due to the boat moving in the water, its relative position and height need to be known in time with each returned ping; GPS measurements and tidal curves are commonly used to correct this. As a result, both measurements of the boat's attitude (Yaw, Pitch, Roll) and position (Navigation) are constantly taken. These sensors are used to measure the position (Navigation), and changes in attitude (Yaw, Pitch, Roll) can gradually shift position and are commonly not next to one another (IHO, 2005). Therefore, data misalignment and time delays can arise, resulting in offset

data. In order to correct this, Patch Tests are performed; this test calculates any errors within each variable and then provides a solution to correct them (Guériot *et al.* 2000; IHO, 2005).

Multibeam systems can even be affected by bubbles. Bubbles naturally occur in the sea through varying factors such as breaking waves, raindrops or gas hydrates bubbling up from the sea floor (Sebastian and Caruthers, 2001). These bubbles can attenuate sound and even appear as an unwanted source of strong backscatter, given the strong impedance mismatch between the bubbles and the surrounding medium and the resonant behaviour of bubbles in the presence of an incident sound wave, hindering any multibeam survey (Urban *et al.* 2017).

Finally, two considerable limitations of multibeam swath bathymetry are the cost and time required to perform these surveys. Due to multibeam systems requiring vessels, specialist personnel are also needed to operate the complex equipment, which raises costs (Yan *et al.* 2018). This high cost reduces the number of times that surveys can be performed. It should be noted that there are exceptions to this low temporal resolution. For example, areas such as busy commercial harbours that require regular dredging will be more frequently surveyed, but this still will come with a high commercial cost (ABP, 2023).

#### *1.1.2.2. Acoustic Doppler current profilers (ADCPs)*

ADCPs, as their name describes, use the Doppler effect to measure the relative radial velocity of the water column. This is performed by emitting a sound pulse at a fixed frequency, particles within the water column then scatter this sound (producing a Doppler shift in sound frequency, and a small proportion is reflected back (and Doppler shifted again) to the ADCP. The Doppler shift in both directions is caused by the relative motion of the particles that are backscattering the sound. During the Doppler shift, the phase and frequency of the emitted and incoming sound change. The ADCP then uses this to calculate the velocity of objects within the water column (Eq. 1.2) (Teledyne RDI, 2011):

$$f_D = 2f_s \left(\frac{V}{c}\right) \quad (1.2)$$

Where  $f_D$  is the doppler shift frequency,  $f_s$  is the frequency of the sound during no movement.  $V$  is the relative velocity between both the sound source and scatterers (m/s).  $c$  is the speed of sound (m/s) (Sontek, 2000; Teledyne RDI, 2011).

ADCPs commonly use multiple (four) beams pointed in different directions. The use of four beams allows trigonometric relations to convert current speed into (East, North and upward) components within the water column (Sontek, 2000; Teledyne RDI, 2011).

As for multibeam echo sounder systems, ADCPs can emit different frequencies. The different frequencies contain very similar trade-offs with higher attenuation for higher frequencies, meaning that the ADCP's effective ranges become shorter. But with the higher frequencies comes better spatial resolution (Sontek, 2000). Manufacturers such as Teledyne and Sontek produce ADCPs with frequencies up to 3 MHz and as low as 25 kHz (Sontek, 2000; Teledyne RDI, 2011; Priego-Hernandez *et al.* 2019).

ADCPs can be affected by numerous limitations. Over the years, corrections have been put in place to reduce the effect of these limitations. The first of which is that ADCP transducer vibrates to produce a sound wave; it does not immediately stop vibrating (Nortek, 2022). Therefore, if any measurement was taken immediately, noise emission from ADCP itself would interfere with the recording. In order to mitigate any interference, ADCP beams always have a blanking distance, which is a distance in which no measurements can be made directly in front of the ADCP (Sontek, 2000; Teledyne RDI, 2011; Nortek, 2022). Adding an area where no measurements are taken helps to improve data quality, as it gives time for the ADCPs transducers to settle before any echo is recorded at the receiver (Nortek, 2022). It should be noted that the blanking distance increases in size with reduced frequency (Sontek, 2000; Teledyne RDI, 2011).

Another limitation is that by using trigonometric relations from measurements in different places, one must assume that for an ADCP, current velocities are horizontally homogenous. Commonly this is a reasonable assumption, but in some situations, such as a turbidity current, velocity is not horizontally homogenous and consequently, accuracy will be reduced (Sontek, 2000; Teledyne RDI, 2011; Paull *et al.* 2018). Therefore, the error velocity (the difference between two estimates of vertical velocity) is recorded to improve accuracy. This allows for the evaluation of horizontal homogeneity (Sontek, 2000; Teledyne RDI, 2011).

ADCPs are also limited by the fact that in order to operate, they require scatterers such as zooplankton and sediment within the water column. In areas devoid of scatterers, measurements might not be returned, or the low number of scatterers can increase the error of

measured water column velocity as, at times, scatterer velocity may not always be equal to the water velocity (Sontek, 2000; Teledyne RDI, 2011).

For ADCPs, the speed of sound within the water must also be computed accurately. When computing the speed of sound, the ADCP assumes that the temperature and salinity measured at the transducer are constant throughout the water column. This is not always the case and can lead to errors in calculations in changing water columns (Sontek, 2000; Teledyne RDI, 2011; Zhang *et al.* 2021).

Just like multibeam systems, ADCPs generate side lobes when emitting their active pulse (Nortek, 2022). These side lobes can reflect off boundaries such as the water surface, creating strong echoes that can contaminate desired received signals from the water column (Nortek, 2022). In order to try and reduce side lobe interference, the ADCPs use narrow beam widths around  $1^{\circ} - 5^{\circ}$  and side lobe suppression (35 dB) in areas outside the beam (Sontek, 2000; Teledyne RDI, 2011).

Bubbles can also affect ADCPs from events such as rough seas creating breaking wave-generated bubbles. The bubbles can severely attenuate the transmission of sound and, in some cases, block any incoming signal from being received (Sontek, 2000; Teledyne RDI, 2011). Furthermore, as is the case also for swath multibeam echo sounder systems on boats and moorings, ADCPs can be rocked around. Therefore roll, pitch and yaw of the ADCP must be recorded in order to self-correct any measurements.

Finally, during the deployment of any ADCP onto a mooring, the measurement frequency and battery life must be considered. This consideration between measurement frequency and battery life is due to ADCPs being active systems. Therefore, ADCPs require a high amount of energy to emit and receive any signal. As a result, ADCP batteries drain rapidly, meaning that they cannot record for very long on the seabed, or they have to be modified to take measurements less frequently, reducing their temporal resolution (Sontek, 2000; Teledyne RDI, 2011; Clare *et al.* 2017,2020).

## **1.3. Understanding sediment transport using passive acoustic signals**

*This section now focuses on how sediment transport generates passive acoustic noise, key parameters that can be calculated from such noise, and the factors that control the amplitude and frequency range of sediment-generated noise. Firstly, this section introduces basic modes of sediment transport within different environments, which is then followed by a description of the physical processes by which sediment transport generates acoustic noise and the types of bedforms which can be produced by these processes.*

### **1.3.1. Sediment transport**

#### *1.3.1.1. Modes of sediment transport*

The mechanisms behind sediment transport are not fully understood and are complex (Margalit, 2017; Cook and Dietze, 2022). Presently, the established theory for sediment transport within the marine environment is that there are often two main modes of sediment transport: bedload and suspended load (Garde and Rang Raju, 1985; Chadwick and Morfett, 1998). As flow velocity or shear stress exerted on the bed increases, a point is reached where particle contact and gravity forces are overcome by the fluid force exerted by the flow, causing bedload transport. This will cause the incipient motion of sediment and is called the critical threshold of velocity or shear stress for motion (Miller *et al.* 1977; Ali and Dey, 2017; Zhang and Yu, 2017). High shear stress relative to the particles settling velocity causes grains to discontinuously roll or slide along a bed while always maintaining contact with the bed (Garde and Rang Raju, 1985; Chadwick and Morfett, 1998). Any further increase in shear stress or velocity will allow particles in motion to rise temporarily from the bed in a ballistic path, which is called saltation (Kok, 2010).

If shear stress increases even further, such that the upward component of turbulent velocity is greater than the settling velocity of a particle, the particle can become permanently suspended in 'suspended load' transport (Garde and Rang Raju, 1985; Chadwick and Morfett, 1998).

### *1.3.1.2. Shear stress variability in tidal and riverine environments*

Within a tidal environment, bed shear stress rises roughly four times a day with the diurnal tide (Brennan *et al.* 2002). Bed shear stress increases on both the flood and ebb tide, and when it increases, erosion may occur (Brennan *et al.* 2002). There is also variation in shear stress depending on spring and neap tides. During spring tide, bed shear stress increases above normal levels, which increases erosion and sedimentation (Allen and Homewood, 1984; Brennan *et al.* 2002; Baeye and Fettweis, 2015). Wave and current action generated during storms can also affect shear stress. During storms, waves can reach the seabed, imparting shear forces onto it, increasing shear stress and causing bed erosion, which in turn may cause bedforms to migrate (Flemming, 1988; Margalit, 2017; Sequeiros *et al.* 2019).

A key control on shear stress in rivers is water discharge (Sime *et al.* 2007; Hackney *et al.* 2018; Ross *et al.* 2018). Increasing discharge may produce increased flow speed and shear stress, causing more erosion of the bed (Sime *et al.* 2007; Ross *et al.* 2018).

In both riverine and tidal environments, shear stress exhibits local variation. This is because bedforms can affect flow dynamics, thus affecting shear stress, which in turn affects many benthic processes, such as sediment transport and bed stability (Parsons *et al.* 2005; Etminan *et al.* 2018).

### *1.3.1.3. Bedform development*

Multiple different types of bedform occur in marine and fluvial environments, depending on flow and sediment bed conditions (Margalit, 2017). The smallest and most common form of bedform are ripples. Ripples are on the scale of a few centimetres and can be classed into two subcategories (Current and Wave; Fig. 1.3). This form of bedform is representative of low-velocity flow conditions (Kennedy, 1969). There are several types of ripples. Current generated ripples form on beds which have stresses just passing the threshold of motion and are comprised of fine sediment (Kennedy, 1969; Ashley, 1990). These ripples are created in streams and tidally dominated flows and are three-dimensional asymmetrical features (Kennedy, 1969). The crest-lines of current ripples are perpendicular to the current and downstream migration direction. The second type of ripples are generated by oscillatory flows such as those due to oceans waves (Baas *et al.* 2016A). Wave generated ripples also have crest lines perpendicular to the direction of flow (Margalit, 2017). Unlike current ripples, wave generated ripples are

symmetrical and can change in polarity with the water motion. The size of ripples is independent of the depth of water and instead correlates to the size of sediment (Flemming, 1988; Margalit, 2017).

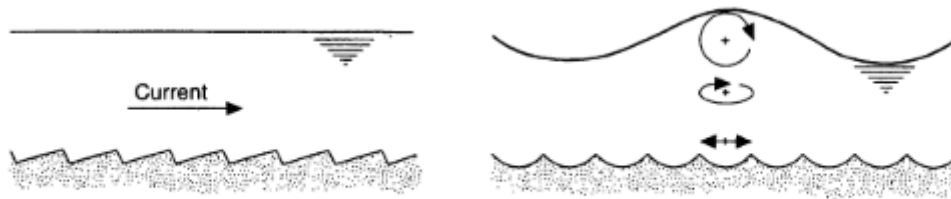


Figure 1.3. Cross-section of ripples. Left) current generated ripples, Right) wave generated ripples (Soulsby, 1997).

The next size class of bedforms are called dunes (Allen, 1980; Flemming, 1988). Depending on flow depth and corresponding flow regime, dunes can range from centimetres to metres in size (Flemming, 1998, 2000). Dunes can be found in strong unidirectional currents such as rivers and marine regions with strong flood and ebb tides. In the marine environment, dunes are sometimes referred to as sandwaves. Sandwaves, like river dunes, are usually comprised of coarser sediments and are found in flows with higher velocities than those which create ripples (Margalit, 2017).

The cross-sectional shape of a dune is moderately sloped upstream (stoss) and steeply shaped downstream (lee) (Allen and Homewood, 1984). Dunes slowly migrate in the predominant current direction. For migration to occur, sediment forming the dunes is transported up the stoss side of a dune by the flow until it reaches the crest. It then avalanches down into the trough to be deposited (Venditti, 2013). On a dune, there is a boundary layer on the stoss side. At the crest, the boundary layer separates from the dune and adjoins onto the next stoss side of the leading dune (Fig. 1.4) (Margalit, 2017). Between this, on the lee side of the aforementioned dune, a vortex is formed within its trough.

Under intermediate flow stage conditions, dunes can have ripples superimposed upon them (Guerrero, 2019). Further increases in current speeds will increase the amount of sediment being transported, which then elongates and flattens dunes present on a bed. If the current speed increases significantly, it will eventually lead to a plane bed layer where sediment is transported by sheet flow (OU, 1999).

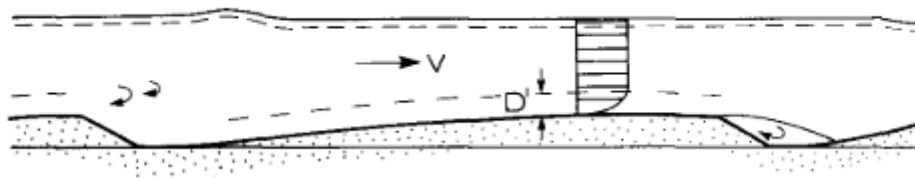


Figure 1.4. Cross-section of dunes in a unidirectional flow (Fredsoe and Deigaard, 1992).

The majority of theory for dunes applies to sandwaves, as they share similar sediment transport characteristics. For example, even if the tides are asymmetrical, unidirectional sandwaves can be asymmetrically shaped towards the mean flow direction, which could arise if one tide is stronger than the other (Allen and Homewood, 1984). Sandwaves usually have lengths that are 2 – 18 times the water depth, and their height is up to a third of the water depth (Margalit, 2017). There are multiple ways of estimating the migration rate of sandwaves; some use the shape information from multibeam/single beam surveys. However, sometimes migration rate estimations can be inaccurate as their accuracy is strongly dependent on the equipment used and the sea condition (Knaapen, 2005). A more suitable method comes from Fredsoe and Deigaard (1992) and van Rijn (1984), which relates the bedform migration rate to bed shear stress and flow depth.

The largest scale bedforms are sand bars, which are found in fluvial environments, and sandbanks and ridges in marine environments (Guerrero, 2019). In the marine environment, sandbanks are sandy bedforms which can be found in shallow seas. Sandbanks have kilometre-scale wavelengths and heights in the order of tens of metres (Amos and King, 1984). Similar to previous bedforms, the orientation of the crest of the bedform slopes with the mean current direction (Amos and King, 1984; Bassetti *et al.* 2006; Li and King, 2007). Sandbanks are generated by currents within the sea, have very low migration speeds and are thought to be relatively stable (Masselink *et al.* 2006). The gentle slopes of a sandbank mean that there is no boundary layer separation as identified for sand dunes and waves (Margalit, 2017).

### 1.3.2. What is sediment-generated noise?

Sediment-generated noise is the acoustic (sound) signal produced from particle-particle collisions (Allstadt *et al.* 2018; Huang *et al.* 2004; Kogelnig *et al.* 2014; Thorne, 2014). Within a sub-aqueous environment, when particles collide, pressure disturbances (compression/rarefaction) arise in the surrounding fluid. This results from the acceleration of a particle, and not from the particle's natural modes of vibration (Akay and Hodgson, 1978; Thorne, 1985, 1986; Koss and Alfredson, 1973). These pressure differences can be detected as an acoustic noise by hydrophones, which are an underwater form of a microphone. The detected acoustic noise is defined as rigid body radiation (Thorne, 1985, 1986; Koss and Alfredson, 1973).

Rigid body radiation can be further explained in Figure 1.5. When a particle impacts another particle, causing the acceleration of one particle ( $a_1$ ) and the deceleration of another ( $a_2$ ). This produces sound waves (rigid body radiation), which then radiate away from the particles in the aqueous environment. If the particles are of different sizes (Fig. 1.5), there is a difference in the arrival time of the sound, resulting in particles having different detected acoustic frequencies (Thorne, 2014).

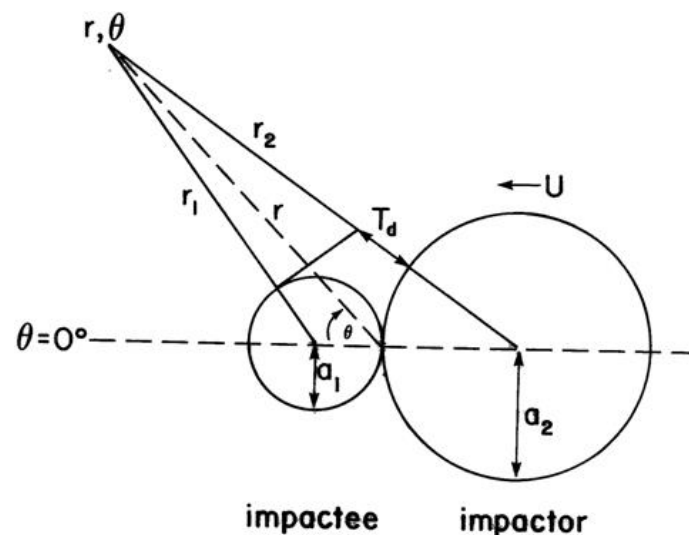


Figure 1.5. Geometry theory for different sized particles impacting and generating sound (Thorne, 2014). Impactor with a radius of  $a_2$  collides with a velocity of  $U$  into the impactee with a radius of  $a_1$ . The angle between the line of the particle's movement and the direction to the field point is  $\theta$  and  $r$  is the distance towards the field point. The variance in the arrival time of the sound emitted from the impactor particle compared to the impactee particle is  $T_d$ .

### **1.3.3. Review of laboratory experiments analysing sediment-generated noise**

*This section highlights past experiments and modelling that were performed to understand sediment-generated noise, and critically reviews each past method and its findings. This is then followed by a review of past fieldwork conducted to understand sediment-generated noise. The broad aim of this section is to understand what has been done in the past, and to identify gaps in knowledge.*

#### *1.3.3.1. Experiments in rotating drums*

Within the literature, diverse types of laboratory experiments have been used to understand sediment-generated noise. The most widely cited set of experiments were conducted by Thorne (1985, 1986, 1990). In these experiments, Thorne used a rotating drum to collide sediment, with resulting acoustic signals measured via a 1 MHz Hydrophone with a 1 – 600 kHz bandpass filter. The experiments used artificial and non-artificial sediments, whose grain diameter was between 0.16 – 97  $\mu\text{m}$  (Thorne 1985, 1986, 1990). These experiments help to determine the range of frequencies emitted by grain collisions (and thus bedload transport) for different grain sizes. The benefit of this method is that it is simple and could eliminate the noise generated by flowing water. Although, unlike marine free field conditions, the drum used was a reverberant environment, meaning that sound could echo around the drum (Rigby *et al.* 2016). In addition, it did not test the full spectrum of sediment sizes, leaving a gap in knowledge about the strength and frequency of noise emitted by flows containing clay.

#### *1.3.3.2. Experiments in flume tanks*

More recently, there have been laboratory experiments in recirculating flume tanks, as opposed to those in rotating drums. The vast majority of these flume experiments are designed to understand fluvial bedload transport, and the experiments are used for testing new methods and equipment (e.g. Wyss *et al.* 2016). Here is a review of experiments in flume tanks that used both hydrophones (for acoustic sound waves) and geophones that measure ground vibration.

There have been few previous flume studies using hydrophones to study acoustic signals from sediment transport (Krein *et al.* 2008; Barrière *et al.* 2015; Wren *et al.* 2015). For example, a study with a Japanese pipe-hydrophone developed by Krein *et al.* (2008) and Barrière *et al.* (2015) identified that the amplitude of signal increased linearly with the momentum of

colliding sediment particles (Wyss *et al.* 2016). But this method struggled to remain accurate at high sediment discharge rates (Mizuyama *et al.* 2011). In addition, it was found that a piezoelectric hydrophone could be used to identify the median grain size ( $D_{50}$ ) of the transported bedload. It was observed during these experiments that  $D_{50}$  was directly proportional to the amplitude of the first arrival waveform, and also inversely proportional to the characteristic frequency of the signal that was registered after a single particle collision.

There has only been a single previous study that used recirculating flume experiments to understand sediment-generated noise. This study used a specialised recirculating flume to test how gravel-sized sediment-generated noise in the recirculating flume (Bogen and Møen, 2003). It was successful in analysing signals emitted by very coarse (18 – 27 mm) bedload. No other studies of sediment-generated noise in a recirculating flume were found, despite such flumes having significant advantages for controlling and simulating sediment transport processes. Some of the main advantages of using recirculating flumes are that they simulate multiple environments from fluvial to tidal, and can easily change the stage and degree of sediment transport occurring. The lack of recirculating flume experiments using acoustic instruments could be the result of similar problems faced by experiments using geophones, such as high levels of pipe resonance generating too much interferant noise (Gimbert *et al.* 2019). This highlights a gap in research which is then exploited in this PhD study, as it opens up the possibility of looking into many forms of sediment transport and migrating bedforms within a laboratory setting.

#### **1.3.4. Review of past theoretical modelling of sediment-generated noise**

In the past, theoretical modelling of sediment-generated noise has also been performed. For example, Geay *et al.* (2017b) modelled a fluvial environment as a Pekeris waveguide to understand the characteristics of sound recorded by hydrophones. Their modelling showed that within a modelled river, lower frequencies exponentially attenuated with increasing range. It has also shown that high suspended sediment concentrations could attenuate sound at frequencies above 1,000 Hz (Geay *et al.* 2017b). Within this modelling, there were a few limitations present. For example, bedload flux was considered to be dependent only on water depth, whereas in reality, it pulses and varies cross-sectionally. Additionally, there were variations in monitored acoustic power in the frequency band representative of bedload transport which were not accounted for.

### **1.3.5. Review of past field studies for sediment-generated noise**

Previous field studies of acoustic noise generation via sediment transfer have often focussed on coarse (gravelly) bedload transport in rivers.

Early attempts to compare bedload transport rates using box samplers and acoustic methods required further development (Thorne, 1985; Gray *et al.* 2010; Marineau *et al.* 2015). More recently, new studies with more sensitive acoustic equipment have been conducted by authors such as Blanpain *et al.* (2007), Marineau *et al.* (2016) and Geay *et al.* (2018). One field study was conducted in the Trinity River, California, USA (Marineau *et al.* 2016), and it successfully showed a strong correlation between sediment-generated noise and bedload transport measurements. This correlation meant that models based on sediment-generated noise could predict the bedload more accurately than a discharge-based model (Marineau *et al.* 2016). The primary limitation of this study was that sediment-generated noise in the higher frequency range (>12 kHz) could not be correlated well to any particle-size class of the bedload size distribution. It was also suggested that larger particle sizes (>16 mm) could easily drown out the sediment-generated noise produced by smaller particle sizes (Marineau *et al.* 2016).

In a similar way to rivers, there have been numerous field studies of sediment-generated noise within shallow marine environments using hydrophones (Williams *et al.* 1989; Bassett *et al.* 2012; Blanpain *et al.* 2015). Data from one of these studies has been used to determine the frequency of sound emitted by different sediment sizes in motion during different tidal periods (Bassett *et al.* 2012). Another study used two different formulae for acoustic sound to predict bedload transport rates of marine sediments such as gravel (Williams *et al.* 1989). These studies provided mixed results and cautioned the use of their modified formulae in future use. Some of the main limitations of the studies were that they were restricted in the range of grain size they could measure (Blanpain *et al.* 2015). In addition, it was noted that these studies could be interfered with at times by other sources of noise within the rivers, such as boats.

### 1.3.6. Understanding controls on sound pressure level

*The following section contains two methods for predicting how sediment transport affects the sound pressure level (i.e. ‘strength’ of the acoustic signal). The first method is for bedload transport via tumbling particles, which is a common form of transport along rivers and the seabed. The second method is used when particles are moving as a sheet flow layer, which can occur at higher (and thus more hazardous) sediment transport rates. Sound pressure level is important as it can be used to infer further properties regarding sediment transport, such as sediment size (Hatcher, 2017; Hay et al. 2021).*

Laboratory experiments identified that the total sound pressure level is mainly a function of the number of particle-particle impacts taking place at a given time. This collision frequency of particles is proportional to the square root of particle concentration (Thorne, 1985; McNaught and Wilkinson, 1997). The velocity of a collision was also seen to affect the sound pressure level whilst also having a minor impact on the frequency of radiated sound (Thorne, 1985).

There are two ways of calculating the sound pressure level as a function of particle impacts. The first approach was developed through rotating drum experiments, which could simulate particles tumbling along the seabed (Thorne, 1985). Through the theory of sound generation by random particle collisions in the free field, it is possible to calculate the sound pressure level using the following equation (Eq. 1.3; Thorne, 1985):

$$P_{rms} = (\sum_{i=1}^N P_i^2)^{1/2} \approx \sqrt{NP_i} \quad (1.3)$$

The sound pressure level  $P_{rms}$  is suggested to increase with the square route of the number of sources of sound (Rigby *et al.* 2016). As predicted by Eq. 1.3, the total number of acoustic sources is  $N$ , whilst  $P_i$  is the total amount of acoustic energy emitted by a single acoustic source (Eq. 1.3). Previous studies have identified in simple cases that the mass of particles is directly proportional to the number of noise sources, and the total energy emitted is roughly equivalent to the mass of sediment creating the sound (Rigby *et al.* 2016).

The other way of calculating sound pressure level firstly involves calculating the number of particle-particle collisions. This method is optimally used when thick sheet flow layers are the main way of sediment transport; such examples may be heads of turbidity currents (Hatcher, 2017; Hay *et al.* 2021). Within the sheet flow layer, the volume concentration of particles is

assumed to be 10%. Then the particle collision frequency can be estimated using the theory of random collisions within an ideal gas (Dorfman and van Beijeren, 1997; Hatcher, 2017).

The likelihood of a collision occurring is based on the size of each particle, impact velocity and the number density of the two size classes of particles that are involved in the collision (Dorfman and van Beijeren, 1997). It is possible to calculate the number of collisions per unit time and unit volume in an ideal gas using the following equation (Eq. 1.4):

$$N_{ij} = u_{rms} \pi (a_i + a_j)^2 n_i n_j / \sqrt{2} \quad (1.4)$$

Eq. 1.4 predicts the number of collisions per unit volume per unit time. The number of collisions per unit volume per unit time for all the particles in a size class is  $N_{ij}$ . In Eq. 1.4,  $u_{rms}$  is particle velocity,  $a_i$  and  $a_j$  are the impactor and impactee sphere radii per size class, and  $n_i$  and  $n_j$  represent the number density of the particles per size class (McNaught and Wilkinson, 1997; Hatcher, 2017; Hay *et al.* 2021). In a similar way to Eq.1.3, Eq. 1.4 collision frequency is proportional to the square root of particle concentration. Once collisions per unit time is known, sound intensity radiated per unit volume per unit time can be calculated by:

$$P_0^2 = \sum_{i,j} N_{ij} \hat{P}_{ij}^2 \quad (1.5)$$

Where  $\hat{P}$  is peak pressure generated by two equally sized spheres colliding in water. It is possible to find that peak pressure ( $\hat{P}$ ) sound is proportional to  $D^{1.07} U_c^{1.25}$ , Where  $U_c$  is the impact velocity and  $D$  is mean grain diameter (Koss and Alfredson, 1973; Hay *et al.* 2021).

Hay *et al.* (2021) proposed that sound intensity radiated per unit volume per unit time ( $P_0^2$ ) is proportional to the seventh power of flow speed (i.e.  $U_0^7$ ). This was based initially on the following theoretical analysis. The flow speed ( $U_0$ ) is related to the vertically averaged sediment concentration ( $\rho$ ) by:

$$U_0 = K \sqrt{g h_0 \left( \frac{\rho - \rho_0}{\rho_0} \right)} \quad (1.6)$$

where  $U_0$  is head speed,  $K$  is a constant of order unity,  $g$  is the acceleration due to gravity,  $h_0$  is the head thickness,  $\Delta_\rho$  is the excess density of the turbidity current (i.e.  $\rho - \rho_0$ ), where  $\rho_0$  is the density of surrounding sea water (Hay *et al.* 2021). It was proposed by Hay *et al.* (2021)

that sediment concentration ( $\rho$ ) in the head of a turbidity current is proportional to flow speed squared ( $U_0^2$ ). Root mean square particle velocity can be expected to scale with mean flow speed ( $U_0$ ) in a high turbulence flow, and the number of grain collisions per unit volume and time is expected to be proportional to  $U_0^5$ , for all the particles in a size-class (see Hay *et al.* 2021). Assuming collisions occur at random, sound intensity radiated per unit volume per unit time is calculated via Eq. 1.5, which in conjunction with the nearly linear proportionality between  $\hat{P}$  and  $D, U_c$ , indicates that  $P_0^2$  should be proportional to  $U_0^7$  (i.e.  $(U_0^2 \times U_0^5)$ ). The relationship between  $P_0^2$  and  $U_0^7$  can thus be displayed by Eq. 1.7a or 1.7b:

$$P_0^2 \propto U_0^7 \quad (1.7a)$$

$$P_0^2 = aU_0^7 \quad (1.7b)$$

Taking  $10\log_{10}$  of both sides of Eq. 1.7b and re-arranging gives:

$$10\log_{10}P_0^2 = 7 \times 10\log_{10}U_0 + 10\log_{10}a \quad (1.8)$$

Equation 1.7 highlights the proportionality between sound intensity radiated per unit volume per unit time ( $P_0^2$ ) and head speed ( $U_0$ ) to the power of 7, with  $a$  being a constant of proportionality.  $10\log_{10}$  is the conversion of sound intensity to a dB scale. Equation 1.8 is thus of the form  $y = mx + c$  with the gradient,  $m$ , defined as the slope when  $10\log_{10}P_0^2$  is plotted on the y axis, when  $10\log_{10}U_0$  is plotted on the x axis.

Hay *et al.* (2021) were subsequently able to empirically verify the relationship between flow speed ( $U_0$ ) and emitted sound intensity ( $I$ ) using field data collected in Bute Inlet, British Columbia. This was done using a single moored ADCP that measured both flow front speed (through the ADCP's 4 beams) and intensity of emitted sound. Using logarithmic axes (using  $\log_e$  rather than  $\log_{10}$ ), flow speeds were plotted against intensity of emitted sound. The gradient of such a log-log plot gives the value of the exponent ( $m$ ) in Eq. 1.8. It was found that the exponent was indeed close to 7 (Fig. 1.6) (Hay *et al.* 2021).

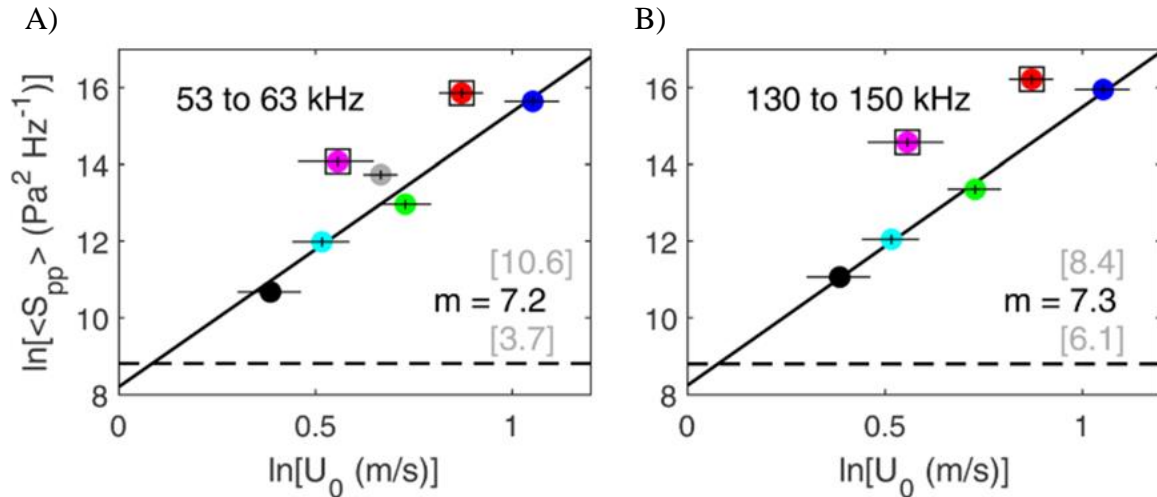


Figure 1.6. Relationship between turbidity current speed and acoustic signal strength for turbidity currents in Bute Inlet, Canada from past work by Hay et al. (2021). Head speed (m/s) versus band averaged noise spectral densities ( $P_a^2 \text{ Hz}^{-1}$ ) for 1-s intervals during turbidity current onset, for two frequency bands. A) 53 to 63 kHz and B) 130 to 150 kHz. Colours indicate the different events, error bars represent  $\pm 1$  standard error and the dashed black line indicates the background noise level. Exponent ( $m$ ), with its upper and lower 95% confidence levels in grey, is indicated in each plot (Hay et al. 2021).

### 1.3.7. Frequency of acoustic noise from particle-particle collisions

The preceding section summarised controls on the strength of acoustic signals from sediment transport. The next section discusses what determines the frequency range of that emitted sound. This section also initially discussed how acoustic signals depend on grain sizes. A summary of work using coarser gravel and sand is discussed, followed by much sparser previous work on silt and clay. The final section is on extracellular polymeric substances (EPS) and how this could influence acoustic noise signals from sediment transport. EPS has recently been found to exert a strong control on sediment stability, sediment transport and bedform generation (Tolhurst et al. 2002; Malarkey et al. 2015; Fang et al. 2017), such that it is reasonable to determine whether they affect sediment-generated noise too. The following three sections highlight ways of estimating grain sizes and bed shear stress from acoustic signals. They also identify gaps in research, such as a lack of work on the effects of finer grains and cohesive substrates on acoustic noise generation.

### 1.3.7.1. Pebbles, Gravel and Sand

A key paper by Thorne (1986) significantly advanced our understanding of sediment-generated noise. Using rotating drum experiments with hydrophones that had a range between 1 kHz - 600 kHz. Thorne (1985, 1986) identified that the peak frequency of sound generated by particle-particle collisions is inversely proportional to the diameter (Fig. 1.7) (Bassett *et al.* 2013).

A series of later papers then further developed understanding around sediment-generated noise, sometimes with conflicting results. They included work exploring how the signal's frequency is related to sediment grain size. For example, papers such as Rigby *et al.* (2016) suggest that smaller-sized sediment (e.g. sand) generates acoustic noise at lower frequencies (60 – 120 kHz), whilst Marienau *et al.* (2015) and Marienau *et al.* (2016) suggested that sand generates a signal at around 50 – 976 kHz. Rigby *et al.* (2016) (Fig. 1.7A) only plotted Thorne's (1986) data, whereas Marienau plotted more data from other papers. Therefore, it could be that the discrepancy in frequency could be due to a lack of data plotted on Rigby *et al.*'s (2016) graph (Fig. 1.7). This could have then reduced the predicted frequency when extrapolated.

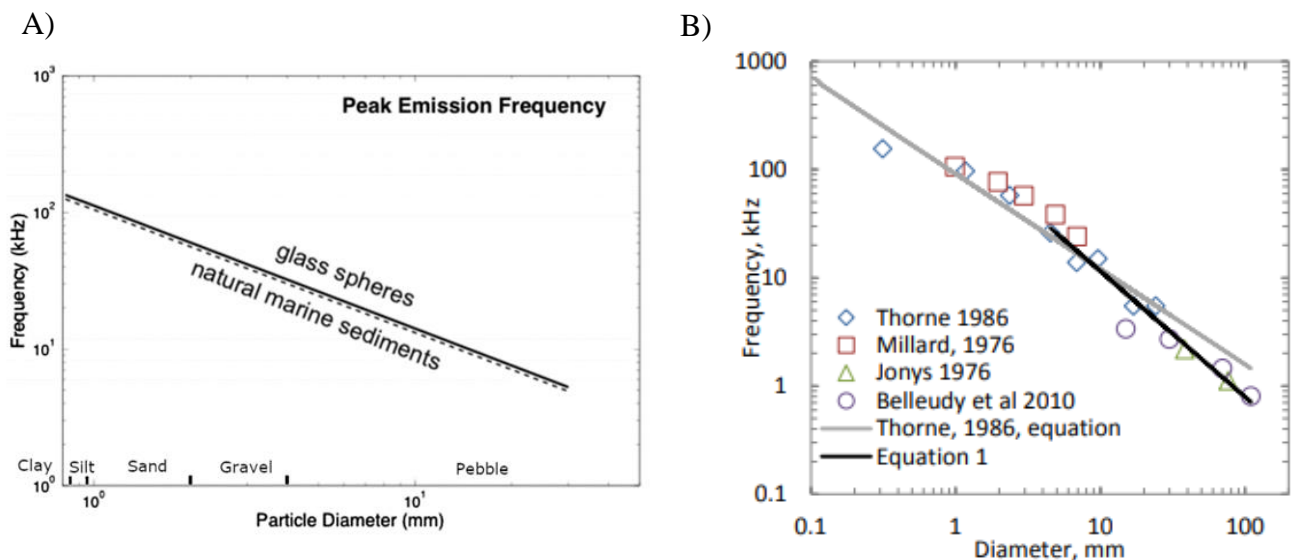


Figure 1.7. Emission frequency of sediment-generated noise from marine sediment of different sizes. A) is a modified version from Rigby *et al.* 2016. B) is a modified version from Marineau *et al.* 2015.

Name of Authors	Frequencies and grain sizes	Type of hydrophone used
Belleudy <i>et al.</i> 2010	1.5 – 2 kHz - 60 – 80 mm Pebbles  2.5 – 4 kHz - 60 – 80 mm Pebbles	44 kHz Hydrophone
Bassett <i>et al.</i> (2013)	4 – 20 kHz - gravel and pebbles	1 MHz hydrophone.
Rigby <i>et al.</i> (2015)	10 – 11 kHz - gravel	Two RESON TC4013 hydrophones which have a frequency range of 1 Hz – 170 kHz
Wood <i>et al.</i> (2015)	8 – 16 kHz - sand	Bruël and Kjaer-type 8103 calibrated hydrophone with a frequency range of 0.1 to 180 kHz
Geay <i>et al.</i> (2017a)	>1 kHz - gravel	Bruël and Kjaer-type 8103 calibrated hydrophone with a frequency range of 0.1 – 180 kHz
Geay <i>et al.</i> (2017b)	2 – 8 kHz - gravel and pebbles	Bruël and Kjaer type 8105 with a frequency range of 0.1 – 100 kHz
Geay <i>et al.</i> (2018)	0 – 20 kHz - 0 – 150 mm	HTI96 hydrophone with a sampling frequency of 312 kHz
Petrut <i>et al.</i> (2018)	4 kHz - 19 mm grains  2 kHz - 38 mm grains  1 kHz - 75 mm grains	HTI96 hydrophone with a sampling frequency of 312 kHz
Choi <i>et al.</i> (2020)	5 – 6 kHz - 9.53 – 12.70 mm sediment	Pipe hydrophone with a sampling rate of 25.6 kHz
Geay <i>et al.</i> (2020)	0 – 100 kHz - 8 – 200 mm sediment	HTI96 hydrophone with a sampling frequency of 312 kHz
Le Guern <i>et al.</i> (2021)	350 kHz - sand	Hydrophone with a frequency range of 0.015 – 480 kHz

Table 1.1. Summarisation of a number of recent studies into sediment-generated noise produced by sand and gravel sized sediment using passive hydrophones.

Most papers observed that sand, gravel and pebbles emitted acoustic signals at different frequencies (Table 1.1). This suggests that Thorne's (1986) measurements are roughly correct and could be used as a basis for using acoustic frequencies to infer sediment size (Fig. 1.7B). Therefore, it is possible to suggest that pebbles/gravel generate acoustic signals at a frequency of 1 – 50 kHz, and acoustic signals from sand have a frequency between 50 kHz to 1 MHz.

These papers also noted the potential for hydrophones to have a sample rate that is too low to measure most sediment-generated noise in the natural environment. This means that these papers, and other studies, such as Barton *et al.* (2010) and Belleudy *et al.* (2010), may have used instruments that could only detect acoustic signals from large (gravel) sediment sizes. Whilst at the same time, they were most likely only able to partially detect or entirely miss acoustic signals from finer sediment sizes, such as sand.

#### 1.3.7.2. *Silt and Clay*

It was not possible to find any direct measurement of acoustic noise from silt and clay-sized sediment in a laboratory experiment or in the field. However, multiple papers (e.g. Bassett *et al.* 2013; Rigby *et al.* 2016) theoretically suggest that silt and clay would increase the frequency of emitted sound compared to that generated by coarser grain sizes. One possible problem with this assumption relates to the structure of clay; in sea water, clay particle's negative charges are cancelled out, allowing them to become cohesive (Brindley, 1952; Carroll and Starkey 1958; Sutherland *et al.* 2014; Baker *et al.* 2017). Thus, because clay particles are cohesive, they can form into flocs when particles collide and adhere together (Winterwerp and van Kesteren, 2004). Flocs have large intravoidal spaces giving them a high water content (Rezar and Lavoie, 1993). This high water content means flocs are not solid scatters, so they might have properties closer to that of fluid spheres rather than solid elastic spheres (Thorne *et al.* 2014). In addition, the number and size of these flocs increase as the concentration of clay particles increases, and if the concentration increases further, the particles can form into a viscous gel that can suppress turbulence (Baas *et al.* 2009). Overall, the cohesive property of clay could potentially alter the frequency of sound emitted/detected, as the flocs are an accumulation of clay particles held together by Van der Waals forces (Baas *et al.* 2009). This cohesive property could have an impact, as research looking at laboratory-generated subaqueous debris flows found that if clay is added into the mixture of a flow, higher frequency sounds are attenuated due to the high viscosity of the slurry (Huang *et al.* 2004). This attenuation not only means that it might make

clay itself harder to detect; any other sediment-generated noise might also be lower in amplitude. There could also be a shift in frequency predominant frequency detected, reducing the accuracy of measurements.

Sediment-generated noise can be further visualised within a noise spectrum. An example of a noise spectrum is shown in Fig. 1.8. This noise spectrum was collected when there were collisions between particles of many different sizes. In Fig. 1.8, the spectral frequency is entirely dependent on sediment size, while the sound pressure level is predominantly dependent on impact velocity (Hatcher, 2017). In addition to this, when there are collisions between particles, the sound produced via an impact radiates outwards in an unequal direction (Hatcher, 2017). The predominant radiating direction is most likely the direction of impact.

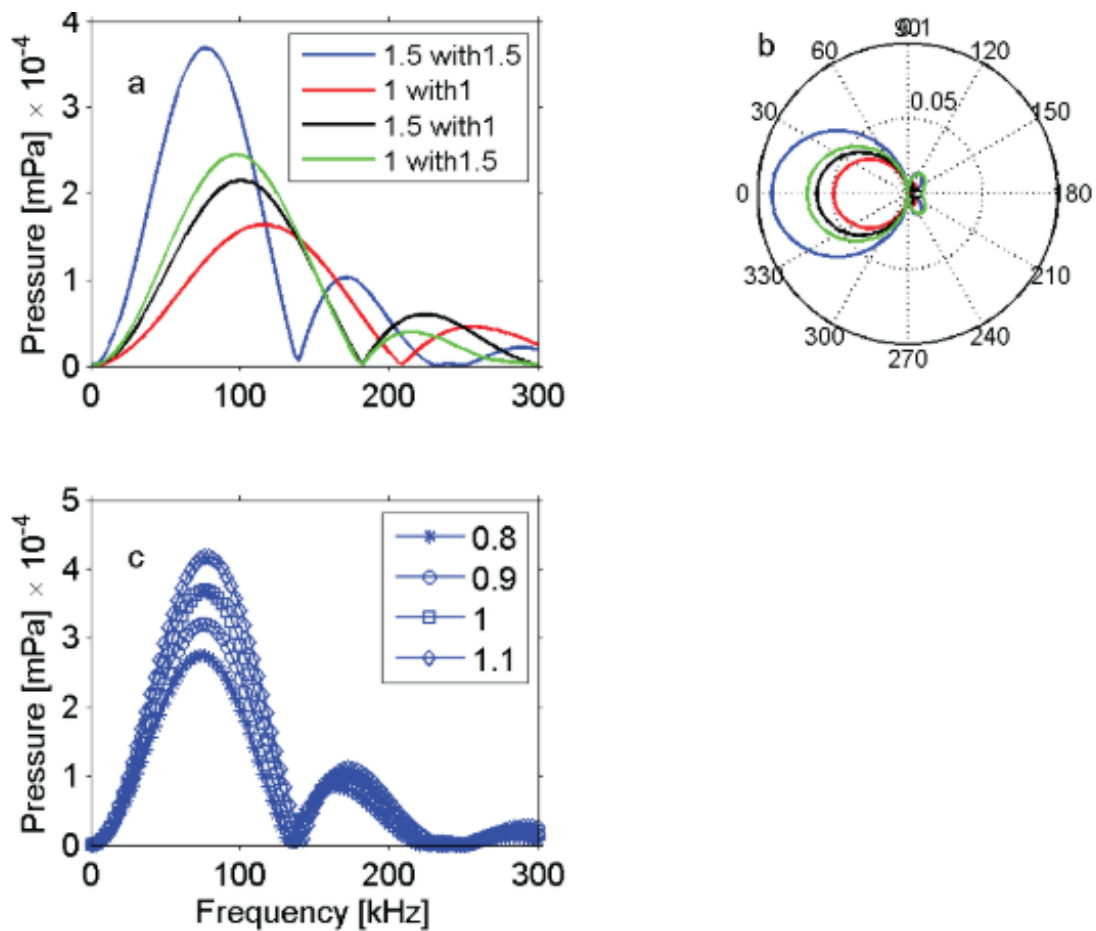


Figure 1.8. Example spectra for particles with different radii and collision speeds. (a) recorded spectra if different sized spheres collided at the same speed. (b) total spectral pressure levels verse the field point coordinate ( $\theta$ ). (c) Spectra from collisions of similar-sized particles (1.5 mm) under different collision speeds (m/s) (Hatcher, 2017).

### 1.3.7.3. Extracellular polymeric substances (EPS)

Within the natural environment, biological products play an important role in the characteristics of marine sediments and bedform dynamics (Malarkey *et al.* 2015). These biological products are called extracellular polymeric substances and are secreted by various benthic organisms such as diatoms and bacteria (Tolhurst *et al.* 2002). These organisms produce EPS as a way of stabilising sediment for their survival (Tolhurst *et al.* 2002). Research has shown that EPS acts as a binding agent for sediment. It can transform non-cohesive into cohesive sediment and increase the erosion threshold for clays or other mixtures (Tolhurst *et al.* 2002). When introduced, EPS can facilitate bio-flocculation (Lai *et al.* 2018). Bio-flocculation is a process similar to the way clays flocculate naturally in seawater (Sutherland *et al.* 2014; Malarkey *et al.* 2015; Lai *et al.* 2018). The EPS's ability to flocculate depends on the type of EPS present, its concentration and its polarity (Tan *et al.* 2014). At present, it is not possible to find any research on the effect of EPS on acoustic noise. A logical approach would suggest that EPS will have a similar effect to adding cohesive clay. EPS will most likely influence the frequency of sound emitted/detected by causing the sediment present to flocculate, attenuating a high percentage of the acoustic noise emitted. As EPS can suppress bedload transport, it could also be expected to reduce the acoustic power of any sediment-generated noise produced (Malarkey *et al.* 2015).

### 1.3.8. Predicting grain size using acoustic signals

*The following section summarises past work that has aimed to determine grain size from acoustic signals.*

Previous studies have shown that the root mean square acoustic pressures from a signal can be correlated to the mean bedload flux being monitored (Geay *et al.* 2017a). In addition to monitoring bedload flux, it is then possible to estimate the bedload diameter from the frequency of a signal (Geay *et al.* 2018). Previous passive acoustic studies in the Isère River, in France, used the following Eq. 1.7, and an inversion method that relies upon a model that predicts the acoustic field generated by the collision between particles (Geay *et al.* 2018). The acoustic measurements undertaken managed to estimate grain sizes between 5 – 100 mm that were reasonably close to those in physical sampling. However, for grain sizes below 1 – 5 mm, grain size estimations were less accurate (Geay *et al.* 2018).

$$f_{peak} = \frac{224}{D^{0.9}} \quad (1.9)$$

$$f_c = \frac{209}{D^{0.88}}$$

In Eq. 1.9,  $f_{peak}$  is the maximum frequency which relates to the largest power spectral density, and  $f_c$  is the central frequency (Geay *et al.* 2018). The measured frequencies are inversely proportional to the grain diameter  $D$ . These equations can calculate then be used to calculate the  $D_{50}$  and  $D_{90}$  grain sizes (Eq. 1.9; Geay *et al.* 2018).

The lack of reliability when estimating smaller particle sizes suggests that further investigation is required to develop new ways of accurately estimating finer grain sizes (< 5 mm) from acoustic noise.

### 1.3.9. Calculating bed shear stress

Acoustic noise has also been used in past work to estimate bed shear stress, which is a fundamental parameter for sediment transport (Bagherimiyab and Lemmin, 2013). Bed shear stress can be calculated using the law of the wall, which states the logarithm of the distance from the bed is directly proportional to the average velocity of a turbulent flow (Von Kármán, 1930; Bagherimiyab and Lemmin, 2013). With this approach, bed shear stress ( $\tau$ ) can be calculated using the following viscous sub-layer equation (Eq.1.10):

$$\tau = \mu \frac{du}{dz} \quad (1.10)$$

This equation assumes that there are two layers of differing density, the top will be water, and the lower viscous sub-layer is the bed load layer. Within Eq. 1.10,  $\mu$  is dynamic viscosity, which would be a known property of the fluid and, for water, is a function of temperature and pressure (Csuka and Olšiak, 2016).  $\frac{du}{dz}$  are the velocity gradient between the top and bottom layers. Finally,  $\tau$  is bed shear stress (Csuka and Olšiak, 2016). To calculate bed shear stress, the flow rate of the water and moving particles measured must also be calculated. One large limitation of using the law of the wall is that values calculated via the wall-function are not able to accurately represent regions of laminar flow (Eça *et al.* 2015).

### 1.3.10. Calculating directionality

*The following sections identify how the direction of acoustic noise can be calculated, and why it is important to determine directionality (e.g. to determine where the signal originates). This is followed by a section identifying some of the sources of uncertainty in acoustic monitoring. These uncertainties are important as they can affect the data being collected.*

It is possible to determine the directivity of acoustic noise using cross-spectral methods (Bassett *et al.* 2013). In order to measure directionality, the hydrophones must be in an array. This allows the phase relationship between two independent signals to be calculated whenever there is a statistically significant value for coherence (Bassett *et al.* 2013). Using the following equation (Eq. 1.11), the square of coherence can be calculated:

$$\gamma_{12}^2 = \frac{|S_{12}(f)|^2}{S_{11}(f)S_{22}(f)} \quad (1.11)$$

In Eq. 1.11,  $\gamma_{12}$  = coherence,  $S_{12}$  is the cross-spectrum.  $S_{11}$  is the first signals auto spectrum and  $S_{22}$  is the second signals auto spectrum, and  $(f)$  – frequency dependant (Biltoft and Pardyjak, 2009; Bassett *et al.* 2013).

It is essential to look at directionality. Indeed, this will be the next step in innovation for passive underwater acoustic methods. This will be carried out by deploying hydrophones in arrays instead of being placed at a single site on the river or seabed. The benefit of placing hydrophones in arrays is that they can identify the direction and distance of a sound source (Bassett *et al.* 2013). This helps to process signals of interest and reduce noise contamination. Arrays can filter out most noise from other directions and increase the signal-to-noise ratio allowing hydrophones to hear hard-to-detect signals (Soni, 2017).

Another future innovation is to use different hydrophones. Instead of using omnidirectional hydrophones, directional hydrophones should be used. This is because directional hydrophones have a higher degree of sensitivity in a particular direction (Soni, 2017). The introduction of arrays and different hydrophones will make it easier for hydrophones to discover more information about underwater processes than previously.

### **1.3.11. Uncertainties involved in acoustic monitoring**

#### *1.3.11.1. Sources of uncertainty in acoustic monitoring*

*This section summarises sources of uncertainty for studies of passively detected noise in both laboratory and marine environments. Within both environments, there are multiple factors which can impact the validity and quality of acoustic data. These factors can be present in some environments or vary in their impact on recorded acoustic noise.*

One factor that affects the quality of acoustic signals is noise pollution from other sources. Acoustic noise can be derived from many underwater sources other than particle collisions, which vary depending on the size of the particles colliding and the square route of the number of sources of sound (Lepper *et al.* 2014; Rigby *et al.* 2016). Some of these sources can be from the water itself; for example, water turbulence generates acoustic noise with a frequency of 0 – 100 Hz, bubbles produce noise between 100 Hz to 40 MHz, and surface waves have a frequency between 5 – 10 Hz (Fig. 1.9) (Wenz, 1962; Kuryanov, 1993; Veeraiyan & Rajendran, 2020). Other sources of noise can be from marine animals, which range from 10 Hz to multiple kHz, and marine traffic that has a frequency predominantly below <1 kHz (Wenz, 1962; Riccobene, 2009; Gervaise *et al.* 2012; Southall *et al.* 2017). Also, it is suggested that within the ocean, noise above >100 kHz is dominated by electronic and thermal noise (Veeraiyan & Rajendran, 2020).

Within the laboratory environment, alternative sources of noise pollution can be found. One source can be the motor used to pump liquids around instruments, such as a flume tank. This could have a similar impact on recorded noise. In general, the acoustic frequency of a motor in water could be expected to range from a few hertz to several kilohertz. However, the specific frequency depends on the specific pump and operating conditions (Liu *et al.* 2022, Fig. 1.9). For example, past experiments, such as Thorne (1985), indicated that their pump's frequency was below 10 kHz.

These sources can increase the level of sound detected, which in turn could alter the estimation of sediment concentrations. In extreme cases, noise can entirely mask any acoustic output being received by the hydrophones (Lepper *et al.* 2014).

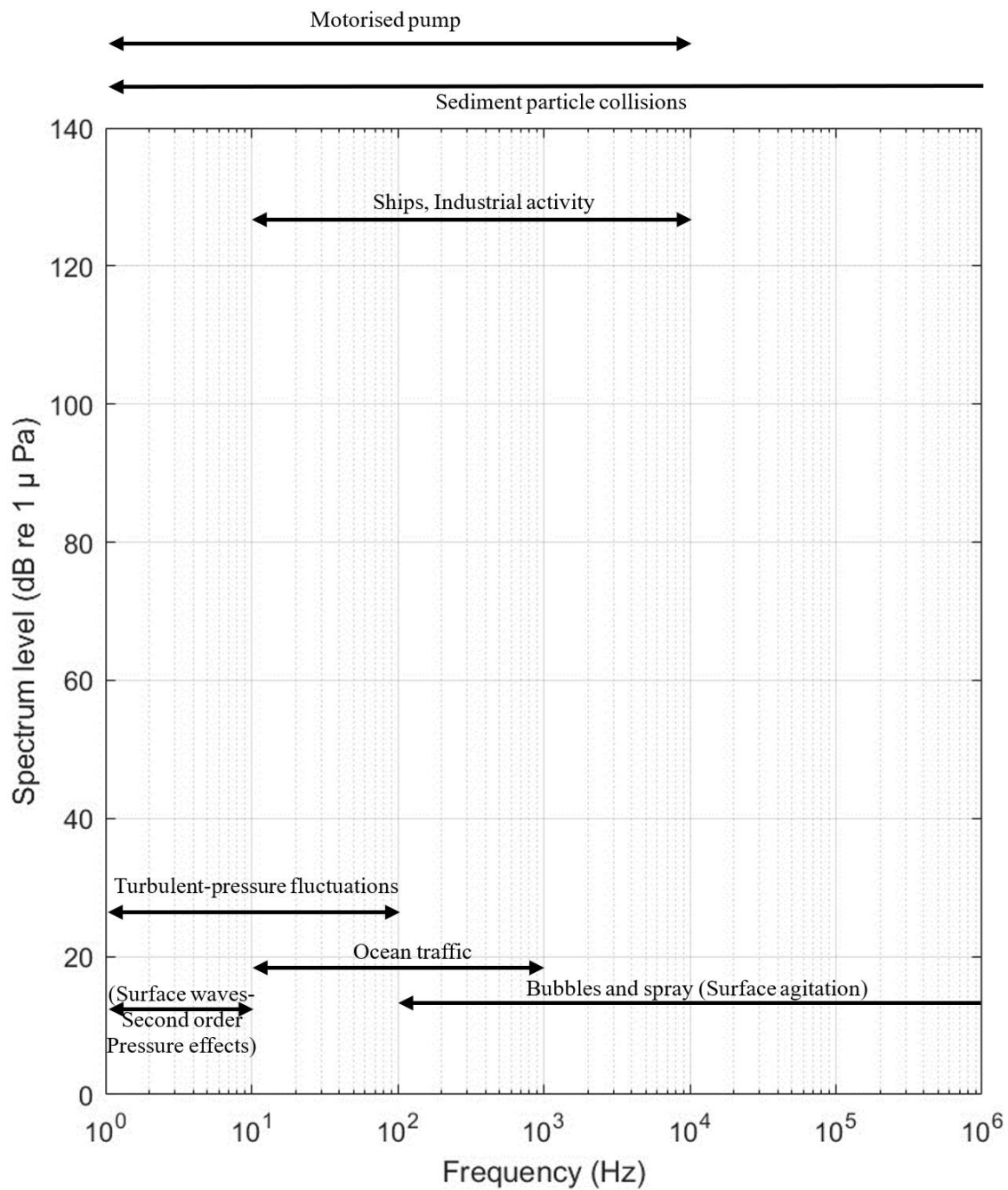


Figure 1.9. Spectrum level (dB) and frequency range for noise within the ocean and laboratory (modified from Veeraiyan and Rajendran, 2020).

Roughness of the bed can also cause diffractions and reflections (sideswipe), which can have large amplitudes (Larner *et al.* 1983; Newman, 1984; Günther, *et al.* 2006). In areas such as submarine canyons, and in laboratory experiments, noise can radiate outwards and be reflected off steep side slopes. This reflection can reverse the phase of the passively generated noise; this noise can then be detected by an acoustic instrument (Zhang *et al.* 2017). The detected noise could cancel out any directly incoming sediment-generated noise. It has been identified

that increased bed roughness can raise acoustic scattering across most frequencies; this can be attributed to a loss of signal received by hydrophones (Briggs *et al.* 2001; Ward *et al.* 2015; Ballard and Lee, 2017).

In addition to sideswipe, past experiments (Deane and Stokes, 2009; Rigby *et al.* 2015; Ward *et al.* 2015) show that the walls of a long and narrow flume tanks, and the shallow water surface, act as very good acoustic reflectors. This means that for some acoustic waves, multiple reflections off the sides of the tank can occur before the acoustic signal is received by a hydrophone. The problem with this process is that with each contact with the flume, there would be a resultant loss of amplitude, meaning that the passively detected noise would be different from the emitted noise (Ward *et al.* 2015). These flumes can also act as rectangular resonance cavities for any sustained sound source, creating a high degree of reverberation (Deane and Stokes, 2009; Rigby *et al.* 2015). These effects can create a complex sound field, meaning that any position change of the sound recording instrument can drastically alter the received result. This needs to be taken into account when recording and interpreting the data.

The matrix of the bed can influence the amount of high-frequency (>10 kHz) diffuse and specular scattering occurring (Briggs *et al.* 2001; Tesei *et al.* 2009). Past work has shown that with reducing particle size sediments increase in reflectivity and their angle of scatter, but create less scatterer, particularly within the Rayleigh scattering regime (Novo *et al.* 1989; Thorne *et al.* 2020).

At low frequencies of < 1 kHz, pressure fluctuations from turbulence can be measured by hydrophones; this is termed pseudo-sound or hydrodynamic flow-noise. Pseudo-sound is also suggested to be an influencing factor on acoustic noise (Basset *et al.* 2013). This noise is related to the wavelengths of spatial velocity fluctuations and the mean velocity of the water column (Strasberg, 1979, 1984, 1988). To calculate the frequency effect upper limit of this pseudo-sound, the following equation can be used (Eq. 1.12):

$$f = |u|\eta_o^{-1} \quad (1.12)$$

In Eq. 1.12,  $f$  is frequency,  $u$  is mean current,  $\eta_o$  is the Kolmogorov microscale. This microscale is the smallest scale in which turbulent fluctuations can occur before viscosity damps it out (Bassett *et al.* 2013).

Another potential issue with acoustic monitoring is the result of attenuation, as the strength of sound signals decreases with distance. This attenuation can also be in the form of scattering from particles in suspension and increased seabed topography which can lead to increased bed roughness (Richards *et al.* 1996, Acrement and Schneider, 1989). Attenuation can also result due to friction, which is the result of the motion of particles and fluid under the forcing of a sound wave (Fisher and Simmons, 1977).

The frequency of sound is important, as higher frequency sounds attenuate more rapidly than lower frequency sounds (Knott and Hersey, 1957). With increased distance, attenuation will alter the ratio of received frequencies, which could alter the interpretation of data. This ties together with the hydrophone listening radius, which determines how far away from a receiver any signal produced can be detected. The maximum range of a hydrophone is a function of the distance and the slant angle from a source (Kerman, 1988).

#### *1.3.11.2. Ways of mitigating uncertainty in acoustic monitoring*

In order to reduce any effect of interferent noise, filters can be applied, such as a bandpass filter to increase the signal-to-noise ratio. This can only be achieved if further amplification can be achieved without saturation. In the event of saturation, amplifiers can be added to the hydrophone after the location where the filters are applied.

To reduce the chance of detecting acoustic interference from marine fauna and shipping traffic, it is also possible to choose different locations or times for measurements (Chen *et al.* 2015). In addition to this, within laboratory experiments, background measurements can be taken. These background measurements can then be compared or subtracted from the experimental data, allowing the data to account for any interferent noise.

When looking at sediment-generated noise, reflections from the roughness of topography and side walls in a flume environment, as well as variance in the scattering of noise from differences in bed matrix, need to be considered in a 3D manner. Their effect cannot be completely removed but can be somewhat mitigated. The use of directional hydrophones and ADCPs where possible, can significantly reduce the amount of reflected incoming noise by focusing their listening points directly towards the bed instead of the surrounding area, thus reducing the chance of reflections being detected. Care must be taken when recording in a laboratory setting to ensure all environmental factors are the same for each experiment. Otherwise, results

could be significantly different, which in turn could create a false positive. Due to the focused listening points of hydrophones and ADCPs, any change in bed topography and roughness will be small over each recording and therefore is highly unlikely to affect measurements taken over riverbeds and submarine channels within this thesis. As a precaution though, the effects of reflection and scattering should be considered in the discussion of any results collected.

It is expected that pseudo-sound, which is derived from turbulent pressure fluctuations measured by hydrophones, does not have any significant impact on recordings of sediment-generated noise above  $>1$  kHz. The lack of impact from pseudo-sound on recordings of sediment-generated noise above  $>1$  kHz stems from the pseudo-sound being masked by propagating ambient noise (Bassett *et al.* 2013). The results of this fact mean that pseudo-sound will not considerably influence any experiment looking at sediment smaller than cobbles.

Finally, attenuation in relation to frequency and scattering from suspended particulate matter should be considered when planning any experiment and discussing any results. The effect, such as attenuation, cannot be fully mitigated but can be easily reduced by making sure any listening instrument, such as a hydrophone, is placed at a distance close enough to detect what is intended to be studied.

## 1.4. Applications of acoustic monitoring of sediment transport

*Acoustic signals can be used to understand sediment transport in many diverse settings. This section briefly provides background to one way in which acoustic signals can improve understanding. It focuses on how acoustic signals can help understand turbidity currents (see Chapter 4) and provides further details of what turbidity currents comprise.*

### 1.4.1. Turbidity currents

Turbidity currents are mixtures of sediment and water that are denser than surrounding sea or lake water, and therefore move down-slope (Kuenen and Migliorini 1950; Wright *et al.* 2001; Chiocci *et al.* 2011; Azpiroz-Zabala *et al.* 2017; Bernhardt and Schwanghart, 2021). They are one type of sediment-driven gravity flow - in which the driving force is linked to excess sediment density (Choux *et al.* 2005; Baas *et al.* 2016b; Hage *et al.* 2019). Turbidity currents can be triggered by submarine landslides that disintegrate and mix with surrounding water, sediment settling from surface river plumes, or river plumes that contain enough sediment to plunge and move along the lake or seabed, as well as via oceanographic processes (waves and tides) that sweep sediment into submarine canyons (Talling *et al.* 2014, 2023). External factors such as earthquakes, river floods and volcanic eruptions may supply sediment that causes a system to be primed to create turbidity currents, such as via seabed landslides (Walter *et al.* 2019; Fan *et al.* 2020; Talling *et al.* 2023). In recent years it has been realised that turbidity currents are more frequent than once thought, and occur in a far wider range of locations than previously thought (Wright and Friedrichs, 2006; Hage *et al.* 2019; Normandaeu *et al.* 2019; Heijnen *et al.* 2020; Talling *et al.* 2023).

Turbidity currents can be generally subdivided into three main sections: head, body, and tail (Fig. 1.10; Kneller and Buckee, 2000). As the flow travels forwards, mixing (entrainment) as well as detrainment can occur along the upper boundary of the body (Liu *et al.* 2023). Also, some sediment can be entrained from the bed (Liu *et al.* 2023). Within a turbidity current, processes within the head are primarily responsible for mixing with surrounding water. This mixing occurs as the ambient fluid is swept backwards ahead the head of turbidity current, and incorporated into the flow via transverse vortices, called Kelvin-Helmholtz instabilities (Fig. 1.10). These Kelvin-Helmholtz instabilities are induced by shear within the ambient fluid (Britter and Simpson, 1978; Sher and Woods, 2015; Liu *et al.* 2023). As the turbidity current

migrates, this mixture of sediment and water may then be detrained over the rear of the head, producing billows (Britter and Simpson, 1978; Baas *et al.* 2004; Liu *et al.* 2023). Lobe and cleft structures, caused by gravitational instabilities from the head's propagation, may also induce mixing at the base of the turbidity current (Fig. 1.10; Mancina, 2012; Liu *et al.* 2023). The front of a turbidity current often has a nose which overhangs, which is due to frictional resistance above the nose and no-slip conditions at the seabed (Britter and Simpson, 1978; Kneller and Buckee, 2000).

The main part of a turbidity current is its body. The structure of a turbidity current is usually dominated by fluid turbulence, where the upward directed components of fluid turbulence keep the particles in suspension (Talling *et al.* 2012). It should be noted that dense near-bed layers may be present with high sediment concentrations within some turbidity currents, where turbulence is strongly damped (Paull *et al.* 2018; Talling *et al.* 2023). This dense layer can occur in both head and body. The tail occurs at the rear of the turbidity current.

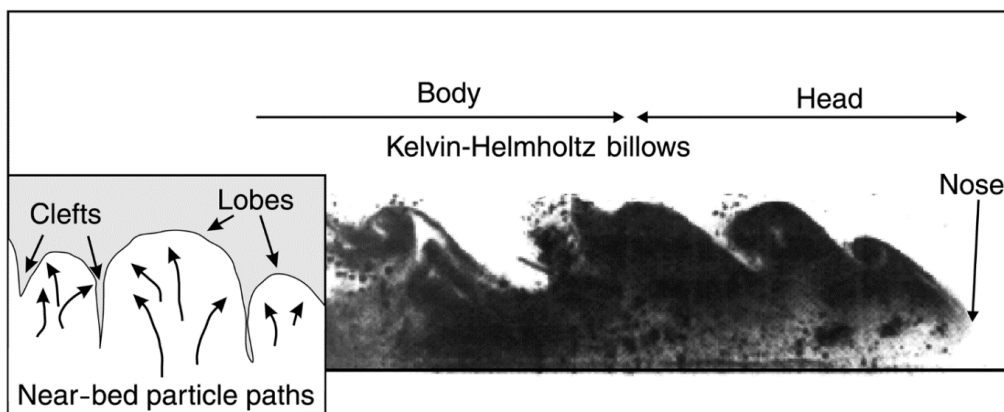


Figure 1.10. Quasi two-dimensional image of the head and body of a gravity flow. Insert shows a schematic view of lobes and cleft structures that form below the flow (figure from Kneller and Buckee, 2000).

As turbidity currents travel, their structure and density may change, such as due to sediment entrainment and deposition. Therefore, in order to try and ascertain what is occurring at any given time within a turbidity current, key parameters are used to define various properties. These properties include the bulk Richardson number ( $Ri$ ; i.e., degree of turbulence) and sediment volume concentration (%) (Pope *et al.* 2022). The bulk Richardson number is a nondimensional measure of the destabilising effect of shear, and stabilising effect of density stratification, at the interface between a turbidity current and ambient water (Salinas *et al.* 2019). Therefore, by determining bulk Richardson number, it is possible to determine the

degree of mixing and stability within a turbidity current (Ortiz and Klompmaker, 2015). Flows which are well mixed are described as having  $Ri$  ( $>0.25$ ), whereas flows with lower  $Ri$  ( $<0.25$ ) contain suppressed or no mixing (Pope *et al.* 2022). There are few direct measurements of sediment concentration in oceanic flows (Talling *et al.* 2023). But turbidity currents can range in volume concentration, with dilute flows typically having sediment concentrations of ( $\ll 1\%_{vol}$ ), and dense flows ( $>10\%_{vol}$ ) (Heerema *et al.* 2020; Pope *et al.* 2022).

The method for calculating bulk Richardson numbers ( $Ri$ ) and sediment volume concentrations via the Chézy equations (Eqs. 4.1 – 4.3) is described fully within Chapter 4.

#### *1.4.1.1. Geohazards due to turbidity currents*

Turbidity currents are geohazards, as they can erode and redistribute sediment on the seafloor, exposing buried marine infrastructure, such as pipelines and cables (Baas *et al.* 2004; Clare *et al.* 2020, 2023; Bailey *et al.* 2021, 2023). There is also a possibility that sediment deposition by flows can further bury the infrastructure. Burying can increase external pressure upon pipes causing buckling and reduce the ability of a soil to thermally dissipate, which can cause overheating of the submarine cables (Watkins and Moser, 1971; CIGRE, 2009). Moreover, if a turbidity current impacts an exposed pipeline, it could cause a rupture (Bruschi *et al.* 2006).

There are multiple historical and recent instances of turbidity currents breaking telecommunication cables (Piper *et al.* 1999; Carter *et al.* 2014; Gavey *et al.* 2017; Tajallibakhsh *et al.* 2020). One of the most notorious examples of damage was the result of the Grand Banks earthquake in November 1929 (Piper *et al.* 1999; Normandaeu *et al.* 2019). During the event, over 13 hours, a single turbidity current flow broke 12 telegraph cables (Piper *et al.* 1999; Mosher *et al.* 2006). These flows pose a significant headache, as ruptures in these cables can run in the hundreds of millions of dollars to fix and even disrupt global supply chains, potentially causing vast economic damage to the global economy (Clare *et al.* 2017).

On some occasions, turbidity currents have even been recorded to travel hundreds of kilometres, and last multiple days (Andrieux *et al.* 2013; Talling *et al.* 2022). Turbidity currents have also been seen to be able to move heavy ( $>800$  kg) objects down canyons at speeds of  $\geq 4$   $\text{ms}^{-1}$  (Paull *et al.* 2018). Most recently, one flow moved a 1,000 kg anchor some 580 m down a submarine canyon, damaging and burying it (Clare *et al.* 2020). This all suggests that turbidity currents are a significant hazard to marine infrastructure. Due to the destructive capability of

turbidity currents, they easily damage valuable equipment. As a result, presently, there are very few ways of monitoring and directly measuring them at an affordable cost (Bruschi *et al.* 2006; Clare *et al.* 2020; Simmons *et al.* 2020).

#### *1.4.1.2. Research on turbidity currents and sediment-generated noise*

There are remarkably few direct measurements of turbidity currents in action on the seabed, and understanding these events remains a grand challenge (Mohrig and Marr, 2003; Talling *et al.* 2012, 2023). Most previous attempts to monitor turbidity currents used ADCPs and multibeam swath bathymetry (Talling *et al.* 2023). The ADCPs were used to measure velocity structures, and sometimes acoustic backscatter signals from ADCPs were inverted to estimate sediment concentrations and thus driving forces (Azpiroz-Zabala *et al.* 2017; Hage *et al.* 2019; Simmons *et al.* 2020). Whilst the multibeam systems were used to try and quantify sediment erosion, and understand changes within submarine canyons over time (Smith *et al.* 2005; Paull *et al.* 2010, 2011; Hizzett *et al.* 2018; Talling *et al.* 2015, 2022, 2023). However, there are major issues with the use of ADCPs and multibeam systems alone. One of the main ones being that ADCPs need to be moored within the flow, and can thus be carried off down-flow by these powerful events (Xu *et al.* 2004; Xu, 2011). There are also significant assumptions involved in estimating sediment concentrations from ADCP backscatter, as this backscatter is equally dependent on sediment grain sizes that scatter the acoustic signal (Simmons *et al.* 2020). For swath multibeam echo sounder systems, their insight into most submarine canyons has been limited by the fact that it is difficult to perform repeat bathymetric surveys due to cost and time constraints (Smith *et al.* 2005; Talling *et al.* 2022). Therefore, multibeam surveys are commonly only carried out in one-off, semi or multi-annual patterns (Smith *et al.* 2005; Talling *et al.* 2022). As a result, there is a lack of understanding of how single turbidity currents are generated, especially in areas that contain multiple types of turbidity current initiation mechanism (Hizzett *et al.* 2018). Within this thesis, ‘preconditioning factors’ are defined as factors that allow for the generation of a turbidity current, for example high excess pore pressures within sub-seabed sediment (Bailey *et al.* 2021). Preconditioning factors may occur well before the turbidity current initiates. A ‘trigger’ is defined as the factor that starts a turbidity current (e.g. Earthquake) and ‘initiation mechanism’ is the mechanism that occurs between the trigger and the formation of a turbidity current (e.g. slope failure that transitions into a turbidity current) (Bailey *et al.* 2021).

Hydrophones could make a major advance in directly monitoring turbidity currents. They can be placed outside the flow, out of harm's way, whilst passive listening devices could be both much lower cost and make measurements for longer periods than ADCPS and multibeam systems. However, there have been very few studies into noise generated by turbidity currents, ensuring this is an important topic for further research (Hatcher, 2017).

Work by Hatcher (2017) and Hay *et al.* (2021) showed that it is possible to detect and monitor turbidity currents through sediment-generated noise. The data these studies collected showed it was possible to measure head speed and sediment concentration throughout a flow, and estimate grain sizes within the flow, based on the sediment-generated noise spectrum recorded.

The vast majority of fieldwork on sediment-generated noise has been performed in rivers and tidal environments. In this research, it is suggested that within a site which has shear stresses high enough to mobilise coarse sediment, it will be unlikely that high frequencies corresponding to fine sediment will be recorded (Bassett *et al.* 2013). The research suggested that it was not possible to detect fine sediment, because the finer sediment would have been winnowed away by the time large sediment was mobilised (Bassett *et al.* 2013). It might not be the case in turbidity currents, as they are sudden mobilisation events, which would mobilise a wide range of sediment sizes at once, allowing for the detection of fine sediments. This would mean that the full spectrum of frequencies could potentially be recorded during a single event. However, this hypothesis is yet to be tested.

## 1.5. Knowledge gaps

In conclusion, it is possible to identify apparent gaps in knowledge, and drawbacks in previous research on sediment-generated noise. A key gap in knowledge is understanding how the frequency of sediment-generated noise varies with grain sizes, especially finer grain sizes. Past work has been performed on non-cohesive large (mainly gravel) grain sizes, with few studies of acoustic noise generation by sand and mud grains. Furthermore, there is a paucity of research specifically focusing on sediment-generated noise within cohesive sediments.

Previous research highlighted a significant lack of direct measurements of turbidity currents. It also shows a need to develop new instruments to monitor these turbidity currents, which commonly damage sensors placed directly in their path. Although there is risk, active acoustic methods should still be used to monitor new sites as they are able help understand the triggering and initiation mechanisms and evolution of turbidity currents. However, in addition to active methods, passive acoustic-based sensors could be used to listen for turbidity currents whilst being located outside harm's way. These passive acoustic sensors usually have a long battery life, allowing them to be deployed for long periods of time, which is advantageous due to the intermittency of turbidity currents. Additionally, passive sensors are cheaper than active systems (e.g. ADCPs and multibeam swath bathymetry), so they can cover larger areas for lower cost.

In this initial chapter, it was only possible to find a single investigation comprising a master thesis by Hatcher (2017) and paper by Hay *et al.* (2021) relating turbidity currents to sediment-generated noise. This indicates the lack of research in this subject area. Hay *et al.* (2021) suggested it was possible to give a rough indication of grain sizes from the sediment-generated noise created during a turbidity current, but further work is required to evidence and test this interpretation this for a range of environments.

In addition to turbidity currents, there is a demand for the development of new methods for monitoring sediment transport and scour around critical infrastructure, notably offshore wind farms which have grown very significantly in number over the past decade. The need for monitoring arises as marine environments are not static, meaning they change over time and because the installation of offshore wind turbines can change a site's hydrographic conditions (Den boon *et al.* 2004; Degraer *et al.* 2012; Christie, 2014; Peterson, 2014). By changing

hydrographic conditions, wind farms can alter the direction of sediment transport and bedform morphology (CIGRE, 2009; Secomandi *et al.* 2017). Both of these could impact the stability of a wind turbine, costing money to rectify (Prendergast *et al.* 2015). The need also comes from the presence of severe issues in modern site monitoring techniques. Such issues as high costs and difficulty of repeatedly surveying sites over the life of a wind farm (Duguid, 2017).

### **1.5.1. Thesis aims**

The overarching aim of the thesis is to develop new ways of using acoustic signals to improve understanding of sediment transport processes. This will be split into two sections, with the first section seeking to determine how different factors (e.g. grain size, flow speed, bedforms etc.) determine the basic character (e.g. strength and different frequencies) of passive acoustic signals. This is followed by studies using both active and passive acoustic signals to understand sediment transport processes in complex aquatic environments, especially turbidity currents.

This aim is delivered via a set of individual chapters, which comprise as follows:

**Chapter 1** (this chapter) has introduced the use of acoustics to monitor sediment transport processes, followed by an introduction to the topic of acoustic signal generation by sediment flows and an explanation as to why it has wider importance. Chapter 1 then summarises past work on acoustic signals, both active and passively generated by sediment transport, including previous laboratory experiments, field studies and theory, in order to determine where gaps in knowledge lie. This helps to identify gaps in previous knowledge, and outstanding science questions, which then form the basis for specific aims addressed in later chapters. These specific aims are then introduced and justified.

**Chapter 2** is based on novel laboratory experiments undertaken at the University of Hull. These are some of the first experiments to use a recirculating laboratory flume to determine what controls the character of acoustic signals from sediment transport, and they involve a wider range of grain-sizes than those in almost all previous experimental studies. Chapter 2 firstly seeks to understand how sediment-generated noise is passively recorded by both a hydrophone at a wide range of frequencies from 1 Hz to 450 kHz and two ADCPs (600 kHz and 1.2 MHz) within a recirculating laboratory environment. ADCPs are included as both Chapters 3 and 4 are able to prove that active equipment such as ADCPs can be used to monitor

various types of subaerial and submarine sediment flows. Therefore, it is important to determine what can be learned from how they passively record noise generated by sediment transport within a more controlled laboratory setting. In addition, the wide range of frequencies from both the hydrophone and ADCPs helps to show how the frequency of acoustic signals vary as other parameters change. The first aim of Chapter 2 is simply to test whether sediment transport generates an acoustic signal in recirculating flume experiments, which can be distinguished from other noise sources. These are some of the first laboratory experiments to use sand-sized material (rather than gravel) and the first without a complex ‘conveyer belt’ geometry. Recirculating flumes have many advantages for studying sediment transport, and it is shown here that they can also be used to study acoustic noise from such transport. This chapter then seeks to understand, using hydrophones and ADCPs, what controls the characteristics of acoustic signals, and specifically how the acoustic signals are related to (i) grain size, (ii) bedforms, (iii) flow speeds, and (iv) mode of sediment transport (bedload or suspended load) that occur as speeds are varied. Finally, Chapter 2 specifically seeks to understand how acoustic signals recorded by ADCPs are related to flow speed during bedload transport.

**Chapters 3 and 4** use a range of unusual field data sets to better understand how acoustic signals can record sediment transport processes in both terrestrial and marine settings. The work in these chapters are informed by the results of experiments and theory developed within Chapter 2. **Chapter 3** determines the extent to which both passive and active acoustic signals recorded by an ADCP can be used to constrain sediment transport in the sandy Río Paraná in South America. Although previous studies using active acoustic methods to understand bedload transport have looked at a variety of rivers, passive acoustic sensors have almost always focussed on gravel-bed rivers, making this one of the very limited number of studies of a much finer-grained sandy river. The first aim is to develop new methods with which to analyse such signals. This chapter then tests if there is a correlation between acoustic signal strength in ADCP data and riverine flow speed, friction velocity (shear velocity,  $u_*$ ), and bedload transport rate. Finally, Chapter 3 seeks to determine if alterations in acoustic signals across bedforms is related to flow speed. In contrast, **Chapter 4** seeks to understand how acoustic signals can be used to monitor turbidity currents. This chapter again used ADCP data to isolate signals generated by sediment transport, as in Chapter 2, but this time in a very different setting. This is one of the first studies using acoustic signals to understand submarine

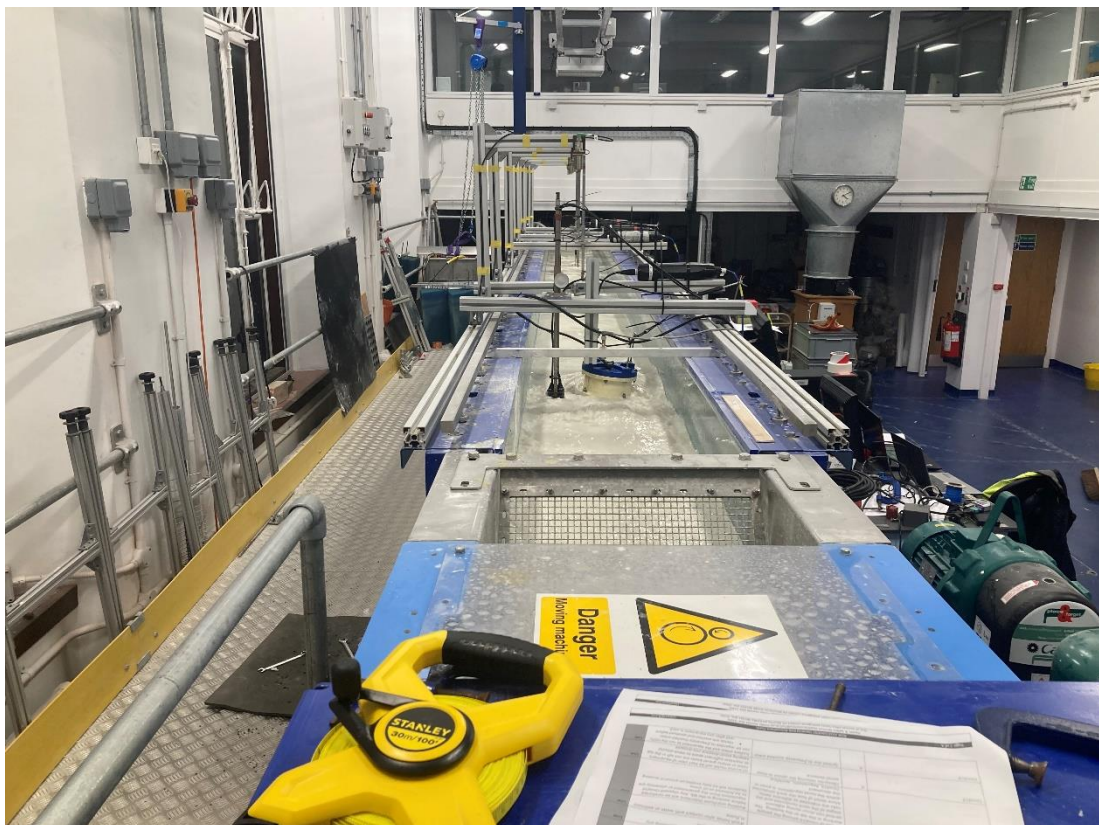
turbidity currents, extending work by Hatcher (2017), and Simmons *et al.* (2020). This chapter is the first study to compare acoustic signals generated by sediment transport from turbidity currents in multiple locations, with ADCP data from flows in Bute Inlet (Canada), Monterey Canyon (USA) and Congo Canyon (West Africa). This chapter specifically seeks to understand how acoustic signals vary through the turbidity currents (i.e. from their front to their back), and with flow speeds, or distance from the seabed to the ADCP. A final aim is to determine what causes differences in acoustic signals in the three different field sites. For example, why are strong passively detected signals recorded in Bute Inlet and Monterey Canyon, but not in the Congo Canyon?

**Chapter 5** seeks to use active acoustic methods to further enhance understanding of turbidity current evolution and their initiation mechanisms. To do this, this chapter analyses time-lapse bathymetry data collected at a new field site (Homathko Delta in Bute Inlet, Canada), which is compared to similar time-lapse bathymetric surveys at another fjord-delta in Canada (Squamish Delta). The overall aim is to improve the understanding of turbidity currents and their initiation mechanisms in river-fed deltas. Chapter 5 specifically aims to test hypotheses generated from Hizzett *et al.* (2018) from past work at Squamish Delta. First, it tests whether the most frequent initiation mechanism of turbidity currents is sediment settling from surface (hypopycnal) river plumes, rather than delta-lip landslides. Second, it tests whether events caused by delta-lip landslides or surface river plumes cause the greatest volume of seabed change. Next, the frequency and volume of seabed change due to turbidity currents in Bute Inlet and Squamish Delta are compared. Finally, Chapter 5 tests if there is a link between the initiation mechanism and runout distance of turbidity currents within Bute Inlet, and compares to past work on this topic at Squamish Delta (Hizzett *et al.* 2018).

**Chapter 6** presents the overall conclusions of the thesis, linking together key results from the preceding chapters. This final chapter then outlines how these conclusions can be used to better understand and monitor sediment transport in other locations, specifically around offshore wind energy structures. The chapter finishes by highlighting further avenues of inquiry that can be undertaken within the next generation of projects.

Appendices contain any key supplementary material required for each chapter.

# Laboratory analysis of passively detected acoustic signals in recirculating flume experiments



*A view of the entire recirculating flume setup (University of Hull, 2021).*

## 2.1. Introduction

*This section summarises previous experiments using hydrophones to understand sediment-generated noise. It introduces why passive acoustic methods can help understand sediment transport in the marine environment, and finishes with the aims and objectives of the chapter.*

### 2.1.1. Previous labwork experiments

In the past, the vast majority of experiments investigating sediment-generated noise have been conducted either in the field, typically within rivers or shallow marine environments, or via laboratory experiments using rotating drums and flume tanks (Rigby *et al.* 2016; Wren *et al.* 2015). Most of these laboratory experiments have been undertaken using rotating drums, and they have solely focused on larger sediment sizes such as gravel (e.g. Millard (1976), Thorne (1985,1986), Rouse (1994), and Barton (2006)). Experiments in recirculating flume tanks are often used to study sediment transport, but this common type of flume has only been used once to study acoustic signals from sediment transport (Bogen and Møen, 2003). Indeed, Bogen and Møen's recirculating flume experiments had an unusual setup that used a conveyor belt to add 18 – 27 mm sized sediment to the flume, and a filter basket to trap any sediment in transport before it was recirculated. This chapter thus investigates how recirculating flumes in a much simpler setup might be used to better understand controls on acoustic signals emitted by sediment transport.

There is also a paucity of data that explores how sediment-generated noise is affected by bedforms (Bogen and Møen, 2003; Geay *et al.* 2017a, 2017b), although it has been proposed that bedforms might affect how much noise is generated along their profile (Wren *et al.* 2015; Le Guern *et al.* 2021). Therefore, there is a need to further explore how recirculating flume experiments can be used to understand acoustic signals from sediment transport, extend this work to finer grain sizes than gravels, as well as studying how bedforms may affect passive noise generation.

## **2.1.2. Incentives to test and develop new passive methods**

### *2.1.2.1. Research into sediment-generated noise within river environments*

In addition to the significant lack of previous laboratory research, there are further incentives to test and develop new methods for understanding passive noise generation by sediment transport. For example, due to the paucity of published work, there is a need to better understand controls on sediment-generated noise within sand-bed rivers. Presently Le Guern *et al.* (2021) is the only field study that has measured sediment-generated noise within a sandy river. This study measured sediment-generated noise as a time series at a fixed point rather than collecting data along transects (Le Guern *et al.* 2021). Collecting data at a fixed point leaves a gap in our understanding of how sediment-generated noise varies spatially within a river, and how it relates to variable bedforms.

### *2.1.2.2. Sediment-generated noise within deep marine environments*

Another motivation of this study is to better understand sediment transport by submarine turbidity currents. Turbidity currents are notoriously challenging to measure in action in the deep sea, ensuring they were poorly understood. However, in recent years, major advances have been made in understanding turbidity currents by measuring them in action, mainly using acoustic methods (Talling *et al.* 2015; Talling *et al.* 2022).

Presently, the vast majority of these acoustic methods used to study turbidity currents involve active sources, especially ADCPs (Khripounoff *et al.* 2012; Andrieux *et al.* 2013; Clare *et al.* 2020; Simmons *et al.* 2020; Talling *et al.* 2022). One of the main problems with these active source methods is that they are energy intensive, and sensors run out of battery relatively quickly (Clare *et al.* 2020). This makes the use of passive acoustic techniques attractive, as they use far less battery power (Hatcher, 2017; Hay *et al.* 2021), and can operate for much longer periods of time compared to their active counterparts. A second, and even larger advantage, is that passive acoustic sensors might be located outside the flow in the future, and thus out of harm's way. The ADCPs used in recent studies of turbidity currents were mounted on moorings, whose anchors were located within the flow (Clare *et al.* 2020; Talling *et al.* 2022). Faster flows tended to break the ADCP's mooring lines from their anchors, resulting in the potential loss of an ADCP and its data (Clare *et al.* 2020; Talling *et al.* 2022).

Passive acoustic equipment such as hydrophones have recently been shown to detect noise emitted by turbidity currents in a pioneering study at Squamish Delta in Canada (Hatcher, 2017; Hay *et al.* 2021). Previous work has focussed on sediment-generated noise that is produced by bedload transport alone (Jones and Mitson 1982; Heathershaw and Thorne, 1985; Williams *et al.* 1989; Bassett *et al.* 2013; Hay *et al.* 2021; Katsnelson *et al.* 2021). However, this work in Squamish Delta also analysed how acoustic noise may be generated by suspended sediment in powerful sediment flows. In particular, Hay *et al.* (2021) suggest that the strength of sound ( $S$ ) emitted by turbidity currents at frequencies of 53 – 63 kHz and 130 – 150 kHz increases with faster front speeds ( $U_f$ ), with sound spectral density ( $S$ ) being proportional to front speed to the exponent of 7. This led to the following equation that allows flow speed to be inferred.

$$S = (U_f)^7 \quad (2.1)$$

This high sensitivity of acoustic signal strength to front speed can be explained by the combined dependencies of sound pressure level on particle collision speed, and that the speed of a turbidity current may increase with higher sediment concentrations and thus faster flows may have more grain collisions. Hay *et al.* (2021) modelled particle collision rate based on comparisons between the behaviour of highly sheared granular flows and ideal gases, and that of particles embedded in a turbulent fluid at the head of a turbidity current (Hay *et al.* 2021).

Eq. 2.1 is derived from the total number of particle collisions per unit time, which Hay's model assumes is proportional to  $U^5$ , whilst the radiated sound pressure that is proportional to  $U^2$  (Hay *et al.* 2021).

It should be noted that Eq. 2.1 has been proposed for turbidity currents. However, there may indeed be a similar relationship between the strength of sound emitted ( $S$ ) and flow speed ( $U$ ) in other types of sediment transport process, even if it is proportional to a different power.

### 2.1.2.3. Alternative passive instruments to monitor sediment-generated noise

A final motivation to develop new passive methods is that ADCPs are essentially complex hydrophones, which emit sound at a single frequency, and are able to heavily process the returned signal into a Received Signal Strength Indicator. ADCPs are typically used as an active instrument with restricted battery life. But if sound is indeed emitted at the correct frequency for the ADCP, it may record a passive acoustic signal emitted by sediment transport. However, work is not yet published that successfully uses ADCPs to passively listen for

sediment-generated noise (Hay *et al.* 2021). As ADCPs are commonly deployed into the natural environment (Khripounoff *et al.* 2012; Andrieux *et al.* 2013; Clare *et al.* 2020; Simmons *et al.* 2020; Talling *et al.* 2022), there is an incentive to determine if ADCPs can be used in a passive manner to detect sediment-generated noise.

One of the main benefits of using ADCPs is that conversion from being an active instrument to a passive one is very simple, and does not increase costs - as they only require modification to the ADCPs operating parameters. If tests prove fruitful, ADCPs could easily and rapidly improve understanding of sediment transport processes via passive signals.

### **2.1.3. Aims and objectives**

Chapter 2 comprises analysis of data from a 1 Hz – 450 kHz hydrophone, and 600 kHz and 1.2 MHz ADCPs with a recirculating flume experiment. These experiments were conducted at the University of Hull between March 2021 and November 2022.

The first aim of Chapter 2 is simply to test whether sediment transport generates an acoustic signal in recirculating flume experiments, which can be distinguished from other noise sources.

The second aim is to understand if sediment-generated noise can be passively recorded by ADCPs, as well as by hydrophones.

Chapter 2 then seeks to understand the controls on acoustic signals recorded by hydrophones and ADCPs, and specifically how acoustic signals are related to (i) grain size, (ii) bedforms, (iii) flow speeds, and (iv) mode of sediment transport (bedload or suspended load). Through investigating relationships between acoustic signal strength and flow speed, Chapter 2 tests whether the relationship in Eq. 2.1 occurs between power spectral density and flow speed. This is followed by an analysis how this relationship between flow speed and passively detected noise changes within flows with lower sediment concentrations than the turbidity currents considered by Hatcher (2017) and Hay *et al.* (2021).

If Chapter 2 is successful, the detection of mixtures of fine and coarse sediments within a more basic recirculating flume setup could help to understand how sediment transport can be monitored via passive acoustic sensors. Additionally, Chapter 2's research will help to determine if sediment-generated noise is related to the presence of bedforms. If ADCPs can be used to detect sediment-generated noise within the laboratory environment, this will help to

validate and understand acoustic remote sensing of turbidity currents in the natural environment at the field scale. Finally, results from these experiments seek to improve methods for experimental analysis of sediment-generated noise with laboratory flumes.

## 2.2. Flume experiment methods

*This section initially describes the equipment used to conduct sediment-generated noise experiments. Next, a description of the methods used to conduct experiments is provided, noting the differences in methods between experimental runs. This is followed by an outline of the procedures used to analyse data using programs such as MATLAB.*

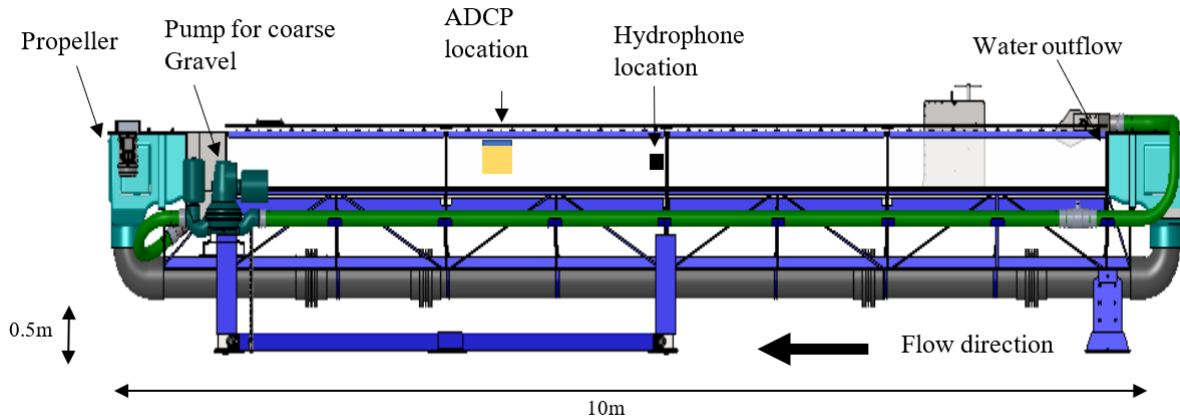


*Figure 2.1. Diagram of the recirculating flume used in Hull (modified from McClelland, 2019).*

A large recirculating flume in Hull was used to conduct a series of experiments to understand controls on sediment-generated noise (Fig. 2.1; Unsworth, 2015). This flume was 0.5 m wide, 0.5 m deep, and 10 m long. Flow of water is driven within the tank by a large propeller located on the far-left end of the tank (Fig. 2.1). These experiments were conducted in three series on different dates (Table 2.1). The first series occurred on 3<sup>rd</sup> May – 21<sup>st</sup> May 2021, the second series between 22<sup>nd</sup> November – 17<sup>th</sup> December 2021, and the final series between 7<sup>th</sup> – 10<sup>th</sup> November 2022.

The experiments used a range of different instruments to understand the nature of acoustic signals generated by sediment transport. For all three sets of experiments, a directional hydrophone with a frequency range stated by the manufacturer as 1 Hz to 600 kHz, and an external oscilloscope were used. A directional hydrophone was used as its focused transducer could help maximise the likelihood of detecting sediment-generated noise, and reduce any effect from scattered noise around the flume tank.

Data provided by the manufacturer (Benthowave) indicated that this 1 Hz to 600 kHz hydrophone has three peaks in frequency response (Fig. 2.2). The first and highest peak in frequency response is between 0 – 150 kHz, with a second peak at 260 – 320 kHz, and a final

peak at 370 – 450 kHz. For the hydrophone, these frequency response peaks are in the same location for each gain setting, except they are at different power levels. It should be noted that the hydrophone is significantly less sensitive in the band from 450 – 600 kHz (Fig. 2.2).

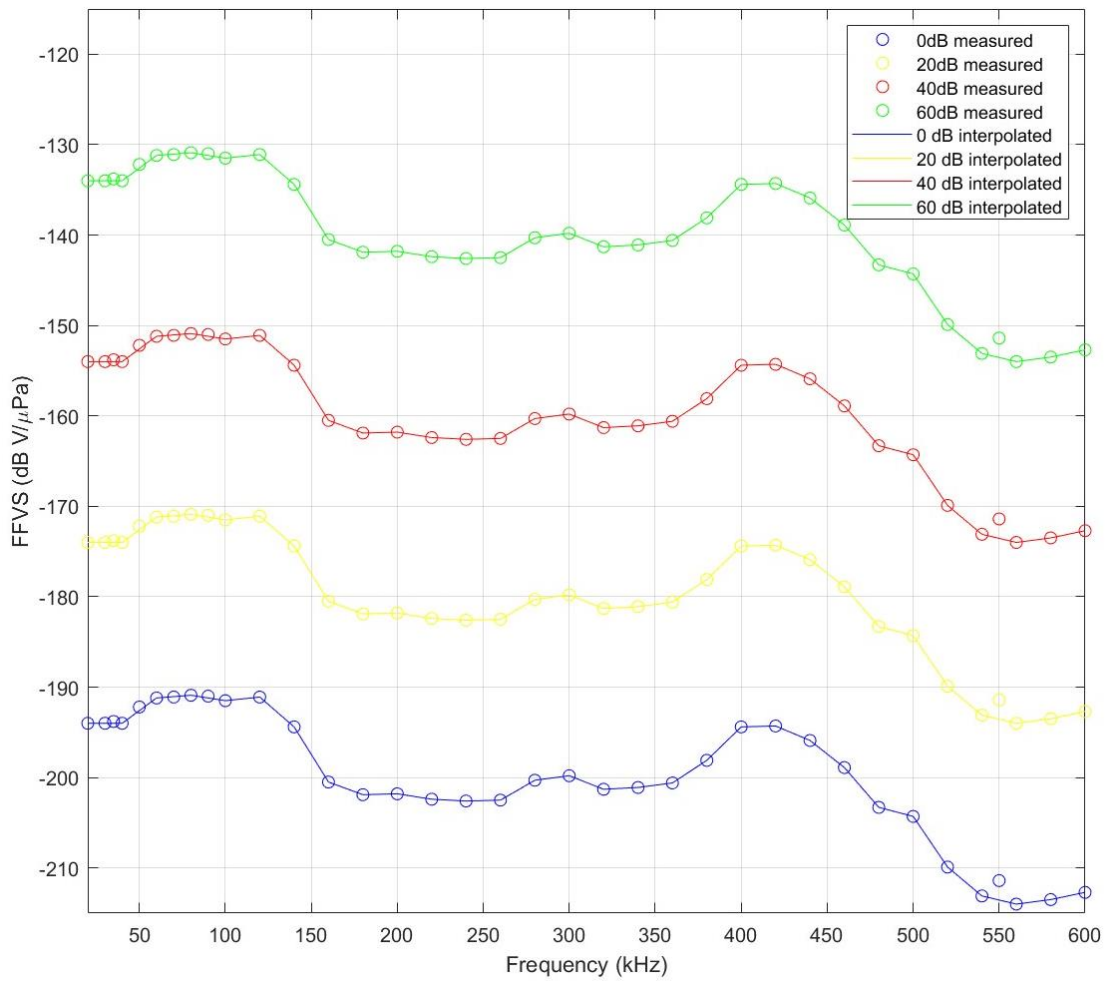


Figure 2.2. Frequency response plot for the 600 kHz hydrophone used within the experiments.

<b>First round</b>						
<b>Sediment type</b>	<b>Pump speed range (% of maximum pump speed)</b>	<b>Equipment type</b>	<b>Gain (dB)</b>	<b>Sample duration (s)</b>	<b>Filters applied</b>	<b>Sample rate (MHz)</b>
No sediment	0 – 100	600 kHz Hydrophone	40	200	N/A	2
Sand	25 – 100	600 kHz Hydrophone	40	200	N/A	2

<b>Second round</b>						
<b>Sediment type</b>	<b>Pump speed range (% of maximum pump speed)</b>	<b>Equipment type</b>	<b>Gain (dB)</b>	<b>Sample duration (s)</b>	<b>Filters applied</b>	<b>Sample rate (MHz)</b>
No sediment	0 – 100	600 kHz Hydrophone	60	300	< 100 kHz > 1 MHz	5
Sand	0 – 100	600 kHz Hydrophone	60	300	< 100 kHz > 1 MHz	5
Sand (repeat experiment)	0 – 100	600 kHz Hydrophone	60	300	< 100 kHz > 1 MHz	5
Sand + Gravel	0 – 100	600 kHz Hydrophone	60	300	< 100 kHz > 1 MHz	5
Sand + Gravel + Clay	0 – 90	600 kHz Hydrophone	60	300	< 100 kHz > 1 MHz	5
<b>Sediment type</b>	<b>Pump speed range (% of maximum pump speed)</b>	<b>Equipment type</b>	<b>Sample duration (s)</b>	<b>Ensemble sample rate (Hz)</b>		
Sand	0 – 100	600 kHz ADCP	300	2.5		
Sand	0 – 100	1.2 MHz ADCP	300	1.6		
Sand + Gravel	0 – 100	600 kHz ADCP	300	2.5		
Sand + Gravel	0 – 100	1.2 MHz ADCP	300	1.6		
Sand + Gravel + Clay	0 – 90	600 kHz ADCP	300	2.5		
Sand + Gravel + Clay	0 – 90	1.2 MHz ADCP	300	1.6		

<b>Third round</b>						
<b>Sediment type</b>	<b>Pump speed range (% of maximum pump speed)</b>	<b>Equipment type</b>	<b>Gain (dB)</b>	<b>Sample duration (s)</b>	<b>Filters applied</b>	<b>Sample rate (MHz)</b>
Sand	0 – 80	600 kHz Hydrophone (Upwards facing)	60	300	< 100 kHz > 1 MHz	5
Clay	0 – 100	600 kHz Hydrophone	60	300	< 100 kHz > 1 MHz	5
No sediment	0 – 80	600 kHz Hydrophone (Upwards facing)	60	300	< 100 kHz > 1 MHz	5
No sediment	0 – 100	600 kHz Hydrophone	60	300	< 100 kHz > 1 MHz	5

Table 2.1. Summary and order of all laboratory experiments conducted between May 2021 – November 2022.

### 2.2.1. The first round of experiments procedures

The first experiment measured the background noise of the flume tank without sediment (Table 2.1). The flow speed of the water was increased by increments of 5% of the maximum pump speed. Each measurement lasted for 200 seconds and used a 40 dB gain. The recordings used a MATLAB script and Picoscope software to control the hydrophone's sampling rate and sampling time. This background data could then be used to remove the background noise of the following experiments for each % increment of the maximum pump speed. The chosen flow speeds were first determined as 5% increments from 5% – 100% in the recirculating flume, and then the actual velocity was identified via measurements with a Vectrino sensor. A Vectrino is a high-resolution acoustic velocimeter that is used to measure 3D water velocity fluctuations (Nortek 2018).

After this initial recording, 1520 kg of sediment ( $D_{50}$  of 0.46 mm) was added into the tank. This sediment will be referred to as sand, as it is sand-sized, but it is a mixture of sand grains and glass beads. The sand was poured into the tank until there was a continuous layer of sand across the tank's width and length. This sediment was then flattened. Afterwards, water was added into the tank until it was 28.5 cm deep. Once filled, the 1 Hz – 600 kHz hydrophone, Vectrino and video camera were attached to the tank, with the hydrophone and Vectrino's sensory ends being permanently submerged.

The pump was turned on and set to the required percentage of maximum pump speed (hereafter, '% max pump speed'). The pump initially ran at its maximum speed to create an upper-stage plane bed. This plane bed was then left to reach an equilibrium state, for a period varying from 20 – 60 minutes. Once the plane bed had equilibrated, data from a hydrophone, video camera, and Vectrino were recorded (Table 2.1). After each set of measurements, the pump speed was lowered by 5% of its maximum speed, and the process was repeated until 25% of % max pump speed was reached. This 25% value corresponded to minimal bedform movement. Instrument records lasted for 200 s when 90 – 100% of % max pump speed was used. At slower pump speeds (i.e. 85 – 25%), the recordings lasted for 400 s. This change in measurement duration occurred because bedform movement was slower at lower flow speeds, ensuring that more time was required to measure any significant movement of bedforms. Each hydrophone measurement was streamed directly to hard drive storage, which had a sample rate of 2 million samples per second, a sample ratio of 8 bit, and a gain of 40 dB. The sample rate of 2 million

samples per second, gave the hydrophone a Nyquist frequency of 1 MHz during these experiments, ensuring that all frequencies across the range to 600 kHz were adequately sampled.

Pump speed of 100 – 90% of the maximum pump speed generated upper-stage plane beds, those with 85 – 65% produced upper-stage plane bed and dunes. Slower pump speeds of 60% produced upper-stage plane bed, dunes, and ripples. Pump speeds of 55 – 30% produced ripples and dunes, and pump speeds of 25% produced only ripples.

Once all experiments with the hydrophone were complete, a sample of the sand was taken and processed through a Malvern 500 particle sizer to measure grain size distribution (Fig. 2.3).

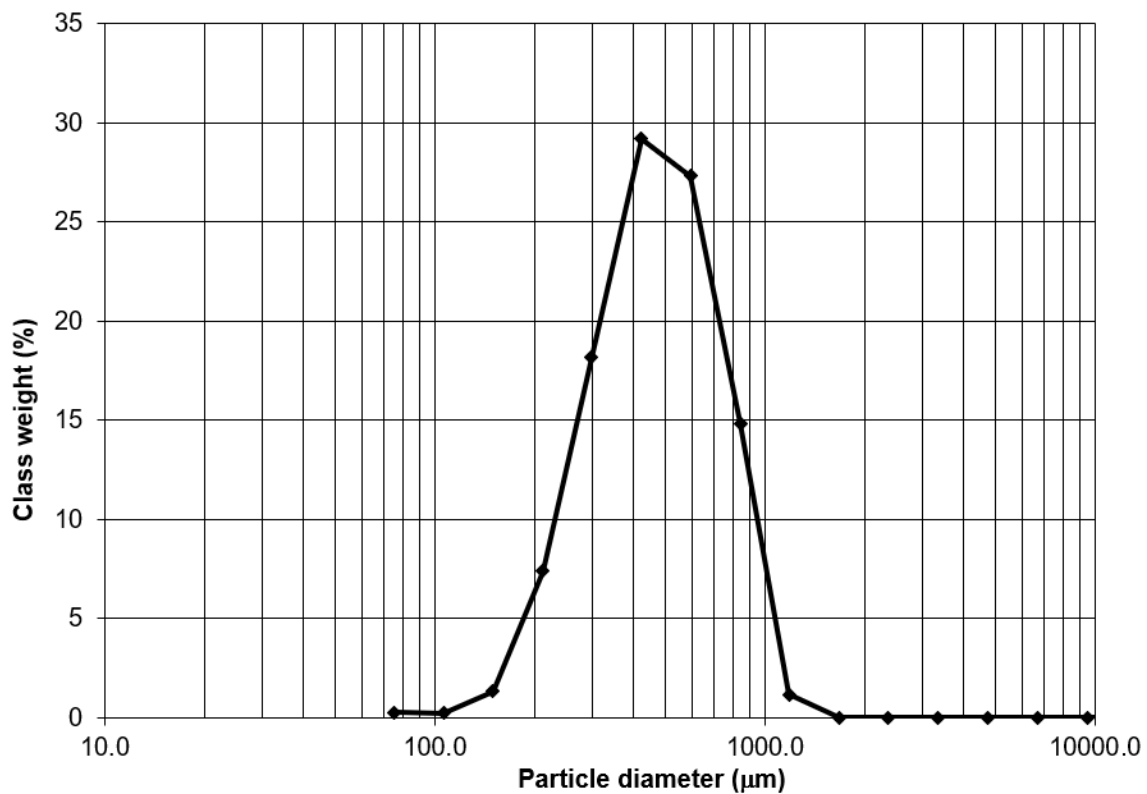


Figure 2.3. Grain size distribution of the sand used in the first set of experiments.

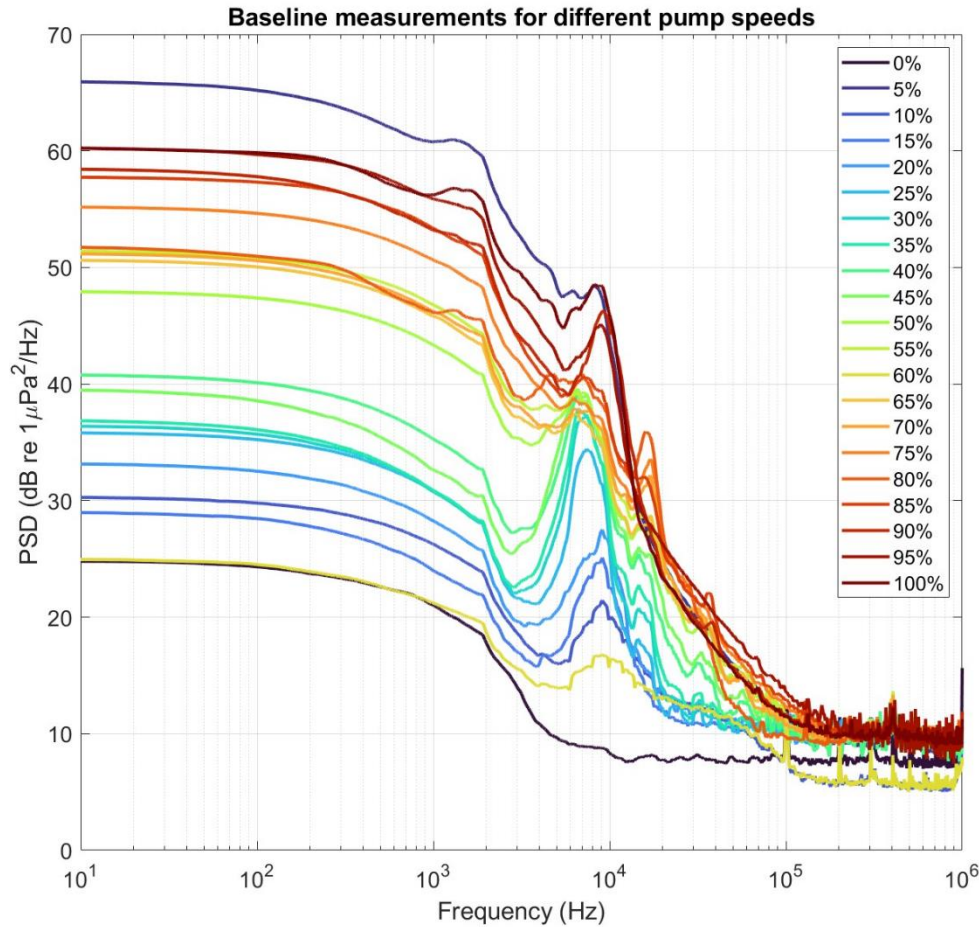


Figure 2.4. Background noise from recirculating flume without filters applied. Each colour represents the percentage of maximum pump speed (%), ranging from 0 – 100%.

It should be noted that background noise during data collection within the first round of experiments (May 2021) indicated that there was an interferent noise within the 1 Hz – 100 kHz range (Fig. 2.4). The interferent noise can be seen by the presence of high levels of passively detected noise within the 1 Hz – 100 kHz frequency range, with strengths ranging from 25 – 66 dB. This high level of background noise can cause quantisation to the lower-strength (7 – 15 dB) passively detected noise within the desired higher frequency ranges (>100 kHz). The impact of this can be assessed via quantisation, which is the mapping of input values from a large mathematical set into output values in a smaller mathematical set. During quantisation the recorded values are rounded in order to fit predetermined intervals, and this rounding leads to a loss of detail and accuracy in the representation of the data (Ayala Castillo *et al.* 2018). In the event of high levels of noise, the size of the rounding intervals will increase further, leading to an increased loss of detail and accuracy within the data. The passively

detected interferent noise measured herein most likely originated from turbulence and bubbles within the water column, and from the electrical pump used to propel the water within the recirculating flume (Fig. 2.4). As a result, later experiments were designed to use filters to exclude high levels of interferent noise, and noise outside the expected particle-particle collision frequency range (<100 kHz and >1 MHz).

## 2.2.2. The second round of experiments procedures

### 2.2.2.1. Hydrophone experimental setup

Flume component	Length (m)	Radius (m)	Pi	Volume (m <sup>3</sup> )	Total volume (%)
Pipework with water	10	0.125	3.142	0.491	100
Flume component	Length (m)	Width (m)	Height (m)	Volume (m <sup>3</sup> )	
Tank with water	10	0.5	0.285	1.425	
	Sediment type in tank	Mass (kg)	Density (kgm <sup>3</sup> )	Volume (m <sup>3</sup> )	Sediment volume (%)
	Sand	1520	1600	0.950	49.586
	Gravel	200	1680	0.119	6.214
	Clay	50	2650	0.019	0.985

Table 2.2. Percentage volume of sediment within the flume tank.

The second series of experiments analysed acoustic signals for three different sediment mixtures, which were (i) sand, (ii) sand and gravel and (iii) sand, gravel and clay (Table 2.1).

Firstly, an analogue band-pass filter was connected between the hydrophone and the external oscilloscope. This filter cuts off any signals outside the following two frequency bands <100 kHz and >1 MHz. Once the filter was applied, and the empty flume was filled to 28.5 cm water depth, background measurements were taken. These background measurements were recorded using a 60 dB gain with the hydrophone having a sample rate of 5 million samples per second and a Nyquist frequency of 2.5 MHz. Similar to the first series of experiments, a recording was performed in intervals of 5% of maximum pump speed. In addition to each recording, a Vectrino measurement was performed to ascertain the actual flow speed in m/s.

Once the background measurements were completed, 1520 kg of sand ( $D_{50}$  of 0.46 mm; Table 2.2) was added into the tank. The flume was run at a 90% pump speed for 2 hours to allow the

tank to flatten the sediment out evenly across the flume tank. After 2 hours, the pump was set to the first measurement, which was 0% of its maximum speed, and a recording was made using the same settings as for the background measurements. When the recording was finished, the speed was increased by 5%, and the tank was left to run for 15 minutes to allow bedforms to develop. After the allotted time, another measurement was repeated following the same process. This was done in total 21 times for each 5% increment.

After all runs with sand were completed, 200 kg of gravel (2 – 20 mm) was added to the tank. The experiment was then continued for 2 hours at a high 90% of maximum pump speed to allow the gravel and sand to mix. Then the process of recording was repeated in 5% increments from 0 to 100% of the maximum pump speed.

Finally, 50 kg of kaolinite clay (0.10 – 10 $\mu$ m) was added into the tank to create a thin mixture of sand, gravel and clay. Following that, the flume was then switched on and run for another 2 hours to allow the clay to be mixed into the bed. Once mixed, recordings using the band-pass filter were completed in increments of 5% from 0 to 90% of the maximum pump speed. In total, 19 out of the expected 21 recordings were completed; this was due to technical difficulties preventing the flume from going any faster with this mixture of sediment.

It should be noted that during all experiments containing gravel, sand and clay, the proportions of sediment within the matrix of the bed could be expected to vary from the initial input between flow speeds (Table 2.1, 2.2). The variance in proportions of sediment could occur due to sediment settling and becoming trapped within the recirculating flumes pipe network (Fig. 2.1). Within the flume experiments, gravel sized sediment was more likely to become trapped due to a higher shear stress requirement for mobilisation than finer sediment sizes (Chadwick and Morfett, 1998). This may create a bias in particle collision frequency with a preference towards finer sediment. This variance in proportion of sediment could be expected to marginally alter the amplitude of particle collisions for specific size classes of sediment across the varying flow speeds of the experiments.

### 2.2.2.2. ADCP experimental setup

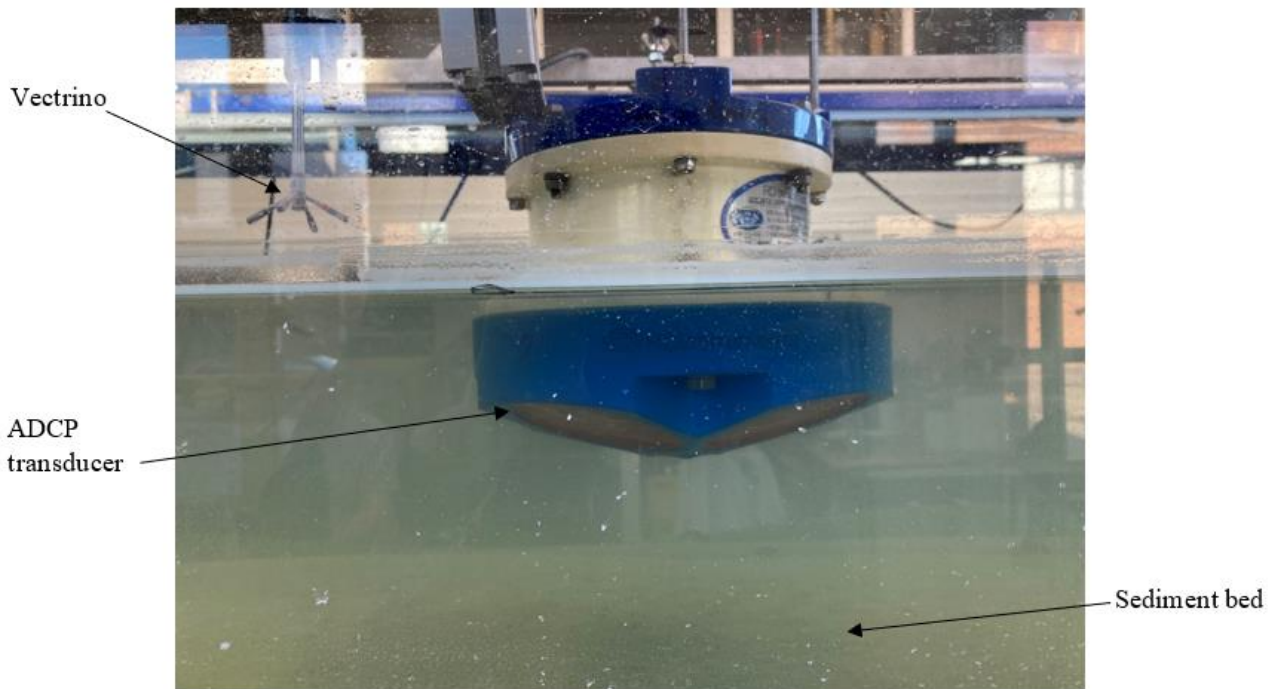


Figure 2.5. ADCP setup within the recirculating flume tank, 7 cm depth between the transducer face and the bed.

As with the hydrophone experiments, the flume tank was firstly filled with water to a depth of 28.5 cm. Then the 600 kHz ADCP was deployed 2.69 m down the length of the tank, at a depth of 7 cm below the water surface (Fig. 2.5). Then, using the program BBtalk, the ADCP was activated, and its settings programmed. In this program, the number of bins for each ADCP was set to 100, and their bin sizes were set to 0.5 m (600 kHz ADCP) and 0.25 m (1.2 MHz ADCP). This procedure was performed in order to make the two-way listening time of either ADCP longer than the depth of the tank  $>50$  cm. With this setup, the ADCP could passively listen to any noise occurring in the tank after the expected active ping from the instrument.

Once the sand was added into the tank, measurements of sediment-generated noise were conducted using the ADCP in intervals of 5% from 0 – 100% of maximum pump speed. These recordings lasted 10 minutes for each pump speed interval and were conducted twice for each sediment type, once for each ADCP (600 kHz and 1.2 MHz) used within the tank. Each ADCP recording produced a .txt and .mat file of the ADCP data that could be used at a later date for data processing. For each pump speed, a 15 min interval was given in order to allow the recirculating flume tank to equilibrate. For both ADCPs, data was recorded for 10 minutes

before termination and pump speed change. In total, each experiment gave 42 measurements (21 each) for both the ADCPs.

The process was then repeated for each consecutive sediment type, testing each ADCP in order, across all pump speeds. This was done except for the final experiment containing sand gravel, and clay. In this experiment, due to technical difficulties of gravel being trapped within the flumes flow filters, the recirculating flume was only run up to 90% of its maximum pump speed. Therefore, only 19 passive acoustic measurements for each ADCP could be collected.

### **2.2.3. The third round of experiments procedures**

The third and final round of experiments followed similar procedures. This round of experiments used a hydrophone and a Vectrino to record how sediment-generated noise changed depending on new sediment mixtures and positions of the hydrophone (Table 2.1).

In this third round, the first experiment to take place was of the hydrophone in a reversed setup, with the transducer face pointing directly towards the surface of the water (Fig. 2.6). In this experiment, the water depth was set to 33 cm, so that the head of the hydrophone was 5 cm below the water surface (Fig. 2.6). In this round of experiments, an analogue band-pass filter between  $<100$  kHz and  $>1$  MHz and an external oscilloscope were attached to the hydrophone, to try and reduce interferent noise.



*Figure 2.6. Reversed hydrophone setup, with hydrophone pointing upwards towards water surface.*

Then at each 5% increment of the maximum pump speed, passive acoustic and flow speed measurements were taken using a hydrophone and a Vectrino. The hydrophone collected measurements for 300 s using a 60 dB gain with a sample interval of 0.2  $\mu$ s. Between the changing of 5% increment of the maximum pump speed and the commencement of any measurement, there was an interval of 15 minutes. This 15-minute interval allowed the flume tank to equilibrate to the new flow speed. This experiment using the reversed hydrophone only recorded data at up to 80% of the maximum pump speed. This was due to the water-level dropping at higher flow speeds, causing the transducer to emerge above the water surface, preventing new recordings.

Once the reverse hydrophone data was collected for a sandy bed, the tank was emptied of sand. Two sets of background measurements were recorded. The first set of background measurements collected data from 0 – 80% of the maximum pump speed in the same manner, using the reversed hydrophone setup at the same water depth of 33 cm. Next, the hydrophone was flipped over to face in a downward direction towards the bed and the water depth was lowered to 28.5 cm. Then new background measurements were taken from 0 – 100% maximum pump speed, all with 5% increments in flow speed. These measurements were used as background measurements for experiments containing corresponding setups and water depth.

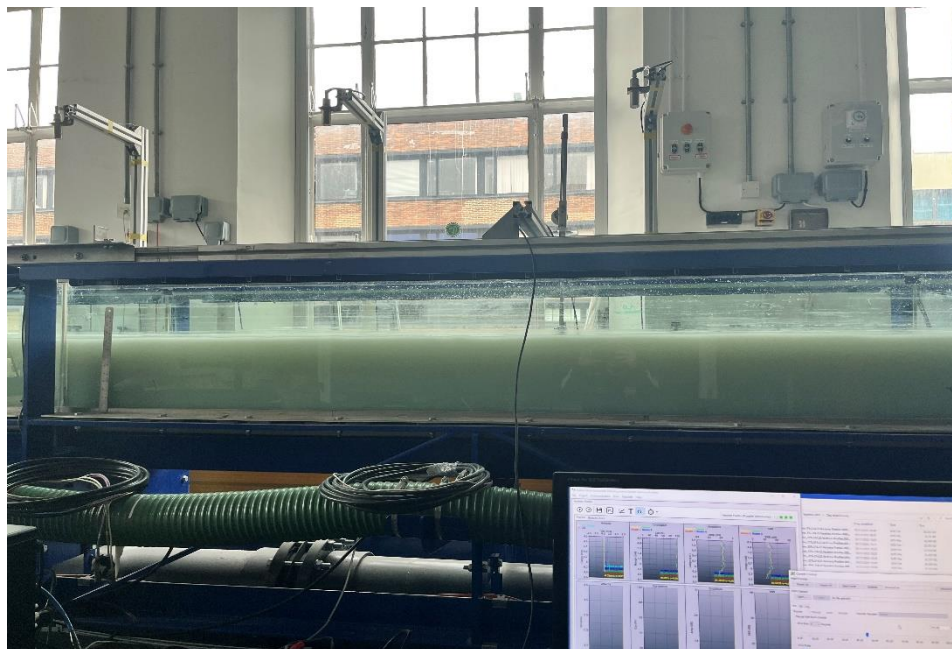


*Figure 2.7. Experimental setup of <1% clay experiments.*

Next, 50 kg of clay was added into the tank creating a 0.99% mixture of clay and water (Fig. 2.7). In order to thoroughly mix the clay, before any new measurement was taken, the pump was set to 100% of its maximum speed for 10 minutes. After 10 mins, recordings from 0 – 100% pump speed were taken following the same procedure, recording for 300 s at a 60 dB gain with a sample interval of 0.2  $\mu$ s.

#### **2.2.4. Data processing procedures**

Firstly, the grain size data from the Malvern 5000, were inputted into Gradistat Excel software. This software calculates the grain size distribution of the sample. From Gradistat, numerous sample statistics were calculated, including  $D_{50}$  and % distribution across all sediment sizes.

Then the Vectrino data was imported into OceanContour software. This specialised software allowed the Vectrino's .ntk data files to be converted into a .mat file. These .mat files were then imported and loaded into MATLAB. Once imported, for each run, the stream velocity of the water column was calculated. In order to do this, firstly, all erroneous values and then any values below 95 – 90% correlation were set as a not-a-number (NaN) format in MATLAB to denote bad data, and then velocity was calculated. This was done by squaring both X and Y flow values, then adding them together and then square rooting them. For the hydrophone data, an additional step was performed, averaging each value for each % pump speed together, creating a single value per point.

##### *2.2.4.1. Hydrophone data analysis*

#### **Passively detected noise against flow speed per sediment type**

Once all data had been collected, the hydrophone's data were analysed. During the plotting of hydrophone data, it was identified that the signal coming out of the built-in pre-amplifier within the hydrophone (that can be set to one of 0, 20, 40, 60 dB) had reached saturation at a maximum value determined by its power supply. On lower amplifier settings, such as 40 dB amplification used during the first set of experiments, the saturation effect disappeared at high flow speeds. However, at higher amplifications of 60 dB, the saturation effect was more pervasive across all flow speeds. The unwanted saturation effect that occurs during the second and third set of experiments, when there is an amplification factor of 60 dB, was potentially caused by the lower-frequency and larger-magnitude noise being amplified beyond the maximum range of

the amplifier output (Fig. 2.4). This artefact that impacts upon higher magnitude noise signals is likely to be caused by interaction of the noise acquisition filters with a signal that is intermittently saturating at maximum output. This resulted in signal processing artefacts that were visible within recorded data, especially with 60 dB amplification values (Fig. 2.8).

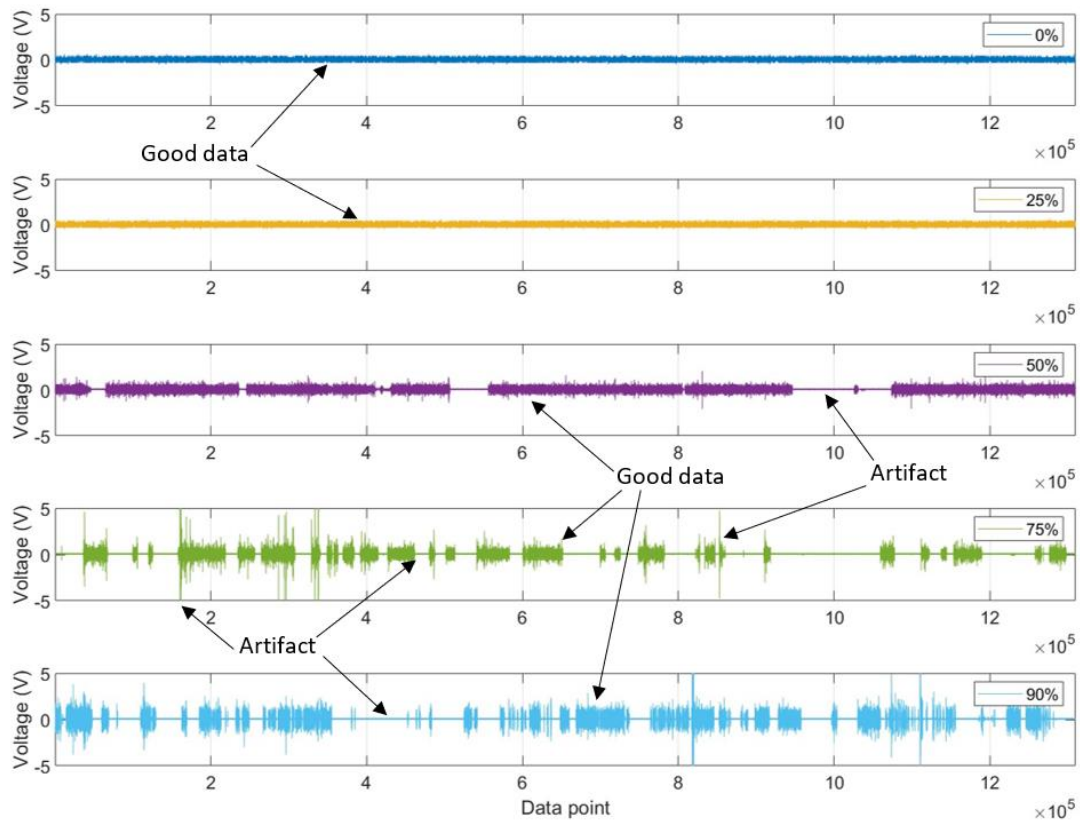


Figure 2.8. Exemplar raw data displaying saturation at high % maximum pump speeds.

In order to counter any effect from the artefacts within the hydrophone data, short sections (<10 ms) of data unaffected by saturation were identified from each data file within each data set. The hydrophone's data values were deemed to be unaffected by saturation if their voltage was neither an anomalously high short-lived spike, nor a null value (0V) (Fig. 2.8). Sections of data were chosen to be analysed primarily based upon their temporal length (duration) between artifacts. At all times, the longest possible consecutive section of data points without any presence of artifacts was chosen. By only choosing the longest string of data points available, as much bias as possible was removed from the data. This process of choosing data also helped to prevent user bias regarding choosing which section of data to analyse. It also allowed for the maximum number of available data points to be used, and this in turn helps to prevent large fluctuations in noise from being expressed.

Once a section of data to be processed was identified, using the Pwelch function, the sections of unaffected data were converted into power spectral density in MATLAB. Pwelch is a function that performs a Fourier transform on the hydrophone data.

Then, each data set separated by sediment type was adjusted to account for the hydrophone's sensitivity. This adjustment used sensitivity data provided by Benthowave. Using the sound sensitivity data, for each gain setting (0, 20, 40, 60 dB) the frequency response of the hydrophone across the frequency spectrum was interpreted in a 1-D function called Interp1 on MATLAB (Fig. 2.2). Then the hydrophones interpreted frequency response at a 60 dB was subtracted from each power spectral density data file, converting them into sound intensity relative to 1  $\mu\text{Pa}$ . Next, the data was plotted. Due to the presence of interfering artefacts within the data (Fig. 2.8), background noise was not subtracted from the data and instead plotted as separate points along the plot. Therefore, this plot contained four data sets, (i) Background noise, (ii) Sand, (iii) Sand + Upward facing hydrophone, (iv) Sand + Gravel and Sand + Gravel + Clay.

In order to understand uncertainties within hydrophone data, for both sand and clay experiments, additional short sections of unsaturated hydrophone data were analysed for both the 'sand-only' and 'clay-only' experiments, for a flow speed of 0.85 m/s. Plotting of these additional points of unsaturated hydrophone data, in conjunction with the previously plotted data on Fig. 2.9, thus provides an indication of the variability within the hydrophone data, including for a constant flow speed.

### **Bedform analysis**

In order to perform an analysis of the bedforms, using a script coded in MATLAB, the videos of each of the first round of experiments runs were displayed as individual frames cycling every 4 seconds. From this, parts of a bedform could be chosen for analysis; these parts were classified into Trough (trough of a bedform), Mid (middle section of stoss and lee side of a bedform), Peak (highest point of a bedform) and Flat (when the bed is featureless). For each part of a bedform, the frame in which it occurred was noted down. This frame's time was then matched with the measurements in the hydrophone data. These runs were recorded without a noise acquisition filter and, therefore, should contain interfering saturating and disconnecting effects resulting from the filters acting on the data recording. Although, as there were no noise

acquisition filters applied during recording, effects from quantisation could be exacerbated by the presence of high levels noise in the data.

Once this data processing was complete, the hydrophone data were plotted. The first type of figures created were for each type of bedform. These plots show different parts of a bedform's profile. With the raw hydrophone measurement data of each bedform and background data, one second of data (two million samples) was converted into power spectral density and frequency using the Pwelch function on MATLAB. Once converted, both the background and bedform data were converted into a linear scale and subtracted from one another to remove any background noise. Then the data was converted back into a power spectral density scale, adjusted by subtracting the hydrophones interpreted frequency response at 40 dB off the recorded data and then plotted. In total, there are nine lines on each figure, totalling nine seconds of data at varying stages of the bedform being examined.

The next figure plotted data points along bedforms in each run, to identify if there is any variation between passively detected noise and the type of bedform.

#### *2.2.4.2. ADCP data analysis*

Using the program WINADCP, all ADCP files were converted from .txt into alternative files. For each file, all data variables and bins 1 – 100 were selected for export. Once exported, the file was saved as a .mat file to be used in MATLAB.

Once converted using MATLAB, both 600 kHz and 1.2 MHz ADCP data sets were processed into fourteen figures. Each ADCP type's data was divided into at least two figures per sediment type tested and six figures, with the exception of the 600 kHz sandy bed experiments having a repeat run performed and plotted. In order to create these plots, the Vectrino data collected during the hydrophone experiments was reused. This Vectrino data gave the flow speed in m/s for each % maximum pump speed increment.

Using MATLAB, data for each sediment type was loaded in separately on a counter to allow both plots to be gradually created, adding a new data point for each new flow speed per sediment type loaded. When a file was loaded in, firstly, the mean far-range (Bins 80:100) raw magnitude data recorded by the ADCP was plotted against flow speed. This data is described as the Received Signal Strength Indicator (RSSI) by the manufacturer (Teledyne RDI, 2001) and result from logarithmic amplification of the received signal by the ADCP. The far-range

RSSI (Bins 80:100) was then immediately converted to sound intensity ( $I$ ) on a dB scale using the measured  $Kc$  value for each transducer (Teledyne RDI, 2001) (Eq. 2.2).

$$I = Raw \times Kc \quad (2.2)$$

The  $Kc$  constant is specific to each transducer of the ADCP, and it converts the RSSI scale that arises as the result of a non-linear amplifier in the ADCP to a relative dB scale (Deines, 1999; Teledyne RDI, 2001). The value is normally within the range 0.4 to 0.45 (Deines, 1999; Teledyne RDI, 2001).

As it was not possible to collect direct measurements of background noise, a proxy was generated in order to remove interferent background noise to improve the quality of sediment-generated noise at low magnitude. This proxy was calculated by looking at the far-range bins at zero flow speed and taking the mean value. The RSSI value of background noise was also converted to sound intensity (dB) using the same  $Kc$  values (Eq. 2.2). The mean background noise was then subtracted using Eq. 2.2, following the method described by Gostiaux and van Haren (2010). This process improved the ratio of the sound intensity of the signal of interest to ambient noise when the signal of interest was of low magnitude.

$$I(\text{noise removed}) = 10\log_{10} \left( \left( 10^{\frac{dB}{10}} \right) - \left( 10^{\frac{dB(\text{Background})}{10}} \right) \right) \quad (2.3)$$

Then a second figure was plotted; this figure contained both  $10\log_{10}$  of the flow speed against sound intensity from Eq. 2.2 and  $10\log_{10}$  of the flow speed against sound intensity with the ambient noise subtracted using Eq. 2.3. This subtraction of ambient noise follows the Gostiaux and van Haren method (Eq. 2.3) (Gostiaux and van Haren, 2010). The Gostiaux and van Haren method for subtracting noise improves the quality of the signal when the signal is small, but within a limited range. When the signal is smaller still then the method breaks down (Gostiaux and van Haren, 2010).

Once the Gostiaux and van Haren method was performed, it was followed by a calculation of the regression of the  $10\log_{10}$  of the flow speed against sound intensity data in the second figure. The regression ignored data that varied from the general trend on the plot. This was usually the first six 5% flow speed increments, all of which were at low flow speeds below 0.5 m/s. These low flow speeds further reduced their signal, making sound intensity indistinguishable from the ambient sound intensity, breaking down the Gostiaux and van Haren method (Gostiaux and

van Haren, 2010). From the regression, an  $R^2$  value could be used to identify if there is any statistical significance. In addition, the slope was used to derive an exponent in which the sound intensity and flow speed were related to one another. This exponent was plotted as a part of the title of the figures.

## 2.3. Results

This section shows how passive acoustic signals measured with a hydrophone vary with sediment type and bedforms. This is followed by results collected using a 600 kHz ADCP and then from a 1.2 MHz ADCP.

### 2.3.1. Acoustic signal variation with sediment type (Hydrophone)

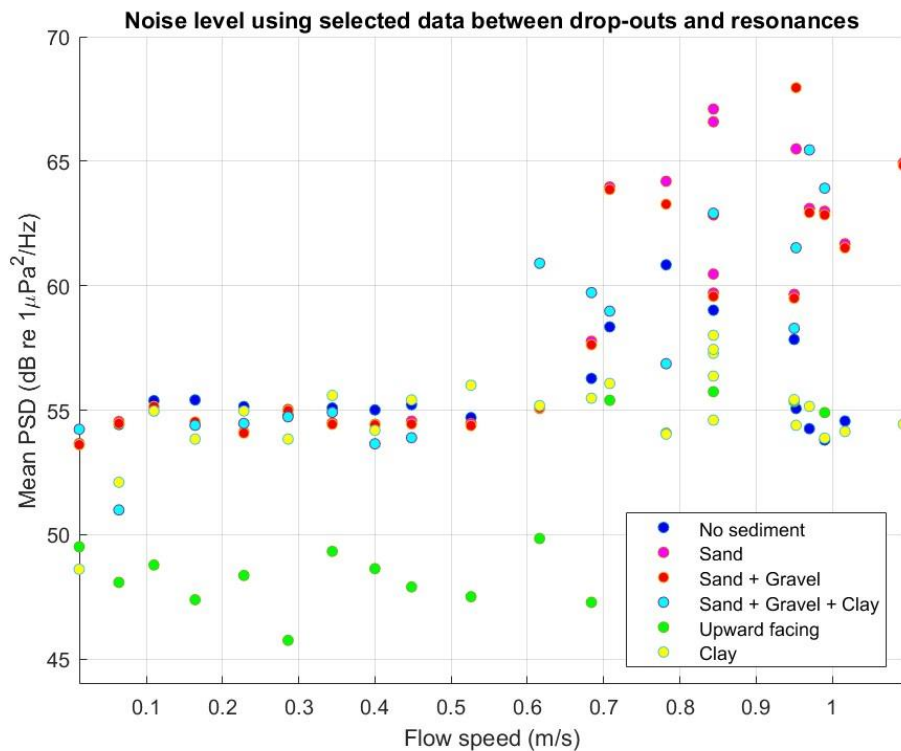


Figure 2.9. Mean power spectral density (dB) for each sediment type in relation to flow speed (m/s), collected using a 60 dB pre-amplifier setting. Coloured dots denote to the sediment types present within each experiment (e.g. red indicates power spectral density data from sand and gravel experiments).

Background data collected when there was no sediment within the recirculating flume tank show that the spectral density is near constant with increasing flow speed up until 0.5 m/s (Fig. 2.9; dark blue points). A spike in passively detected noise follows at flow speeds around 0.8 m/s, and the level of passively detected noise then drops at even higher flow speeds (Fig. 2.9). Comparing alternative sediment types to the background noise, for flow speeds of <0.5 m/s, most power spectral density values (except for the initial values in beds containing clay and the upwards facing hydrophone) are of similar value to the background noise (Fig. 2.9). Thus, the signal from sediment transport cannot be distinguished from background noise, for flow

speeds of  $< 0.5$  m/s. Generally, it can be seen that the upwards facing hydrophone is around 8 dB quieter than the rest of the recorded data sets (Fig. 2.9). It should be noted that there could be visible air pockets between the transducer face and the transparent acoustic medium (Fig. 2.6).

However, at flow speed in excess of 0.6 m/s, acoustic data from runs with sediment increase in power spectral density, so that they exceed background noise with no sediment (Fig. 2.9). Thus, there is a clear signal from sediment transport at these faster flow speeds. The sand, sand + gravel and sand + gravel + clay beds all rise above the background noise level, increasing from +1 dB up to + 12 dB at around 1 m/s. Between these three runs (sand, sand + gravel and sand + gravel + clay), there is no clear separation in the mean power spectral density (Fig. 2.9).

It is possible to see that on the experiment using an upwards-facing hydrophone, after 0.7 m/s power spectral density jumps up by 8 dB to around a constant 55 dB. As flow speed increases, the dB level stays constant until flow speeds of 1 m/s.

Experiments containing  $< 1\%$  clay do not increase in power spectral density for flow speeds of  $> 0.5$  m/s, with acoustic power remaining around 54 – 56 dB. At most points throughout the experiments containing  $< 1\%$  clay, power spectral density is level with or below the recorded background noise (Fig. 2.9).

It should be noted that these experiments were undertaken using a 60 dB pre-amplifier setting, unlike the bedform analysis section below. The value of 60 dB was chosen as an alternate value to the 40 dB value in the bedform analysis section. This was done to avoid data saturation experienced within the bedform analysis. This 60 dB method proved unsuccessful in preventing saturation. However, the data presented within Fig. 2.9 are short sections of hydrophone data ( $< 10$  ms) where it is thought that saturation is not occurring.

Plotting of additional sections of hydrophone data, for flows with constant speeds of 0.85 m/s, indicates that acoustic sound strength in such flows varies by around 9 dB in flows containing sand, and by around 3 dB in flows containing clay (Fig. 2.9).

## 2.3.2. Bedform analysis

### 2.3.2.1. Acoustic variation across a bedform profile

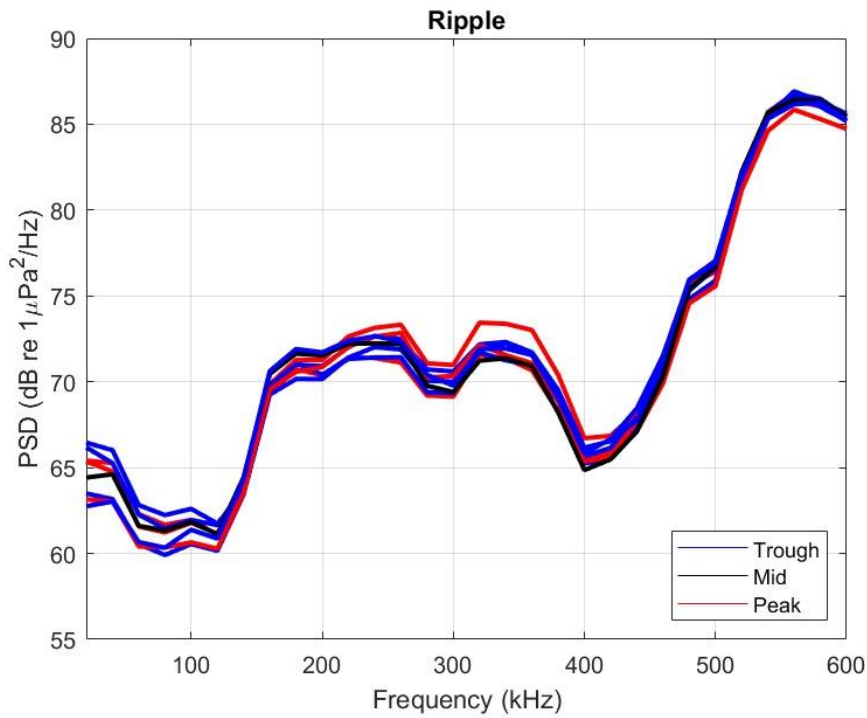


Figure 2.10. Power spectral density across a sand ripple (Trough, Mid and Peak refer to positions along a bedform).

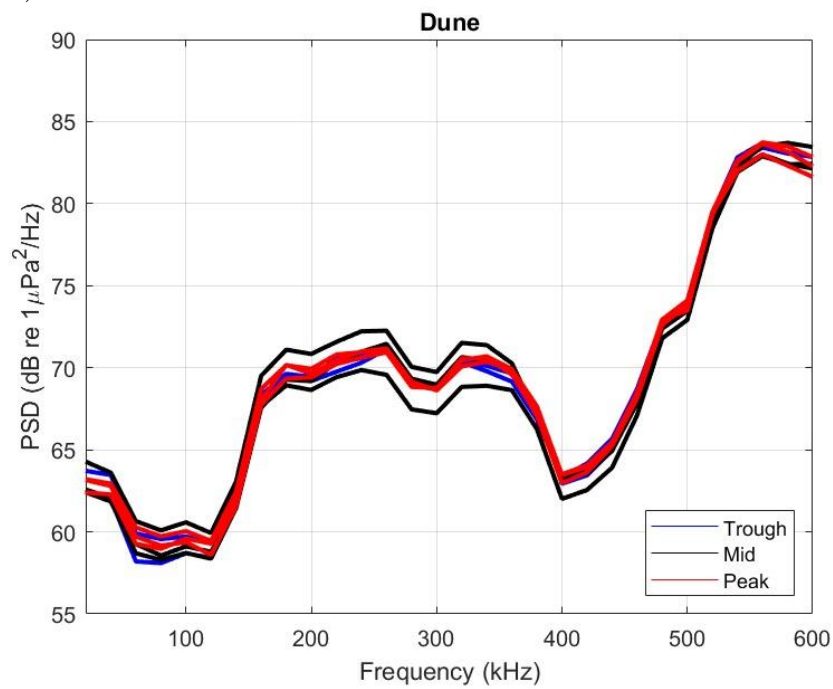


Figure 2.11. Power spectral density plot across a sand dune (Trough, Mid and Peak refer to positions along a bedform).

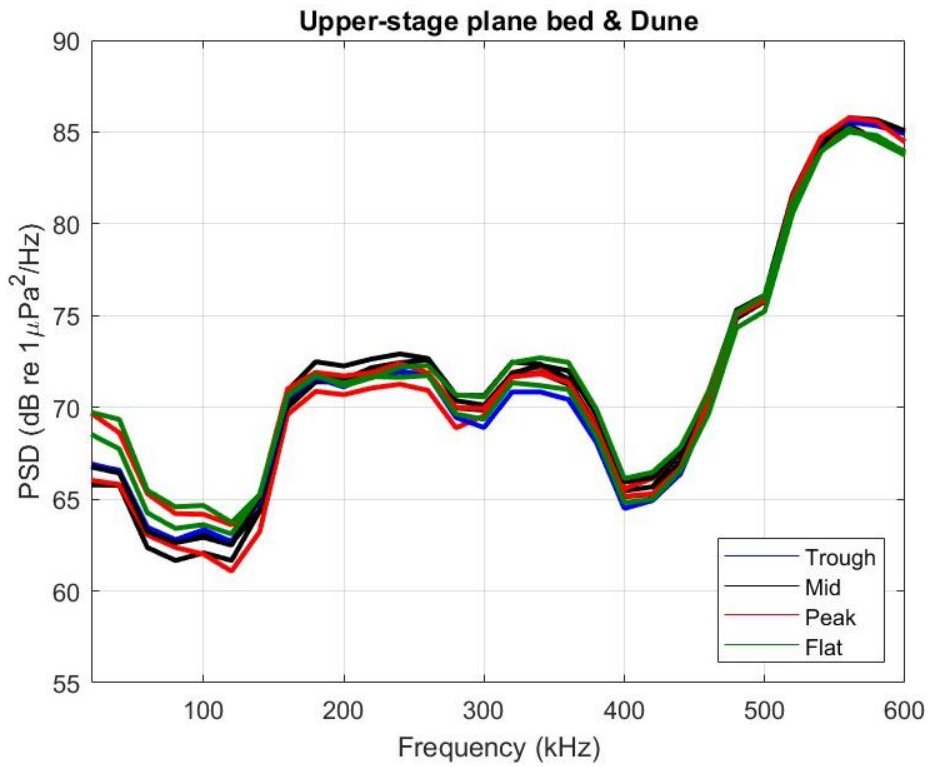


Figure 2.12. Power spectral density during a transitional stage between upper-stage plane bed and dunes (Trough, Mid and Peak refer to positions along a bedform).

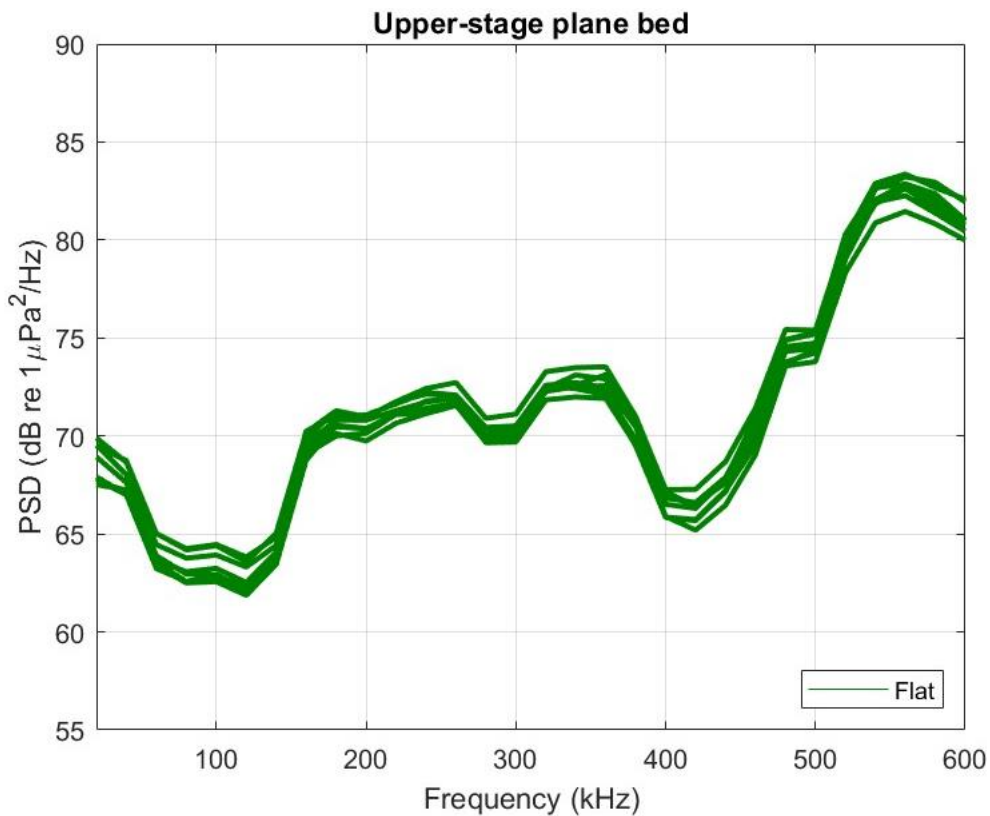


Figure 2.13. Power spectral density across upper-stage plane bed (Trough, Mid and Peak refer to positions along a bedform).

For experiments with ripples, the acoustic power decreases and then gradually increases, before a plateau occurs at a frequency of 200 kHz (Fig. 2.10). This plateau is followed by a decrease of 5 dB between 300 – 410 kHz. After this decrease, the power spectral density increases to 86 dB, and peaking at 550 kHz (Fig. 2.10). At most frequencies, between sections of a bedform, there is little variation in acoustic power. The greatest variation in acoustic power is at lower frequencies between 20 – 125 kHz. Across this entire plot, there is no clear separation between sections of a bedform and the level of acoustic power.

Dune bedforms show a similar pattern to ripples, with two decreases in acoustic power and an overall gradually increasing trend of acoustic power with increasing frequency (Fig. 2.11). Dune bedforms do not seem to exhibit any pattern, nor any considerable variation in acoustic power, between the different sections of a bedform. It is possible to observe that the largest variations in acoustic power (5 dB) of the dune occur between 125 – 350 kHz.

There are no significant variations in acoustic power between sediment beds with upper-stage plane beds or dunes (Fig. 2.12). The largest variations in acoustic power are around 20 – 125 kHz. There is a double peak in acoustic power in the low-frequency range 150 – 350 kHz and 410 – 500 kHz, and the highest acoustic power is around 86 dB at 550 kHz.

All sections of the upper-stage plane bed have a very similar level of acoustic noise across the entire profile, varying by only ~1 dB. The largest variations in acoustic power are between 20 – 125 kHz and 410 – 500 kHz, and the highest peak of 83 dB can be observed at 550 kHz. Similar to the previous profiles, there are two distinguishable peaks in acoustic noise in the 150 – 350 kHz and 410 – 500 kHz frequency range (Fig. 2.13).

It should be highlighted no noise acquisition filters used in the collection of the data in Figs. 2.10 – 2.13, and that the data was collected on a 40 dB gain setting. This means that any low-frequency (<100 kHz) background noise within the tank will be present within the data, and the lower 40 dB gain will reduce the signal-to-noise ratio (Fig. 2.4).

### 2.3.2.2. Relationships between bedform types and acoustic power

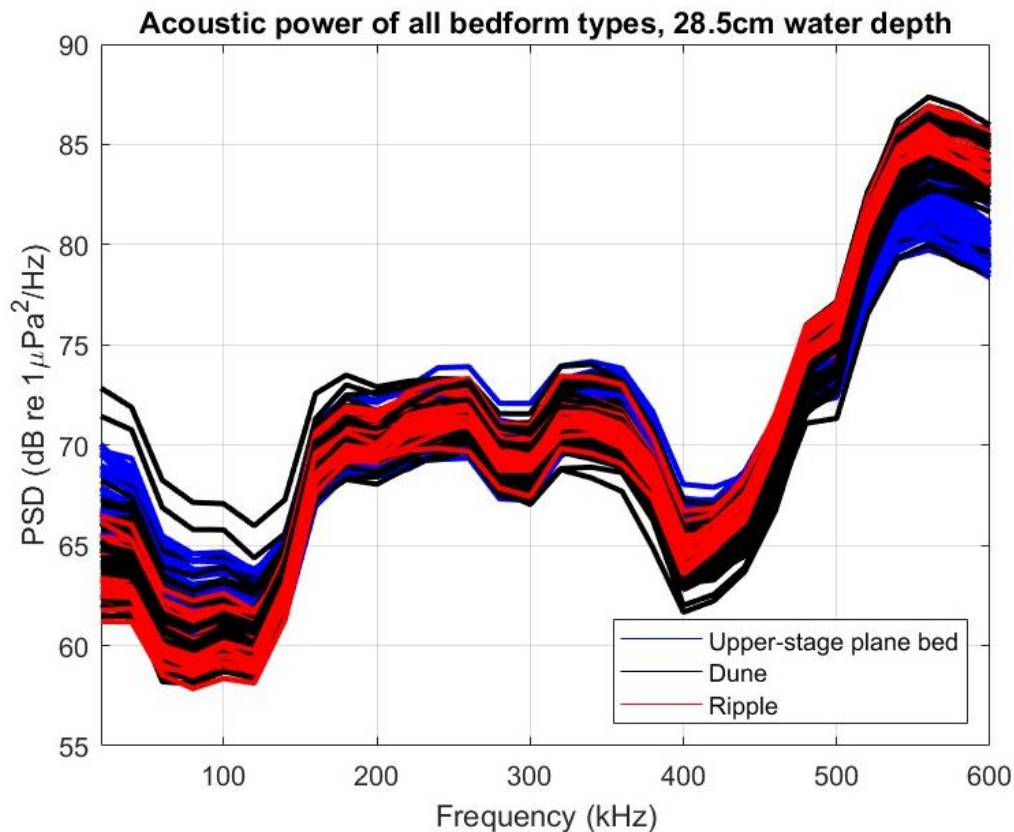


Figure 2.14. Power spectral density across all bedforms within 28.5 cm water depth.

Comparing all bedforms to one another, at the lower frequency end 20 – 125 kHz, it is possible to see a weak pattern where ripples tend to have one of the lowest strengths of acoustic signals, followed by dunes, and then upper-stage plane bed (Fig. 2.14). Within the middle frequencies of 125 – 450 kHz, the pattern is obscured and not present. Between 450 – 600 kHz it is possible to see the opposite pattern where the lowest power spectral densities (dB) are for upper-stage plane bed, followed by intermixed dune and ripples. As before, this trend is very weak as it is not possible to see a clear separation between any bedform type. Between the highest and lowest acoustic power for most given frequencies, there is a 10 dB variation in spectral density.

### 2.3.3. 600 kHz ADCP analysis

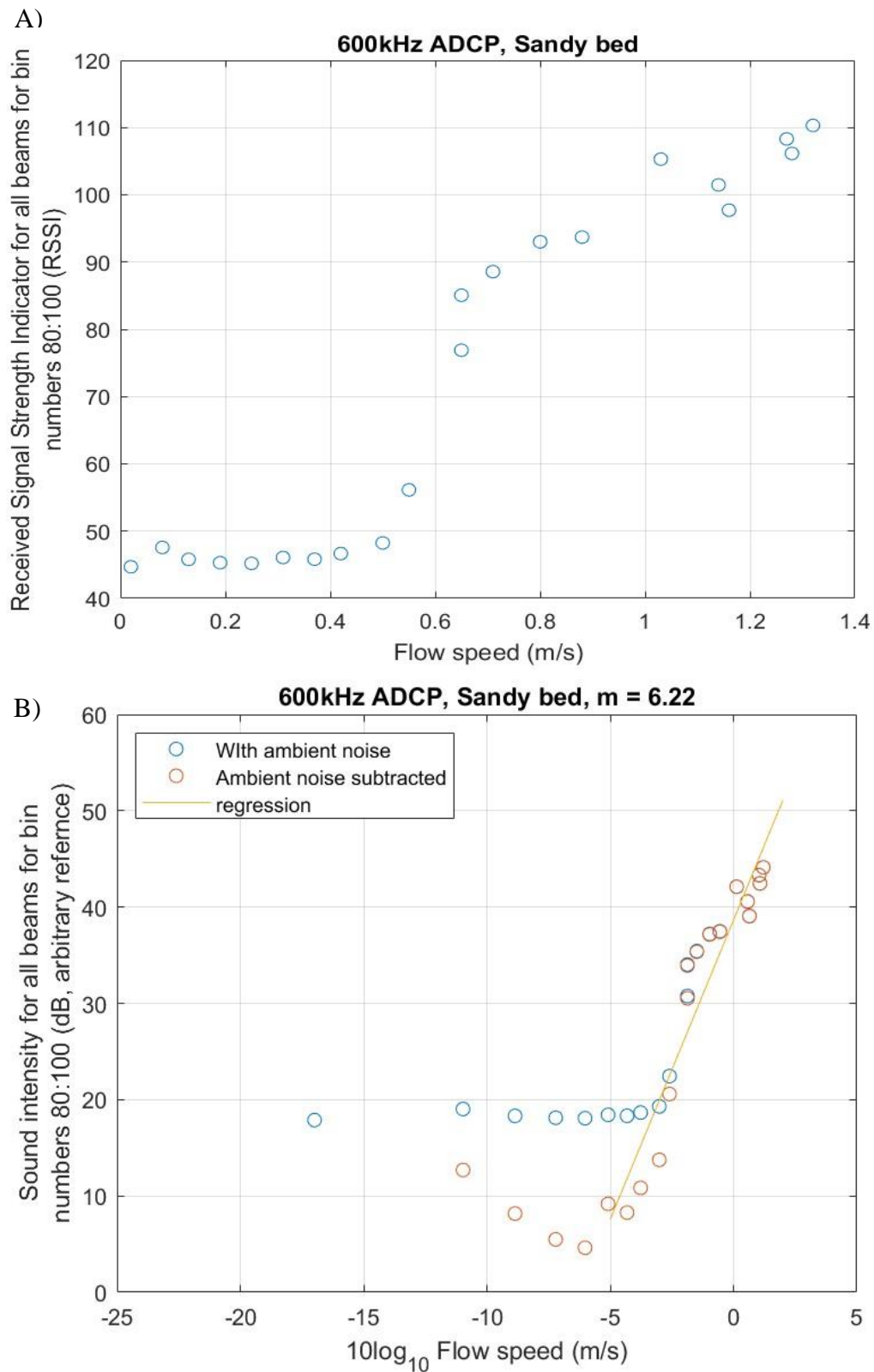


Figure 2.15. A) Far-range RSSI (Bins 80:100) from a 600 kHz ADCP for each flow speed in a sandy bed. B) Sound intensity (dB) against  $10\log_{10}$  flow speed in a sandy bed.

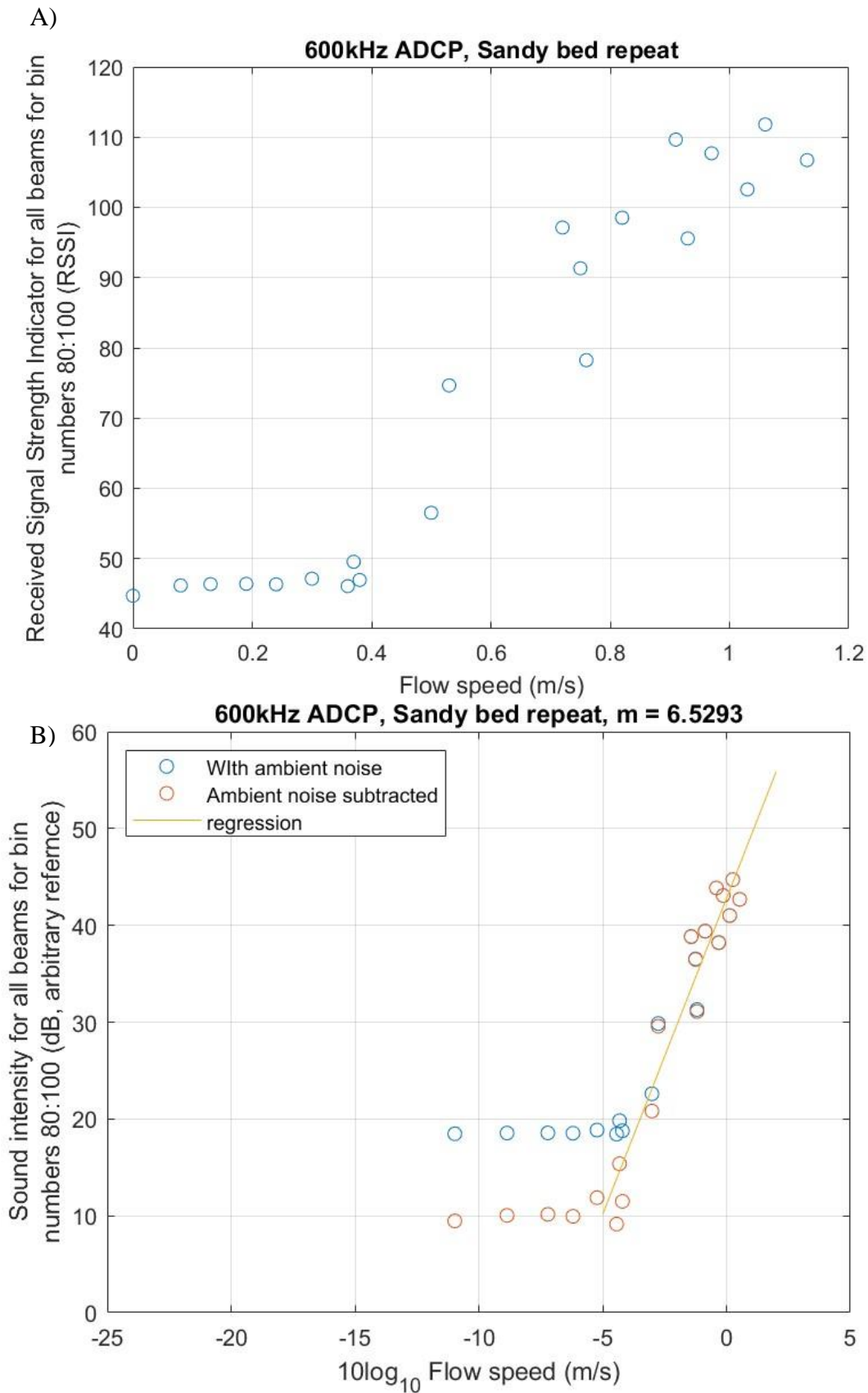


Figure 2.16. A) Repeated experiments far-range RSSI (Bins 80:100) for each flow speed in a sandy bed. B) Repeat run of sound intensity (dB) from a 600 kHz ADCP against  $10\log_{10}$  flow speed in a sandy bed.

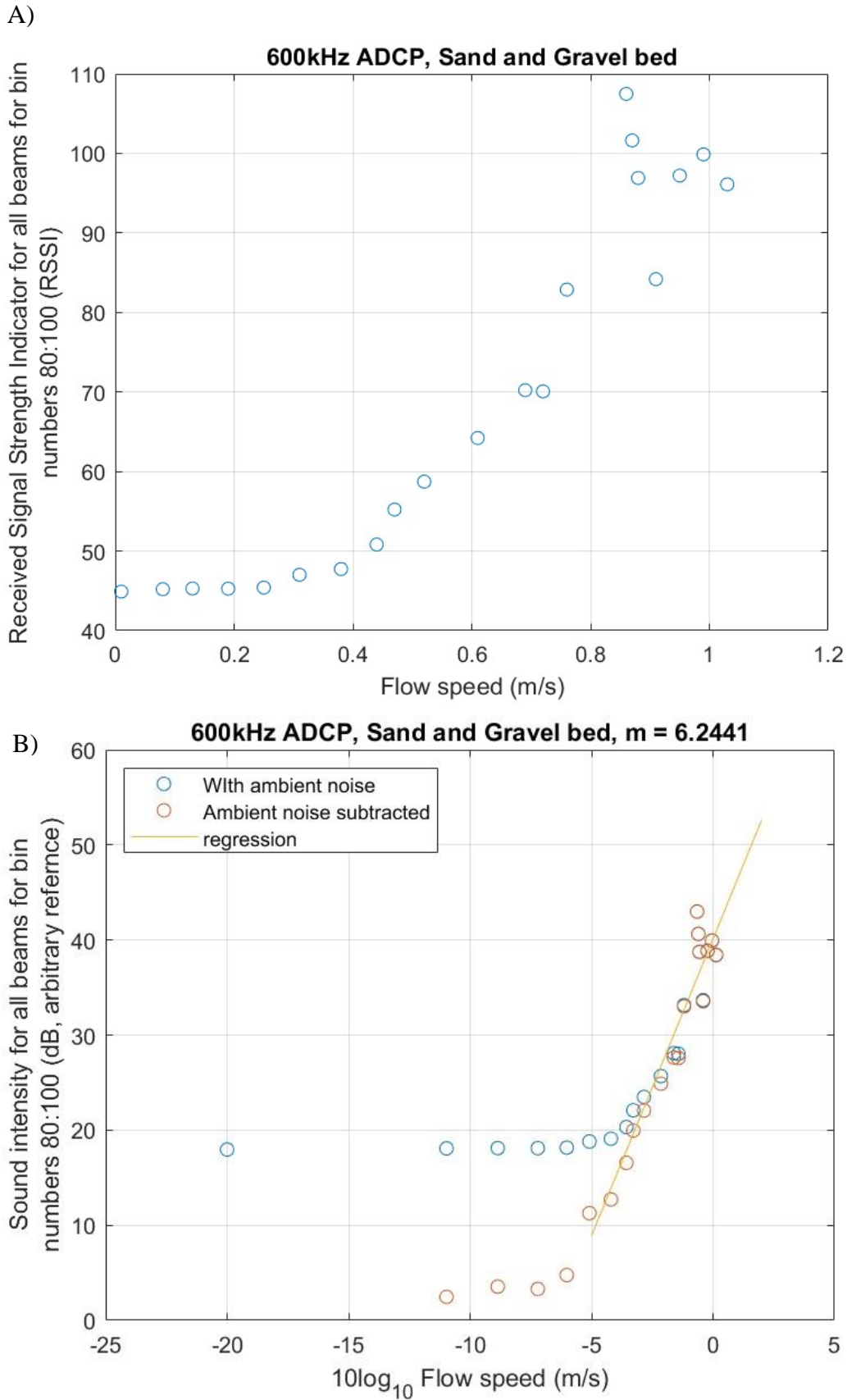


Figure 2.17. A) Far-range RSSI (Bins 80:100) against flow speed in a sandy gravel bed. B) Sound intensity (dB) from a 600 kHz ADCP against  $10\log_{10}$  flow speed in a sand and gravel bed.

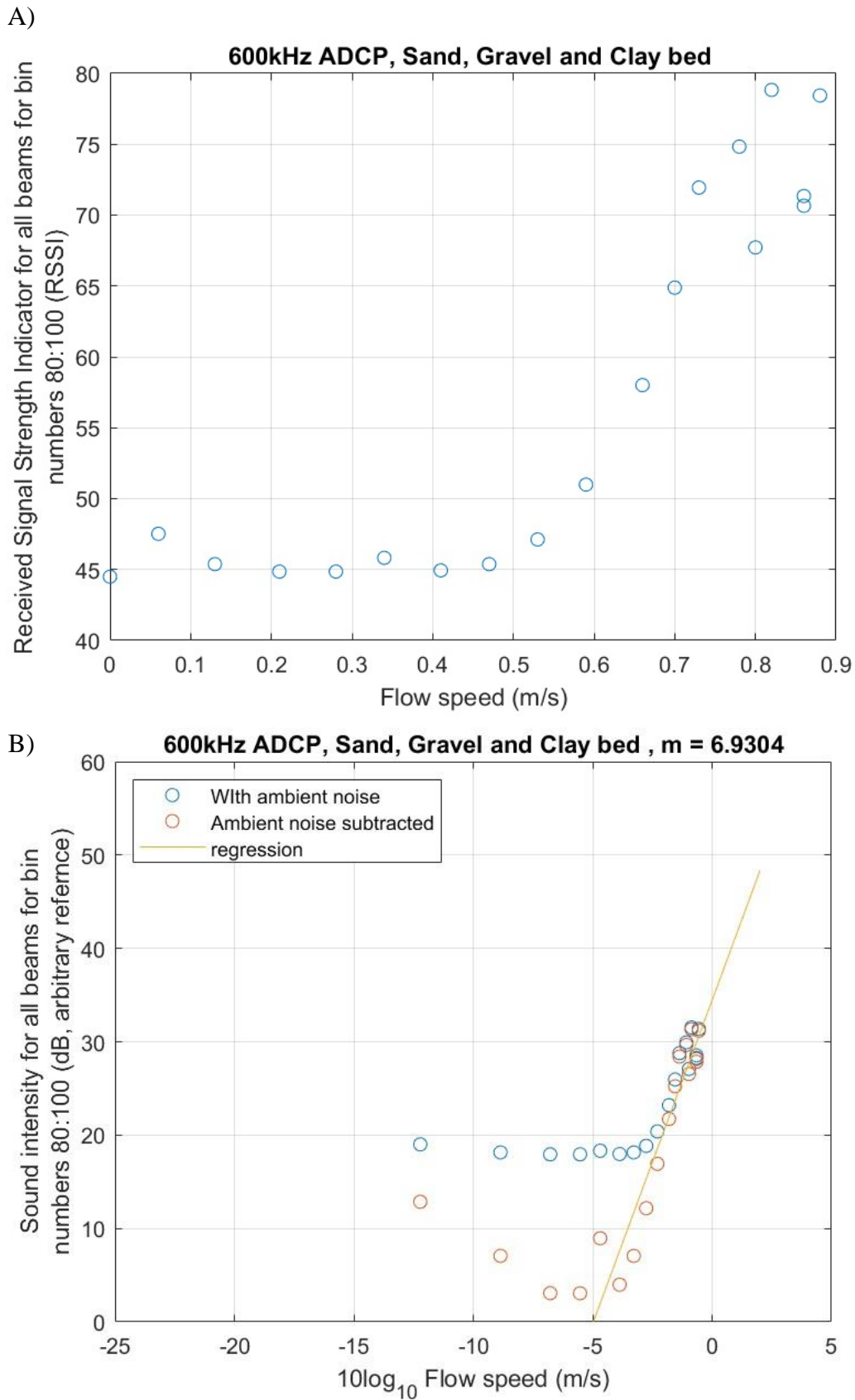


Figure 2.18. A) Flow speed against far-range RSSI (Bins 80:100) from a 600 kHz ADCP in a sand, gravel and clay bed. B) Sound intensity (dB) from a 600 kHz ADCP against  $10\log_{10}$  flow speed.

*Section 2.3.3. displays and reports on the data passively recorded via a 600 kHz ADCP. This section provides data on a range of bed types: Sand, Sand + Gravel and Sand + Gravel + Clay. In order to improve the reliability of the passively recorded data section 2.3.6 displays a repeat of the sand bed type experiment.*

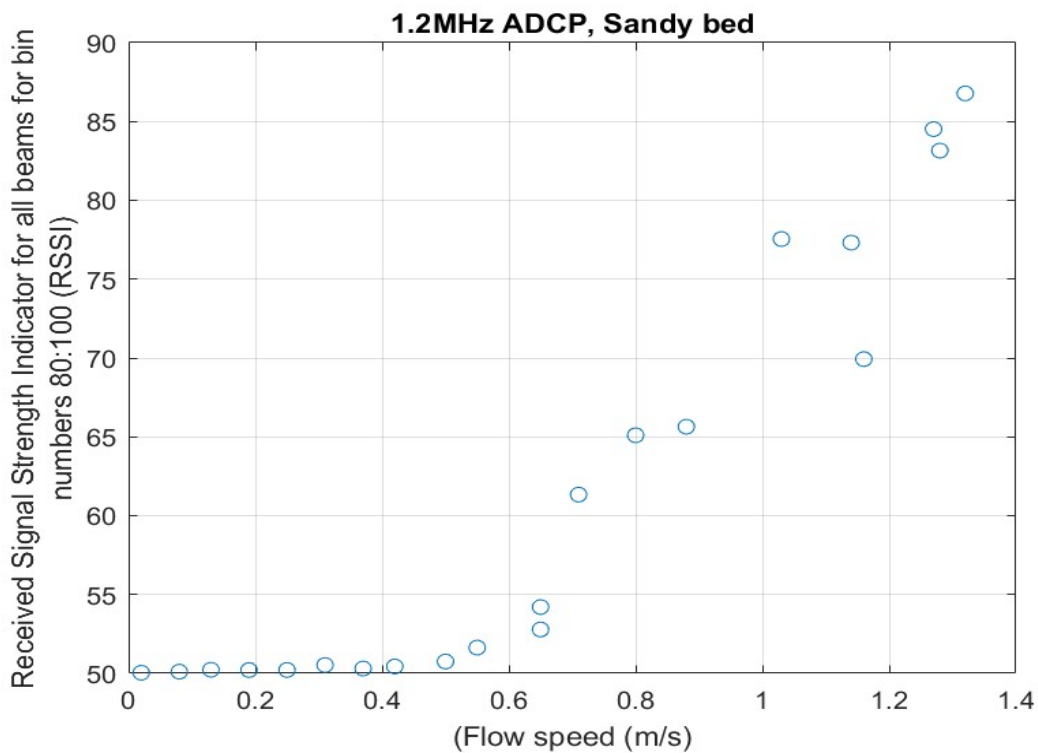
Within experiments containing a sandy bed, it is possible to observe a clear increasing trend between sound intensity and  $10\log_{10}$  flow speed (Figs. 2.15 & 2.16). The vast majority of data fit closely to the trend line. In both experiments with sand at low flow speeds between 0 – 0.5 m/s, there are significant decreases in passively detected noise when the surrounding ambient noise is subtracted; this pattern disappears at higher flow speeds up to 1.3 m/s (Figs. 2.15 & 2.16). The regression suggests that when using 600 kHz ADCPs, sound intensity in a sandy environment is related to flow speed to an exponent of between 6.22 and 6.53, with an  $R^2$  of 0.95. Both experiments show that the maximum level of dB is around 55 dB.

Using a 600 kHz ADCP, sandy gravel environments are suggested to have similar relationships to sandy environments (Fig. 2.17). This is supported by the regression performed on sandy gravel beds giving an exponent value of 6.24 between flow speed and passively detected noise, and an  $R^2$  of 0.97. Similar to sandy beds at low flow speeds, there are significant drops in sound intensity when the ambient noise is subtracted. These significant drops stop occurring for flows faster than 0.47 m/s (Fig. 2.17). In sandy gravel environments, the passively detected noise seems to increase for the first four flow speeds, and then after 0.19 m/s, the dBs recorded rapidly increase. The maximum sound intensity in sandy gravel environments is 55 dB. This is very similar to experiments with sand.

Similar to the first experiment with a sandy bed (Fig. 2.9). The experiments with sand, gravel, and clay seem to have a similar trend (Fig. 2.18). The maximum sound intensity for experiments with sand, gravel, and clay, compared to experiments with just sand, is lower by nearly 20 dB. Similar to the previous experiments, there are significant drops in passively detected sound intensity when the ambient noise is subtracted. When a regression is performed on the sand, gravel, and clay data collected via a 600 kHz ADCP, the value derived suggests that the relationship between passively detected noise and flow speed is to the exponent of 6.93, and the  $R^2$  was 0.96. This is higher than the previous mixtures of sediment.

### 2.3.4. 1.2 MHz ADCP analysis

A)



B)

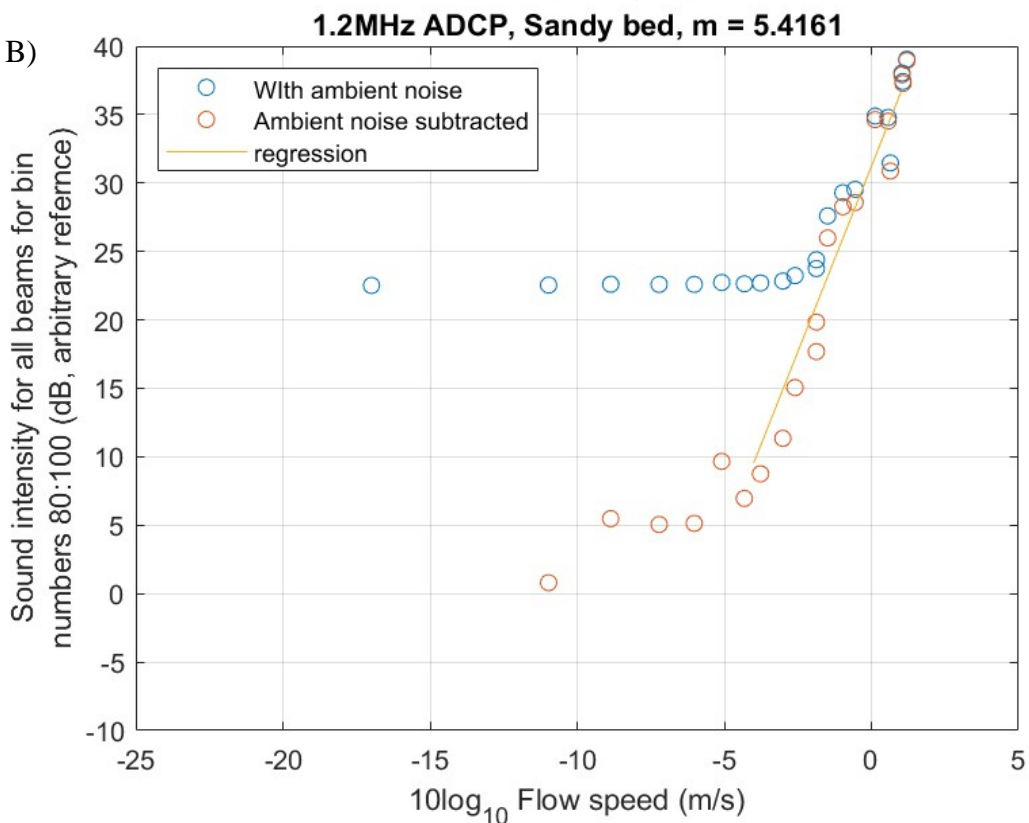


Figure 2.19. A) Far-range RSSI (Bins 80:100) from a 1.2 MHz ADCP for each flow speed. B) Sound intensity (dB) from a 1.2 MHz ADCP against  $10\log_{10}$  flow speed in a sandy bed.

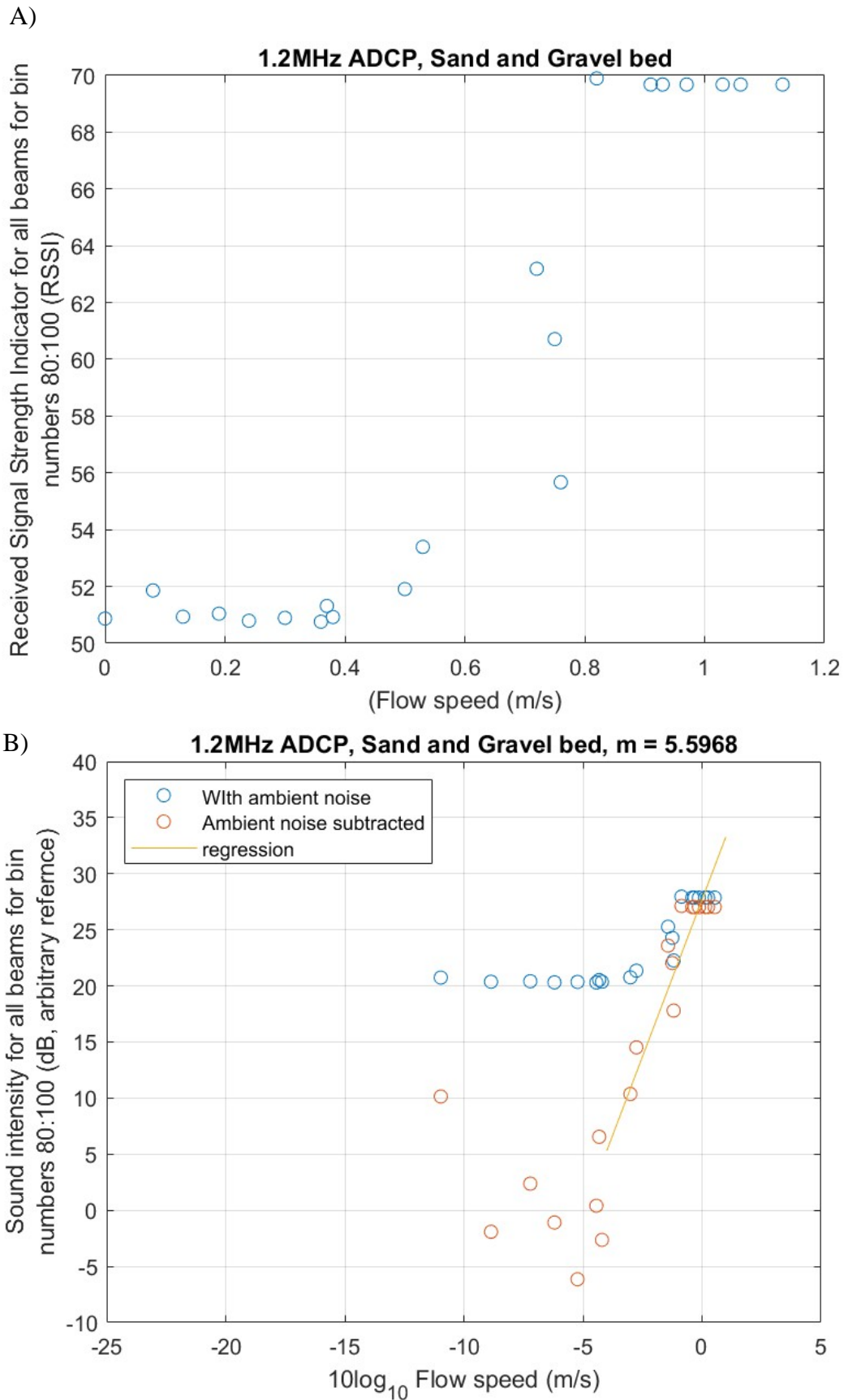


Figure 2.20. A) Flow speed against raw far-range RSSI (Bins 80:100). B) Sound intensity (dB) from a 1.2 MHz ADCP against  $10\log_{10}$  flow speed in a sand and gravel bed.

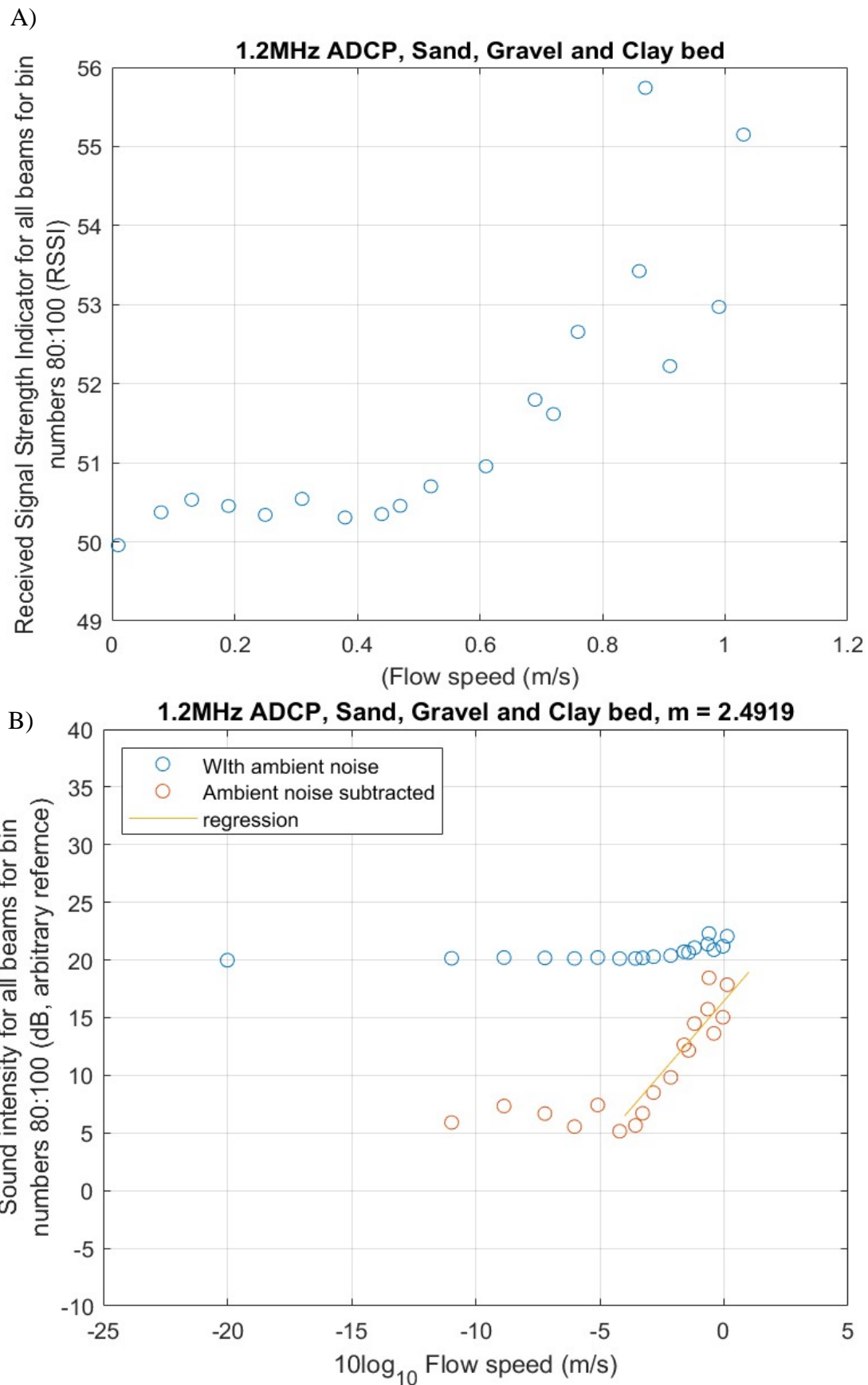


Figure 2.21. A) Raw far-range RSSI (Bins 80:100) from a 1.2 MHz ADCP against flow speed in a sand, gravel and clay bed. B) Sound intensity (dB) from a 1.2 MHz ADCP against  $10\log_{10}$  flow speed.

*Section 2.3.4. analyses data passively recorded via a 1.2 MHz ADCP. This section provides data on a range of bed types: Sand, Sand + Gravel and Sand + Gravel + Clay.*

Sandy bed experiments using the 1.2 MHz ADCP showed a clear trend of increasing flow speed with increasing sound intensity (Fig. 2.19). The maximum sound intensity for these experiments was around 40 dB at the highest flow speed of 1.32 m/s. The data also showed significant changes in sound intensity when ambient noise was subtracted from data between 0 and 0.65 m/s. When a regression was performed on this 1.2 MHz ADCP data, it suggested that passively detected noise was proportional to flow speed to the exponent of 5.42; with an  $R^2$  of 0.97.

In sand and gravel experiments, there is significant variation in passively emitted noise until flow speeds of 0.53 m/s (Fig. 2.20). When the background noise is also removed, there is a considerable reduction in sound intensity from data at flow speeds between 0.36 to 0.72 m/s. At flow speeds of >0.72 m/s, unlike the previous profiles, there is no increase in emitted sound intensity, and instead, sound intensity is more uniform (Fig. 2.20). This maximum peak in sound intensity is lower for gravel, than for beds containing exclusively sand. The regression performed on the sand and gravel data gave an  $R^2$  of 0.94. It also suggests that passively detected noise is related to flow speed at an increased exponent of 5.59.

When clay is added to the sand and gravel mixture, it is possible to see a noticeable difference in noise on the 1.2 MHz ADCP (Fig. 2.21). Across the entire profile from 0 – 1.2 m/s with increasing flow speed, there are large decreases in sound intensity when the ambient noise is subtracted. In addition, the maximum sound intensity is the lowest of any of the profiles, sitting at a maximum of 17 dB. When the regression for this 1.2 MHz ADCP data was calculated, the  $R^2$  derived was 0.91, and it suggested that flow speed was related to passively detected noise at an exponent of 2.49. This exponent is significantly lower than the other bed types for this 1.2 MHz ADCP.

## 2.4. Discussion

*The following section discusses the findings found throughout this chapter and experiments in order to answer the proposed hypothesis and aims.*

### 2.4.1. Relationships derived from the passively recorded hydrophone data

Data collected from the hydrophone show that within the recirculating flume, only at high flow speeds ( $>0.6$  m/s) is it possible to detect sediment-generated noise. This is indicated by an increased level of noise that is above background noise for faster flow speeds, as seen for experiments with Sand, Sand + Gravel and Sand + Gravel + Clay sediment types (Fig. 2.9). For these three sediment types, as flows speeds increase above 0.6 m/s, so does the level of acoustic noise, showing that there is a relationship between flow speed and passively detected noise. However, due to the lack of separation between noise values for each sediment type, it is not possible to further discern any additional information regarding this relationship between sediment type and acoustic signals. This lack of information regarding the relationship between grain size and acoustic signal strength could result from the setup of the hydrophone.

For Chapter 2's experiments, the hydrophone is setup with a pre-amplifier before the analogue filters. In addition, during the second round of experiments, a 60 dB gain was used to amplify the signal of interest above 100 kHz. These two factors resulted in large amplitude, low-frequency noise below 100 kHz, likely generated by the pumps, dominating the recorded signal. Noise from the pump thus overprinted the higher frequency ( $>100$  kHz) noise that the experiments were trying to study. Unfortunately, the saturation occurred on the pre-amplifier rather than at the acquisition stage on the oscilloscope. This means that in order to filter and then amplify, new experiments would need to set the pre-amplifier to a low setting, filter the signal, and then place an additional amplifier between the filters and the acquisition.

Furthermore, manual picking of unsaturated data from the hydrophone data sets was required due to intermittent saturation, and disconnection of the hydrophone could further inhibit the detection of a relationship. Evidence of saturation and disconnection of the hydrophone can be seen in Fig. 2.8. The common occurrence of saturation within the hydrophone data meant that the number of unsaturated values picked per data point was very low, further decreasing in number of unsaturated values with increasing flow speed (Fig. 2.8). As a result, hydrophone

data may have a low signal-to-noise ratio, which then led to large variations in mean power spectral density seen across each flow speed ( $>0.6$  m/s) (Fig. 2.9).

Experiments with 1% clay mixture are around or below background noise levels, for flows speeds of  $< 0.6$  m/s (Fig. 2.9). At faster flow speeds, the acoustic noise level decreases significantly below background levels. Reductions in acoustic noise levels during 1% clay experiments may result from the clay mixture increasingly absorbing sediment-generated noise with increasing flow speed.

Experiments with the hydrophone's receiver in a reversed position show significantly different results to the rest of the experiments (Fig. 2.9). At flow speeds of  $<0.7$  m/s, the noise detected is significantly lower. It is proposed that this is due to the hydrophone's face not properly engaging with the water, such as due to air pockets present during the experiments. At flow speeds above 0.7 m/s, it is suspected that the hydrophone has started to engage with the water, and hydrophones record mean power spectral density values closer to those of other experiments.

For flow speeds of 0.7 to 1 m/s, the reversed hydrophone noise values are around the background level or below. The absence of noise above background level for the reversed hydrophone suggests that sediment-generated noise is produced by bedload transport when there is a sandy bed.

It should be noted that the lack of detection of sediment-generated noise at lower flow speeds ( $<0.6$  m/s) could be explained by a low signal-to-noise ratio within the data. Noise from alternate sources, such as bubbles and the pump, could have masked the detection of any sediment-generated noise. Furthermore, this low signal-to-noise ratio was further hindered by the low sample size plotted due to the effects of saturation and disconnection of the hydrophone during the experiments.

The plotting of additional sections of hydrophone data for flows with constant speeds of 0.85 m/s highlights significant variance in sound strength (in dB) within each data set. The large variance in sound strength is most likely masking any potential controls of grain size (sediment mixture) for mean power spectral density. This variability needs to be taken into account when interpreting these data, as it is clear that large variations in dB can arise depending on what section of data is analysed, without a change in flow speed. It is worth noting that mean power spectral density for sand is still above the background level, and this suggests that there is

potential detection of sediment generated noise (Fig. 2.9). In addition, sound levels for all flows with clay are below the background noise level, and therefore similarly suggest that clay may be absorbing noise.

### **2.4.2. Acoustic output variation across a bedform**

It was not possible to determine if there is a relationship between positions along a bedform and acoustic power. Observations suggest that power spectral density values across each section of a bedform are erratic (Figs. 2.10 – 2.12). Similarly, there are no significant changes in acoustic signals along upper-stage plane bedforms (Fig. 2.13).

This is contrary to the findings of Le Guern *et al.* (2021) who suggested that bedload transport rates increased over the crest and stoss of bedforms, compared to their trough. It could be expected that bedload transport rates would increase in these crest and stoss areas, and thus so would particle collisions. Therefore, there should have been a visible increase in power spectral density at crest and stoss positions.

The lack of any relationship could be the result of a low signal-to-noise ratio, resulting from the absence of filters and the lower 40 dB gain setting used during these experiments (Fig. 2.4). If a low signal-to-noise ratio is present, it could be masking any observable relationship. Further investigation is required to ascertain if this relationship is actually present and just being masked during these experiments.

### **2.4.3. Acoustic variation in bedform type**

At lower frequencies of between 20 – 100 kHz, power spectral density decreases by around 5 dB from the upper-stage plane bed to ripples (Fig. 2.14). It should be noted that at any given frequency, dunes in these experiments vary significantly in their power spectra density values. These results suggest a trend in power spectral density, increasing in value from ripples to upper-stage plane bed (Fig. 2.14). In addition, due to the lack of filters during the 40 dB experiments, the high level of interferent low-frequency (20 – 100 kHz) noise from the pump and bubbles could be interfering with the signal, producing a trend that is not actually real (Fig. 2.15).

Looking at the higher frequency end (400 – 600 kHz) of Fig. 2.14, the opposite trend appears. As power spectral density increases, the bedforms change from upper-stage plane bed to

ripples. It could be expected at these frequencies (400 – 600 kHz), the previously described interferent noise from the pump and bubbles are not present or very minor, and therefore the presented hydrophone data is showing an actual trend (Veeraiyan and Rajendran, 2020). The reduction in interferent noise between 400 – 600 kHz could be expected as noise from the pump and bubbles is usually most prevalent in the 1 Hz – 100 kHz range (Veeraiyan and Rajendran, 2020).

If the trend of increasing power spectral density between upper-stage plane bed to ripples is real, it would suggest that upper-stage plane beds produce lower sediment-generated noise levels than dunes and ripples. Furthermore, dunes produce the greatest variation in power spectral density, and ripples most commonly produce the highest values of power spectral density. It would also suggest that there is a gradation from the upper-stage plane bed to dunes and ripples, and no clear separations in acoustic power. This is similar to how the bedforms are generated in the flume experiments, as they gradually change in the regime dominance of bedform type as the flow speed decreases.

Caution is needed when interpreting the potential trend of increasing power spectral density between upper-stage plane bed to ripples between 400 – 600 kHz (Fig. 2.14). Due to the lack of analogue filters during these 40 dB experiments, quantisation from a low level of amplification of a weak high-frequency (100 kHz – 600 kHz) signal most likely has occurred. This quantisation could have distorted the recorded signal and produced a falsely positive result. In addition, the data presented was the same data for each section of a bedform (Figs. 2.11 – 2.13); this data used a low number of data points for each line on a plot. This low number of data points could have exacerbated any effect from quantisation and increased any potential effect from a low signal-to-noise ratio due to the lack of filters.

The possible trend suggesting that with increasing power spectral density, bedforms change from upper-stage plane bed to ripples is the opposite of what would be expected. This is because in order to produce upper-stage plane bed, the flow speed usually has to be increased (OU, 1999; Margalit, 2017; Guerrero, 2019). An increase in flow speed could then be expected to then produce more particle collisions, which should increase the level of detected power spectral density (Hay *et al.* 2021). Further investigation is required to ascertain if this trend is real and then determine if it is produced by sediment-generated noise (Fig. 2.14).

#### **2.4.4. Relationships between passively detected noise and flow speed**

Experiments using both 0.6 and 1.2 MHz ADCPs suggest a relationship between passively detected noise and flow speed. However, the relationship between passively detected noise and flow speed appears to break down at lower flow speeds of  $<0.5$  m/s in 600 kHz ADCPs, and  $<0.6 - 7$  m/s in 1.2 MHz ADCPs (Figs. 2.15 – 2.21). At low flow speeds, it could be expected that there are low levels of mobilised sediment, and thus there are fewer collisions to detect. As a result, any random noise produced by turbulence that cannot be fully removed could be more easily observed, which then could mask any relationship. Additional investigation should be conducted to determine whether, at low flow speeds, the magnitude of the signal has just become too small to compare with baseline noise, making it appear as if the relationship has broken down.

The relationship is also weak at high flow speeds, as there is a noticeable variation in acoustic noise seen as clustering of values at speeds around  $0.9 - 1.2$  m/s (Figs. 2.15 – 2.21). These changes in the relationship between passively detected noise and flow speed could be due to changes in either the flow state or sediment transport modes.

The relationship between passively detected noise and flow speed is more significant for the 600 kHz ADCP, than for the 1.2 MHz ADCP. This could be due to the predominant sediment type being sand, so it is more likely that 600 kHz would be in the correct frequency range and therefore see a relationship between noise produced by sediment and flow speed more clearly.

##### *2.4.4.1. Comparisons to Hatcher (2017) and Hay et al. (2021)*

*Subsection 2.4.4.1 compares and investigates how the relationships between flow speed and passively detected noise discovered in both 600 kHz and 1.2 MHz ADCP experiments within Chapter 2 differ from Hatcher (2017) and Hay et al. (2021).*

Investigating the relationship between flow speed ( $U$ ) and acoustic power ( $S$ ), in the 600 kHz ADCP experiments of Chapter 2, the derived exponents varied between 6.22 – 6.93. The exponents from the 600 kHz ADCP experiments increased in value as gravel and then clay were added into the recirculating flume tank (Figs. 2.15 – 2.18). It is also possible to see that the calculated exponents of the 600 kHz ADCP experiments of Chapter 2 (6.22 – 6.93) are similar to the exponent derived by Hay et al. (2021). Between the front speed of a turbidity current and acoustic power, Hay et al. (2021) derived exponents of 7.2 for frequency ranges 53

– 63 kHz and 7.3 for frequency ranges 130 – 150 kHz. As a result, it is possible to suggest a similar relationship between flow speed and passively detected noise to the one suggested by Hatcher (2017) and Hay *et al.* (2021) (Eq. 2.1). Furthermore, the closeness of the relationship between flow speed and passively detected noise in the experiment containing sand, gravel and clay (Fig. 2.18), to that of Hatcher (2017) and Hay *et al.* (2021), could be the result of the sediment mixture being closer to the natural environment of Squamish Delta, rather than pure sand or sand-and-gravel.

Although the 600 kHz ADCP exponent values suggest a similar relationship between flow speed and passively detected noise to the one found by Hatcher (2017) and Hay *et al.* (2021), it is not exactly the same. There are a number of factors that could have created the difference in the relationship between ADCP data within the laboratory environment and the natural environment data presented by Hatcher (2017) and Hay *et al.* (2021). The first factor could be related to the state of flow and processes occurring within the experiments. Hay *et al.* (2021) propose that there are different frequency responses at different stages of the turbidity current, due to different grain size interactions at different stages of the flow. The laboratory experiments are not wholly representative of processes occurring within turbidity currents as the flume was well constrained in having the same type of sediment distributed throughout the flume. Therefore, this could have resulted in discrepancies in the relationship between flow speed and passively detected noise and resulted in a different value from the proposed relationship in Eq. 2.1 ( $S = U^7$ ) suggested by Hay *et al.* (2021).

The second factor is related to the limited number of data points and the limited frequency range investigated (53 – 63 kHz and 130 – 150 kHz) within Hay *et al.* (2021)'s Figure 5. For the second factor, Hay *et al.*'s (2021) data does not include a large range of flow speeds, and instead just extrapolates for low flow speeds. This is because although they detected turbidity currents with speeds ranging from 0.73 – 1.1 m/s using active ADCP data, their passively detected noise could not be discerned using the same ADCPs (Hay *et al.* 2021). This meant that only high-speed turbidity currents were used to calculate the regression between acoustic noise and flow speed, this could have created a bias within the calculated exponent. The presence of a potential bias within Hay *et al.* (2021) is highlighted by the analysis of the ADCP data in Chapter 2, which showed that there were significant changes in the level of acoustic noise depending on flow speed ranging from 0 – 1.2 m/s (Figs. 2.15 – 2.21). Therefore, if additional data points at lower flow speeds (<0.73 m/s) could be collected, and used with data

in Figure 5 of Hay *et al.* (2021) to calculate a new regression, the new exponent calculated could be closer to the ones derived within Chapter 2.

When looking at 1.2 MHz ADCP data, the exponent calculated from the regression generally decreases as more sediment types are added to the flume tank, changing from an exponent of 5.42 in a sandy bed, to an exponent of 2.50 when sand, gravel and clay are mixed together. It should be noted that it is still possible to determine a relationship between sound intensity and flow speed, but this relationship is very far away from the suggested exponent of 7 by Hay *et al.* (2021) in Eq. 2.1. It is not possible to fully determine why there is a significant variance from Eq. 2.1 in the 600 kHz ADCP data from the flume experiments.

Considerations should be made around the containment of both the 600 kHz and 1.2 MHz ADCP experiments. During both experiments, the shallow depth of the flume meant that the ADCPs interfered with the flow/sediment interactions, causing enhanced scour at higher flow speeds. The enhanced scour at higher flow speeds due to the shallow depth of the tank could have then created uncertainty in the interpretation of the results. For example, the anomalous reduction in exponent value for varying sediment sizes in the 1.2 MHz data (Figs 2.19 – 2.21). Further experiments and an improved experimental procedure could be performed using a larger flume in which the ADCP is less of a flow obstruction and further from the bed. This could then help reduce the presence of anomalous results, thus allowing for a broader understanding of the relationship between sound intensity and flow speed to be ascertained.

#### *2.4.4.2. The effects of different equipment on the level of detected sediment-generated noise*

Experiments show clear similarities, but also some distinct differences between the passively detected noise for both 600 kHz and 1.2 MHz ADCPs. Both ADCPs show a drop in sound intensity when gravel is added, followed by a further drop in noise when clay is introduced into the bed mixture. The reduction in sound intensity for both ADCPs is likely due to gravel armouring the bed, reducing the ability for sand to be mobilised and transported. This could then be exacerbated by the addition of clay, which could further hinder sediment transport, and potentially act as a noise absorption mechanism due to its fine size, creating a large surface area for sound to be trapped within. This reduction in passively detected noise for ADCPs when clay is added to the flume is also seen in the hydrophone data. This further suggests that the addition of clay is the cause of a reduction in noise.

## 2.5. Conclusion

*This final section concludes the research discovered throughout this chapter. Then it proposes future studies to be performed with the aim of further enhancing the understanding of sediment-generated noise.*

With varying degrees of success, results have shown that both hydrophones and ADCPs can be used in a recirculating laboratory flume environments to study sediment-generated noise. It should be noted that the data collected by hydrophones is limited. Only at high flow speeds ( $>0.6$  m/s) was it possible to detect sediment-generated noise above background noise. Furthermore, due to the lack of separation between acoustic noise values for each sediment type, it is not possible to further discern any relationship between sediment type and acoustic signals.

The most significant findings from the hydrophone data are that clay may act as an acoustic dampener, and that at high flow speeds, it might be possible to detect suspended particle collisions within the water column.

The experiments with hydrophones suggest that it is not possible to see any significant change in acoustic power across the profile of a bedform (for ripples to upper-stage plane bed). Comparing variations in acoustic power between bedform types shows an unclear trend, with increasing power spectral density bedform type changes from upper-stage plane bed into ripples. This is unexpected and should be viewed with caution. The unanticipated trend of increasing power spectral density from upper-stage plane bed to ripples could result from the lack of analogue filters and high levels of low-frequency noise in the 40 dB hydrophone experiments. The aforementioned issue could have exacerbated any effect from quantisation, potentially producing a falsely positive result. As a result, further investigation is required.

The detection of sediment-generated noise by ADCPs means that there is now the potential to detect turbidity currents within the natural environment. Results from both 600 kHz and 1.2 MHz ADCPs show that there are strong positive correlations between sound intensity and flow speed, as presented within Hay *et al.* (2021). However, these correlations differ from one another. The 600 kHz ADCP provides an exponent between flow speed and passively detected noise that is between 6.2 – 6.9, similar to the value in Hay *et al.* (2021), whereas the exponent for the 1.2 MHz ADCP is significantly lower (5.6 – 2.5). It is not possible to fully determine

why there is a significant variance within the 1.2 MHz ADCP data when compared to the Hatcher (2017), Hay *et al.* (2021) and the 600 kHz ADCP.

## **2.5.1. Future work**

### *2.5.1.1. Future studies into hydrophones*

Future studies should utilise hydrophones and ADCPs, both in the laboratory and natural environment to explicitly study sediment transport processes. Although in this study, the data collected from the hydrophone on sediment-generated noise was fairly limited in helping to improve understanding of sediment movement. This most likely was due to the setup of the hydrophone, and not the actual ability of the hydrophone to detect sediment-generated noise. If an amplifier was added to the hydrophone after the location where the filters were applied, it could then help improve the signal-to-noise ratio, preventing saturation and disconnection of the hydrophone. This would then help enlarge the sample size, which in turn could potentially reduce the large variations in noise seen in Fig. 2.9.

Another study should be conducted on larger bedforms to test whether it is possible to tell if there are changes in acoustic power across bedforms, and if these changes depend on the bedform type in question. In order to do this, a deeper flume with a more powerful motor is required to generate high enough flow speeds whilst keeping the hydrophone submerged. Using filters in this new study will further ascertain whether there is an actual trend between power spectral density and bedform type.

### *2.5.1.2. Future studies using ADCPs*

Due to the visible impact of the ADCP on the bed during Chapter 2's experiments, any new ADCP experiments should be conducted in a larger flume tank. If new experiments were conducted in a larger flume tank, any obstruction caused by the ADCPs would be less likely to have an impact on the relationship between the flow and the bed.

Due to the possible relationship between flow speed and passively detected noise shown by both the 600 kHz and 1.2 MHz ADCP, other ADCPs, such as a 2 MHz ADCP should be used to investigate the flume environment further. In addition to using alternative ADCPs, background measurements of acoustic signals in flows without any sediment should be collected

for both these ADCPs, in order to determine that sediment-generated noise was detected in these experiments.

Alternative mixtures of sediment should be studied to determine how the recorded sediment-generated noise changes with grain size. These mixtures should identify how more complex mixtures, such as bimodal sand and gravel, change the noise generated. In addition, a study should be conducted to determine if changes in the properties of clay further affect the level of noise attenuation. This can be performed by creating a mixture of clay and seawater within the recirculating flume tank. Adding seawater will cause the clay to flocculate, changing its properties and bringing it closer to what would be found in the marine environment (Sutherland *et al.* 2014). This could also be used as a proxy for biological polymers like EPS that are found commonly in the natural environment (Lai *et al.* 2018).

Finally, a mixture of sediment similar to that found at Squamish Delta, the field site of Hay *et al.* (2021), should be tested using ADCPs in the similar frequency range of 60 – 150 kHz. By testing this in the laboratory environment, it will be possible to confirm the results collected by Hay *et al.* (2021) that flow speed is related to acoustic noise to the exponent of 7 (Eq. 2.1). It should be noted that within a laboratory environment, it is difficult to create the conditions of a turbidity current head. Therefore, alternative setups, such as lock-release experiments, might be required (De Rooij and Dalziel, 2001; Heerema *et al.* 2020).

# Can acoustic signals help to understand sediment transport in a sand-bed river?



*Aerial view of the Río Paraná study area (University of Brighton, 2022).*

### **3.1. Introduction**

*This section introduces the importance of studying acoustical signals from rivers and past work on this topic. It then defines the aims and objectives of this new study, which is followed by a brief description of the field site on the Río Paraná.*

#### **3.1.1. The importance of studying sediment-generated noise in rivers**

The measurement of bedload transport is critical for understanding and managing fluvial systems (Barrière *et al.* 2015). Erosion and remobilisation of bed materials can cause several environmental problems, such as the structural failure of bridges and overheating of buried cables (Richardson and Davis, 2001; CIRGE, 2009).

Previous methods to measure bedload transport in rivers include sediment traps placed directly onto the bed (Voulgaris *et al.* 1995; Le Guern *et al.* 2021) and repeated multibeam echo sounder surveys (Li and King, 2007; Arnot *et al.* 2014; Weinert *et al.* 2015) that calculate bedload transport rates from the geometry and celerity of migrating bedforms (Leary and Boscombe, 2020). A more recent method pioneered by Latosinski *et al.* (2017) uses the bottom tracking signal from ADCPs paired with Differential Global Positioning System (DGPS) to estimate apparent bedload velocities and thus calculate the bedload transport rate (Le Guern *et al.* 2021).

However, these methods are expensive, not always scalable, time-consuming and lack temporal resolution (Marineau *et al.* 2016; Leary and Boscombe, 2020). Their high cost is due to the intensity of labour needed and the high amounts of equipment required to conduct surveys. As a result, these past methods are typically only deployed for a short time, resulting in a low temporal resolution or short time series. With humanity's ever-increasing need to place structures into fluvial and marine environments, the demand for monitoring of these structures over large periods of time will rapidly outpace the capacity of these present methods (Gourvenec and Sykes, 2021). As a result, new methods need to be developed to reduce cost and increase the accessibility and temporal precision of bedload transport monitoring.

Another factor holding back the development of new methods to monitor bedload transport is that sediment transport is complex and not fully understood (Margalit, 2017). Therefore, new research needs to be conducted to improve understanding of the processes occurring.

Author	Instrument types	Acoustic type	River Name	River bed type	
Belleudy <i>et al.</i> (2010)	Hydrophone	Passive	Isère River (France) Torrent de Saint-Pierre (France)	Gravel	
Conevski <i>et al.</i> (2018), Conevski <i>et al.</i> (2020)	Three Stationary ADCPs, 1 – 3 MHz, 1.2 MHz, 600 kHz Camera	Active	Oder River (Germany)	Coarse Sand	
		Active	Elbe River 1 and 2 (Germany)	Fine-Coarse Sand	Coarse Sand – Fine Gravel
Gaeuman and Jacobson (2006), Gaeuman and Jacobson (2007)	600 kHz ADCP	Active	Missouri River (USA)	Sandy	
Geay <i>et al.</i> (2017a)	Hydrophone	Passive	Drau River (Austria)	Gravel	
Geay <i>et al.</i> (2017b)	Hydrophone	Passive	Arc-en-Maurienne River (France)	Gravel	
Geay <i>et al.</i> (2018)	Bedload sampler Hydrophone	Passive	Arve River (France) Isère River (France) Grand Buëch Isère (France) Romanche River (France) Séveraisse (France)	Gravel-Pebble	
Jamieson <i>et al.</i> (2011)	ADCP	Active	Missouri River (USA)	Sandy	
Kostaschuk <i>et al.</i> (2005)	500 kHz and 1.5 MHz ADCP	Active	Fraser River (Canada)	Medium sand-gravel	
Latosinski <i>et al.</i> 2021	ADCP, GPS, DGPS – RTK and SBES	Active	Río Paraná Río Tercero	Sandy	
Latosinski <i>et al.</i> 2017	600 kHz and 1.2 MHz ADCP – DGPS	Active	Río Paraná	Sandy	
Le Guern <i>et al.</i> (2021)	ADCP bottom tracking Dune tracking method Hydrophone	Active and Passive	Loire River (France)	Sandy-Gravel	
Marineau <i>et al.</i> (2016)	Hydrophone	Passive	Trinity River (USA)	Gravel	
Rennie <i>et al.</i> (2002) Rennie and Villard (2004), Rennie and Millar (2004)	1.5 MHz ADCP	Active	Fraser River (Canada)	Medium sand– Gravel	
Rickenmann <i>et al.</i> (2012)	Bedload sampler Geophone	Passive	Erlenback Stream (Switzerland)	Gravel– Pebble	
Sime <i>et al.</i> (2007)	600 kHz ADCP	Active	Fraser River (Canada)	Sandy	
Villard <i>et al.</i> (2005)	ADCP	Active	Fraser River (Canada)	Gravel	

Table 3.1. A brief summary of past fieldwork conducted to understand passive or active acoustic signals from bedload transport in rivers.

Various field studies have used both active and passive acoustic methods to understand bedload transport in rivers (Table 3.1). However, the vast majority of studies using passive acoustics are for coarse-grained rivers, and only a handful of studies have attempted to use ADCPs for bedload assessment in sand-bed rivers (Table 3.1). Furthermore, it was not possible to find a single study using ADCPs to passively monitor sediment-generated noise emitted during bedload transport (Table 3.1).

The lack of passive acoustic studies regarding rivers, and limited usage of ADCPs to monitor bedload transport, has left gaps in knowledge hindering the ability to monitor rivers, especially those which are predominantly sandy. This chapter aims to help fill that knowledge gap.

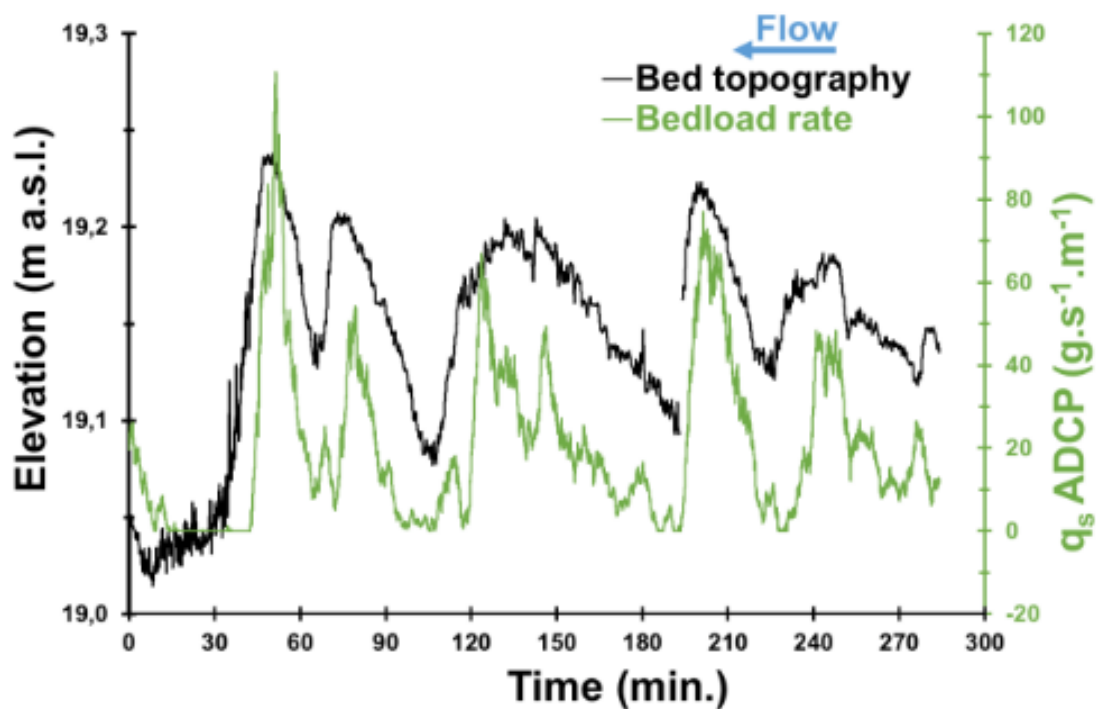


Figure 3.1. Bedload transport rate and bed topography (elevation) from a static ADCP in the Loire River (Le Guern *et al.* 2021). The figure shows how the strength of acoustic signals recorded by the ADCP at a frequency of 3 MHz correlate with changes in bed elevation due to changes in the presence of bedforms in a sandy-gravel river, and to calculated bedload transport rates ( $q_s$ ).

Studies of sandy rivers have highlighted new ways to monitor bedload transport using hydrophones and ADCPs (Fig. 3.1; Latosinski *et al.* 2017,2022; Conevski *et al.* 2018, 2020; Le Guern *et al.* 2021). For example, Latosinski *et al.* (2017), followed by Conevski *et al.* (2018), indicated that it was possible to accurately measure bedload transport rate from apparent velocity using stationary ADCP measurements and correcting for changes in the

moored boat's velocity using a DGPS. This research indicates a promising novel way to monitor bedload transport for finer (sand) sediment sizes using acoustic signals.

Le Guern *et al.* (2021) suggested that a hydrophone was the most efficient and accurate way to passively determine bedload fluxes. This is because the hydrophones in Le Guern *et al.*'s (2021) study were shown to give a good representation of the measured bedload flux, and they were easier to deploy than traditional methods such as the Helley-Smith pressure difference sampler (Rennie and Millar, 2002). Pressure difference samplers are meshed boxes that are used to trap sediment over a given time in order to calculate the sediment transport rate of a given river. In the future, passive ADCP measurements might be able to replicate this, helping accurately determine bedload flux.

Le Guern *et al.* (2021) also suggested that higher bedload rates were found on the crest of the dune and lower values in the trough. This was supported by Latosinski *et al.* (2022), who found that bed-particle velocity magnitudes increased from troughs to the crests of dunes.

However, further work on acoustic signals from sand bed rivers is needed, as there are limitations to these previous studies. For example, Le Guern *et al.* (2021) indicated that work is needed to identify the main controls on sediment-generated noise. Additionally, Conevski *et al.* (2018) stated that there is a need for new methods to be developed to help monitor bedload transport.

By conducting more research into bedload transport, a greater understanding of the controls of sediment-generated noise could be developed, especially for less studied sand-bed rivers. New research could also develop novel software and code, which can help aid in the interpretation of large data sets collected to monitor bedload transport. Research conducted in rivers can also be applied to the marine environment, for example, monitoring of geohazards or monitoring offshore wind energy structures.

### **3.1.2. Aims and objectives**

This chapter investigates acoustic noise generated by sediment transport in the sandy Río Paraná. The first aim is to develop methods that can be used to help with monitoring bedload transport. The second aim is then to understand better the main controls on sediment-generated noise. This involves testing four specific hypotheses proposed by previous field and experimental studies.

(1) A first hypothesis is that there is a link between flow speed and passively detected noise within sandy rivers, as seen within Chapter 2's laboratory experiments. This is perhaps the simplest hypothesis as both flow speed and strength of acoustic backscatter are measured in the same profile at the same location by an ADCP, and they do not involve using velocity profiles to calculate more complex parameters (e.g.  $u_*$ ), as in the next hypotheses.

(2) The second hypothesis is that there is a link between passively detected noise and friction velocity (friction velocity,  $u_*$ ) (Hatcher *et al.* 2017; Hay *et al.* 2021). For example, it has been suggested that the strength of acoustic signals emitted by the head of a turbidity current, are strongly affected by its speed and thus the strength and overall number of grain collisions. This led to a prediction that sound pressure scales with flow speed ( $U$ ) to the power of 7, and thus friction velocity ( $u_*$ ) to the power of 7 (Hatcher *et al.* 2017; Hay *et al.* 2021). Thus, it could be expected that some relationship between flow speed and strength of acoustic signals also occurs in other environments such as a river.

(3) A third hypothesis is there is a link between bedload transport rate ( $q_s$ ) and acoustic signal strength, as bedload transport rates are themselves correlated with bed shear stress and friction velocity. Previous work (Le Guern *et al.* 2021; Fig. 3.1) has shown such a correlation, with bedload transport rate being derived in these studies from the apparent velocity of the bed measured via ADCPs.

(4) Finally, previous work has implied that changes in acoustic signals might record bedform dynamics (Le Guern *et al.* 2021). Therefore, a final hypothesis is that the difference in passively detected noise generated between the trough and the peak of a bedform is related to flow speed.

### 3.1.3. Background

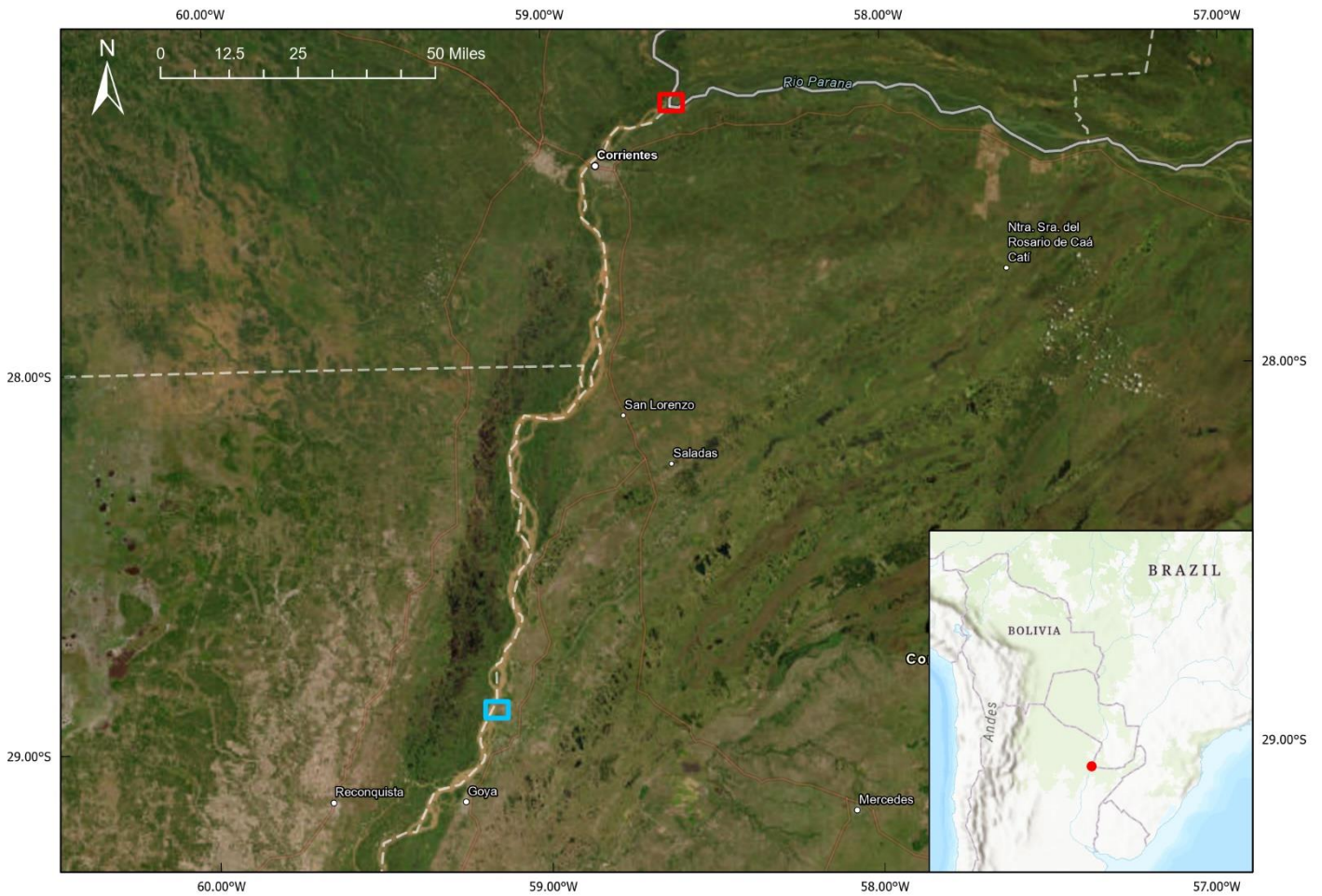


Figure 3.2. Location map of the Río Paraná. The red square denotes the northern 2004 survey area for both multibeam and 600 kHz ADCP transects. The blue square denotes the southern 2011 survey area containing a 1.2 MHz ADCP transect.

Field data was collected in the Río Paraná (Fig. 3.2). This river flows along the northeastern side of Argentina along the Argentina-Paraguay border (Parsons *et al.* 2005). Within the northern study area (red box in Fig. 3.2) the river flows from east to west, followed by a change to a northeast to southwesterly flow direction in the southern study area (blue box in Fig. 3.2; Parsons *et al.* 2005). In a study conducted in 2004, data was collected from the Río Paraná–Río Paraguay confluence and up to 30 km upstream of the confluence (Fig. 3.2; Smith *et al.* 2009; Reesink *et al.* 2014). Within the northern area of study, there are seven sand bars that have been previously studied, which are 10s to 100s of metres in length (Reesink *et al.* 2014). These bars are up to several metres in height, and host superimposed ripple-sized bedforms (Reesink *et al.* 2014). The southern study area was conducted in a stretch of the Río Paraná

containing no bars (Fig. 3.3B). Near the southern study area there are multiple large bars, which can be in excess of 1 km in length and width. Within the main channel of the Río Paraná, dunes increase with size as flow depth increases, reaching 1.2 to 2.5 m in height, with a wavelength from 45 – 85 m (Parsons *et al.* 2005).

Previous studies of the Río Paraná indicated that the bed of this river is predominantly medium-grained sand (60 – 80%) and fine-grained sand (20 – 40%) (Smith *et al.* 2009; Reesink *et al.* 2014). This bed sediment ranged between 0.18 mm and 0.99 mm, with an overall mean size of 0.38 mm. The channels of the Río Paraná are 1.9 – 4.8 km in width, with a maximum width of 9 km. Within both areas of study, the average width of the Río Paraná was 2.5 km, and the depth of the main channel of the Río Paraná is typically 5 – 12 m (Fig. 3.3; Parsons *et al.* 2005; Smith *et al.* 2009; Sandbach *et al.* 2010; Reesink *et al.* 2014).

Detailed multibeam surveys conducted in 2004 are available for the Río Paraná – these surveys partially cover the area of the 2004 ADCP transects measurements. Thus, these multibeam surveys help to understand the general types of bedforms and channel morphologies in the Río Paraná. However, multibeam surveys are only available for parts of areas for which there are ADCP transects to directly monitor bedform and channel morphological changes (Fig. 3.3A).

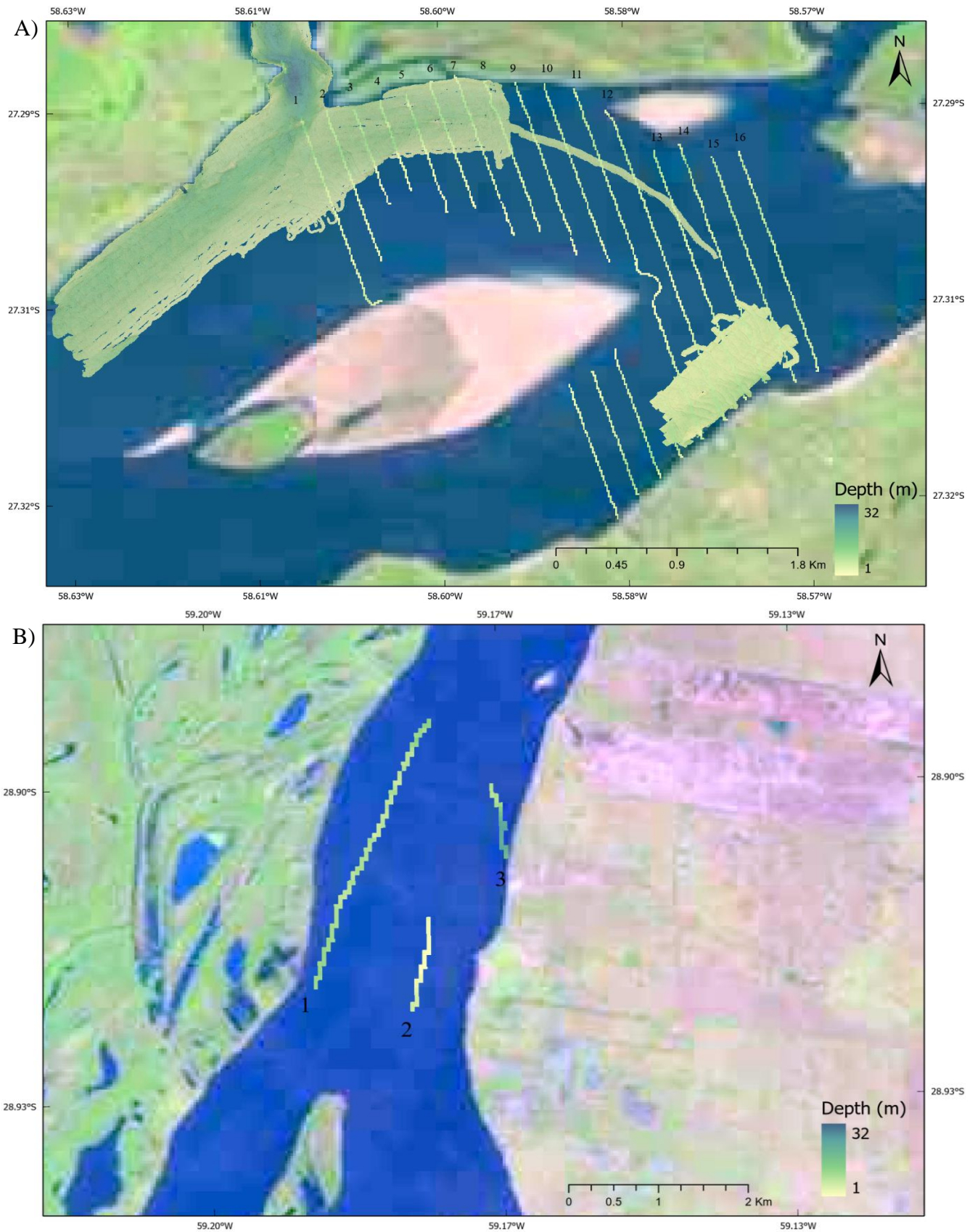


Figure 3.3. Bathymetry maps of the Río Paraná. Numbers denote transect lines within each study area. A) Northern study area of the Río Paraná (field study conducted in 2004). B) Southern study area of the Río Paraná (field study conducted in 2011). Locations shown in Figure 3.2.

## 3.2. Methods

*This section contains the methods used to analyse and display the ADCP data and bathymetry data sets collected within the Río Paraná. It also provides the equations used to perform the calculations required to analyse the ADCP data.*

### 3.2.1. ADCP data processing methods

Two ADCP data sets from the Río Paraná were analysed. The data were collected in 2004. A boat with a mounted 600 kHz ADCP collected data along multiple transects, using a sample frequency of 1.4 Hz (Fig. 3.3A; Parsons *et al.* 2005). The data collected in 2004 is denoted as the northern study area (red box in Fig. 3.2, also see Fig. 3.3a). Then in 2011, another study was conducted using a 1.2 MHz ADCP with a sample frequency of 1.5 Hz, in the southern study area (blue box in Fig. 3.2, and see Fig. 3.3b).

During the collection of both 2004 and 2011 data sets, along each transect line, the vessel only collected a single cross-section of the water column via an ADCP. Therefore, the velocity data sets used within Chapter 3 are instantaneous flow velocities within the water column. Unlike time averaged flow data (e.g. the mean velocity structures from multiple repeat ADCP surveys of the same transects), instantaneous flow velocity data can be easily effected by random turbulence within the river. Random turbulence causes variability in flow velocities, and velocity values can be in a different direction to the general flow of the river. As a result of such fluctuations, trends relating to flow speed to other variables may become obscured, especially within small data sets. In large data sets, it is possible to mitigate the effects of turbulence by averaging large amounts of the data, and over longer time scales.

#### 3.2.1.1. Collecting and understanding passively detected noise

In addition to ADCPs providing a velocity measurement, ADCPs provide a value of Received Signal Strength Indicator (RSSI) or sound intensity (dB) (Sontek, 2000; Teledyne RDI, 2011). RSSI is a measure of the signal strength of the received signal returned to the ADCP after a transmitted pulse (Teledyne RDI, 2011). The RSSI values represent the received signal which is a combination of reflected sound from scatterers and any other noise in the environment, particularly from a sound source that is within the ADCP's beams (i.e. central lobe of transmit/receive pattern) (Teledyne RDI, 2011). With further processing, RSSI values can be converted into sound intensity, which are commonly displayed in decibels (dB). Within

Chapter 3, RSSI and sound intensity values are derived from passively detected noise. This passively detected noise is from all objects within the water column (fish, turbulence, particles, anthropogenic), but with the vast majority of noise potentially being generated by particle-particle collisions.

After an ADCP sends out a pulse, as time increases between the initial acoustic pulse and the return of any acoustic signal, the returning signal's origin increases in apparent depth. This relates to the time taken for a signal to be emitted, scattered and return to the receiver face of the ADCP (Teledyne RDI, 2011). For example, if an ADCP received a signal 0.1 s after emitting it, the origin of the signal would be at 75 m depth ( $D$ ) (Eq. 3.1).

$$TWT \times C \div 2 = D \quad (3.1)$$

Where ( $C$ ) relates to the speed of sound in fresh water (1500 m/s) and ( $TWT$ ) indicates the two-way time taken for the signal time for the signal to be emitted and return to the receiver (Teledyne RDI, 2011; DUG, 2023). Generally, ADCPs are often setup to only listen for noise within the water column above the bed, with distance to the bed used to set the timing between emit and detect modes of the transducer. This prevents detection of the next active pulse, and any unwanted noise after the vast majority of the signal has returned. In order to passively listen for particles within the water column, this listening period after the ADCP has sent out a pulse is extended for as long as possible, whilst avoiding the detection of the next active pulse.

When an ADCP is listening for passive noise, if the passively detected noise is sufficiently loud and is relatively constant for the listening period, then there will be an elevated signal level for all range bins in addition to reflections. For example, if an ADCP with a range of 75 m listens for a period 0.1 s (Eq. 3.1) and if the noise source is near-constant for that 0.1 s, then there will be a vertical 'stripe' apparent in the RSSI plot (e.g. Fig. 3.8). The vertical 'stripe' results from a near-constant noise for all range gates on the ADCP. Range gating on ADCPs breaks any received signal into successive segments (depth cells) for independent processing. On ADCPs, acoustic reflections from far-ranges take longer to return to the ADCP than do acoustic returns from close ranges. As a result, successive range gates correspond to acoustic reflections from increasingly distant depth cells but will also have an additional noise component that is independent of range when there is a detectable near-constant passive signal (Teledyne RDI, 2011).

If the passively detected noise signal can be distinguished from ambient noise (at far-range usually) then it can be extracted and processed. In the case of noise generated by sediment particle collisions, the noise level is near-constant over a period of 0.1 s due to multiple particle collisions within that time frame. Each particle collision will have a different magnitude and frequency due to differences in magnitude of impacts and size/shape of the particles (Thorne, 1985, 1986, 1990; Marineau *et al.* 2015; Rigby *et al.* 2016). When combined into large mixtures of size classes, particles collisions produce a broad frequency noise spectrum.

Between the production of acoustic noise and detection by the ADCP, as the noise travels within the water column, the acoustic noise can be absorbed and attenuated by physical and chemical processes within the water column (Teledyne RDI, 2011). Attenuation along the single acoustic travel path is determined as  $\alpha R$  where  $\alpha$  is the absorption coefficient (dB/m) and  $R$  is the range from the transducer to the depth cell (m).

Generally, for actively emitting ADCP's, attenuation can occur via beam spreading. Beam spreading is the geometric cause of attenuation as a function of range from the ADCP. Beam spreading results in a logarithmic loss in sound intensity with increasing range (Teledyne RDI, 2011). However, following the inverse square law, when passively detecting sediment generated noise, beam spreading should not affect noise signal strength provided that the passively detected noise is being generated across the entire ADCP footprint. The reason for this is that an ADCP's footprint increases in proportion to  $R^2$  which cancels out the spreading which is equal to  $1/R^2$  (Basuki & Palupi, 2020).

$$\frac{\alpha \times R}{2} = \alpha^{(total)} \quad (3.2)$$

$$100 - 100 \times 10^{(-\alpha^{(total)} \div 10)} = \% \text{ reduction in } I \quad (3.3)$$

Based on experiments by Francois and Garrison (1982), using a 614.4 kHz (600 kHz) ADCP, with a water temperature of 20 °C, and a water depth of 8 m, the absorption coefficient ( $\alpha$ ) is  $\sim 0.083$  dB/m (Francois and Garrison, 1982a,b; NPL, 2023). Therefore, within the Río Paraná, at a range of 8 m from the ADCP, total attenuation for a one-way travel path ( $\alpha^{(total)}$ ) is 0.332 dB (Eq. 3.2). On a linear scale equating to a 7 % reduction in sound intensity (% *reduction in I*) (Eq. 3.3). A one-way travel path is used within the total attenuation calculation (Eq. 3.2) to equate for passively detected noise originating from particle collisions along the

bed and not the ADCP itself. Using 1228.8 kHz (1.2 MHz) ADCPs, attenuation per meter is ~ 0.332 dB/m (Francois and Garrison, 1982a,b; NPL, 2023). This equates to a total attenuation of 1.33 dB for a one-way travel path at 8m depth and a 26 % reduction in sound intensity (Eq. 3.2, 3.3).

### 3.2.1.2. WinADCP data conversion

Firstly, the raw 600 kHz and 1.2 MHz ADCP data files were converted by WinADCP into accessible MATLAB data files. WinADCP allows values present within the raw data (Table 3.2), such as RSSI backscatter and velocity, to be exported into a .mat file that could be used within the coding program MATLAB.

<b>Parameter</b>	<b>How are they measured</b>
Flow velocity (including maximum flow velocity and bottom tracked northern and eastern velocity components)	Measurements of the velocity magnitude of the water column from the ADCP corrected via bottom track data
Vessel velocity (northern and eastern components)	Direct measurements of velocity from the GPS
RSSI (at 600 kHz and 1.2 MHz)	Average Received Signal Strength Indicator (RSSI) of all four ADCP beams
Flow depth (Range to bed)	Measured using bottom-tracking with a finer resolution than the water-column depth bins of the ADCP
Latitude and Longitude	GPS derived coordinates

*Table 3.2 Parameters extracted via WinADCP and WinRiver II.*

During this conversion, it was not possible to extract all data available within the 1.2 MHz ADCP files. As a result, WinRiver II was also used to export the GPS latitude and longitude, Bottom track east and north velocity and the vessel east and north GPS velocity. The extraction of these variables allows the data to be used in further data processing. In addition to data extraction, using WinRiver II, plots of both RSSI and velocity magnitude were generated for transect 2 of the 1.2 MHz ADCP data (Fig. 3.8). A plot of average RSSI was chosen over average sound intensity (dB) to eliminate the internal corrections for spherical spreading and water attenuation conducted via WinRiver II. As a result, any potential sediment generated noise should manifest as vertical stripes of near-constant signal magnitude. This because any

attenuation along the one-way travel path from the noise source to the receiver will apply equally to the passive noise signal for all range gates (Fig. 3.8).

### 3.2.1.3. ADCP data calculations

This subsection describes the calculations used to determine variables such as friction velocity and bedload transport rate. Firstly, within both the 2004 and 2011 data sets, all RSSI measurements were converted into sound intensity (dB). Sound intensity (dB) was calculated via the multiplication of all RSSI measurements by a RSSI scale factor ( $K_c$ ) of 0.42 (Kim *et al.* 2004). Then, within each data set, passively received noise (dB) from the ADCP was derived from the final data bin in each ADCP vertical profile. Due to the furthest bin being far away from the ADCP, the active emitted pulse from the ADCP has dissipated, and the ADCP at this point is only passively detecting noise from its surroundings.

Data were screened from each ADCP vertical profile, for both velocity and acoustic backscatter, to remove any poor GPS positions, and obviously flawed flow velocity data. Poor GPS data was characterised by GPS coordinates not being in the vicinity of the survey area. Poor flow velocity data was indicated to be any data that was suggesting an alternative direction to the actual flow of the river.

#### **Friction velocity ( $u_*$ )**

The friction velocity was then calculated. Friction velocity ( $u_*$ ) is important for understanding the development of near-bed turbulence and sediment transport. It can be related to bed shear stress ( $\tau$ ), where  $\rho$  is water density (Eq. 3.4; Bagherimiyab and Lemmin, 2013). This is important as bed shear stress is fundamental for understanding the causes of morphological changes within the natural environment (Bagherimiyab and Lemmin, 2013).

$$\tau = \rho u_*^2 \quad (3.4)$$

Friction velocity was calculated using a rearranged version of the classical Karman-Prandtl equation for the Law of the Wall and was based on a sequence of velocity measured in a profile at different heights above the bed (Eça *et al.* 2015; Peng *et al.* 2020).

$$\frac{U}{u_*} = \frac{1}{k} \ln\left(\frac{Z}{Z_0}\right) \quad (3.5)$$

In order to use the Law of the Wall (Eq. 3.5), the equation had to be modified to work within MATLAB.

$$b = \frac{U-a}{\ln\left(\frac{Z}{Z_0}\right)} \quad (3.6)$$

$$u_* = (b) k$$

Eq. 3.6 is a modified version of the Karman-Prandtl equation for the Law of the Wall to calculate friction velocity (Peng *et al.* 2020). Within this equation,  $U$  is current velocity,  $U^*$  is bottom friction velocity,  $k$  is the Karman constant (0.41),  $Z$  is the height above bed and  $Z_0$  is bed roughness length,  $b$  is slope and  $a$  is the intercept (the value of  $U$  when  $\ln\left(\frac{Z}{Z_0}\right)$  is at 0).

Friction velocity was calculated from Eq. 3.6 through the regress natural log of relative height above the bed against mean flow magnitude above the bed. Then the output, which are the y-intercepts, were multiplied by the Karman constant, which is approximately 0.41 (Peng *et al.* 2020). Due to the limitations of the Law of the Wall method, there are numerous factors that need to be taken into account, which may lead to uncertainty of friction velocity ( $u_*$ ) estimates.

For example, the Law of the Wall method only holds in the first ~20% of the water column above the bed, which is the turbulent wall shear layer (Ali and Dey, 2017; Song *et al.* 2020). Therefore, the lower 20% of measured depth was identified for each ADCP profile. This allowed ADCP velocity data from higher than 20% of the flow depth to be excluded from any bed friction velocity calculations. It should be noted that the setup of the ADCP resulted in wide measurement bins. This means that there were, at times, few measurements available within the 20% threshold to calculate friction velocity. This paucity of data in the lower 20% of the flow, together with other sources of noise, may potentially lead to significant uncertainties in friction velocity. In order to improve this, large amounts of temporal averaging of flow velocity profiles would be needed to achieve a satisfactory mean value at a particular location.

Another limitation of this method is the choice of the von Kármán constant value used; this matters most on very rough walls as the effect it has on the calculated results increases (Wilcock, 1996; Placidi, 2015).

Further limitations are present with the Law of the Wall method. For example, local velocity profiles at the crest of a dune will underestimate friction velocity, and those in a dune's trough will overestimate bed friction velocity (Kostaschuk *et al.* 2004). The most accurate way of measuring friction velocity is by only measuring the centre point between a crest and trough of

a bedform, but this would leave too few values to analyse. Therefore, we chose to generate a friction velocity value for each ADCP measurement thus limiting spatial changes to reduce any effect of overestimated or underestimated values (Kostaschuk *et al.* 2004).

It should also be noted that, due to limitations performing regression using negative  $10\log_{10}$  friction velocity values, once friction velocity was calculated, all negative friction velocity values were set as no data (NaN). If these values were not removed, (complex) numbers would be generated by regression.

Once friction velocity was calculated for each transect in both the 2004 and 2011 ADCP data. Figures of  $10\log_{10}$  flow speed,  $10\log_{10}$  friction velocity against passively detected noise converted to dB scale were generated. These figures plotted all data points for all transects in their respective study area.

### **Apparent bed velocity ( $V_a$ ) and flow direction**

Following a modified version of Rennie and Millar's (2002) and Rennie and Villard's (2004) methods, a correction was generated to calculate bottom-track speed (apparent bed velocity) from ADCP data. First, for both the northern and eastern velocity components, the boat speed was subtracted from the bottom track velocity recorded by the ADCP. Within Eq. 3.7, bottom tracked velocity correction,  $V_{DGPS}$  is the boat velocity,  $V_{BT}$  is bottom track velocity. Then the northern and eastern bed velocity components are calculated together to provide a corrected apparent bed velocity (Eq. 3.8).

$$\begin{aligned} V_{BT \text{ corrected}}^{North} &= V_{DGPS}^{North} - V_{BT}^{North} \\ V_{BT \text{ corrected}}^{East} &= V_{DGPS}^{East} - V_{BT}^{East} \end{aligned} \quad (3.7)$$

$$V_a = \sqrt{V_{BT \text{ corrected}}^{2North} + V_{BT \text{ corrected}}^{2East}} \quad (3.8)$$

At this point, to ensure data quality, a check was conducted on both the 2004 and 2011 data. This check looked at the direction of the apparent velocity values to ensure that they were in the same direction as the actual flow of the river. It was performed by calculating the direction (Eq. 3.9). Where  $V_{BT \text{ corrected}}$  is the northern and eastern corrected bottom tracked velocity,  $\pi$  is Pi and  $\tan^{-1}$  is the inverse tangent function.

$$Direction = 180 + 180 \times \tan^{-1} \left( \frac{V_{BT \text{ corrected}}^{East}}{V_{BT \text{ corrected}}^{North}} \right) / \pi \quad (3.9)$$

At this point, it was identified that the 2004 data did not provide reliable results in terms of the direction of the velocity vector after removing the motion of the boat. Each successive transect gave a different direction to the previous one. Therefore, it was decided to only proceed with further bedload transport rate calculations using 2011 data (i.e. from the southern study area).

### **Bedload Transport Rate ( $q_s$ )**

Then, bedload transport rate ( $q_s$  ADCP) was calculated via Eq. 3.10, where  $P_s$  is sediment density ( $2650 \text{ kg.m}^{-3}$ ),  $r$  is the particle radius where  $r = D_{50}/2$  and  $V_a$  is the corrected apparent bed velocity (Eq. 3.10; Le Guern *et al.* 2020). Due to the lack of reliable results in the 2004 data, only one single figure was generated comprising all calculated bedload transport rate data in 2011 from the 1.2 MHz ADCP. The results were determined to be unreliable when the velocity directions derived from Eq. 3.9 were not consistent with the flow direction of the 2004 data. Finally, to verify previously suggested relationships that bedload transport rates are correlated with friction velocity, a plot of shear stress against bedload transport was generated (Wilcock and Kenworthy, 2002).

$$q_s \text{ ADCP} = \frac{4}{3} P_s r V_a \times 10^3 \quad (3.10)$$

It should be noted that after each plot was generated, regression analysis was performed on the data to determine the significance of the relationship between each plotted variable, and also determine the slope of the regression fit ( $m$ ). For example, a  $m$  value of 7 between sound pressure per collision and head speed would indicate that sound pressure per collision are related to head speed to the power of 7.

### **Uncertainty within the flow speed data**

In order to explore uncertainties regarding water flow speed, a histogram was created that shows the difference from mean velocity for each ADCP data point within both 2004 and 2011 data sets (Fig. 3.9). To create these plots, the mean flow speed of the unprocessed flow speed data was isolated for each transect. Then, this mean flow speed was subtracted from individual flow speeds. The creation of these histograms allowed visualisation of the distribution and uncertainties in velocity data collected during both the 2004 and 2011 studies. Each histogram shows both 1 and 2 standard deviations in the distribution of the flow speeds from the overall mean flow speed.

### 3.3. Results

#### 3.3.1. Cross-plots to show the relationships between different variables

Subsection 3.3.1. aims to determine if flow speed, friction velocity and bedload transport rate are related to passively detected noise. To finish, this subsection shows the relationship between friction velocity and bedload transport rate.

##### 3.3.1.1. The relationship between flow speed and passively detected noise

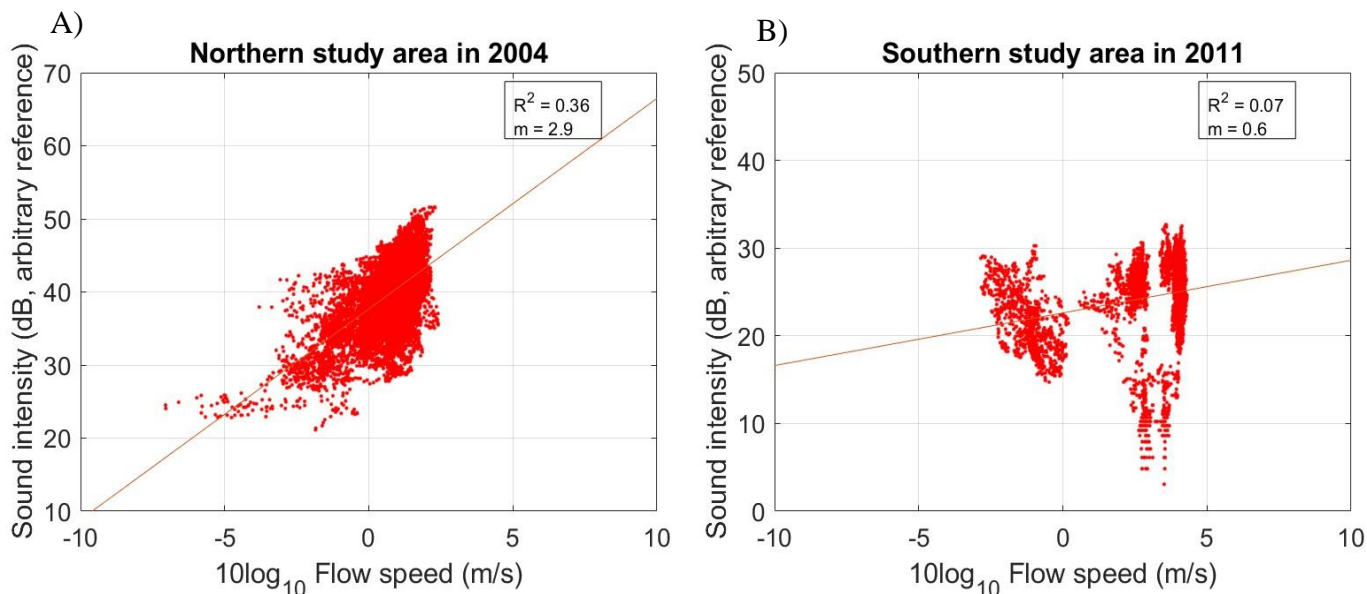


Figure 3.4. Plots showing  $10\log_{10}$  flow speed (m/s) against passively detected sound intensity (dB). A) Flow speed plotted against the strength of passively detected noise in transects 1 – 16 within the northern study area, with these data collected via a 600 kHz ADCP. B) Flow speed plotted against the strength of passively detected noise along transects 1 – 3 from the southern study area using a 1.2 MHz ADCP.

Statistical analysis of the 2004 data set in the northern study area (Fig. 3.4A) suggests that sound intensity (dB) is related to  $10\log_{10}$  flow speed (m/s) to the power of 2.9. However, this relationship is weak and has a low statistical significance, with an  $R^2$  value of 0.36, as a large amount of data points are widely scattered on either side of the trend line (Fig. 3.4A).

The 2011 data from the southern study area (Fig. 3.4B), collected by a 1.2 MHz ADCP, similarly displays an increasing trend between sound intensity (dB) and  $10\log_{10}$  flow speed. However, this trend is much weaker than the previous data set, and the  $R^2$  value of 0.07 suggests that the relationship is not statistically significant. It is possible to see that within the data, there

is a significant level of scattered data points, suggesting a lot of random variation in acoustic levels for a given flow speed and the presence of artefacts (Fig. 3.4B).

### 3.3.1.2. The relationship between friction velocity and passively detected noise

There is no clear relationship between flow speed and friction velocity ( $u_*$ ) in data from the northern study area (Fig. 3.5A). Statistical analysis provided an  $R^2$  of 0.0001, suggesting that noise (dB) and  $10\log_{10}$  friction velocity exhibit no relationship towards one another (Fig. 3.5A).

The data set from the southern area collected in 2011 similarly shows no relationship between  $u_*$  and passively detected noise, with sound intensity values predominantly spread over a large 30 dB range, from 5 to 35 dB (Fig. 3.5B). The slight increase in spread from the previous data set resulted in a slightly steeper increasing trend between sound intensity (dB) and  $10\log_{10}$  friction velocity, with a slope of 0.06. Statistical analysis of the 2011 data provided an  $R^2$  0.006, thus suggesting that sound intensity and  $10\log_{10}$  friction velocity exhibit no statistically significant relationship (Fig. 3.5).

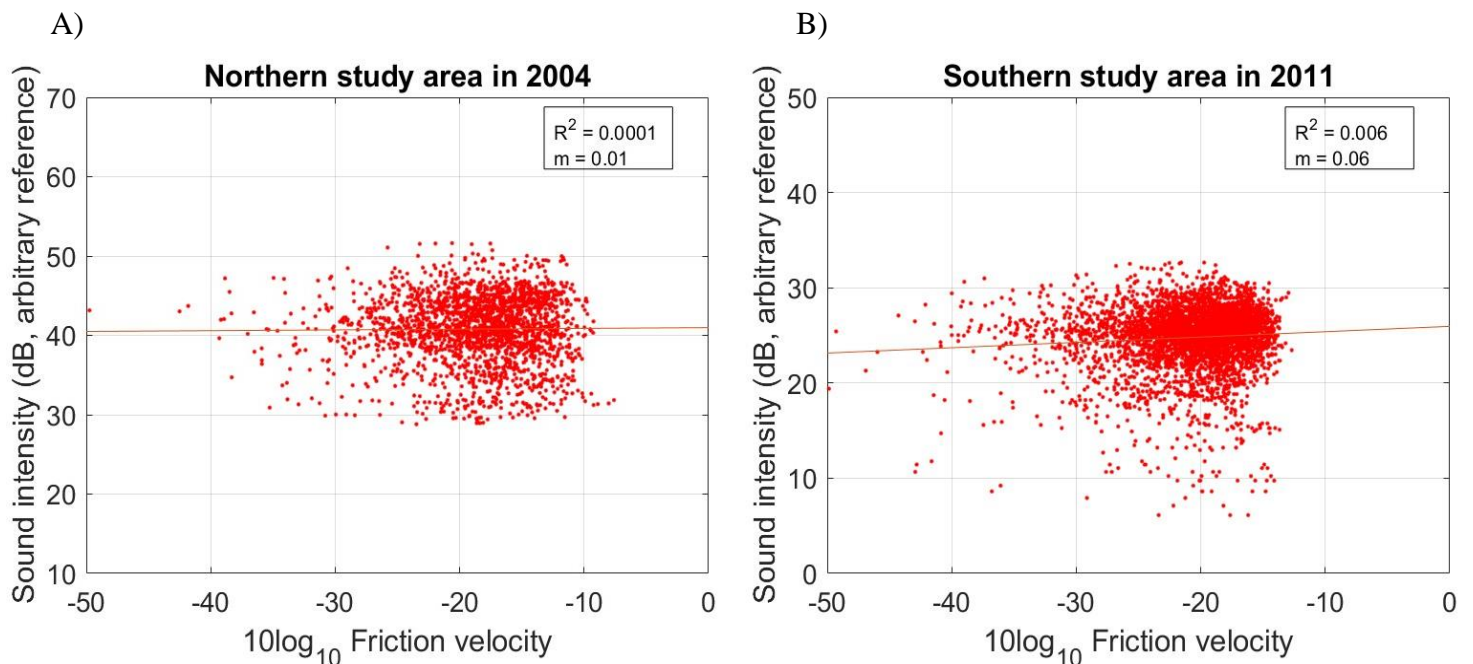


Figure 3.5. Plots showing  $10\log_{10}$  friction velocity against sound intensity (dB). A) Transect 1 – 16 within the northern study area collected via a 600 kHz ADCP. B) Transects 1 – 3 from the southern study area using a 1.2 MHz ADCP.

### 3.3.1.3. The relationship between bedload transport rate and passively detected noise

$10\log_{10}$  bedload transport rate values are predominantly spread between 12 and 20  $\text{g}\cdot\text{s}^{-1}\cdot\text{m}^{-1}$  (Fig. 3.6). As in the previous figures (Figs. 3.4 & 3.5), it is possible to see that the data is rather noisy, with a large spread in values (Fig. 3.6). Analysis of the bedload transport rate data provides an  $R^2$  of 0.06, suggesting that the  $10\log_{10}$  bedload transport rate<sup>0.6</sup> and passively detected noise are not closely related to one another.

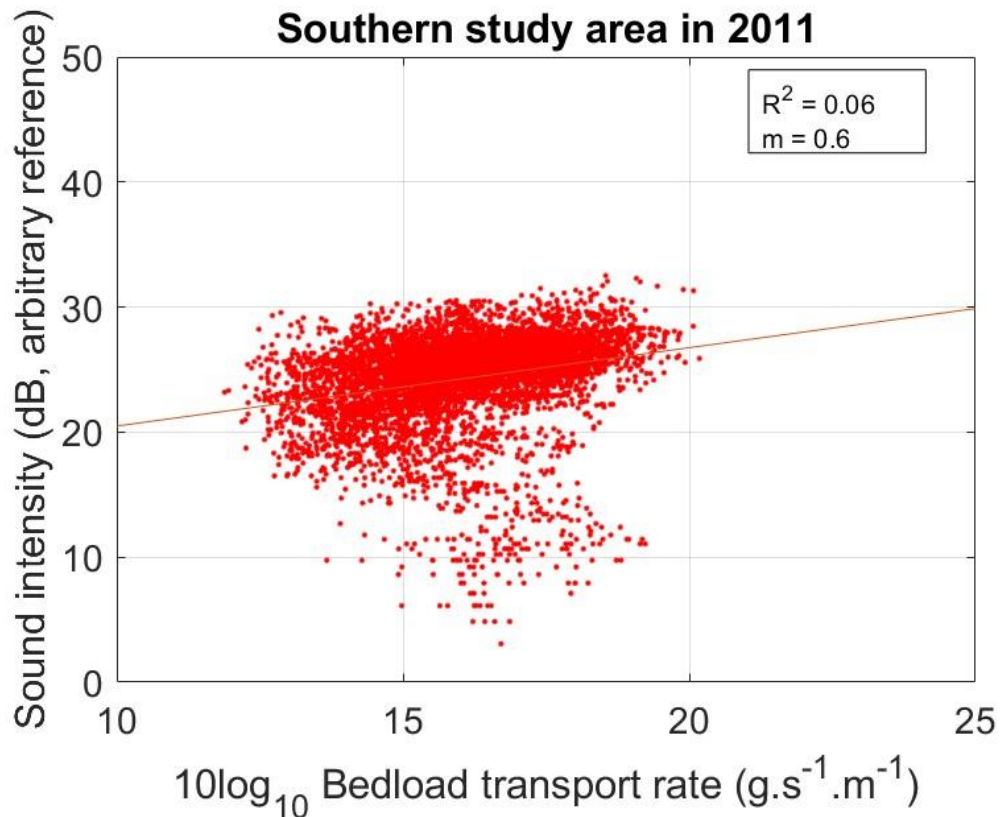


Figure 3.6. Plots showing  $10\log_{10}$  bedload transport rate ( $\text{g}\cdot\text{s}^{-1}\cdot\text{m}^{-1}$ ) against sound intensity (dB), transects 1 – 3 from the southern study area using a 1.2 MHz ADCP.

#### 3.3.1.4. The relationship between friction velocity and bedload transport rate

Statistical analysis between  $10\log_{10}$  bedload transport rate and friction velocity ( $u_*$ ) derived an  $R^2$  of 0.00002, suggesting that neither variable exhibit a relationship to one another (Fig. 3.7). As in the previous figures (Figs. 3.4 – 3.6), there is a high degree of instrument noise with a large spread in values (Fig. 3.7).

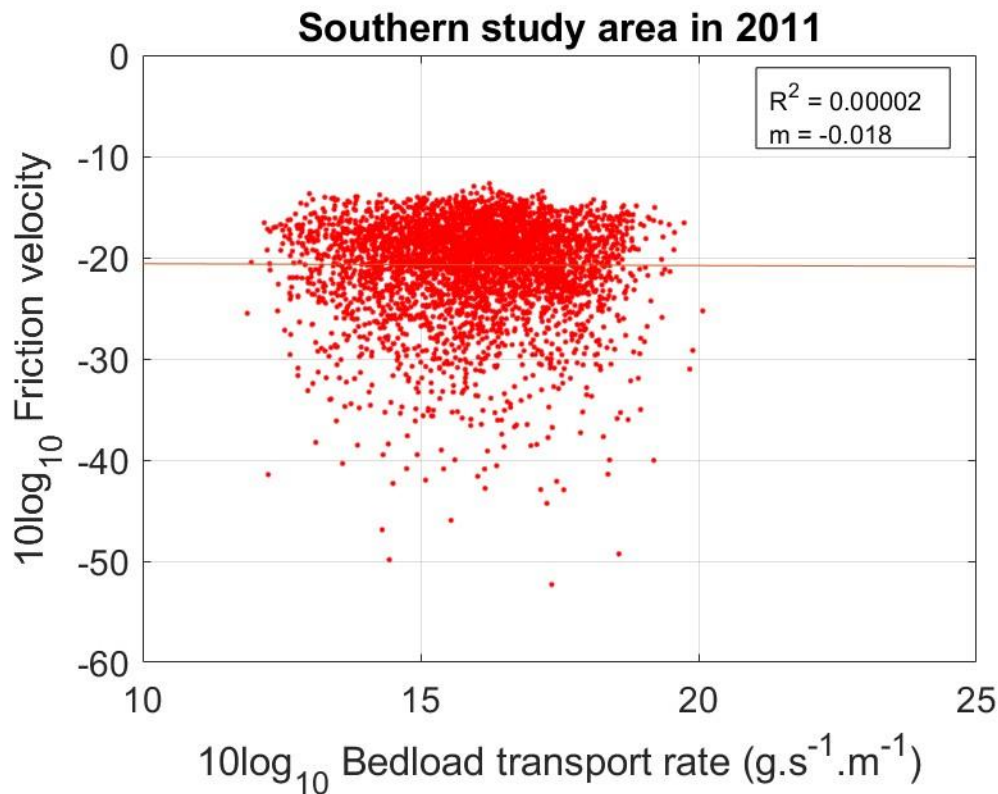


Figure 3.7.  $10\log_{10}$  bedload transport rate ( $\text{g}\cdot\text{s}^{-1}\cdot\text{m}^{-1}$ ) against  $10\log_{10}$  friction velocity, transects 1-3 from the southern study area using a 1.2 MHz ADCP.

#### 3.3.2. The relationship between Received Signal Strength Indicator and flow speed

This subsection displays the RSSI, and flow speed (m/s) derived from a 1.2 MHz ADCP collected in 2011.

The water depth in the Río Paraná dataset is around 8 m (Fig. 3.8A), and RSSI within the water column is fairly constant, at around 160 to 180 RSSI. Along the riverbed, the undulations in bed height are dune bedforms. These dunes are commonly around 2 m high and between 100 – 200 m long (Parsons et al., 2005). RSSI, recorded by the 1.2 MHz ADCP, is highest around the crests of the dunes (200 RSSI), followed by the lowest values in the troughs (170 RSSI) (Fig. 3.8A).

Due to how the 1.2 MHz ADCP was set up and deployed, it continued to passively listen to noise within the water column after the initial active ping returned. Any additional listening time (i.e. time after initial return arrives) is presented as increasing depth below the bed in Fig. 3.8.

At an inferred depth of 16 m, the ADCP detected a signal that is a multiple of the riverbed (Fig. 3.8A). This multiple is known to be of the riverbed as it follows a similar profile and is twice the known depth (8 m) of the riverbed (Fig. 3.8A).

Elsewhere in the ADCP data, vertical bands of noise are passively detected; these bands are visible from range gate depths of 20 to 32 m (Fig. 3.8A). The vertical band implies that this signal is present in all of the bins in the ADCP data, and this is an additional passive acoustic signal produced via sediment transport. The vertical bands are due to sediment generated noise, as they do not follow the profile of the riverbed, nor are they double the time of the previous multiple. It should be noted that the passively detected sediment generated noise is derived from bedload/ near bed particle collisions. Due to the high RSSI nature of the ADCP's active pulse, this sediment generated noise was drowned out, and it could only be detected once the active ping from the ADCP had dissipated. Therefore, any detected sediment generated noise is displayed at a greater apparent depth than the initial active ADCP returns from the river's bed at 8 – 14 m, and after its multiple at 16 m (Fig. 3.8A).

The passively detected sediment generated noise peaks around 80 RSSI is coincident with the location of the crests of bedforms, and it is around 60 RSSI at the location of the trough of the bedforms. The highest peaks in sediment generated noise (90 RSSI) can be found at the marked bedforms (1 & 2) on Fig. 3.8A.

Water flow velocities are fairly constant throughout the water column, at around 1 m/s (Fig. 3.8B). The fastest velocities are most commonly seen in the highest sections of the water column, closest to the water surface (1.7 m/s). Across these dunes within the Río Paraná, it is possible to determine differences in flow speed between the crest and the trough of the bedform. Highest flow speeds along a dune are found along its crest (0.8 m/s – 1.2 m/s), followed by low flow speeds commonly found within the trough of the dunes (0.3 m/s – 0.5 m/s) (Fig. 3.8B).

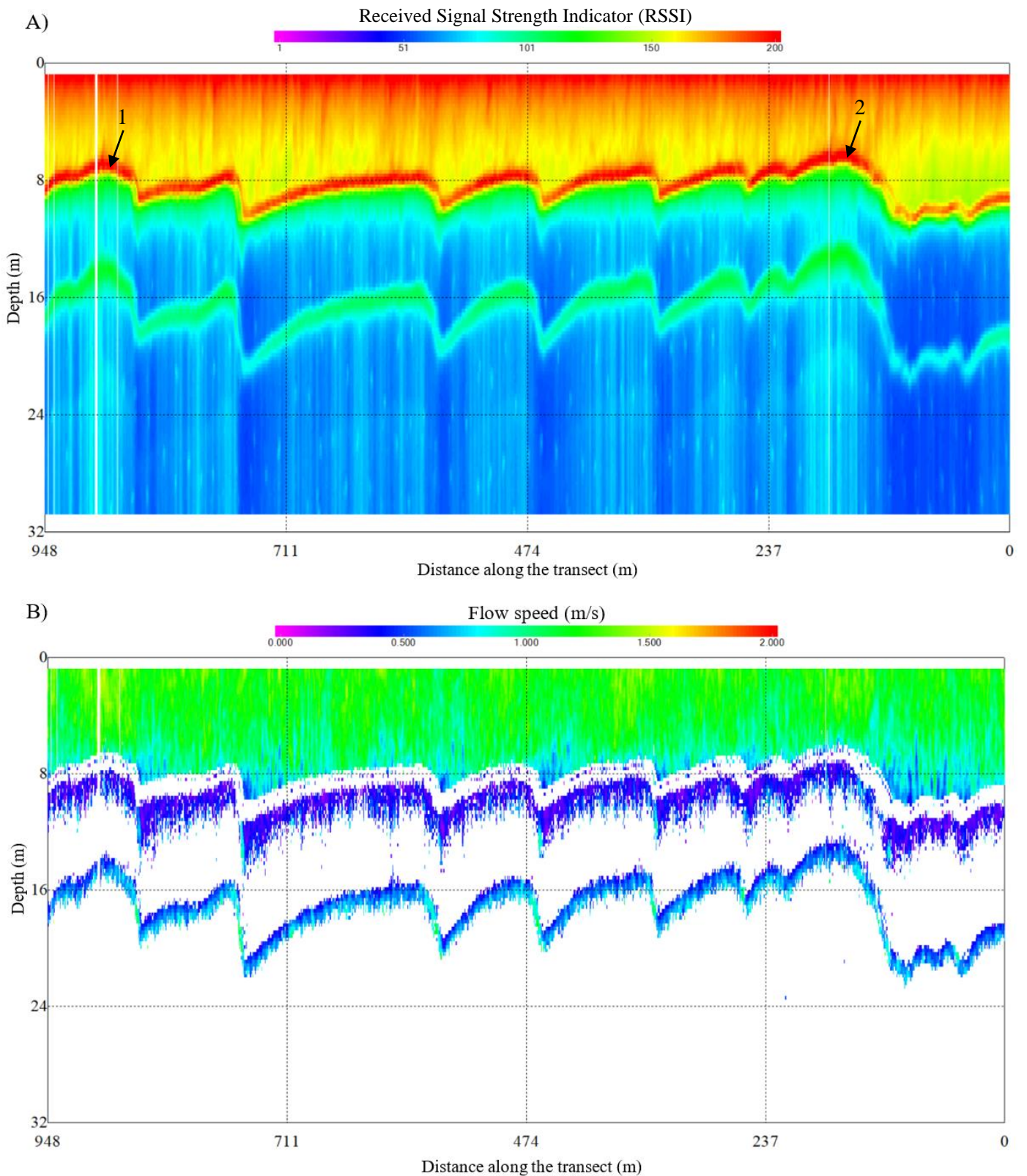


Figure 3.8. Flow speed (m/s) and Received Signal Strength Indicator (RSSI) return from a 1.2 MHz ADCP, along transect 2. A) Plot of Received Signal Strength Indicator (RSSI) with depth (m). B) Plot of flow speed (m/s) with depth. Note an extended listening time allowing the ADCP to continue listening beyond the initial return of the ADCPs active pulse (8 m depth). Any additional listening time of the ADCP is displayed as increasing depth.

### 3.3.3. Uncertainties within water flow speed (m/s)

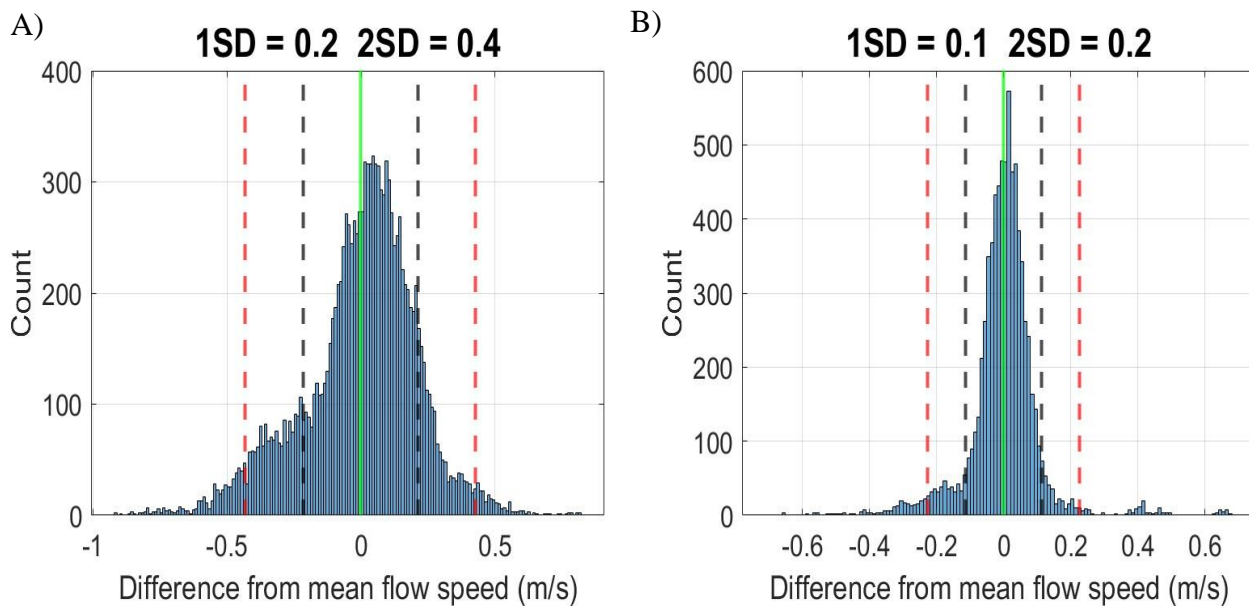


Figure 3.9. Plots showing deviance from mean flow speed for each data point. A) Transects 1 – 16 within the northern study area, with these data collected via a 600 kHz ADCP. B) Transects 1 – 3 from the southern study area using a 1.2 MHz ADCP. Green line indicates 0, Black line indicates 1 standard deviation and red line indicates 2 standard deviations.

For both the 2004 and 2011 data, deviations from the mean flow speed are quasi-normally distributed, with a small positive skew to higher flow speeds (Fig. 3.9). Furthermore, both 2004 and 2011 data sets exhibit large deviations in flow speed from the mean speed, with such deviations ranging between -1 m/s to 0.8 m/s (2004 data set; Fig. 3.9a) and -0.7 m/s to 0.7 m/s (2011 data set; Fig. 3.9b). It should be noted that the overall mean velocity per transect ranged from 1 – 1.3 m/s within the 2004 (northern study area) data set, and 0.8 – 2.5 m/s within the 2011 (southern study area) data set.

## 3.4. Discussion

*This section presents the main conclusions. It explores whether the aims and objectives were achieved and the answers to the four hypotheses being tested.*

### 3.4.1. Relationships between flow speed and passively detected noise

Data collected in 2004 from the northern study area provides a weak relationship ( $R^2$  of 0.36) between flow speed and passively detected noise; whereas data collected in 2011 from the southern area suggest that there is no relationship ( $R^2$  of 0.07) between flow speed and passively detected noise (Figs. 3.2, 3.4). The presence of a relationship in one of the two study areas supports the work by Hatcher (2017) and Hay *et al.* (2021), who also propose a link between these two variables.

The exponent that related flow speed to the power of acoustic signals can be constrained, although noting the low  $R^2$  values and weak statistical relationship. This exponent is also much lower exponent than in previous studies (e.g. Hatcher, 2017; Hay *et al.* 2021), or seen in the laboratory experiments of Chapter 2. Previous studies by Hatcher (2017) and Hay *et al.* (2021) advocated that flow speed and passively detected noise are related by an exponent of 7. Furthermore, in the laboratory setting (Chapter 2), the 600 kHz ADCP suggested that the exponent between flow speed and passively detected noise was closer to 6.5 and 5.4 for a 1.2 MHz ADCP. The derived exponents from Hatcher (2017) and Hay *et al.* (2021), and Chapter 2 are all much higher than those observed in Río Paraná data. It is not possible to identify the cause of the significantly lower exponent of 2.9 found in the Río Paraná.

The lack of a statistically significant relationship between flow speed and passively detected noise may result from the presence of high amounts of scatter within the data (Fig. 3.4A). The presence of scatter within the data is further indicated by the large differences in flow speed from the mean, and large number of points outside the 2<sup>nd</sup> standard deviation in Fig. 3.9. In addition, comparing between data sets (2004 and 2011), the 2011 southern study area has the largest variation in mean flow speed between transects. Within the 2011 data, mean flow speed can differ by up to 1.7 m/s, compared to 0.3 m/s in the 2004 northern study area. Therefore, large variations in flow speed within the (2011) southern study area are most likely obscuring any trend between flow speed and sound intensity (Fig. 3.4B). Significant amounts of scatter

have been noted to be an issue in other studies such as Latosinski *et al.* (2017, 2022) and Le Guern *et al.* (2021), both who aimed to measure bedload transport rate within rivers.

In addition to scatter, attenuation should be considered in the obscuration of any relationship comparing to passively detected noise. For example, at a range of 8 m within the Río Paraná, a 600 kHz ADCP can experience a 7 % reduction in sound intensity, and a 1.2 MHz ADCP can even experience a 26 % reduction in sound intensity (Eq. 3.3). Therefore, attenuation may have helped in the obscuration of any relationship between acoustic power and flow speed for the 1.2 MHz ADCP. The higher frequency of the 1.2 MHz ADCP has a greater level of sound absorption than the 600 kHz ADCP, thus obscuring its relationship (Francois and Garrison, 1982a,b; NPL, 2023). Although, it is difficult to know where the passive noise generation is originating from, it is likely that the majority of passive noise is generated along the bed of the river.

### **3.4.2. Relationships between friction velocity and passively detected noise within the Río Paraná**

Data derived from both northern and southern study areas implies that there is no relationship ( $R^2$  of 0.0001 and 0.006) between friction velocity ( $u_*$ ) and passively detected noise (Fig. 3.5).

The results between friction velocity and passively detected noise differ substantially from the results presented between flow speed and passively detected noise. This difference between flow speed, friction velocity and passively detected noise values is unexpected as previous research by Hatcher (2017) and Hay *et al.* (2021) suggested that sound pressure per collision is related to head speed to the power of 7, and thus friction velocity to the power of 7. This should mean that the results between flow speed, friction velocity and passively detected noise all exhibit a similar relationship and exponent (Figs 3.4, 3.5). It should be noted though, that results from Hatcher (2017) and Hay *et al.* (2021) are based upon a new model of collisions within a granular flow. Therefore, if there was a relationship between sound pressure per collision, head speed and friction velocity, the relationship between each value might be to a different exponent other than the suggested power of 7 (Hatcher 2017; Hay *et al.* 2021).

In addition, research conducted by both Sime *et al.* (2007) and Hossein and Rennie (2009) further support the expectation of a relationship between friction velocity, flow speed and passively detected noise. Sime *et al.* (2007) first indicated that it was possible to estimate shear stress from a moving boat acoustic Doppler velocity measurement. Whilst Hossein and Rennie

(2009) proposed that faster flow speeds should lead to a steeper velocity gradient and higher  $u_*$ .

The lack of relationship between friction velocity and passively detected noise could have firstly resulted from the amount of scatter within the data. Both sites presented within Figs. 3.4 and 3.5 contain a large degree of noise within the data, seen by a large degree of scatter, especially in Fig. 3.5B. Past research that estimated shear stress from moving boat ADCP measurements proposed that this scatter could have originated from a variety of sources (Sime *et al.* 2007), such as random noise associated with temporal flow variability, and bias due to sidelobe interference and bed movement (Sime *et al.* 2007).

The scatter in these data could have been further exacerbated by the instrumental setup and the method used to calculate friction velocity (Sime *et al.* 2007). This is because the method used to calculate friction velocity only uses measurements from the lower most 20% of the water depth. This reduces the number of ADCP measurements available to calculate friction velocity. Therefore, the ADCP measurement bins were very large. The size of the measurement bins would have resulted in even fewer potential ADCP measurements within the first 20% of the water depth. The limited data is further hindered by the removal of negative  $u_*$  values to allow for the regression calculation. The reduced number of measurements from these factors could then have exacerbated any scatter and resulted in the lack of an expected relationship between friction velocity and passively detected sediment-generated noise.

It is proposed that by averaging data over adjacent ensembles before or after using the log law method and increasing the number of data points available, scatter within the data can be reduced (Sime *et al.* 2007). Additionally, with the increased averaging, the very low  $R^2$  values on Fig. 3.5 may be increased, thus helping identify a relationship between friction velocity ( $u_*$ ) and passively detected noise.

Similar to acoustic power and flow speed, attenuation for both the 600 kHz and 1.2 MHz ADCPs may have played a role in the obscuration of any relationship between acoustic power and friction velocity.

### **3.4.3. Relationships between bedload transport rate and passively detected noise within the Río Paraná**

Previous work by Latosinski *et al.* (2017) and Le Guern *et al.* (2021) indicated that not only is it possible to measure bedload transport rate from the apparent velocity of the bed measured via fixed ADCPs, but there is also a relationship between sound intensity and bedload transport rate.

During the processing of data from the Río Paraná, it was identified that the 2004 data did not provide reliable results in the direction of the flow velocity vector, after removing the motion of the boat. Thus, data collected in 2004 from the northern study area were omitted from this investigation.

When measured from a moving vessel with a mounted ADCP, bedload transport rate do not correlate with acoustic signal strength ( $R^2$  of 0.06; Fig. 3.6). It should be noted that the 2011 southern study area data contains significantly more scatter than the previous results presented within Latosinski *et al.* (2017) and Le Guern *et al.* (2021).

Previous research has suggested that bedload transport rates themselves correlate with bed shear stress and friction velocity (Wilcock and Kenworthy, 2002). This is not seen within Chapter 3 (Fig. 3.7). This is likely due to the previously noted high level of scatter, attenuation of noise and the method used to calculate friction velocity exacerbating any scatter present within the data.

### **3.4.4. Variations in passively detected noise across the profile of bedforms**

It is possible to identify sediment-generated noise across several bedforms on transect 2 within the 2011 southern study area (Fig. 3.8). This sediment-generated noise is exhibited as vertically striped lines below the surface of the riverbed.

This sediment-generated noise increases in RSSI from the trough to the crest of bedforms (Fig. 3.8A). With the possible link between sediment-generated noise and bed load transport rate, it could be expected that the rise in the RSSI of sediment-generated noise would be followed by an increased bedload transport rate. This, in turn, would support the findings by Le Guern *et al.* (2021) that higher bedload rates are found on the crest of the dune, and lower values in the trough.

There is a link between the RSSI sediment-generated noise, flow speed and bedforms position (Fig. 3.8). The slowest flow speeds coincide with the troughs of bedforms, which coincides with the lowest sediment-generated noise magnitudes. Slower flow speeds at the troughs of bedforms are also observed by Latosinski *et al.* (2022). However, statistical analysis of all 2011 data provided an  $R^2$  of 0.07, suggesting no relationship between passively detected noise and flow speed (Fig. 3.4B). The lack of relationship present during statistical analysis could be the result of significant levels of interferent noise within the data. Further investigation is required to determine the visual and statistical discrepancies in relationship between passively detected sediment-generated noise and flow speed.

### 3.5. Conclusion

*This section summarises the main conclusions. It provides suggestions for future studies to remedy the lack of correlation seen between passively detected noise and other parameters within the data used here.*

This chapter succeeds in the first aim of developing new methods that can be used to monitor bedload transport. The newly developed methods could be used to help analyse new data sets collected in the future. It also addresses Conevski *et al.*'s (2018) request that new methods are needed to help monitor bedload transport via acoustic signals. It has also proven that it is possible to identify and analyse sediment-generated noise recorded from a moving vessel via an ADCP.

Data from the 2004 northern study area show a possible positive, low-significance relationship ( $R^2$  of 0.36) between flow speed and passively detected noise generated by particle-particle collisions (Fig. 3.4A). However, it should be noted that in the 2011 southern study area, a low  $R^2$  of 0.07 indicates no significant relationship between flow speed and passively detected noise (Fig. 3.4B).

In the northern study area, where there is a potential relationship between flow speed and passively detected noise, the exponent of 2.9 was significantly lower than that observed within a more controlled laboratory setting (Chapter 2). This potentially results from a number of factors, such as differences in environment between the laboratory and the river, or it is due to high levels of interferent noise within data from both the northern and southern study areas and the presence of attenuation. Further work is required to determine the presence of a relationship between flow speed and passively detected noise within a river.

Chapter 3 finds that there no relationship between sediment-generated noise and friction velocity. This differs from the proposal by Hatcher (2017) and Hay *et al.* (2021) that sound pressure is strongly related to flow speed to the power of 7 and thus friction velocity to the power of 7. The lack of relationship potentially relates from the high level of scatter within the data, attenuation of passively detected noise, and the methods used to collect the data and to calculate friction velocity.

Results from the southern study area data set (collected in 2011) indicated that there is no relationship between bedload transport rate and sediment-generated noise ( $R^2$  of 0.06). The

lack of relationship between both bedload transport rate and sediment-generated noise is unexpected as previous work by Le Guern *et al.* (2021) linked acoustic signal strength and bedload transport rate within the Loire River (France). Similar to previous results, the lack of relationship most likely originates from the presence of scatter within the data and attenuation. With further work, the amount of interferent noise could be reduced, allowing for the detection of a relationship between bedload transport rate and sediment-generated noise.

Finally, it is possible to visually identify that across a bedform, sediment-generated noise and velocity magnitude rise from the trough to the crest (Fig. 3.8). This further supports the notion that sediment-generated noise is related to flow speed. The links between sediment-generated noise, flow speed and bedload transport rate suggested within this chapter could help explain why in Le Guern *et al.* (2021) higher bedload rates are found on the crest of the dune and lower values in the trough.

### **3.5.1. Future work**

Future work should aim to reduce scatter and improve the signal-to-noise ratio of the field data. It should also reduce the chance of particle collision strikes on the transducer faces of the ADCP, as these strikes, to a lesser degree, could have potentially also occurred during the recording of the Río Paraná data. For example, a streamlined housing could be built around the ADCP, with acoustically permeable mediums over the transducer faces. This would then help prevent any particle collisions against the transducer face, thus helping to reduce scatter. These improvements could help increase the reliability of any new findings and allow the detection of relationships between friction velocity, bedload transport rate, flow speed and passively detected noise.

During future work, a new or improved method should be used to calculate friction velocity. For example, during the next experiment to collect new data, a reduced measurement bin size with more samples for each ADCP measurement point should be used to collect more data within the first 20% of the water column range from the bed. This will then increase the amount of data available to be used to calculate each  $u_*$  value with the Law of the Wall method. In addition, to help reduce scatter within the data, averaging should be performed over adjacent ensembles. Future work should also aim to ascertain the degree in which attenuation in relation to differences in range and ADCP frequency can affect and obscure the presence of any relationship relating too passively detected noise.

It would be preferential to repeat all measurements using an anchored boat as per Le Guern *et al.* (2021). Anchoring the boat would significantly reduce errors due to boat movement and enable averaging over timescales associated with the migration of bedforms. Given that Le Guern *et al.* (2021) successfully tested an ADCP at the same time as making similar measurements with a hydrophone, it would provide a useful comparison before trying to collect transects.

## Chapter Four

---

# Passive acoustic monitoring of turbidity currents within submarine channel systems



*RRS James Cook during its voyage to monitor the Congo Canyon (BODC, 2019).*

## 4.1. Introduction

*This chapter aims to develop new passive monitoring techniques that will be able to monitor turbidity currents within submarine channel systems. This introduction section provides a background into the three submarine channel system environments that are studied, and provides a brief description of the methods used to monitor turbidity currents in the field.*

Active acoustic techniques (such as ADCPs) are commonly used to measure the velocity structure of sediment-laden flows, including turbidity currents. This chapter tests whether turbidity currents also emit passive acoustic signals, and whether these passively emitted signals can be recorded by ADCPs with frequencies ranging from 75 kHz to 1.2 MHz. It is found that turbidity currents at some locations emit passively detected noise at this frequency, whilst others do not. Thus, the chapter also aims to explain why some turbidity currents emit signals, but not others, and what these passively emitted signals can tell us about turbidity current processes.

Turbidity currents are underwater sediment flows driven by the excess density of sediment they carry, and they are one of the most important processes for moving sediment across our planet, sometimes for up to thousands of kilometres into the deep ocean (Kuenen and Migliorini, 1950; Piper *et al.* 1999; Talling *et al.* 2007; Talling, 2013; Simmons *et al.* 2020). These flows may also play a key role in the transfer and burial of organic carbon (Galy *et al.* 2007; Hage *et al.* 2022). Turbidity currents are also a major hazard to critical marine infrastructure, such as pipeline and telecommunication cables (Heezen *et al.* 1964; Piper *et al.* 1999; Clare *et al.* 2020; Simmons *et al.* 2020).

Due to the destructive capability of turbidity currents, instruments and moorings deployed to monitor these currents are often damaged (Sequeiros *et al.* 2019; Clare *et al.* 2020). The highly episodic nature of these flows also makes them challenging to measure in action. As a result, there are remarkably few direct measurements of turbidity currents, ensuring they are still poorly understood (Clare *et al.* 2020; Simmons *et al.* 2020). This also means that a high percentage of what we know is based upon indirect methods such as laboratory-scale experiments and analysis of their deposits (Kuenen and Migliorini, 1950; Lowe, 1982; Gani, 2004; Baas *et al.* 2005; Talling *et al.* 2015; Simmons *et al.* 2020).

Direct monitoring methods have slowly advanced in order to reduce the level of damage to moored instruments by turbidity currents. Presently, most attempts to monitor turbidity

currents have used ADCPs. These ADCPs can be located outside the flow, although their anchor still needs to be on the seabed within the flow. This means that the anchor line is often broken in faster moving turbidity currents, such that ADCP and data can be lost. In a few studies, moorings have been deployed with two anchors, with those anchors located entirely outside the flow (Pope *et al.* 2022). There have also been efforts to use ADCPs to measure sediment concentrations as well as profiles of flow velocity. For example, Simmons *et al.* (2020) used 75 kHz and 300 kHz ADCPs to make detailed measurements of suspended sediment concentrations, albeit with major assumptions about sediment grain sizes within the flow.

This chapter seeks to understand how acoustic signals produced by particle-particle collisions in turbidity currents are passively detected by ADCPs, and whether passive acoustic signals can be used to monitor turbidity currents within submarine canyons. Passively acoustic signals are being used to remotely sense other types of sediment flows (Allstadt *et al.* 2018; Huang *et al.* 2004; Kogelnig *et al.* 2014; Thorne, 2014). A key question is whether these passive signals only record when a turbidity current happens or provide further information about flow characteristics. Past work has shown that with decreasing particle size, the frequency of sediment-generated noise increases in a linear fashion (Thorne 1985, 1986). Hatcher (2017) used field data from Squamish Delta in British Columbia, Canada, to propose that turbidity currents passively emit acoustic signals, whose strength is related to the flow's speed. Hay *et al.* (2021) extended the work from Hatcher (2017), identifying the frequency spectra of noise generated within turbidity currents, and proposing that flows generate sediment-generated noise not only during bedload transport but also when particles are in a more expanded state (i.e. a granular flow with more vigorous collisions and lower particle concentrations). The notion by Hay *et al.* (2021) that suspended particles can collide and create sediment-generated noise departs from previous work on bedload sediment-generated noise (e.g. Jones and Mitson 1982; Heathershaw and Thorne 1985; Thorne 1985, 1986; Williams *et al.* 1989; Bassett *et al.* 2013; Katsnelson *et al.* 2021). The relationships between flow speed and passively detected noise found by Hatcher (2017) and Hay *et al.* (2021) potentially opens the way for passively detected noise to remotely sense not only when turbidity currents happen, but also constrain their speeds.

Here we aim to extend this past work by Hatcher (2017), Simmons *et al.* (2020) and Hay *et al.* (2021) to determine whether turbidity currents in a series of other locations can be remotely

sensed using passive acoustic signals. This is one of the first studies using passive acoustic signals to isolate and understand sediment transport processes occurring within submarine turbidity currents, and the first such study to compare signals at multiple different field sites.

#### **4.1.1. Research Aims**

The first aim is to analyse how passive acoustic signals generated by sediment transport within turbidity currents are recorded by ADCPs. This is undertaken by comparing ADCP records of turbidity currents at three different sites: Bute Inlet (Canada), Monterey Canyon (USA) and Congo Canyon (West Africa) (Figs. 4.1 – 4.3).

This chapter then examines how passive acoustic signals vary throughout the duration of a turbidity current (from their head to tail), and how those passive acoustic signals are related to flow speeds and distance from the seabed to the ADCP. It is then tested whether head speed to the power of 7 is proportional to sound pressure per collision, as suggested by Hay *et al.* (2021) based on work at Squamish Delta in Canada, in this wider range of settings.

Finally, this chapter aims to determine what caused differences in acoustic signals in the three different field sites. For example, why are strong passively detected signals recorded by ADCPs in Bute Inlet and Monterey Canyon, but not in the Congo Canyon?

## 4.1.2. Background to the field sites

The next sections describe the field sites used in this study, where ADCP data is available.

### 4.1.2.1. Bute Inlet, British Columbia, Canada

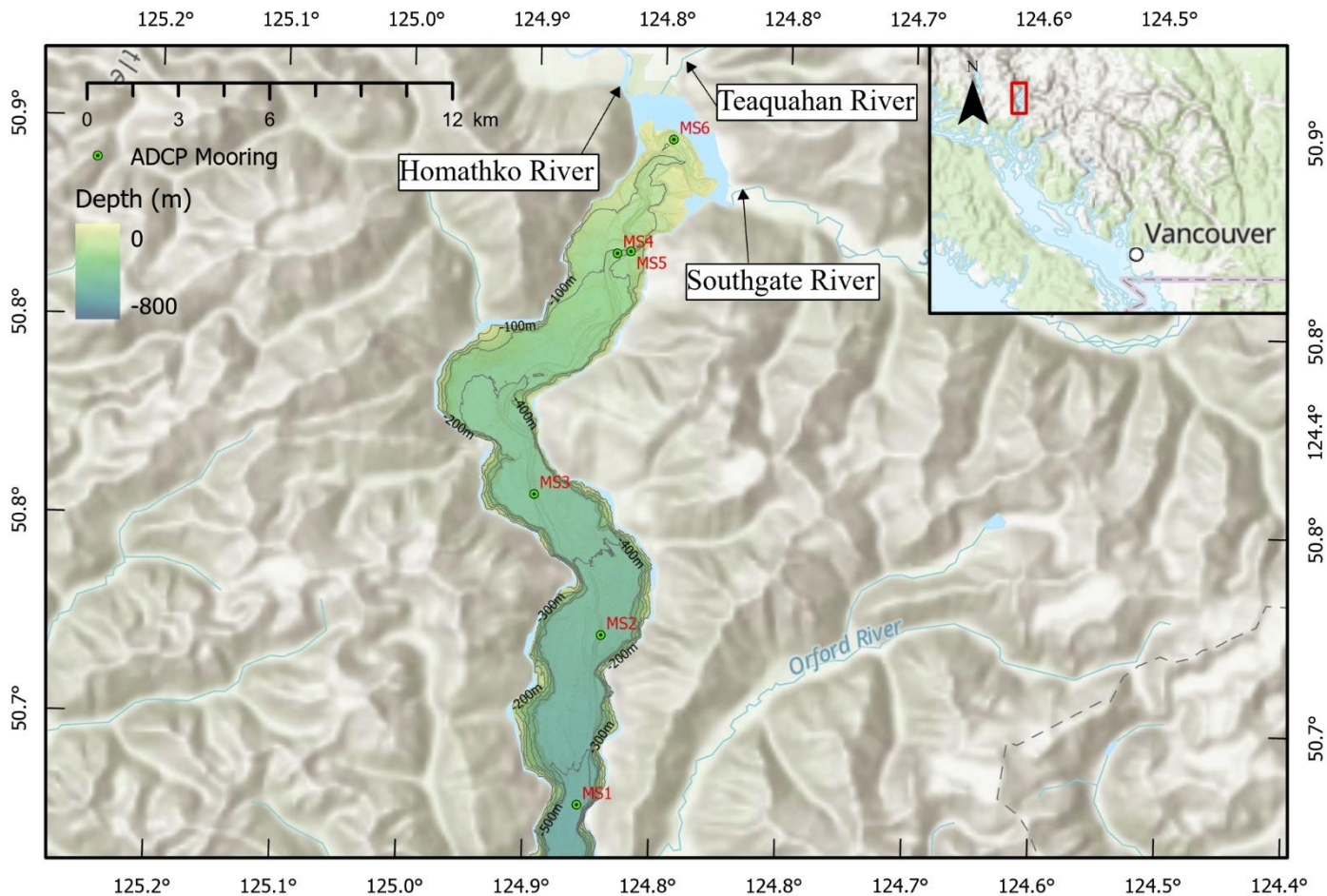


Figure 4.1. Detailed bathymetric map of Bute Inlet, indicating the locations of each ADCP mooring along the submarine channel system.

Bute Inlet is a fjord in British Columbia, Canada, that is fed by two fjord-head deltas formed by the Homathko and Southgate Rivers (Fig. 4.1). There is a ~50 km long channel on the floor of the fjord that has been formed by turbidity currents (Heijnen *et al.* 2020; Pope *et al.* 2022). There have been multiple studies to characterise and understand the channel system in Bute Inlet (Fig. 4.1; Prior *et al.* 1987; Zeng *et al.* 1991; Zeng and Lowe, 1997; Pope *et al.* 2022). The submarine channel in this fjord starts at the Homathko and Southgate River-deltas, and extends for 50 km to a water depth of ~350 m (Heijnen *et al.* 2022). Zeng *et al.* (1991) indicated that the submarine channel's floor comprised predominantly of sand, with the overbank areas

are dominated by silt. This sediment is primarily derived from the Homathko River, which has a sediment load of 15% gravel, 65% sand, 15% silt and 5% clay (Zeng *et al.* 1991; Pope *et al.* 2022). The Homathko River accounts for around 75% of the freshwater input into the inlet; this is followed by the Southgate River (15%), with the remainder sourced from small streams entering the fjord's sides (Zeng *et al.* 1991). The majority of turbidity currents within this submarine channel occur during the summer months when the river discharge is high, and during the low tide period (Heijnen *et al.* 2022; Bailey *et al.* 2023). Time-lapse surveys of the channel show that it is maintained by rapid migration of internally generated knickpoints, (i.e. waterfall-like steps) that may be 20 –30 m high and migrate for 300 – 500 m/year (Heijnen *et al.* 2022). Recent studies have also investigated the structures of turbidity currents present within Bute Inlet (Pope *et al.* 2022). Pope *et al.* (2022) found that flows within this region split into three categories: dense, transitional and dilute. Dense flows are fast (>15 m/s), thin (<10 m) and have concentrations up to 38%<sub>vol</sub> and are dominated by grain-to-grain interactions (Pope *et al.* 2022). Dilute flows, on the other hand, are slower <1 m/s, well mixed with turbulence supporting sediment, and have concentrations <0.01%<sub>vol</sub> (Pope *et al.* 2022). Transitional flows are turbidity currents that are transitioning between those two flow regimes.

#### 4.1.2.2. Congo Canyon-channel, offshore West Africa

The Congo Canyon and Channel is around 760 km long, making it one of the longest submarine canyon-channel systems on Earth (Fig. 4.2; Babonneau *et al.* 2002, 2011; Andrieux *et al.* 2013; Dennielou *et al.* 2017). The canyon begins within the estuarine mouth of the Congo River, some 30 km inland. The main source of sediment into the canyon is the Congo River, with many turbidity currents occurring during the peak flow of the river (Andrieux *et al.* 2013; Cooper *et al.* 2013, 2016; Azpiroz-Zabala *et al.* 2017). Studies have shown that the Congo Canyon is a mud-dominated submarine channel system, unlike the Bute Inlet and Monterey Canyon systems which are sand-dominated (Azpiroz-Zabala *et al.* 2017; Dennielou *et al.* 2017; Baas *et al.* 2021). Within the Congo Canyon, sandy deposits are primarily restricted to the floor of feeding channels and distributaries within the submarine system, with lobe deposits at the end of the channel having ~13% sand (Babonneau *et al.* 2002, 2011; Andrieux *et al.* 2013; Cooper *et al.* 2013, 2016; Azpiroz-Zabala *et al.* 2017; Dennielou *et al.* 2017; Clare *et al.* 2020; Talling *et al.* 2022).

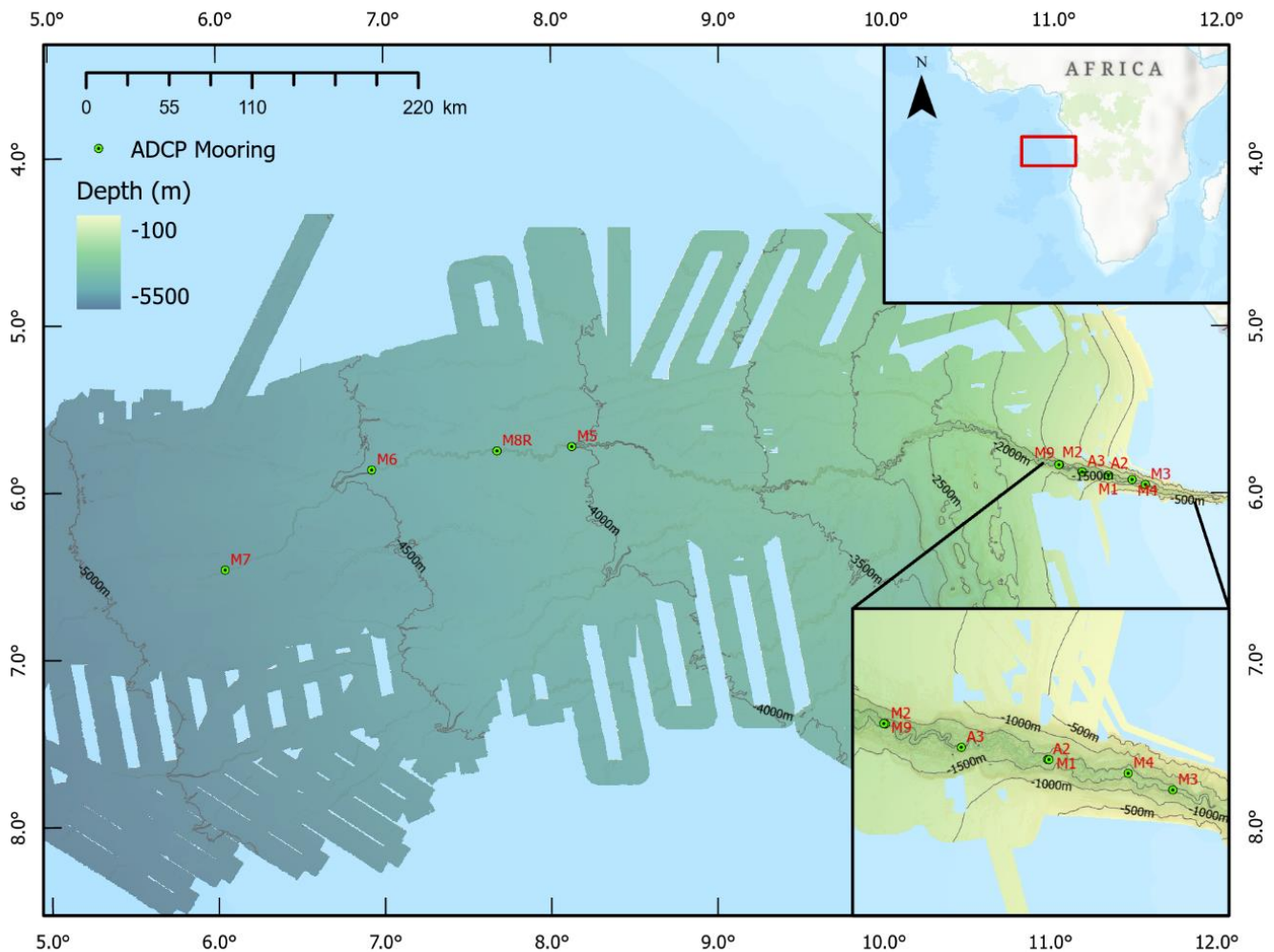


Figure 4.2. Bathymetric map of the Congo Submarine Fan system. (M1 – 9) NERC provided (600, 300 or 75 kHz) ADCP moorings, (R) indicates redeployment of mooring. (A2– 3) IFREMER (75 kHz) Anitra ADCP moorings.

#### 4.1.2.3. Monterey Canyon, California, USA

Monterey Canyon is situated in Monterey Bay (Fig. 4.3; Paull *et al.* 2010). The canyon starts only a few hundred metres from the shoreline and extends for several hundred kilometres to water depths of > 4,000 m (Klaucke *et al.* 2004; Paull *et al.* 2010; Maier *et al.* 2019). Unlike the previous two canyons, turbidity currents in Monterey Canyon are mainly triggered by wave action rather than river outflow (Talling *et al.* 2015). However, there is sometimes not a one-to-one link between turbidity currents and external triggers (Bailey *et al.* 2021). There have been a number of studies within this canyon, tracking turbidity currents and characterising their deposits (Xu, 2011; Paull *et al.* 2010; Paull *et al.* 2018; Maier *et al.* 2019). These studies showed that turbidity currents generally had flow speeds between 2 – 4 m/s, with some reaching

speeds of up to 7.2 m/s (Paull *et al.* 2018). The floor of the canyon comprises mainly sand and gravel, but it is rapidly replaced by muddier sediment a few metres above the canyon floor (Paull *et al.* 2010; Azpiroz-Zabala *et al.* 2017; Paull *et al.* 2018; Symons *et al.* 2017).

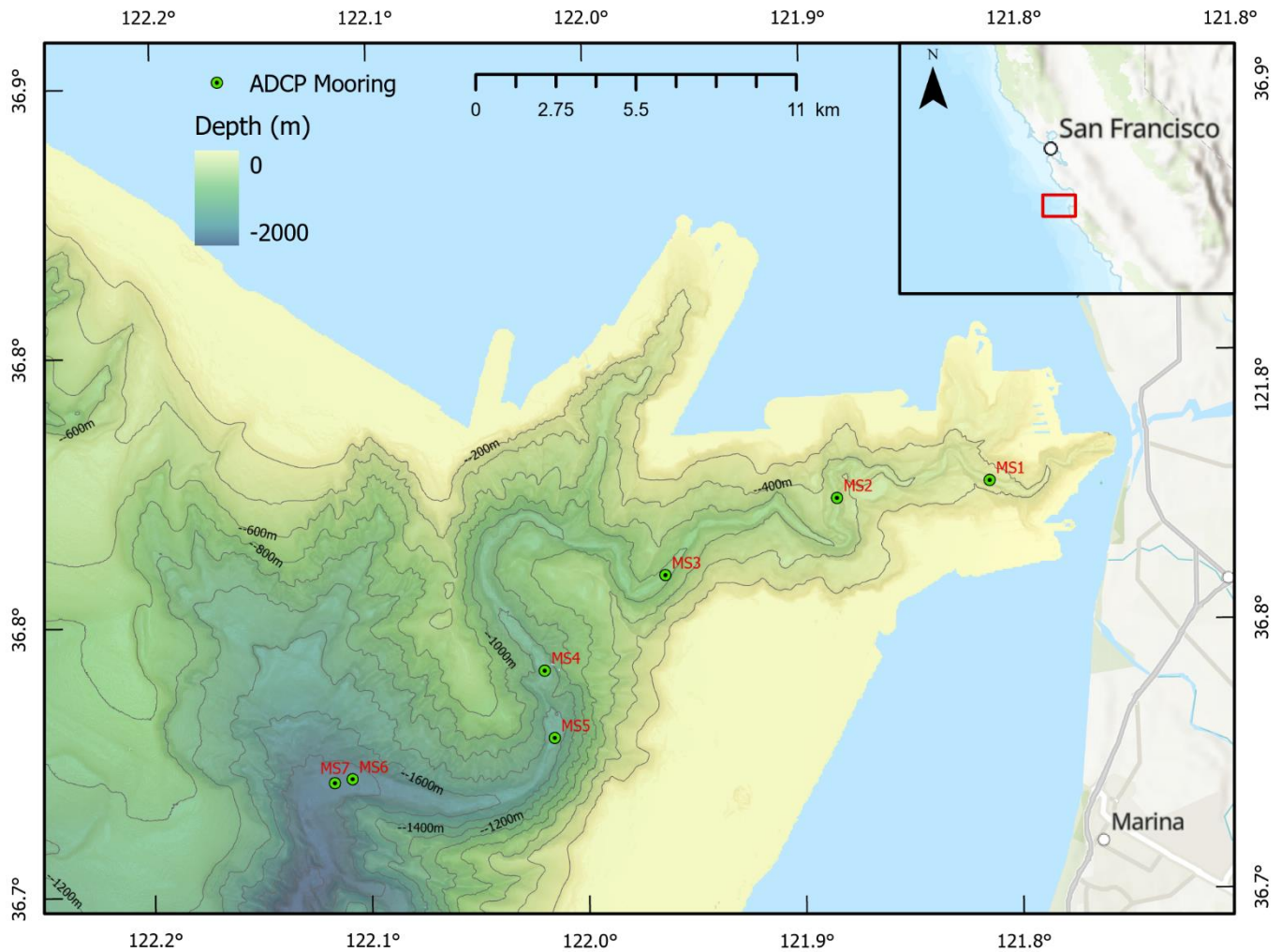


Figure 4.3. Detailed bathymetric map of Monterey Canyon, indicating the locations of each ADCP mooring along the submarine channel system.

## 4.2. Methods

*This section highlights the methods used to collect, convert and display the sediment-generated noise data collected via ADCPs from three different turbidity current systems.*

### 4.2.1. Analysis of ADCP data sets

In order to improve our understanding of turbidity currents, ADCPs were deployed in 2015 – 2020 at multiple sites along Bute Inlet, Congo Canyon and Monterey Canyons (Paull *et al.* 2018; BODC, 2019; Clare *et al.* 2020; Hage *et al.* 2020; Pope *et al.* 2022; Talling *et al.* 2022). These deployments included moorings with ADCPs ranging in frequency from 75 kHz to 1.2 MHz (Paull *et al.* 2018; BODC, 2019; Clare *et al.* 2020; Hage *et al.* 2020; Pope *et al.* 2022; Talling *et al.* 2022).

Once these deployed moorings were retrieved, the raw data recorded by ADCPs were initially converted into a MATLAB-acceptable format. Depending on their file length, either a file conversion script in MATLAB or the program WinADCP was used to do this. Both of these conversion tools converted the raw .000 file into a .mat file containing the following variables: RSSI, north, east and vertical velocity and depth.

Once all the ADCP recordings were converted into a .mat format, each ADCP file from Bute Inlet, Congo and Monterey Canyons was examined for possible passively-emitted sediment-generated noise due to turbidity currents. To identify sediment-generated noise, each ADCP record was plotted as RSSI against time. Then, the entire plot was analysed to find vertical bands of noise (i.e. the same noise recorded simultaneously at many different heights above the bed) associated with flows. Such vertical bands are formed when particles collide, and radiate sediment-generated noise in all directions to be detected by the passive instrument. It is possible to easily identify passively detected signals from the returns active signals by the fact these passively detected vertical bands can stretch across the entire depth range of an ADCP. Furthermore, across a vertical band, the level of detected noise is fairly consistent. When a band of passive noise was found, the file name, timing in decimal days and ADCP frequency were noted down to allow easier reidentification at a later date. This search was narrowed down using notes from previous analyses of active ADCP signals to determine when the turbidity currents had occurred (Clare *et al.* 2020; Simmons *et al.* 2020).

Once all the files were examined, further data processing was carried out on the files with sediment-generated noise. This further processing calculated Far-range RSSI, velocity (m/s) and velocity maximum (dB) of the water column. Far-range RSSI values were identified by isolating the ADCP measuring range (termed a bin) furthest away from the seabed. It is expected that at the furthest bin, the active emitted pulse from the ADCP has dissipated, and the ADCP at this point is only passively detecting noise from its surroundings.

Far-range RSSI values from turbidity currents in Monterey Canyon was further subdivided into Far-range RSSI - recorded in each of the four beams emitted from each individual ADCP. This was performed to identify if there are variations in noise level depending on the direction of the received radiating sediment-generated noise.

The water column velocity for each ADCP was calculated using the XYZ velocity components of the ADCP recordings. Then, the maximum value for each vertical ADCP data profile per unit time was isolated to find the water column's velocity maximum (m/s) over the duration of the recorded turbidity current.

Data extracted from each ADCP record produced a figure showing a time series of a turbidity current (e.g. Fig. 4.4). Each of these figures can be broken down further into plots of RSSI, flow speed, far-range RSSI (final data bin of each ADCP vertical profile) and maximum flow speed, and finally a plot of the water depth (pressure) of the ADCP (e.g. Fig. 4.4). Each figure presented within Chapter 4 displays the RSSI and flow speed across each section of a turbidity current (i.e. its head, body, and tail) (Figs 1.10; 4.4). On each ADCP record, as stated previously (see section 4.2.1), sediment generated noise can be identified by the presence of vertical stripes of noise that can stretch across the entire depth range of an ADCP. The seabed is clearly identified as a horizontal line that is a strong acoustic reflector. The plots of RSSI and flow speed within Fig. 4.4. can be used to help identify passively detected noise and understand processes occurring within the turbidity current. Far-range RSSI and maximum flow speed are plotted against one another to compare and identify how both variables relate to one another (e.g. Fig. 4.4). Finally, the depth of the ADCP (i.e. pressure) can be used to determine if the ADCP itself was affected by the passing of the turbidity current. For example, if the ADCP and its mooring were dragged by the turbidity current, the depth may rapidly increase by 10s of metres whilst the turbidity current passes.

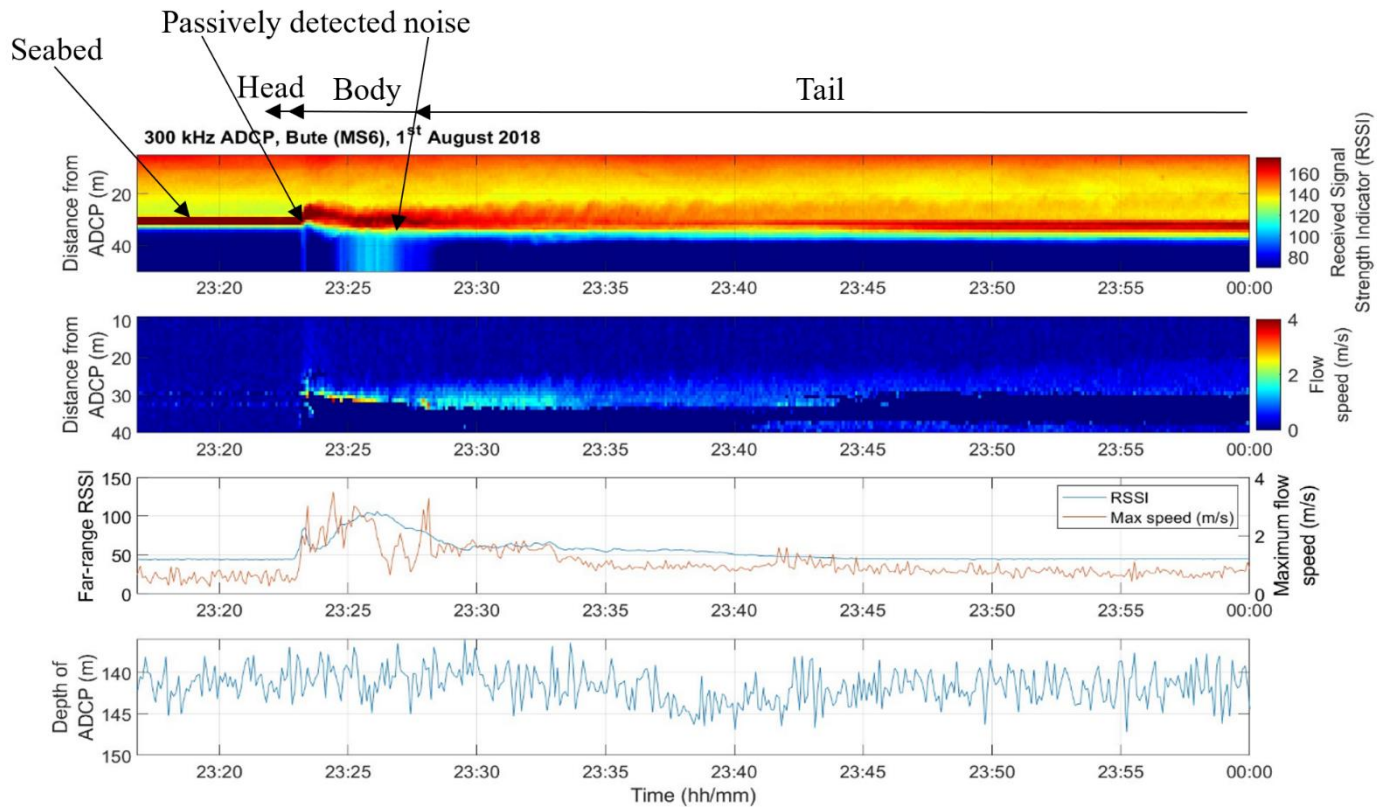


Figure 4.4. Archetypal plots summarising 300 kHz ADCP record of a turbidity current occurring within Bute Inlet on the 1<sup>st</sup> August 2018. All ADCP measurements comprise of Received Signal Strength Indicator (RSSI), flow speed (m/s), maximum flow speed (m/s), Far-range RSSI, and depth of the ADCP (m).

#### 4.2.2. Estimating sediment concentrations using the Chézy equation

Here we use data provided by Pope *et al.* (2022), who used the Chézy equation to calculate sediment concentrations in turbidity currents. In the past, the Chézy approach, which is commonly used for rivers, has been used to analyse characteristics within turbidity currents and to define the relationship between flow speed, gravitational driving force and friction (Kuenen, 1952; Middleton, 1966; Mulder *et al.* 1998; Konsoer *et al.* 2013; Pope *et al.* 2022). It should be noted that within Pope *et al.* (2022) most observed flows were entirely dilute ( $<0.01\%$  vol), low velocity (0.5 m/s), thick ( $\geq 10$  m), and well-mixed ( $Ri < 0.25$ ) heads. Thus, they were of his slow and dilute category.

Considerations must be made when using the Chézy approach. This is because the Chézy approach defines a balance for the gravitational driving and frictional retarding forces at a measurement location, and does not take into account any momentum inherited from upstream.

The Chézy approach assumes a consistent slope gradient, and does not take into account upstream changes in topography, such as locally adjacent knickpoints that have an increased slope gradient that can result in an accelerated flow.

This study used Chézy-derived sediment concentrations (volume %) and bulk Richardson numbers (degree of mixing and stability in the turbidity current) previously calculated using a bottom friction coefficient ( $C_{fb}$ ) of 0.004 by Pope *et al.* (2022). Depth-averaged sediment concentration ( $C$ ) was calculated using:

$$U^2 = \frac{1}{C_{fi} + C_{fb}} RCgHS \quad (4.1)$$

$U$  is depth-averaged flow velocity,  $H$  is flow height,  $R$  is the submerged specific gravity of sediment, taken for quartz (1.65).  $g$  is the gravitational acceleration;  $S$  is slope gradient. The friction of the top interface ( $C_{fi}$ ) was calculated using:

$$C_{fi} = \frac{0.0075}{\sqrt{1+718Ri^{2.4}}} (1 + 0.5Ri) \quad (4.2)$$

Bulk Richardson ( $Ri$ ) number was calculated using:

$$Ri = \frac{RgCH}{U^2} \quad (4.3)$$

The Chézy-derived sediment volume concentrations (%) and bulk Richardson number were compared to corresponding flows that contained sediment-generated noise and occurred within Bute Inlet. This was performed to identify if there is any form of relationship between these values and the strength of sediment-generated noise detected.

## 4.3. Results

*This section firstly describes how detected sediment-generated noise and other variables, such as sediment concentration, vary in each field site. This is followed by how the detected noise varies for turbidity currents measured in Monterey Canyon, Bute Inlet and Congo Canyon. Finally, the discussion section compares how the data varies between each submarine canyon.*

### 4.3.1. Passive acoustic signals from turbidity currents within Bute Inlet

The level of passively detected noise noted as far-range RSSI (Fig 4.5A) was initially compared to the timing of turbidity currents, which was known independently from ADCP velocity data. Observations from both 1.2 MHz and 300 kHz ADCPs exhibit a brief < 1 minute period of passively detected sediment-generated noise around (115 – 85 RSSI) at the head of the detected sediment gravity flow on the 24<sup>th</sup> June 2018 at 17:56 (Figs. 4.5A, B). This initial peak in far-range RSSI is followed by a second fainter (76 RSSI) spike of passively detected sediment-generated noise at 17:59 on the 300 kHz ADCP (Fig. 4.5B).

Both the 1.2 MHz and 300 kHz ADCPs suggest similar head speeds of around 1 – 3 m/s, as measured independently via distances and times of arrivals at different ADCP sites (Figs. 4.5A, B). The relationship between passively detected noise (far-range RSSI) and maximum flow speed (m/s) varies depending on the frequency of the ADCPs. When the head of the turbidity current reaches the ADCP, the 1.2 MHz ADCP exhibits a short sharp peak of passive noise up to 115 RSSI (Fig. 4.5A). However, for the 300 kHz ADCP, there are two peaks which are lower in RSSI, and the second peak is prolonged for the duration of the flow (Fig. 4.5B). For the 1.2 MHz ADCP, when looking at maximum flow speed (m/s), the data blanks out, followed by a rise in flow speed for 20 minutes (Fig. 4.5A). This is different to the 300 kHz ADCP, which contains two peaks in maximum flow speed, which are either close or coincide with the increase in passively detected noise (Fig. 4.5B).

Both the 1.2 MHz and 300 kHz ADCP data sets show rapid ~5 m changes in ADCP depth, which record a movement in the position of the 1.2 MHz ADCP on the seabed, when the turbidity current arrived (Figs. 4.5A, B).

Height above bed data (i.e. distance from ADCP to the seabed return) indicates the occurrence of initial erosion (4 m) followed by (2 m) levels of deposition. Additionally, there is a presence

of three anomalous increases in height above bed (Fig. 4.5C). These anomalous increases may relate to changes in the position of the mooring during the turbidity current.

Sediment concentrations (%) derived via the Chézy equation, and bulk Richardson number, exhibit two peaks in their respective values at 17:56 and 18:00 (Fig. 4.5D). Both spikes in sediment concentration (%), and bulk Richardson number start rising at the same time as the detection of sediment-generated noise on the 300 kHz ADCP plots (Fig. 4.5D). It should be noted that these two peaks observed in sediment concentration (%) and bulk Richardson number reach their maximum values shortly after the sediment-generated noise has dissipated and, in fact, coincide with the increases in maximum flow speed on the 300 kHz ADCP plots (Fig. 4.5D).

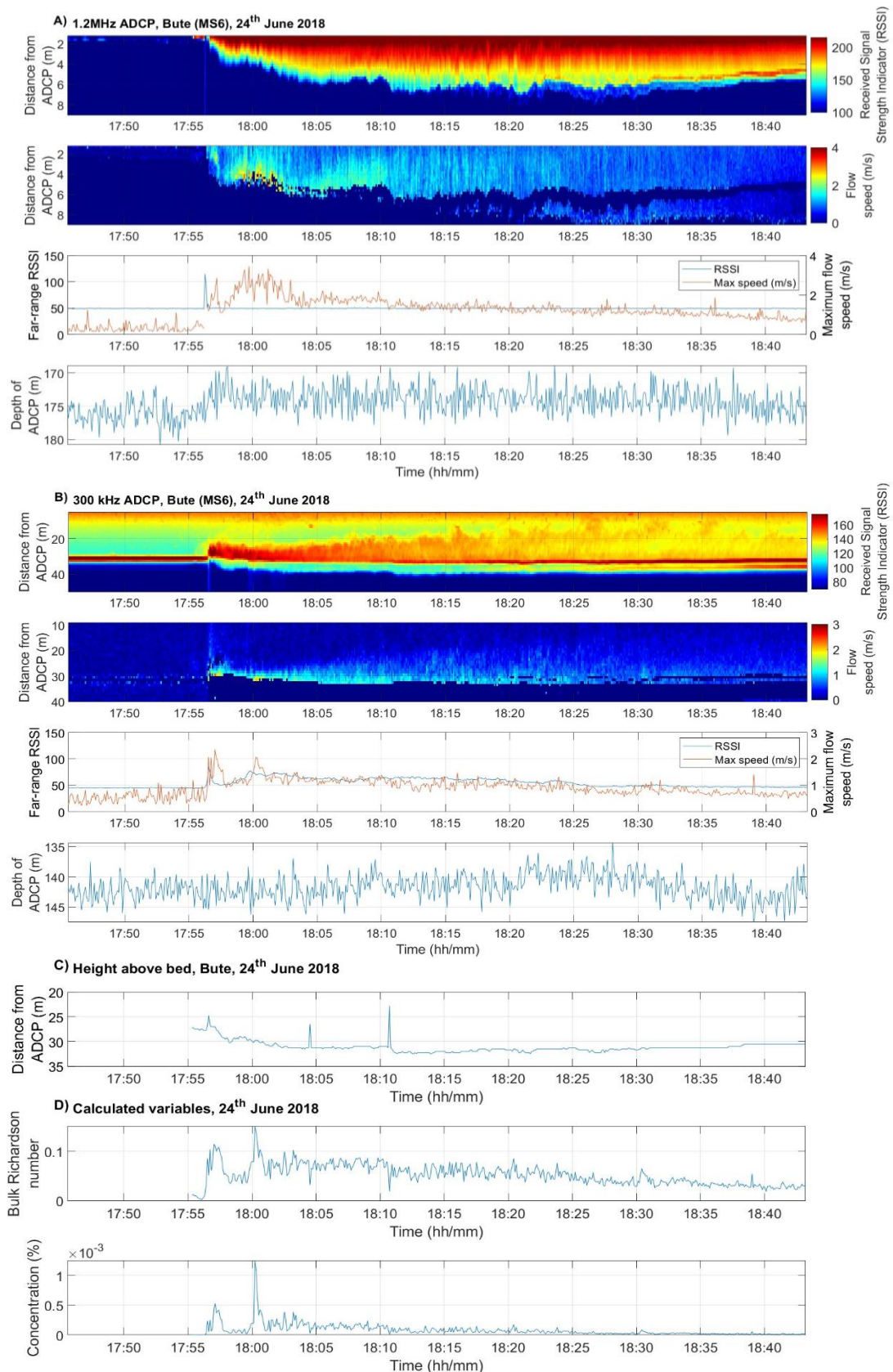


Figure 4.5. ADCP and predicted measurements for a single submarine turbidity current on the 24<sup>th</sup> June 2018 that occurred within Bute Inlet. ADCP measurements comprise of Received Signal Strength Indicator (RSSI), flow speed (m/s), maximum flow speed (m/s), Far-range (RSSI), and depth of the ADCP (m). A) ADCP measurements derived from a 1.2 MHz ADCP on mooring MS6. B) 300 kHz ADCP measurements on mooring MS6. C) Height above bed (m). D) Bulk Richardson number and concentration (%) derived from Chézy equations.

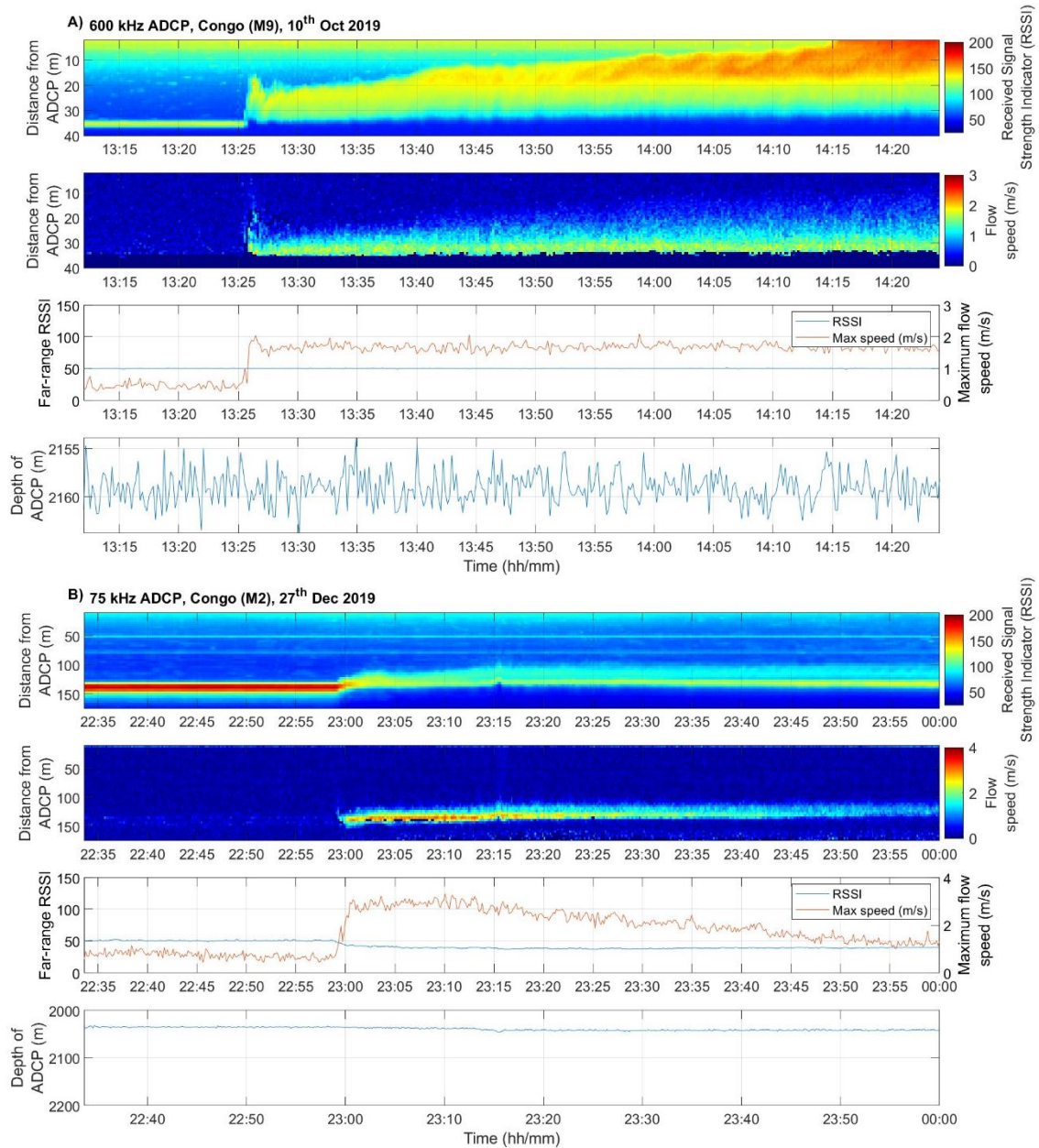


Figure 4.6. Measurements from three different ADCPs for turbidity currents within the Congo Canyon. All ADCP measurements comprise of Received Signal Strength Indicator (RSSI), flow speed (m/s), maximum flow speed (m/s), Far-range (RSSI), and depth of the ADCP (m). A) 600 kHz ADCP measurements of a landslide that occurred on the 10<sup>th</sup> October 2019. B) Measurements from a 75 kHz ADCP on the 27<sup>th</sup> December 2019.

### 4.3.2. Observed turbidity currents within the Congo Canyon

All turbidity currents within the Congo Canyon displayed no clear evidence of emitting passively detected sediment-generated noise (Figs. 4.6A – B). Fig. 4.6A and B show two flows within the Congo Canyon using both 75 and 600 kHz ADCP data, which occurred on 10<sup>th</sup> Oct and 27<sup>th</sup> Dec 2019. Both turbidity currents (10<sup>th</sup> Oct and 27<sup>th</sup> Dec 2019) are generally moving at 1 – 2 m/s, and it is not possible to passively detect any acoustic signals from sediment transport (Figs. 4.6A, B).

For both the Oct 10<sup>th</sup> and Dec 27<sup>th</sup> events, the pressure sensor on both the 75 and 600 kHz ADCP in the Congo Canyon indicates that the depth of the ADCP oscillated by ~5 m multiple times a minute. This oscillation was not seen to have a visible effect on the data (Figs. 4.6A, B). It is not possible to determine the exact cause of this oscillation (Figs. 4.6A, B). It should be noted that when the 75 kHz turbidity current arrives at 22:59 on Dec 27<sup>th</sup>, the level of passively detected noise decreases by 8 RSSI (Fig. 4.6B).

### 4.3.3. Observed turbidity currents within the Monterey Canyon

Data from 300 kHz ADCPs deployed at multiple sites along Monterey Canyon show how a turbidity current can evolve, waxing and waning over time (Figs. 4.7, 4.8; Paull *et al.* 2018; Heerema *et al.* 2020). Moorings MS1 – MS2 (Figs. 4.7A, B), which are located closest to the shoreline (Fig. 4.3), clearly show sediment-generated noise being emitted at the front of the flow. This is followed by a quiet period, with either no emission of passive acoustic signals, or significant attenuation of any sediment-generated noise that was generated. Sediment-generated noise then resurges in the main body of the turbidity current (Figs. 4.7A & B). Sediment-generated noise can also be detected in the MS3 mooring. However, at MS3, the location where sediment-generated noise was detected has moved towards the head of the flow (Fig. 4.7C). On the next two moorings located further down canyon, moorings MS4 and MS5 (Fig. 4.3), sediment-generated noise further increased in strength. It also started to migrate towards the tail of the turbidity current. By the final deepest-water mooring MS7, this passively emitted sediment-generated noise was absent and undetectable to the ADCP (Figs. 4.8A – C).

Each ADCP collects data with four individual acoustic beams, which ensonify adjacent areas on the seabed. The width of each beam is between 1° – 5°. Comparing beams for each mooring, most moorings (except for MS4 and MS5) initially show little variation between beams in

passively detected noise. On both MS4 and MS5 a single ADCP beam at times becomes more dominant than the others suggesting directionality to the passively detected noise (Fig. 4.8B). This is because more noise seems to be coming from the area ensonified on the seabed by a particular beam.

Looking at other variables recorded by the ADCP, maximum flow speed is potentially linked to an increase in passively detected noise, with both on occasion increasing when the head of the flow arrives (Figs. 4.7A & 4.8A). However, there are exceptions to this relationship. For example, at moorings MS2, MS3, MS5, flow speed increased either before or after the passively detected sediment-generated noise increased.

It should be noted that some 300 kHz ADCPs in the Monterey Canyon were placed on moorings at greater depths than their pressure sensors were rated for, and pressure data, therefore, appear as a flat line on some depth plots (Figs. 4.7A & 4.8A – B; Paull *et al.* 2018). As a result, at times, it is not possible to use the pressure sensor data to identify disturbances resulting from the impacting turbidity current. Therefore, for the ADCPs affected, visual confirmation of disturbances within the RSSI and velocity data was relied upon (Figs. 4.7A & 4.8A – B).

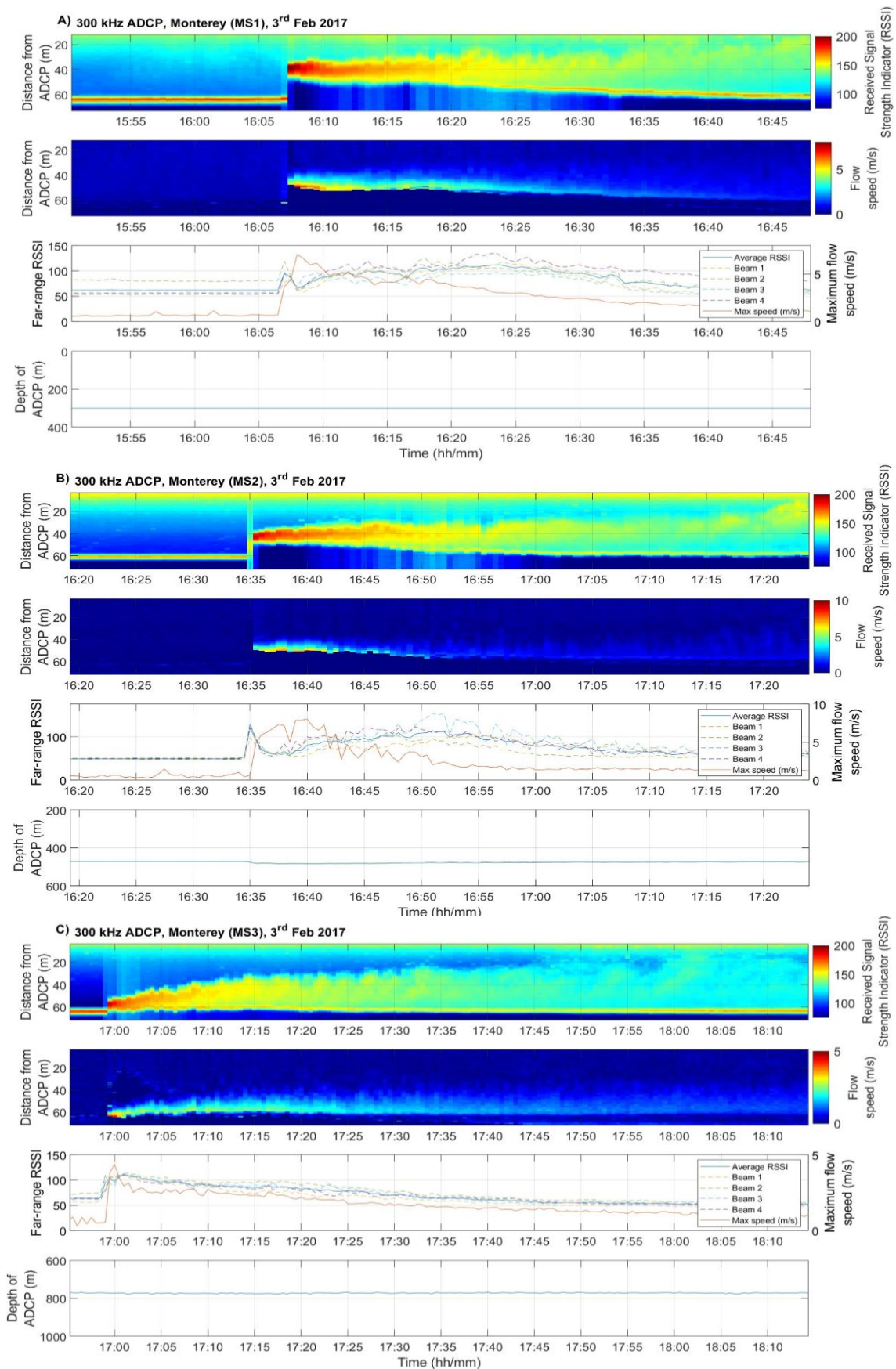


Figure 4.7. Measurements from turbidity currents in Monterey Canyon on the 3<sup>rd</sup> February 2017 from moorings (MS1, MS2 and MS3) at different sites along the canyon. All ADCP measurements comprise of Received Signal Strength Indicator (RSSI), flow speed (m/s), maximum flow speed (m/s), Far-range (RSSI), and depth of the ADCP (m). Figures A – C are of each successive mooring MS1 – MS3 along the canyon.

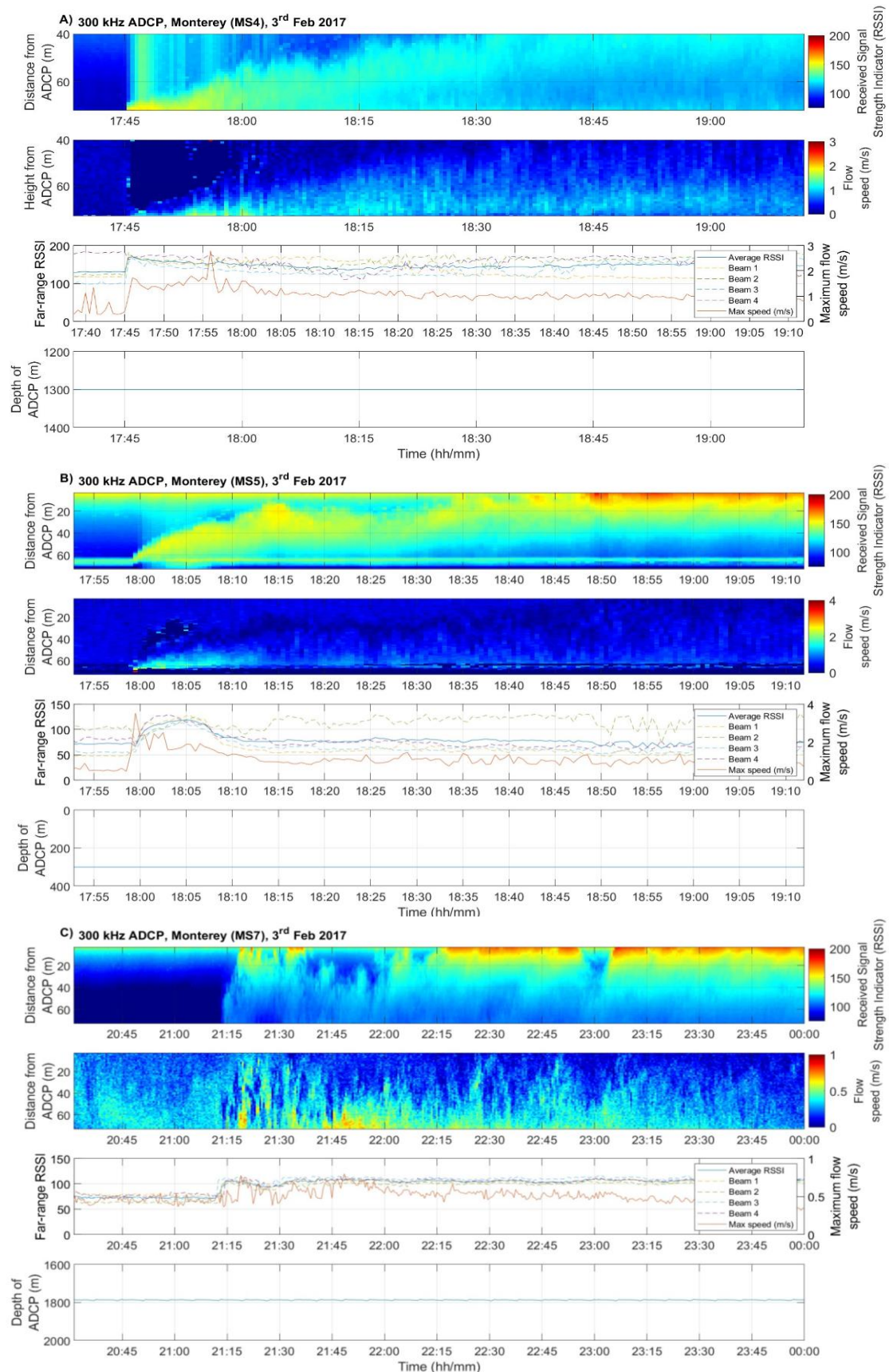


Figure 4.8. Successive measurements from a submarine landslide occurring within the Monterey Canyon on the 3<sup>rd</sup> February 2017. All 300 kHz ADCP measurements comprise of Received Signal Strength Indicator (RSSI), flow speed (m/s), maximum flow speed (m/s), Far-range (RSSI), and depth of the ADCP. Figures A – C are of moorings MS4 – MS7, excluding MS6 along the canyon.

#### 4.3.4. Comparison of the occurrence of passively detected noise between each submarine system

System	Total number of observed turbidity currents	Number of flows without particle collision noise	Number of flows with particle collision noise	% of total with particle collision noise	Dominant grain sizes
Bute Inlet	83	69	14	17	15% gravel 65% sand 15% silt 5% clay
Congo Canyon	15	15	0	0	Mud
Monterey Canyon	14	2	12	86	Coarse sand

*Table 4.1. Summary of dominant grain sizes and turbidity currents observed at each submarine canyon (Zeng et al.1991; Azpiroz-Zabala et al. 2017).*

Based on the analysis of all the ADCP data at each field site, the number of turbidity currents with sediment-generated noise are compared to the total number of flows (Table 4.1). Monterey Canyon has the highest percentage (86%) of flows that produced sediment-generated noise. The two flows that did not exhibit any sediment-generated noise in Monterey Canyon were recorded when mooring MS1 had become detached from its anchor on the sea bed.

Bute Inlet contained the highest number of observed flows (83) and the second-highest percentage (17%) of flows containing sediment-generated noise, but this percentage of flows with sediment-generated noise was lower than in Monterey Canyon (i.e. 17% v 86%).

However, none of the flows detected by (75 kHz, 300 kHz and 600 kHz) ADCPs deployed within Congo Canyon produced clear sediment-generated noise.

## 4.4. Discussion

*The following discussion section examines how passively detected sediment-generated noise varies between each submarine canyon. Then it discusses the causes of variation in levels of sediment-generated noise along Monterey Canyon. Finally, this section determines the causes of differences in acoustic signals within turbidity currents at the different field sites.*

### 4.4.1. Variations in acoustic signals between different submarine canyons

Turbidity currents within Bute Inlet, Congo Canyon, and Monterey Canyon show clear variation in the intensity of passive acoustic signals, and number of flows with detectable sediment-generated noise (Figs. 4.5 – 4.8 & Table 4.1). The Congo Canyon had some of the longest and fastest turbidity currents ever recorded by ADCPs. In addition, these flows broke the mooring wires, such that all the moorings had surfaced by 16<sup>th</sup> January 2020. Passive ADCP signals from flows within the Congo Canyon are around 25 RSSI quieter than for flows in Bute Inlet, and 50 RSSI quieter than flows in Monterey Canyon. Within the Congo Canyon, flows show no clear evidence of sediment-generated noise (Table 4.1; Fig. 4.6).

In the Congo Canyon, turbidity current head speed raised to the exponent of 7 is not proportional to acoustic signal power, as suggested by Hay *et al.* (2021). For these Congo Canyon flows, there is either no detectable sediment-generated noise, or any sediment-generated noise does not correspond to increases in flow speed (Fig. 4.6).

Due to the lack of any detectable sediment-generated noise by ADCPs with frequencies of 75 – 600 kHz in the Congo Canyon, it is not possible to determine if changes in ADCP frequency have any impact on the level of passive sediment-generated noise detected.

Bute Inlet contained the second-highest number of turbidity currents with detectable sediment-generated noise (17%). Flows here showed a weak relationship between flow speed and passively detected (i.e. sediment-generated) noise, with both increasing when the turbidity current arrived or sped up (Fig. 4.5B). Flows within Bute Inlet varied as to their level of detected sediment-generated noise, with some flows emitting noise for up to 20 minutes (Fig. 4.5B), whilst others only emitted this noise for short periods of time (Fig. 4.5A). Data from Bute Inlet suggests there is a potential link between height of the ADCP above the bed (m), sediment concentration (%), bulk Richardson number ( $Ri$ ) and the presence of passive noise.

For example, for the turbidity current shown in Fig. 4.5, the flow arrives at 17:56, and there is a significant level of erosion - as seen as an increased distance between the ADCP and the bed (Fig. 4.5C). This bed erosion most likely increased sediment concentration, causing reduced mixing in the turbidity current, as implied by the increase in bulk Richardson number (Fig. 4.5D). The increase in sediment concentration and bulk Richardson number could have caused detectable sediment-generated noise, but as the increases of both sediment concentration and bulk Richardson number was short lived, so was the generation of sediment-generated noise. However, times of increases in flow speed, concentration, and bulk Richardson number are close to the times when it was possible to detect sediment-generated noise (e.g. at 17:56 and 17:59), but they are not exactly synchronous with those times (e.g. at 17:56 and 18:00) (Fig. 4.5).

Within Bute Inlet there is variability in the level of sediment-generated noise detected by ADCPs with different frequencies. Whilst both 1.2 MHz and 300 kHz ADCPs detected the initial head of the turbidity current, only the 300 kHz ADCP detected another peak in noise just after some erosion occurred, whilst flow speed and sediment concentration rose again for a second time (Figs. 4.5A – C). The differences in passively detected noise between both 1.2 MHz and 300 kHz ADCPs at this second spike in the noise around 17:59 most likely relate to either shifts in dominant sediment type or changes in suspended sediment concentrations (Fig. 4.5).

In Monterey Canyon, 86% of flows contained some sediment-generated noise, with the exception of two flows that occurred when there was a fault with the initial MS1 mooring system (Table 4.1). These two flows only travelled from MS1 to MS2. However, when they arrived at the MS2 mooring, it was not possible to detect any sediment-generated noise. These flows were travelling slowly at MS2, and this may explain why no passive acoustic signals were recorded.

In a similar way to Bute Inlet, increases in flow speed and passively detected noise were not always synchronous for flows in Monterey Canyon, albeit the timings were close (Figs. 4.7 & 4.8). As a result, due to the asynchronous timings between flow speed and passively detected noise for both sites, it was not possible to ascertain an exponent value to compare to Hatcher (2017) and Hay *et al.* (2021) to determine if the strength of passively detected noise was related to frontal speed to the exponent of 7. Although maximum flow speed and passively detected noise do not always match up exactly, it is still possible to suggest a relationship between flow

speed and passively detected noise, but it is more complex than suggested by Hatcher (2017) and Hay *et al.* (2021). The differences in the timing of the increases in maximum flow speed and passively detected noise could be the result of structural changes within the turbidity current.

#### **4.4.2. Acoustic variations within individual turbidity currents**

*Section 4.4.2 now analyses changes in passive acoustic signal strength through time for turbidity currents within Monterey Canyon. This analysis seeks to understand which part of the flows generated passive acoustic signals, and how that varied between mooring sites.*

At mooring MS1 located closest to shore, sediment-generated noise was detected at the same time at the arrival time of the turbidity current at the mooring (Fig. 4.7A). At other mooring sites, there could be a delay between the onset of sediment-generated noise and arrived of the turbidity current head (Figs. 4.7 & 4.8). For example, at mooring MS2, there was a 1-minute delay between the arrival of the flow and the detection of particle generated noise (Figs. 4.7B).

The next section of the turbidity current contains significant attenuation of sediment-generated noise. This is most likely partially caused by the presence of a highly concentrated basal layer of sediment absorbing or preventing any sediment-generated noise production (Fig. 4.7A; Hughes Clarke *et al.* 2016). This hypothesis is preferred because previous work on the same flows suggests that faster flows have dense near-bed layers, based on evidence including the movement of heavy objects (Paull *et al.* 2018) (Fig. 4.7A). It is inferred these dense near bed layers attenuate the passive acoustic signals.

As flow speed decreases towards the rear of the turbidity current, the dense basal layer would thin and suspended sediment concentration would also be expected to decrease. A reduction in basal layer thickness and suspended sediment concentration could reduce the level of attenuation, thus allowing sediment-generated noise to be detected once again by the ADCP suspended above the flow.

Through time, as the turbidity current evolves, the strength of the acoustic signal changes, as does the part of the turbidity currents that produce sediment-generated noise. For example, as the turbidity current speeds up between moorings (MS1 and MS2), the length of the flow containing significant attenuation of any sediment-generated noise within the turbidity current grows in size (Fig. 4.7A, B). This is most likely due to the flow scouring sediment from the

bed which increases the length of the highly concentrated basal layer, as well as suspended sediment concentration (Pope *et al.* 2022). This enhanced basal layer and additional suspended sediment could potentially prevent sediment-generated noise production and absorb the noise emitted, producing and increasing the size of zone with significant attenuation of sediment-generated noise (Simmons *et al.* 2020).

At MS2, initial detection of passive noise occurs before the turbidity current's front arrives at the mooring (Fig. 4.7B). Therefore, the noise radiated outwards from the front of the flow, and reached the ADCP's location before the flow arrived.

The turbidity currents typically decelerated once they passed the MS2 mooring (Paull *et al.* 2018; Heerema *et al.* 2020). Between the MS2 and MS3 moorings, the turbidity currents also lengthened and became less dense (Figs. 4.7B – C). Flows thus waned, and some of the flows no longer contained a dense near-bed layer (Paull *et al.* 2010). If the turbidity current is waning, suspended sediment concentration levels within the flow might drop. The elimination of a dense near-bed layer and reduction in suspended sediment concentration after mooring MS3 could explain why it is possible to start to detect noise within the central part of the flow, where the noise was previously damped (Figs. 4.7A & B; Paul *et al.* 2018; Simmons *et al.* 2020).

Further down the canyon, the strength of the detected noise increases, and the location of the peak in noise moves towards the tail of the turbidity current. This could result from reductions in flow speed, causing sediment to be deposited towards the tail of the turbidity current (Manica, 2012), thereby further reducing sediment concentration, and attenuation, allowing sediment-generated noise to be detected more strongly by the ADCP.

By the final MS7 mooring (Fig. 4.8C), the flow had dissipated, leaving a dilute cloud of sediment devoid of sediment-generated noise. As this dilute cloud lacks any sediment-generated noise, it further supports the suggestion that the majority, if not all, of sediment-generated noise is produced by bedload collisions (Hay *et al.* 2021).

Turbidity currents within Monterey Canyon do support the suggestion that the strength of passively detected noise is related to flow speed (Hatcher, 2017; Hay *et al.* 2021). Passively detected noise (Far-range RSSI) and maximum flow speed (m/s) have a consistent relationship, as on multiple occasions, both rise at the same point when a turbidity current arrives. But this relationship is clearly more complex than suggested by Hay *et al.* (2021) and potentially related to changes in the structure of the turbidity current itself. With available data from Monterey

Canyon, it is not possible to explain why maximum flow speed increases for some flows before the detection of sediment-generated noise, but not for other flows (Fig. 4.8B).

The relationship between flow speed and passively detected noise is thus complex and most likely due to the variability of suspended sediment concentrations and changes in the structure of the turbidity current, such as the presence of a thick, dense basal layer. This dense layer may both emit sound due to particle collisions, but also attenuate sound that has to pass through the layer.

The ADCP data shows that there is no clear relationship between the direction of the incoming noise, and that this noise is normally radiating outwards from all directions towards the ADCP, causing little variation in the level of noise being detected per ADCP beam (Figs. 4.7 & 4.8). There is also typically minimal change in the level of passively detected noise depending on the distance of the ADCP above the seabed (Fig. 4.8B).

#### **4.4.3. Causes of differences in acoustic signals between each field site**

Three main factors that cause variations in sediment-generated noise between each field site are: (i) differences in the ADCP frequency used, (ii) the dominant sediment grain-size present, and (iii) changes in suspended sediment concentration.

As shown in Fig. 4.5, the frequency of the deployed ADCP can influence the level of sediment-generated noise detected in a flow. Due to the specific wavelength of an ADCP, not all ADCPs can detect sediment-generated noise when it occurs, if that noise is of a different frequency. For example, experiments show frequency of sediment-generated noise is linked to particle size (Thorne 1985, 1986). Smaller grains will tend to emit higher frequency signals. This dependence of passively detected noise frequency on grain size may explain why turbidity currents failed to emit signals recorded by ADCPs at some sites, but emitted signals at others.

In the Congo Canyon, low-frequency (75, 300 and 600 kHz) ADCPs were used, and it was not possible to detect any sediment-generated noise across any of the 15 recorded turbidity currents. As the environment was relatively muddy, even higher-frequency ADCPs (>1.2 MHz) should have been deployed, and therefore any noise that could have occurred may have been missed by the 75, 300 and 600 kHz ADCPs. Conversely, 300 kHz ADCPs were deployed into Monterey Canyon, where it was then possible to detect sediment-generated noise at a frequency of 300 kHz due to the sandier nature of these Monterey Canyon flows.

Another important factor for acoustic noise generation is the fraction of clay within a flow. Laboratory flume experiments described within Chapter 2 show that clay can attenuate the levels of noise recorded. A high fraction of clay in the Congo Canyon turbidity currents, may thus have therefore attenuated or prevented sediment-generated noise. Attenuation from clay can potentially be seen in the 75 kHz ADCP data as a 8 RSSI reduction in the level of passively detected noise, when the turbidity current arrives at 22:59 (Fig. 4.6B).

As suggested by Hay *et al.* (2021) and Simmons *et al.* (2020), changes in sediment concentration can cause variations in the level of detectable sediment-generated noise. However, elevated sediment concentrations can either increase or decrease the level of sediment-generated noise (Geay *et al.* 2017; Haught *et al.* 2017). As the flows increase in sediment concentration, there may be more collisions, which will produce more noise. But if sediment concentration increases above a threshold, such as within the head, noise can also be attenuated.

In addition to differences in ADCP frequency used, the dominant sediment grain-size present, and changes in suspended sediment concentration, attenuation may also cause variations in the intensity of detected particle collision noise between the ADCPs deployed within a canyon. In addition, systematic water depth changes between each field site (Bute Inlet, Monterey Canyon, and Congo Canyon) may also affect attenuation levels (Teledyne RDI, 2011).

For example, within Bute Inlet, using a 1228.8 kHz (1.2 MHz) ADCP, and at a water depth of 400 m, a salinity of 35 psu and 8 °C water temperature, the absorption coefficient ( $\alpha$ ) is  $\sim 0.56$  dB/m (Francois and Garrison, 1982a,b; NPL, 2023). At a maximum range of 8 m from the bed,  $\alpha$  provides a total attenuation of 2.24 dB between bedload transport collisions and the ADCP transducer (Fig. 4.5A, Eq. 3.2). Similarly in Monterey Canyon at a water depth of 1,000 m, using a 307.2 kHz (300 kHz) ADCP, an absorption coefficient ( $\alpha$ ) is calculated as  $\sim 0.065$  dB/m (Francois and Garrison, 1982a,b; NPL, 2023). With an ADCP range of 61 m,  $\alpha$  provides a total attenuation of 1.98 dB between bedload transport collisions and the ADCP transducer in Monterey Canyon (Fig. 4.7A, Eq. 3.2). It should be noted that it is not fully known yet if particles can also collide and produce sound during suspension (Hay *et al.* 2021). As a result, it is difficult to fully determine the exact location of the source of the passively generated noise within this study, and this source location may affect the calculations of attenuation above.

Variance in the level of attenuation of passively detected noise due to its frequency may potentially change the level of particle noise recorded depending on the ADCP used, and therefore generate bias during the interpretation of quantitative changes in sound power. In addition, if a passively emitted acoustic signal is low in power, attenuation may potentially prevent the detection of the noise and thus could obscure trends.

Losses due to beam spreading are not expected to be a major issue within Chapter 4's data set, due to the inverse square law (Basuki & Palupi, 2020). The inverse square law indicates that spreading losses are cancelled out by the increase in size of the beam footprints of the sea floor, providing that passively detected noise is being generated across the entirety of the beam footprint of the ADCP (Basuki & Palupi, 2020).

In terms of detection, after attenuation, the passively detected noise signal from particle-particle collisions is visibly above the ambient noise (Figs 4.5, 4.7 & 4.8). However, the exact degree to which attenuation losses affect detection of sediment generated noise is not known. Therefore, the extent to which attenuation can affect the detection of passively detected particle collision noise should be investigated further within future studies.

## 4.5. Conclusions

This chapter compares passively emitted acoustic signals from three turbidity current systems (Bute Inlet, Congo Canyon and Monterey Canyon). It is the first study to use ADCP data at multiple sites to understand controls on passive acoustic signals generated by particle-particle collisions within turbidity currents.

The number of flows with sediment-generated noise varies between each submarine channel system. The probable explanation for this disparity is a link between sediment grain sizes present and whether flows produced sediment-generated noise, at least at the frequency of the ADCPs present. Across the sites, with increasing clay content, there was a reduction in the number of flows with sediment-generated noise and the intensity of the passively detected noise received by the ADCP. This is in line with laboratory experiments within Chapter 2 of this thesis, which found that flows with fine clay may not emit acoustic signals.

ADCP data from Monterey Canyon showed significant variance in the strength of particle generated noise, and where that noise came from within the flow. These changes are possibly related to the internal character of the flow, and could result from changes in turbidity current structure, sediment type and suspended sediment concentration as turbidity currents evolve (Simmons *et al.* 2020). Observations suggest that both turbidity current structure and suspended sediment concentration play an important role in controlling the level of sediment-generated noise detected by the ADCPs deployed. It is worth noting that it is very difficult to disentangle noise generation and attenuation, as high near-bed concentrations are likely capable of generating high levels of noise, and high levels of attenuation depend on concentration, flow speed and thickness (Hughes *et al.* 2016; Hay *et al.* 2021).

Variance in the strength of sediment-generated noise between the 600 kHz and 1.2 MHz ADCPs located on mooring MS6 within Bute Inlet showed that ADCP type plays a factor in detecting sediment-generated noise. This must be taken into consideration in future studies.

Velocity data from the majority of ADCPs across each field site, except within the Congo Canyon, showed a relationship between flow speed and passively detected noise. Both flow speed and passively detected noise increase synchronously on numerous occasions during a turbidity current.

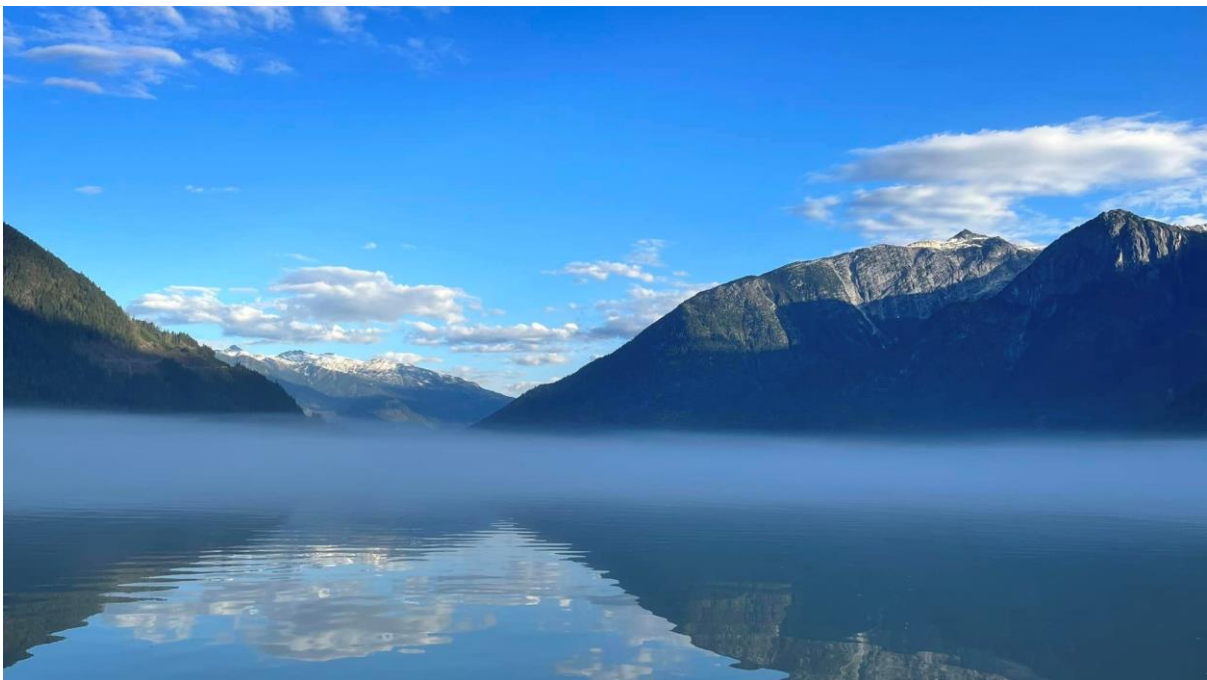
Due to the asynchronous timings of passively detected noise and flow speed within Bute Inlet and Monterey Canyon, it was not possible to directly ascertain an exponent to determine if the strength of passively detected noise was related to frontal speed to the exponent of 7, as proposed by Hay *et al.* (2021). Even though maximum flow speed and passively detected noise do not always match up exactly, it is still possible to suggest a relationship between flow speed and passively detected noise, but it is more complex than suggested by Hatcher (2017) and Hay *et al.* (2021). The differences in the timing of the increases in maximum flow speed and passively detected noise could be the result of structural changes within the turbidity current. In addition to flow speed, the strength of acoustic signals may be related to factors such as ADCP frequency, sediment grain size and type, and suspended sediment concentration within the flow.

#### **4.5.1. Future work**

Future work should tailor the frequency of the ADCPs used to the dominant sediment types within a submarine canyon (as this affects the frequency of acoustic signals that sediment emits). Multiple ADCPs with different frequencies could be deployed on multiple moorings down a submarine canyon, albeit with greater costs. This will also help to determine how sediment type (e.g. grain size) changes during the flow. Data collected via multi-frequency ADCPs should also use grain size data independently measured via seabed cores or sediment traps within the flow. Work should be undertaken to quantify and determine the level of attenuation due to ADCP frequency on the detection of passively detected particle collision noise. This work would then determine the actual effectiveness and accuracy of using ADCPs in a passive capacity.

By undertaking new studies at more submarine canyons, it will help to corroborate the results of this study, suggesting that the number of flows containing detectable sediment-generated noise is related to the dominant sediment types present within an environment.

# Initiation mechanisms of turbidity currents occurring at Bute Inlet and Squamish Delta



*View beyond the mouth of Homathko River during fieldwork in 2022 within Bute Inlet.*

## 5.1. Introduction

*The following section provides a brief introduction into the research around turbidity currents, and their basic nature. This is followed by a synopsis of past research into the initiation mechanisms and behaviour of turbidity currents. After that, this section summarises previous research at Bute Inlet and Squamish Delta. This introduction ends with the aims and objectives of this chapter.*

This chapter seeks to understand how sediment transport occurs via turbidity currents and slope failures (landslides) on river deltas, using unusually detailed time-lapse swath multibeam echo sounder surveys of a river delta. Swath multibeam echo sounding is an active acoustic source in contrast to passive acoustic techniques in previous chapters. This study is based on near daily time-lapse bathymetric surveys of a delta in Bute Inlet, a fjord located in British Columbia, Canada. It is one of only two places worldwide where such detailed (near daily) time-lapse surveys have been collected in the world's oceans (Hughes Clarke, 2016; Clare *et al.* 2017; Vendettuoli *et al.* 2019; Chen *et al.* 2021; Pope *et al.* 2022), with the other being a second fjord (Howe Sound) also in British Columbia.

These detailed time-lapse surveys help to understand the timing (and thus initiation mechanisms) of events on the delta, and how those events remould the seabed, thereby also recording flow runout distance. It is important to understand processes of sediment transport on river deltas for a wide range of reasons. For example, river deltas play a significant role in global sediment and carbon cycles (Milliman and Farnsworth, 2013). Indeed, it was once thought that almost all terrestrial organic carbon from rivers was trapped on deltas (Berner 1982; Berner and Cranfield, 1989). However, it has become apparent that seafloor sediment flows called turbidity currents may occur frequently on deltas, and they may redistribute and bury significant amounts of sediment, and its associated organic carbon, within deeper water areas (e.g. Hage *et al.* 2020, 2022; Heijnen *et al.* 2020). Turbidity currents have multiple initiation mechanisms along a delta, such as via collapse of the delta-lip or other types of seafloor landslides, as well as due to sediment settling from offshore river plumes (Hage *et al.* 2019, or even the plunging of especially sediment-laden river water to form 'hyperpycnal turbidity currents' on the adjacent seafloor (Mulder *et al.* 2003).

Turbidity currents and submarine landslides can pose a significant risk to seabed infrastructure, including pipelines (Sequiros *et al.* 2019), cables (Piper *et al.* 1999; Carter *et al.* 2014; Talling

*et al.* 2022) and potentially in the near future, floating offshore wind anchors located in deeper water. For example, past field studies have shown that turbidity currents can move an 800 kg object for 7 km at 4 m/s and even move a 1000 kg over 580 m down a submarine canyon (Paull *et al.* 2018; Clare *et al.* 2020). With the constantly increasing level of deployment of infrastructure on the seabed, understanding these flows becomes a priority. This includes how turbidity currents are generated, and thus their frequency, as well as their runout.

### **5.1.1. Previous research**

#### *5.1.1.1. Initiation mechanisms of turbidity currents*

There is still debate over the initiation mechanisms and triggers of turbidity currents on deltas and river mouths. This is because there have been very few direct observations of turbidity currents that have precisely timed their occurrence, which is needed to unambiguously know how they are triggered and generated (Clare *et al.* 2016; Hizzett *et al.* 2018; Bailey *et al.* 2021). Furthermore, some turbidity currents have been observed to occur without any major external triggers (e.g. Earthquakes), thus making it more difficult to determine the main causes of turbidity currents in the natural environment (Bailey *et al.* 2021).

Presently, the three main proposed initiation mechanisms are landslides, hyperpycnal flows and dilute river plumes (hypopycnal) (Hage *et al.* 2019). First, slope failures (submarine landslides) can disintegrate and mix with seawater to form a turbidity current (Kuenen and Migliorini, 1950; Piper *et al.* 1999; Hizzett *et al.* 2018; Hage *et al.* 2019; Bailey *et al.* 2021). Second, if a river plume contains enough sediment, it can be denser than lake or ocean water. In this situation, the sediment mixture can continue as a hyperpycnal turbidity current along the sea floor (Mulder and Syvitski 1995; Mulder *et al.* 2003, Hage *et al.* 2019). Hyperpycnal turbidity currents were originally thought to be produced when suspended sediment concentration in the river plume exceeds  $40 \text{ kg.m}^{-3}$  (Mulder *et al.* 2003; Hizzett *et al.* 2018; Hage *et al.* 2019). Although more recently, it has been indicated that hyperpycnal turbidity currents can occur at lower suspended sediment concentrations ( $> 1 \text{ kg.m}^{-3}$ ) due to double diffusion or settling-driven convection (Hoyal *et al.* 1999a,b; Jazi and Wells, 2016; Parsons *et al.* 2001; Sutherland *et al.* 2018; Hizzett *et al.* 2018; Hage *et al.* 2019). Third, turbidity currents can be generated by much more dilute surface river plumes, with sediment concentrations as

low as  $0.07 \text{ kg.m}^{-3}$  (Hage *et al.* 2019), via sediment settling from surface plumes, in ways that are not yet fully understood (Hage *et al.* 2019; Pope *et al.* 2022).

#### 5.1.1.2. Evolution of turbidity currents

Once a turbidity current is generated, it travels from its source towards deeper water. Whilst travelling, it can show three different basic types of behaviour. Sufficiently powerful turbidity currents can erode and pick up sediment, becoming denser and thus faster, leading to more erosion and self-acceleration ('ignite'; Parker *et al.* 1986). Alternatively, sediment may settle from slower moving flows, such that they become less dense and even slower, causing yet more sediment settling, such that the flow decelerates and eventually dies out ('dissipation'; Parker *et al.* 1986; Hizzett *et al.* 2018; Heerema *et al.* 2020). Finally, flows could achieve a near-equilibrium state in which deposition and erosion are balanced, and flow speeds are near constant, which is termed 'auto suspension' (Parker, 1978; Stevenson *et al.* 2015; Hizzett *et al.* 2018).

### 5.1.2. Aims and objectives

The overall aim of Chapter 5 is to use time-lapse bathymetry to understand the timing and initiation mechanisms of turbidity currents on the Homathko Delta in Bute Inlet. Results from Bute Inlet are then compared to similar work at Squamish Delta, to determine if there are consistent and thus fundamental patterns. Chapter 5 specifically aims to test four hypotheses proposed by Hizzett *et al.* (2018) based on past work at Squamish Delta.

1) The first hypothesis is that the most frequent initiation mechanism of turbidity currents are hypopycnal flows from surface river plumes, rather than delta-lip failures or other landslides (Hizzett *et al.* 2018). Suspended sediment concentrations in both the Homathko River and Southgate River in Bute Inlet, and in the Squamish River, are not high enough to generate hyperpycnal flows (Hizzett *et al.* 2018; Pope *et al.* 2022).

2) The second hypothesis is that turbidity currents generated by surface (hypopycnal) river plumes rework the largest volume of sediment on these deltas (Hizzett *et al.* 2018).

3) The third hypothesis is that the frequency and volume of turbidity currents in Bute Inlet and Squamish Delta are similar. Previous work has identified that both Bute Inlet and Squamish

Delta have similar sediment types and regional factors such as weather and tide (Hage *et al.* 2019; Porcile *et al.* 2020; Heerema *et al.* 2020; Talling *et al.* 2022).

4) Finally, Hizzett *et al.* (2018) found that turbidity current initiation mechanism does not dictate its runout distance at Squamish Delta. Therefore, the final hypothesis is that there is no link between the initiation mechanism and runout distance of a turbidity current within Bute Inlet.

### 5.1.3. Regional background

#### 5.1.3.1. Bute Inlet

This chapter studies the shallow water part of a submarine channel system within Bute Inlet, British Columbia, Canada (Fig. 5.1; Heijnen *et al.* 2022; Pope *et al.* 2022). The submarine channel system extends 50 km from the pro-deltas of the Homathko and Southgate Rivers, and extends to a lobe beyond the submarine channel's mouth that is situated at a depth of 650 m (Prior *et al.* 1987; Zeng *et al.* 1991; Zeng and Lowe, 1997; Heijnen *et al.* 2022; Pope *et al.* 2022). In this submarine channel system, sediment comprises 15% gravel, 65% sand, 15% silt and 5% clay, which is primarily derived from the Homathko River, with this river accounting for 70 – 80% of freshwater input (Zeng *et al.* 1991; Pope *et al.* 2022). It has been noted that the suspended load discharge of the Homathko River is approximately  $270 \text{ kg s}^{-1}$  and during the summer freshet, whilst bedload discharge can peak at up to  $400 \text{ kg s}^{-1}$  (Syvitski *et al.* 1985). Furthermore, suspended sediment concentrations in the surface river plumes are usually very dilute, similar to the value of  $0.07 \text{ kg/m}^3$  observed at Squamish Delta (Pope *et al.* 2022). The Southgate River supplies 15 – 25% of the freshwater input, and smaller streams along the fjord making up the remaining 5% (Syvitski and Farrow, 1983; Zeng *et al.* 1991; Pope *et al.* 2022).

In the uppermost sections of the submarine channel, seabed gradients are  $\sim 3^\circ$ , whereas the lobe has a gradient of  $\sim 0.1^\circ$  (Chen *et al.* 2021; Heijnen *et al.* 2020; Zeng *et al.* 1991). On average, the submarine channel has a gradient of  $0.6^\circ$  and a sinuosity of 1.4 (Pope *et al.* 2022). Zeng *et al.* (1991). The submarine channel's floor is comprised predominantly of sand, with the overbank areas being dominated by silt.

There are tens of turbidity currents each year within the upper part of this submarine channel (Pope *et al.* 2022). These flows mainly occur during the summer months when snow melt is high, resulting in elevated discharge of the Homathko River ( $>200 \text{ m}^3/\text{s}$ ) (Prior *et al.* 1987;

Zeng *et al.* 1991; Chen *et al.* 2021; Heijnen *et al.* 2022; Pope *et al.* 2022). During winter, river discharge drops ( $<100 \text{ m}^3/\text{s}$ ), probably resulting in minimal activity in the submarine channel system (Prior *et al.* 1987; Pope *et al.* 2022).

Previous studies around Seymour Narrows, just south of the mouth of Bute Inlet, record that in the upper 100 m of the water column, mean tidal flow is westward and around 0.3 m/s. In the lower 200 m of the water column, flow is reversed, moving at 0.2 m/s in an eastward direction (Shanmugam, 2022). It should be noted that studies into tides within the Johnstone Strait suggest a regional diurnal tidal inequality of 0.2 m/s between the flood and ebb tide, with the flood tide being the faster one (Huggett and Woodward, 1981; Shanmugam, 2022).

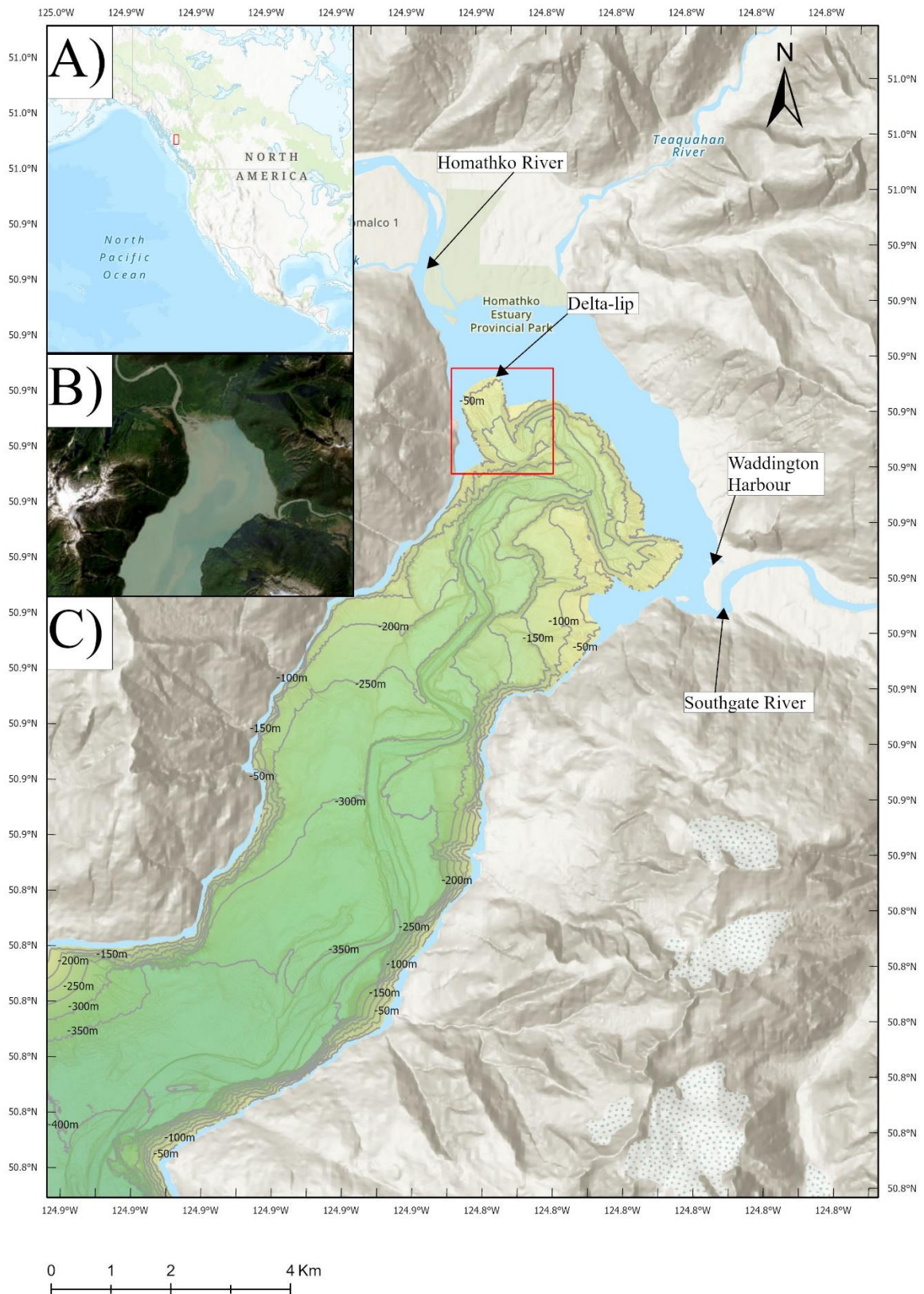


Figure 5.1. Bathymetric map of Bute Inlet and its submarine channel system. The red square indicates the study area within this chapter, which is on the Homathko River delta-lip. A) indicates the location of Bute Inlet, Canada. B) is a satellite photo of Bute Inlet. C) Bathymetric map of the Bute Inlet area.

### 5.1.3.2. Squamish Delta

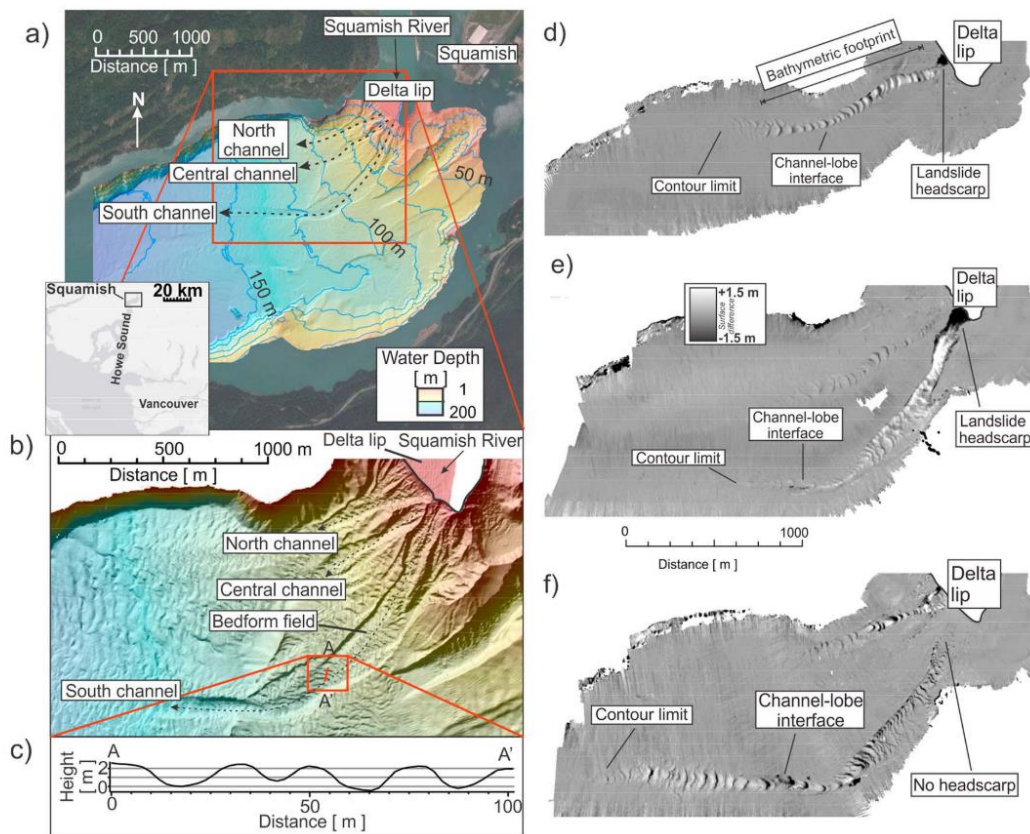


Figure 5.2. Overview map of Squamish Delta. A) Map of Squamish Delta, and its location in Canada. B) Bathymetric map of Squamish Delta indicating submarine channel locations. C) Cross section showing morphology of bedforms present within the submarine channel system. D – F) Difference maps showing changes in seafloor elevation over ~24 hour periods, based on pairs of time-lapse surveys (from Hizzett *et al.* 2018). White indicates deposition, and black indicates erosion.

Results from Bute Inlet are compared to similar (near daily) time-lapse surveys collected at Squamish Delta, which is situated within Howe Sound (Fig. 5.2). Squamish Delta is a river-fed fjord system where water depth increases to >100 m within 1 km of the shoreline (Fig. 5.2; Hughes Clarke *et al.* 2014; Hizzett *et al.* 2018; Pope *et al.* 2022). Squamish Delta comprises three channel lobe systems (northern, central and southern) that only extend ~2 km, and are thus shorter than the Bute Inlet channel (Hughes Clarke *et al.* 20121; Heijnen *et al.* 2020).

Similar to the Homathko River that feeds Bute Inlet, Squamish River is most active during the summer months with a discharge of around 350 – 500 m<sup>3</sup>/s (Clare *et al.* 2016; Hughes Clarke *et al.* 2014). Squamish Delta is generally composed of fine-medium sand, which is finer than the gravel-dominated bedload in the Squamish River. The fine-medium sand originates from

suspended load transport out of the river (Hughes Clarke, 2016; Hizzett *et al.* 2018). This suspended sediment is often carried offshore in a surface plume (Hughes Clarke, 2016; Hizzett *et al.* 2018).

At Squamish Delta, rapid ( $>3,000 \text{ m}^3$  per low tide) sediment deposition and associated delta-lip progradation can occur, especially during river floods. This can lead to delta-lip failures and landslides. The largest delta-lip failures ( $50,000 - 150,000 \text{ m}^3$ ) most commonly occur a few hours after river flood peaks (Clare *et al.* 2016).

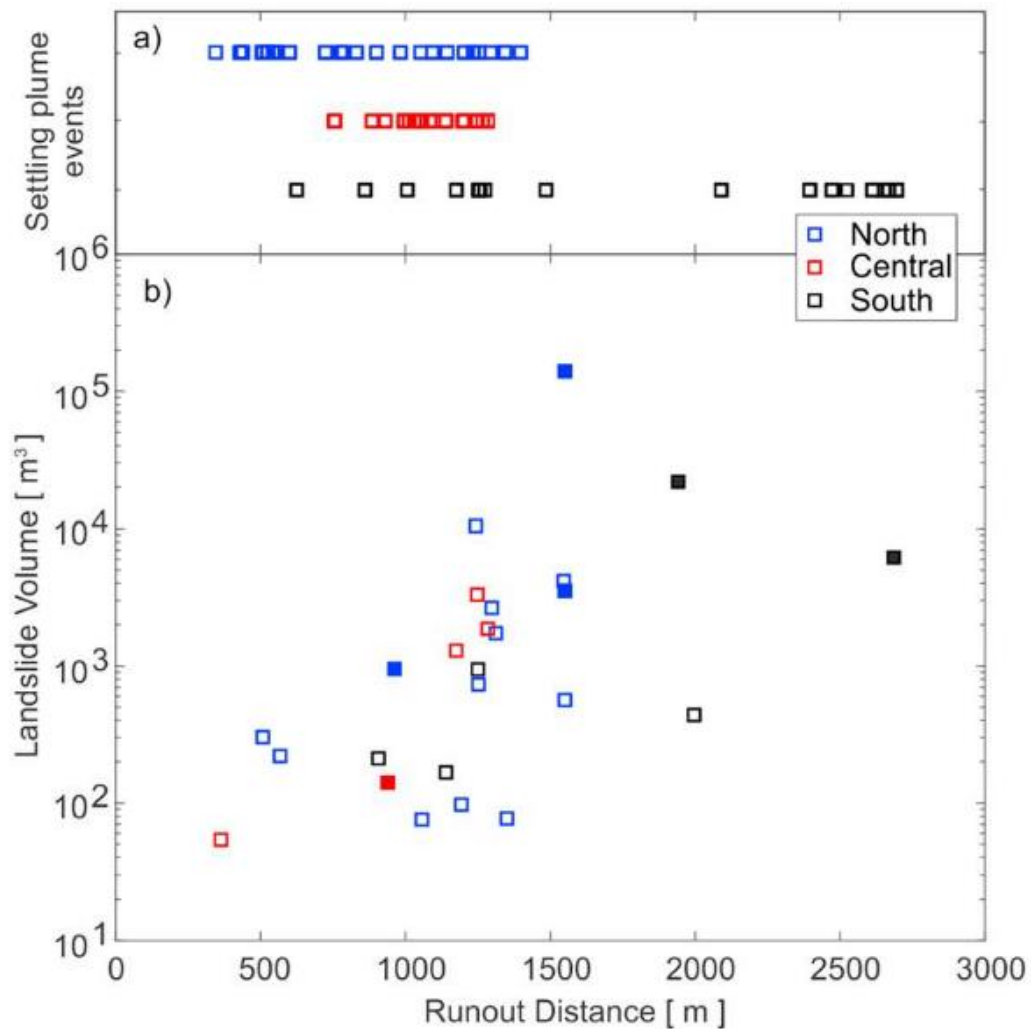


Figure 5.3. Runout distance of turbidity currents generated by surface river plumes and landslides, which originate from the North, Central and South submarine channel systems in the Squamish Delta. A) Runout distance of settling plume events. B) Landslide volume and runout distance (Figure 5.3 is modified from Hizzett *et al.* 2018).

Furthermore, previous studies by Hizzett *et al.* (2018) found that over a 104-day window of surveying, a total of 95 turbidity currents were observed within the difference maps, giving a

frequency of 0.92 turbidity currents of per day. These flow events occurred in three different submarine channel systems on the delta front, with the largest flows commonly originating from the southern channel system (Fig. 5.3).

## **5.2. Methods**

*The following section describes the methods used in this chapter. It initially highlights the equipment and techniques used to collect bathymetry data in Bute Inlet in 2022. This is followed by a subsection on techniques used to process and display the data.*

### **5.2.1. Initial data collection**

Between the 17<sup>th</sup> August 2022 and the 23<sup>rd</sup> September 2022 a slope stability survey of Bute Inlet was undertaken. During this study, daily multibeam bathymetry soundings of the survey area were collected. This data was collected via a single-head Norbit iWBMS (Wide Band Multibeam System) using the Norbit iWBM acquisition system. The entire multibeam system was side mounted to a shallow draft power boat (Sea Dog).

In total, 18 time-lapse multibeam bathymetry surveys were collected within the Homathko Delta area of Bute Inlet, with the most extensive surveys also covering the surrounding submarine channel system being collected approximately every five days. Each day a survey was collected, the vessel ran transects over and around the delta-lip following transect lines with the aim to minimise oversampling and gaps within the data. During each survey, sound velocity profiles of the water column were collected whenever possible. The collected sound velocity profiles were then stored and used to process the swath multibeam data. Each survey was matched to the UK Julian calendar format (e.g. Survey 1 was collected on JD 241, 29/08/2022), and the last multibeam survey Homathko Delta area of Bute Inlet was collected on JD 258 (15/09/2022).

### **5.2.2. Data processing and analysis**

#### *5.2.2.1. Data processing within Caris*

Once all data was collected, it was imported and processed in Caris, which is a multibeam data processing system. Initially, for each individual survey, all raw transects were imported into a common project file. Then a vessel configuration file, tide and sound velocity profile were imported (GC, 2022). For all survey transects, the closest-in-time sound velocity profile was applied onto the data to remove any ‘frowns’ and ‘smile’ artefacts present within the data (Beaudoin, 2010). Frowns are artefacts that curve in a downward crescent, and smiles are

artefacts that curve upwards. These frown and smile artefacts are refraction errors that occur due to the wrong sound velocity profile being applied to the data (Beaudoin, 2010).

The vessel configuration file, tide predictions every 15-minutes for Waddington Harbour in Coordinated Universal Time (UTC), and sound velocity profile files aimed to minimise errors from multibeam positioning and changes in the water column (GC, 2022; WSC, 2022). These three corrections were applied and merged with the raw transect data. Then a new mosaic of the multibeam data was then generated, collating all transect lines into a single image of each day's multibeam survey.

Once this gridded bathymetric dataset ('mosaic') was created, each individual transect was manually processed to remove any user-identified erroneous values. This was performed after the mosaic was generated, as it allowed the user to identify areas that needed further processing, and because the process updated the mosaic once a transect was processed. After all the data was cleaned up, removing any erroneous values, the most up-to-date mosaic was exported as a GeoTIFF bathymetry map from Caris into ArcGIS Pro. All mosaics were exported with a horizontal resolution of 0.5 m.

#### *5.2.2.2. Data processing within ArcGIS Pro*

Once the GeoTIFF was imported into ArcGIS Pro, these gridded bathymetric data were used to create seabed gradient maps for each survey area. These slope maps were overlain over each survey's bathymetry map to help interpret changes in bathymetry between surveys. 17 difference maps of seabed elevation change between pairs of consecutive surveys were then generated. These time-lapse survey pairs were used to document daily changes to the delta-lip and submarine channel.

For each difference map of the Bute Inlet, the delta-lip area was subdivided into three regions: east, middle, and west. These regions were used to identify where turbidity currents originated that caused seabed change. In some cases, seabed change between consecutive bathymetric survey-pairs was seen along multiple pathways that coalesced (e.g. Fig. 5.5C & D). If an event originated from multiple regions along the delta-lip, it was noted down as "multiple".

The initiation mechanism for each turbidity current event was then categorised. This was performed by looking for delta-lip failures (i.e. an area of seabed lowering between surveys, with abrupt margins), and continuous downslope scour. If there was a delta-lip failure, then it

was noted that the event was derived from a "landslide". Furthermore, if there was no delta-lip failure (i.e. no landslide scar), then it was inferred that sediment settling from a surface river plume ("settling plume event") caused the turbidity current. This is the same approach as used by Hizzett et al. (2018) and Hage et al. (2020).

Where seabed change was seen along multiple pathways that merged, in such situations, there may either be multiple turbidity currents that are separated in time, albeit will all events occurring in the time period between the two surveys. Alternatively, it is also possible that multiple turbidity currents occurred at the same time, and amalgamated with one another as they moved downslope. In these situations, there are also multiple points on the delta where turbidity currents were initiated, and thus there may be more than one type of initiation mechanism. These multiple pathways of seabed change may also be associated with multiple different initiation mechanisms. For example, some pathways of seabed change have a landslide scar at their start, but others do not. In cases when there were multiple initiation mechanisms comprising both landslide and settling plume, the event was noted as "both", and the larger of the two initiation mechanisms was also noted down separately. The largest initiation mechanism could be easily identified by it being the turbidity current path with the largest volumetric change (from initial start location to termination) (e.g. Fig. 5.5D). For example, when the path with largest seabed change had a landslide scar at its start, then that landslide-initiated component was deemed to be dominant.

There was a single event on the western side of the delta, where both the runout distance and initial starting initiation mechanisms were not observable due to spatial limits to surveys, and this event was excluded from any analysis.

It should be noted that for potential turbidity current events labelled as "both" and "multiple", there is a likelihood that some of events are multiple separate events, which started at distinctly different times and places. On the other hand, some of these "both"/"multiple" events may have occurred at the same time across the delta-lip, from both landslides and hyperpycnal plumes. However, with the available time-lapse bathymetry data, it is not possible to determine whether such events occurred at different times (albeit all between consecutive surveys), or are single synchronous events that merged-downslope. Therefore, to avoid discrepancies within interpretations, flows that produced multiple coalescing pathways of seabed change between survey pairs have been identified as "both" and "multiple", denoting if events contain both landslide and settling plume initiation mechanisms and if they originate from multiple sections

of the delta-lip. Changes in interpretation could affect the runout distance, volume and event frequency during this study.

Next, using the difference maps, the runout distance of each turbidity current event was then identified. The endpoint of any event was defined as the last point within the submarine channel system on the difference map that showed no discernible change. Once the runout (or minimum runout) distance was noted, an outline from the initiation point to the end of the event was created. Then the elevation change at each grid cell, across this area were isolated and exported to Matlab. Events can, at times, runout beyond the areas of available bathymetric surveys, or dissipate and cause seabed change below the vertical resolutions of the bathymetric survey pairs.

#### *5.2.2.3. Data processing within MATLAB*

A series of different methods were used to assess the uncertainties in estimates of volumes of seabed change between surveys, linked to vertical resolution of the two individual surveys (Schimel *et al.* 2015).

#### **CUBE algorithm**

In a best-case scenario, CUBE algorithm would be used to correct for any uncertainties in volume estimates (Schmitt *et al.* 2008; Schimel *et al.* 2015). The CUBE algorithm produces an estimate of uncertainty for the elevation of the seabed for each grid cell in the bathymetric data. It is generated using Caris, and can be used to account for many sources of error such as the survey system used, auxiliary sensors, configuration and conditions of operation, bottom detection algorithm, seabed slope, sound velocity, sounding depth, sounding density and sounding distance from the applied digital elevation models grid nodes (Schimel *et al.* 2015). The advantage of the CUBE algorithm is that it can take into account different uncertainties at different locations, such as having greater uncertainties in the outer beams of an individual ship track. However, due to a lack of information regarding specific swath multibeam systems sources of error, such as its auxiliary sensors and configuration, the CUBE algorithm could not be used to quantify the error in the volumetric data (Schimel *et al.* 2015).

## Sites where seabed change should not have occurred

A second method was thus used for correcting volumes of seabed change. This second method was based on studying an area where it was assumed that seabed had not changed in elevation, such as in flat areas away from the submarine channel. Changes in seabed elevation between a pair of surveys were assumed to be in error at such sites, and thus represent measurement uncertainty. In order to calculate the error in seabed elevation, an area of the seabed was chosen where it was assumed there was no real change, and a distribution of observed seabed change was generated (Fig. 5.4A, B).

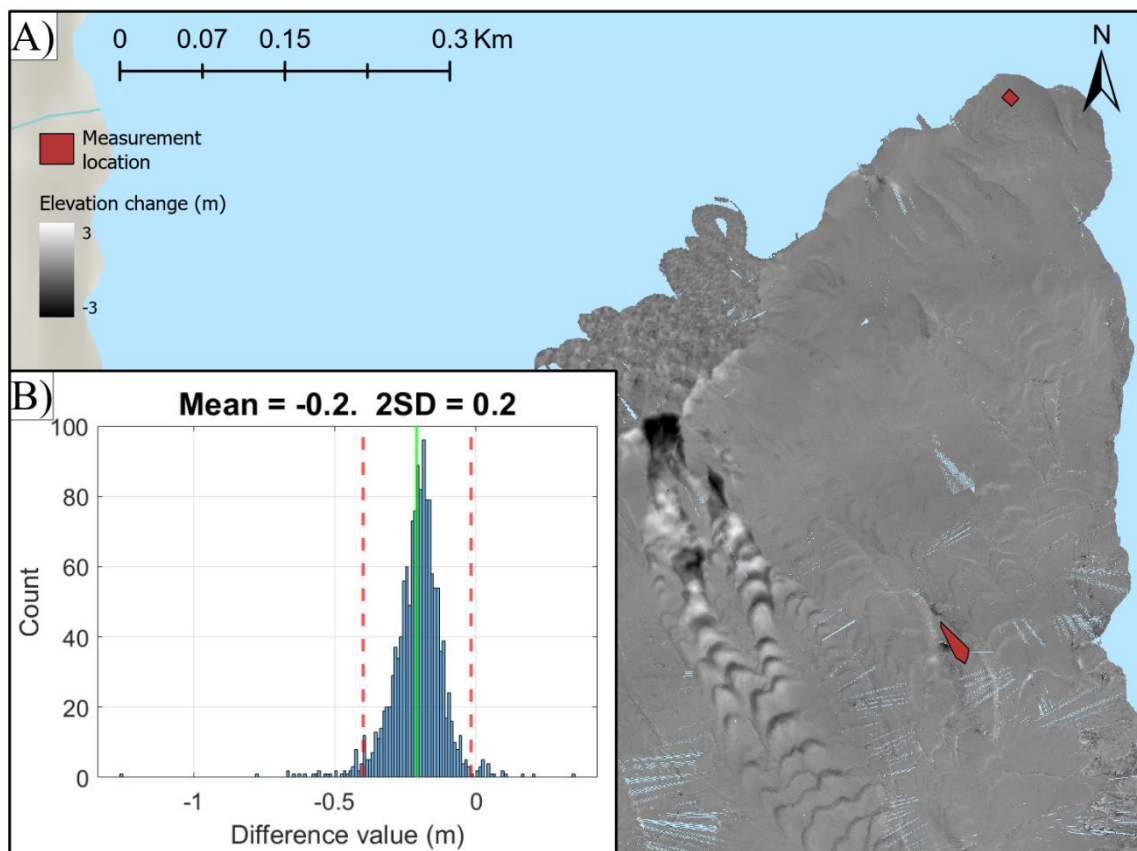


Figure 5.4. Method to calculate measurement uncertainties in seafloor elevation, based on analysing observed changes in seabed elevation, at a site where it is assumed that no real changes occurred. A) Measurement locations (in red) used to collect data on the uncertainties in seabed elevation, where assumed no real change occurred. B) Distribution of changes in seabed elevation in the areas in red on part A between 29/08/2022 and 30/08/2022, displaying mean elevation change and error to two standard deviations.

Survey days	Mean (m)	1 SD ( $k=1.00$ )	2 SD ( $k=1.96$ )
29/08 – 30/08	0.03	0.09	0.19
30/08 – 31/08	-0.08	0.09	0.18
31/08 – 01/09	0.13	0.09	0.18
01/09 – 02/09	0.01	0.10	0.21
02/09 – 03/09	0.08	0.13	0.25
03/09 – 04/09	-0.15	0.09	0.18
04/09 – 05/09	0.19	0.14	0.27
05/09 – 06/09	-0.13	0.09	0.19
06/09 – 07/09	0.09	0.08	0.16
07/09 – 09/09	0.04	0.11	0.21
08/09 – 09/09	-0.01	0.05	0.11
09/09 – 10/09	-0.21	0.10	0.19

Table 5.1. Observed changes in seabed elevation for a number of different survey pairs, at the sites shown in red on Fig. 5.4A. The mean and standard deviations of seabed elevation error between each survey-pair to one standard deviation (68% confidence limit) and two standard deviations (95% confidence limit).

Next, in order to define a limit for detection, for each survey, two standard deviations (95% confidence limit) of the error in seabed elevation were calculated using a value of  $k = 1.96$ , which is a dimensionless threshold factor (Schimel *et al.* 2015; Talling *et al.* 2022) (Table 5.1).

Then, the elevation change at each grid cell, for each survey pair, was compared to the 95% confidence limit (i.e. 2 standard deviations in the distribution of seabed elevation change, where no change should have occurred) (Table 5.1). If the elevation change was below this 95% confidence limit, it was assumed that no seabed elevation change occurred at that grid cell, and the grid cell was not then used to calculate the volume of seabed change in that grid cell. This process was repeated for all grid cells, for each pair of surveys.

A limit of detection at two standard deviations was chosen over a single standard deviation (68% confidence,  $k = 1$ ) as the more conservative limit of detection (95% confidence limit) provides greater confidence that seabed change is real (Schimel *et al.* 2015; Talling *et al.* 2022). Furthermore, a limit of detection at two standard deviations for any volume estimate is a commonly used standard for industry and fluvial geomorphology (Smith *et al.* 2005; Wheaton *et al.* 2010; Schimel *et al.* 2015). However, it should be noted that a limit of detection at two standard deviations will cause more grid cells to be discarded than through the use of a single standard deviation, potentially leading to an underestimation of volumetric change within the bathymetry data.

### Calculating the volume of each event

Next, following the method of Talling *et al.* (2022), elevations of seabed change in all grid cells were summed together - in order to provide a single value of elevation change within the area of the event. Then, using the horizontal grid-cell dimensions of 0.5 m x 0.5 m, the total sum of all elevation change within the limit of detection (95% confidence limit) was converted into a summed volume (Eq. 5.1):

$$V_{total} = X \times Y \times Z_{total} \quad (5.1)$$

In Eq. 5.1,  $V_{total}$  denotes the total volume of the event ( $m^3$ ), where X and Y are horizontal dimensions of each grid cell (0.5 m), and  $Z_{total}$  is total vertical seabed change (m).

Volumes from all grid cells were summed together, instead of calculating the root mean square volume change. This approach was chosen due to volumetric error exacerbation being associated with the root mean square method, because when using the root mean square method, positional (XY) axis errors can gradually add up into large errors (Huang *et al.* 2017; Urban *et al.* 2017). Such positional errors may result from inaccuracies in the positioning system and random noise detection errors from bubbles and particles in the water column. These errors can be so large that the International Hydrographic Organisation allows for up to 2 m horizontal positioning errors in special order surveys (Iwen, 2017). Errors in positioning and noise detection can increasingly shifting the volumetric estimate of seabed change due to a turbidity current away from the correct value. Therefore, in order to reduce compounding errors into volumetric estimations, volume was calculated via the summing of all seabed elevation change and grid cell areas, as described above. Furthermore, by not using the root mean square method, random noise tends to cancel itself out during the summing of all seabed elevation values, assuming noise deviations are evenly distributed around a zero value.

It should be noted that for each event, the summing of all seabed elevation change values will lead to the cancelling out of some positive (deposition) and negative (erosion) volumetric estimates for each event. However, due to there always being an input of sediment from the connecting rivers in Bute Inlet (e.g. Homathko and Teaquahan Rivers), even over a wide area, the cancelling out of some volumetric values will not lead to a total net zero volumetric change estimate.

## **Plotting of figures**

Two figures were then generated. The first figure used changes in colour to indicate where seabed change occurred along the delta-lip (e.g. Fig. 5.6). The second figure used colour to separate the events into the type of initiation mechanism (e.g. Fig. 5.7). On Figs 5.6 and 5.7, events which extended beyond the margins of the available survey data, and thus did not have true runout distance observed, had their markers infilled. The infilling of their markers allowed for easy differentiation from flows with known runout distances, and those which are minimum estimates of runout.

Once all bathymetry data processing was completed, a final figure was generated (Fig. 5.8). This figure shows the volume of all events, tidal data and river discharge data per day. This figure used the bathymetry data collected within the Bute Inlet study, the previously collected tide gauge prediction data for Waddington Harbour and historical hydrometric river discharge data collected at a gauge situated at the Homathko River mouth (GC, 2022; WSC, 2022).

## 5.3. Results

*This section describes the results of the study of Bute Inlet. It first describes, with examples, some of the sediment transport events. This is then followed by an analysis of the volume and runout distance of these events. This analysis highlights how the events differ in volume and runout distance as a function of position on the delta-lip, and how they were caused. Finally, the results section describes how the timing and character of seabed events is related to changes in tidal cycles, and river discharge, during the study period in Bute Inlet in 2022.*

### 5.3.1. Identification and logging of all events within Bute Inlet

Difference maps show significant variance in the initiation mechanism, size, runout distance and location of daily events recorded within Bute Inlet (Fig. 5.5). The largest events usually originated on the eastern side or middle of the delta-lip survey area. Once generated, these turbidity currents either petered out rapidly, or ignited into large flows, as inferred from the migration of channel bedforms over a large distance (Fig. 5.5A). These turbidity currents followed small feeder channels into a larger channel. This ensured that many small flows could merge, creating a larger flow that ran out beyond the survey area (Fig. 5.5B, D). The degree of erosion and number of turbidity current events occurring each day varied considerably (Fig. 5.5).

Over the duration of the survey, there was great variety in the type of turbidity currents occurring. The vast majority of turbidity currents were net-erosional, picking up sediment as they travelled. Turbidity currents evolved as they traversed the submarine channel, having stages of bypass, erosion and deposition even over the 2 km long survey area (Fig. 5.5). In addition, during a single event, this variation in phases of erosion and deposition could vary laterally between the east and west sides of the delta-lip area.

Generally, plume-derived events were erosional, whereas events derived from a landslide had a large initial depositional phase, followed by erosional phases further down the channel.

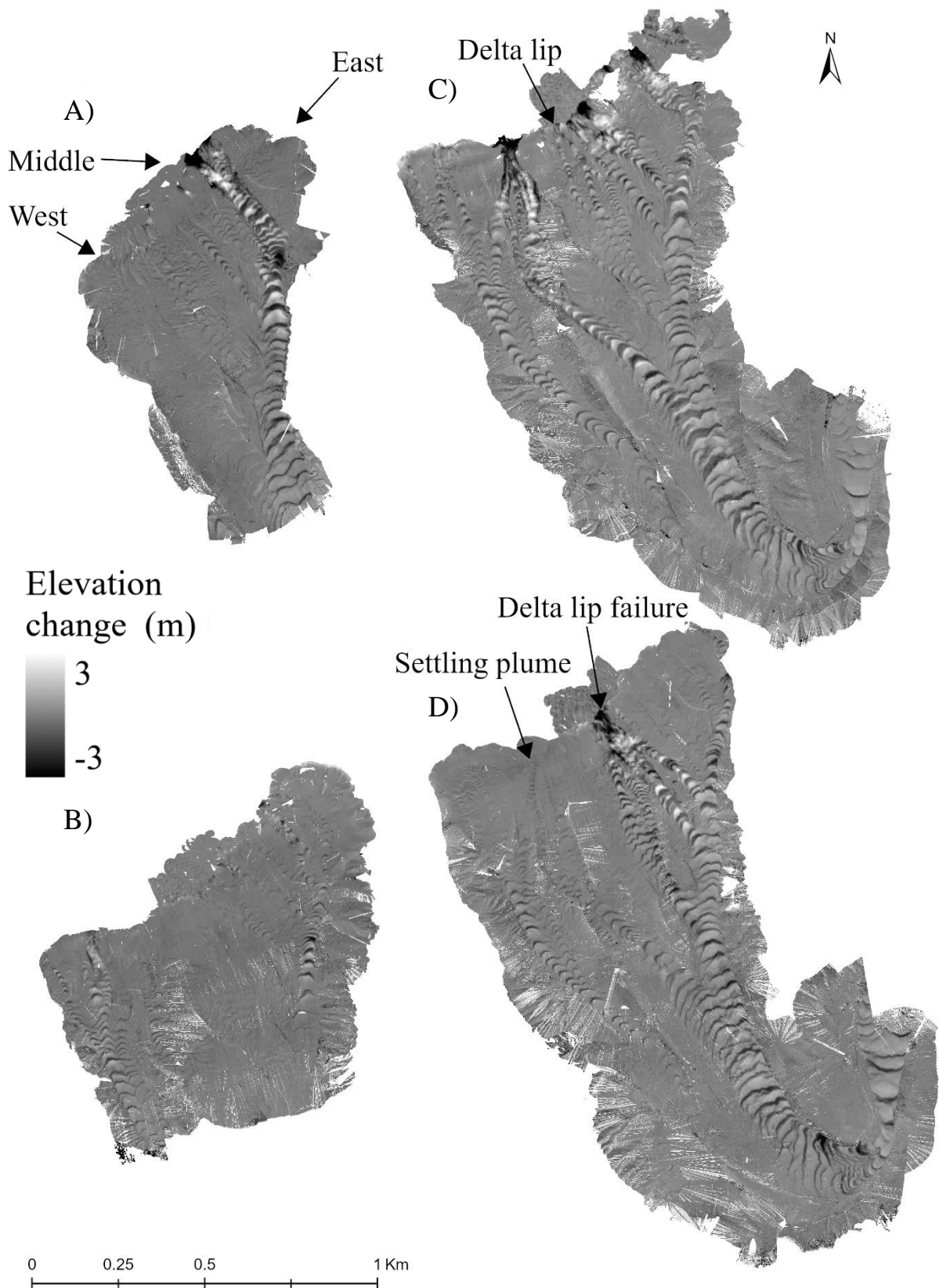


Figure 5.5. Maps showing amount of seafloor change between pairs of surveys at Homathko Delta in 2022. Seabed elevation change occurring between (a) 31/08/22 to 30/08/22, (b) 04/09/22 to 03/09/22, (c) 05/09/22 to 04/09/22 and (d) 07/09/22 to 06/09/22.



generated by a landslide, transformed into a turbidity current which had a maximum runout distance of 623 m. In this study, landslides accounted for 50% of all events.

Surface river-plume derived turbidity currents caused significantly different volumes of seabed change between 90 m<sup>3</sup> to 6,780 m<sup>3</sup>. Events generated in this way travelled for distances of between 200 to 1,250 m, and accounted for 16.7% of all events (Fig. 5.6). It was noted that for one of these plume-generated events, its true runout distance was not observed, as it carried on beyond the end of our survey area.

The turbidity currents that caused the largest volumetric changes to the seabed were generated by both settling plumes and landslides. In these events with multiple initiation mechanisms, it was observed that small flows were generated across the delta, which in turn merged into a single larger flow that travelled for long distances. Of the data collected, the flows with "both" initiation mechanisms accounted for 33.3% of all events observed, their volumes ranged from 3,230 to 76,060 m<sup>3</sup>, and they had runout distances of 215 to 2,400 m (Fig. 5.6). All but one of these turbidity currents had runout lengths that exceeded the survey area, so total volumetric changes to the seabed are underestimated. Further analysis into turbidity currents with both settling plume and landslide initiation mechanisms, revealed that the majority of sediment remobilisation was caused by an initial landslide.

Over the duration of the Bute Inlet slope stability study, a total of 31 events were observed that caused seabed change. The observed events occurred between 29/08/2022 – 10/09/2022, followed by 5 days of dormancy until final time-lapse survey on the 15/09/2022. 16 of these events were turbidity currents (Appendix. 8.1). The remainder were landslides that terminated rapidly without evidence of a continuing turbidity current (Fig. 5.6).

#### *5.3.2.2. Variations in the location of events along the delta-lip*

Four events (13.3%) were derived exclusively from the western side of the delta-lip (Fig. 5.7). The volume of these events ranged from 230 to 6,930 m<sup>3</sup>, and they had runout distances between 220 to 1,225 m. However, significant areas of the western side were missing from the bathymetry surveys, and therefore, there is likely an underestimation of size and runout distance for some events. A single event was excluded from the data as the initial start location was missing.

36.7% of events were initiated within the centre of the delta-lip (Fig. 5.7). Just over half of these events were small, between 9 to 90 m<sup>3</sup>, with a runout distance of up to 212 m. The rest of the events in the middle section of the delta-lip had volumes of seabed change that ranged up to 11,990 m<sup>3</sup>, with runout distances up to 1,050 m (Fig. 5.7).

On the eastern side of the study area, the events had volumes of seabed change between 20 to 340 m<sup>3</sup>, with runout distances up to 90 m. These events account for 26.7% of the total events during the study.

The largest events generally contained sediment derived from multiple locations along the delta-lip area. These events ranged in volume from 3,230 to 76,060 m<sup>3</sup> had runout distances between 600 to 2,400 m (Fig. 5.7), and accounted for 23.3% of all events. All but one of the events containing sediment derived from multiple locations ran out beyond the survey area. As a result, the runout distances and total volumes of seabed change could be much larger than reported.

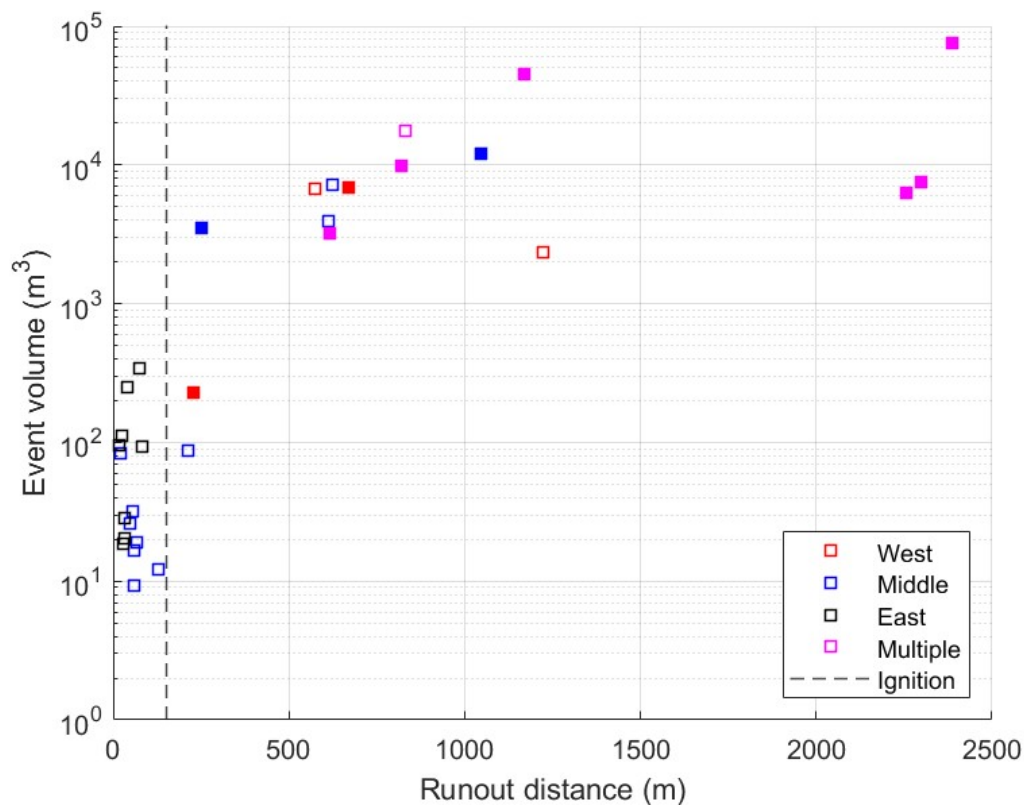


Figure 5.7. Volume of seabed change (m<sup>3</sup>) and runout distance (m) of each event between 29/08/2022 – 15/09/2022, separated into the region along the delta-lip. Solid squares indicate that the full runout distance was not observed, as the flow continued beyond the area surveyed. The dotted ('ignition') line indicates the point at which landslide events ignited into turbidity currents, based on seabed geomorphology.

### 5.3.3. River discharge, tidal height and total volume of events within Bute Inlet

Subsection 5.3.3. analyses how fluctuations in river discharge and tidal range are linked to the occurrence of events, and the volume of seabed change in those events. This subsection is then used to help determine the dominant cause of the mass sediment transport events within Bute Inlet.

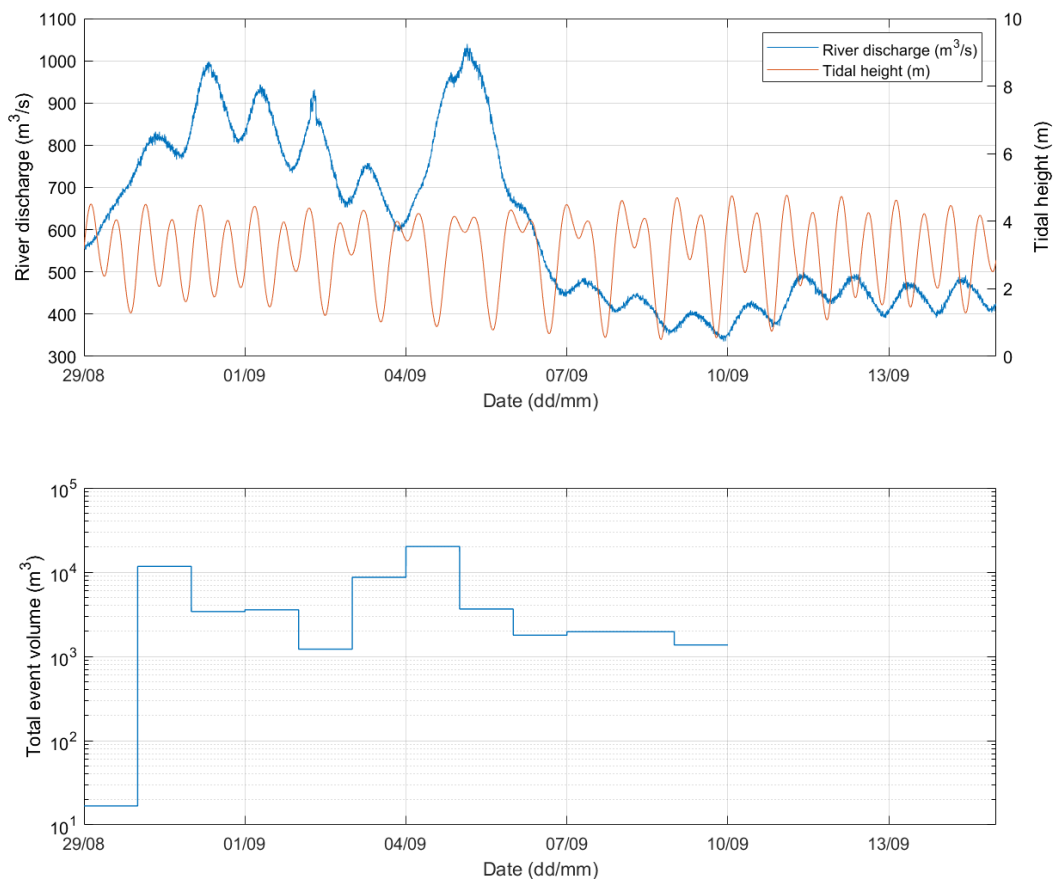


Figure 5.8. Changes in river discharge, tidal height and total event volume between the days when events occurred 29/08/2022 – 15/09/2022. A) Changes in river discharge (m<sup>3</sup>/s) of the Homathko River (blue line), and tides predicted at Waddington Harbour (orange line) near to Bute Inlet. B) Total volume of seabed change (m<sup>3</sup>) due to events each day, for survey pairs between 29/08/2022 and 15/09/2022, using 95% confidence limits for changes in seabed elevation.

River discharge initially increased from <600 to ~1,000 m<sup>3</sup>/s, and then remained relatively high (600 to 1,050 m<sup>3</sup>), peaking in the early morning on 05/09/22. After this peak, there was a rapid drop in river discharge, and it remained between 350 – 500 m<sup>3</sup>/s for the rest of the study (Fig. 5.8A).

In the area of Waddington Harbour within Bute Inlet (Fig. 5.1), tidal height varied between 0.5 to 4.8 m, indicating it is a macro-tidal environment. A neap tide occurred on 01/09/22 and spring tide on 10/09/22 (Fig. 5.8A). Inside Bute Inlet, clear differences in flood and ebb tides exist. It is observed that within a tidal cycle, one tide (flood or ebb) is usually larger than the other, which is usually exacerbated during the spring tide period (Fig. 5.8A).

A total of 31 sediment transport events occurred over during the Bute Inlet study. The total number of events per day, and the associated volume of seabed change, varied considerably across the 17 difference maps (Fig. 5.5; 5.8B). However, two large peaks in volume of seabed change occurred between 30/08/22– 31/08/22 and 04/09/22 – 05/09/22. These two large peaks in total volume of seabed change both exceeded 10,000 m<sup>3</sup> (Fig. 5.8B). Finally, after 10/09/22 and until the end of the survey on the 15/09/22, no sediment transport events occurred.

## 5.4. Discussion

*The following section compares how Squamish Delta and Bute Inlet differ in relation to the turbidity currents observed, and answers the four hypotheses set out at the start of the chapter.*

### 5.4.1. The initial cause of the sediment transport events in Bute Inlet

Hizzett *et al.* (2018) proposed that there is a link between the changes in the total volume of seabed change in events per day ( $\text{m}^3$ ), river discharge ( $\text{m}^3/\text{s}$ ) and tidal height (m). However, in this study of Bute Inlet, the total event volume per day does not correlate with river discharge and tidal height (Fig. 5.8). Furthermore, it is not possible to explain why after 10/09/2022 the system became inactive for the remainder of the time-lapse bathymetry study, which ended on 15/09/2022. As a result, it is not possible to discern a pattern between the changes in the total volume of events per day ( $\text{m}^3$ ), river discharge ( $\text{m}^3/\text{s}$ ) and tidal height (m). The lack of pattern is unexpected, as previous studies within Bute Inlet have suggested that more frequent turbidity currents are linked to increased river discharge (Pope *et al.* 2022). It possible that the absence of a link between the changes in the total volume of events per day ( $\text{m}^3$ ), river discharge ( $\text{m}^3/\text{s}$ ) and tidal height (m) during the Bute Inlet study (2022) is related to the window of the study. The bathymetry surveys were collected over a small time window of 18-days, which could be too small a time period for any significant pattern to arise.

### 5.4.2. The most frequent location and form of initiation mechanism for sediment transport events

Within the Homathko Delta, most events originated from the eastern side or middle of the delta-lip (Fig. 5.7). This is most likely due to the Homathko River predominantly transporting sediment to the eastern side of the delta (Fig. 5.1B). Additionally, another small feeder river (Teaquahan River) is present on the eastern side of the delta (Fig. 5.1). These factors could mean that more sediment is sent towards the delta-lip's middle or eastern side than the western side, resulting in more frequent and larger mass sediment transport events in those eastern and central areas.

Within the Homathko Delta area, the most common initiation mechanism of sediment transport events were landslides. This was then followed by events initiated by settling plumes. In

addition, sometimes flows were generated by both landslides and river plumes, and then merged into a single turbidity current event - categorised as "Both" (Fig. 5.6).

Due to previous observations that suspended sediment concentrations in the Homothko River are very dilute ( $<0.07 \text{ kg/m}^3$ ), it is thought that all river plumes at this site are hypopycnal, occurring along this fjord's surface (Hage *et al.* 2019; Pope *et al.* 2022). However, in future studies of turbidity currents at this site, direct surface river plume data should be collected to confirm presence or absence of a hypopycnal or hyperpycnal flow. These data can be collected via Conductivity Temperature Depth probes (CTDs), and probes that directly measure sediment concentrations in the river plume.

The findings from the Homathko Delta support the notion within Prior *et al.* (1981) and Obelcz *et al.* (2017) that landslides are the most common sediment transport mechanism from river deltas. This is counter to the finding of Hizzett *et al.* (2018), who found that settling from surface river plumes generated more turbidity currents than landslides at Squamish Delta.

#### **5.4.3. Which initiation mechanism reworks the most sediment in Bute Inlet**

Within the study area in Bute Inlet, there was a wide variety of initiation mechanisms. Landslides alone reworked the smallest volumes of sediment, followed by events generated by surface river plumes (Fig. 5.6; Hage *et al.* 2019; Pope *et al.* 2022).

Flows which contained multiple landslides and settling plumes (the "both" category), were observed to rework the most sediment (Fig. 5.6). In the large events containing multiple subsidiary flows, it was found that the main flow was always caused by a large delta-lip failure (Fig. 5.5). Flows containing both types of initiation mechanism were not mentioned by Hizzett *et al.* (2018). The generation of these flows resulting from both landslides and river plumes most likely results from two factors. The first factor is that Bute Inlet has a much larger river discharge and probably sediment supply than Squamish Delta. The larger river discharge and sediment supply could result in Bute Inlet being more active than Squamish Delta (Hizzett *et al.* 2018; Pope *et al.* 2022). The second factor is the shape of the submarine channel system in Bute Inlet that funnels flows together, and this favours creating hybrid flows with both landslides and surface river plume initiation mechanisms.

#### **5.4.4. Links between sediment type, frequency and volume of turbidity currents**

##### *5.4.4.1. Links regarding the frequency of turbidity currents between both Bute Inlet and Squamish Delta*

Both Homathko Delta in Bute Inlet and Squamish Delta in Howe Sound have similar sediment grain sizes, although Squamish Delta is slightly finer-grained (Hizzett *et al.* 2018; Pope *et al.* 2022). Bute Inlet comprises of 15% gravel, 65% sand, 15% silt and 5% clay, and Squamish Delta mostly comprising of fine-medium-grained sand (Hizzett *et al.* 2018; Pope *et al.* 2022).

Comparing sites, the frequency of events that became turbidity currents are very similar. Squamish Delta has a frequency of 0.92 turbidity currents per day, and the Homathko Delta has around 0.94 per day (Hizzett *et al.* 2018). As both sites are sand-dominated, the conditions required to ignite the flows are similar, and result in the closely matched daily frequencies (Hizzett *et al.* 2018; Heerema *et al.* 2020; Pope *et al.* 2022). The small differences in frequency could potentially relate to other factors, such as higher river discharge in Bute Inlet during the time of the 2022 study (Fig. 5.8A) (Hizzett *et al.* 2018; Heerema *et al.* 2020; Pope *et al.* 2022).

However, one potential limitation that should be considered with the idea that Squamish Delta and Bute Inlet have similar frequencies of events. Two major rivers enter Bute Inlet (Homathko and Southgate Rivers), and in this 2022 study, only the main sediment source (Homathko Delta) was studied. If the Southgate Delta was also taken into account, the frequency of events in Bute Inlet could potentially be significantly higher than that in Squamish Delta.

##### *5.4.4.2. Variations in turbidity current volume between both Bute Inlet and Squamish Delta*

Within Bute Inlet, turbidity currents tended to produce larger volumes of seabed change than those at Squamish Delta. The turbidity currents within Bute Inlet tended to produce volumes of seabed change that are  $> 1,000 \text{ m}^3$ , whereas those within Squamish Delta were commonly between 100 and  $1,000 \text{ m}^3$ . The maximum volume of seabed change caused by turbidity currents in Squamish Delta and Bute Inlet was very similar (up to  $11,0000 \text{ m}^3$ ) (Figs 5.3, 5.6).

Consideration should be made regarding the differing number of survey days. The number of days between studies varied significantly, with 18 time-lapse surveys being collected in Bute Inlet over 18 days, compared to the 93 time-lapse surveys over 104 days in Squamish Delta

(Hizzett *et al.* 2018). If a more prolonged number of time-lapse surveys were conducted at Bute Inlet, there might be a more comparable pattern to that at Squamish Delta.

Furthermore, many of the largest flows within Bute Inlet and, at times, Squamish Delta outran the survey area; this most likely would result in an underestimation as to the volume of sediment. If these events were fully surveyed, potentially significant changes in volume might arise.

#### **5.4.5. Links between turbidity current runout distance: comparing Bute Inlet and Squamish Delta**

The runout distance of turbidity currents that have developed from settling plumes is now compared between events within Bute Inlet and Squamish Delta. Both sites contain numerous small flows that travel similar distances up to ~1,500 m (Figs. 5.3, 5.6 & 5.7; Hizzett *et al.* 2018). Although within Bute Inlet, most small landslides petered out after a few metres, so that they did not ignite into well-developed turbidity currents. The small landslides which did ignite tended to travel similar distances to those within the Squamish Delta (Figs 5.3, 5.6).

Considering only flows that travelled >2,000 metres, differences arise in the most common type of initiation mechanism. In Squamish Delta, these longer runout flows were mainly initiated by sediment settling from surface river plumes. However, in Bute Inlet, flows generated by large landslides tended to travel further (Figs. 5.3, 5.6). For both sites, problems arise when looking at these long runout distance flows, as flows extended beyond the surveyed areas. It was thus common that the full runout distance was not observed. Therefore, it is not possible to identify which site had the longest runout distances and fully determine if there is a link between the runout distance and the type of turbidity current initiation mechanism. (Hizzett *et al.* 2018).

## 5.5. Conclusion

*This final section outlines the main findings, which is followed by a section on future work.*

There is no clear link between Homothko River discharge, or magnitude of tidal cycles, and the volume of seabed change due to turbidity currents in the upper Homothko Delta in Bute Inlet. This lack of a clear relationship is potentially related to the limited time window of the study (18-days) in 2022.

Most events within the Homathko Delta originated from the eastern and middle sections of the delta-lip. Although, Hizzett *et al.* (2018) showed that turbidity currents were most commonly generated from surface river plumes at Squamish Delta, this is not the case in Bute Inlet, as the most common type of initiation mechanism appears to be a landslide.

Time-lapse surveys of Bute Inlet suggest turbidity currents generated by multiple landslides always rework the largest volume of sediment, followed by turbidity currents initiated from surface river plumes. Events entirely generated by landslides rework the smallest volume of sediment.

The Homothko and Squamish Deltas have broadly similar sediment grain sizes, although the bedload of the Homothko River is slightly coarser. The Homothko River also has somewhat higher discharges, including during the study interval in 2022. Turbidity currents are slightly more frequent in Homathko Delta, with a rate of 0.94 per day, compared to the 0.92 turbidity currents per day at Squamish Delta. The higher rate of flows at the Homothkoa Delta may relate to the higher river discharge and sediment supply, but it does not appear to be affected strongly by grain size.

### 5.5.1 Future work

Future work should aim for longer time series of bathymetric surveys to capture larger flow events, and to also have more extensive surveys that cover the entire runout length of these larger flows. This more extensive data set (with the full runout of the event) will help to test if there is a link between the runout distance and the type of turbidity current initiation mechanism.

Time-lapse bathymetry study should be conducted at additional field sites with significantly different local and regional factors such as river discharge, sediment grains sizes and tidal amplitudes. Such studies are needed to determine how the volume of seabed change and runout distance of events is related to their initiation mechanism. Further studies can determine if similar or different patterns occur to those reported here for Bute Inlet and Squamish Delta.

Finally, future work should include monitoring with ADCPs and CTDs to better understand how flows develop in the delta region with respect to observations of seabed change in the bathymetric difference maps. Additionally, ADCPs should be deployed further down the channel to understand if the runout distance is greater than seen in observations of bathymetric change.

Resulting from the fact that turbidity current events labelled “both” and “multiple” may either be multiple separate events overlapping one another (Fig. 5.5C), or large single compound events (Fig. 5.5D), it is challenging to determining which interpretation is correct at any given time. Therefore, future studies should also aim to deploy ADCPs across the delta-lip. Deploying these ADCPs will help determine the timings of all turbidity currents helping ascertain if events classified as “both” and “multiple” are in fact single compound events, or multiple single events.

## Chapter Six

---

# Conclusions and future work



*RV Richardson Point during PhD fieldwork at Bute Inlet, Canada.*

*This chapter initially outlines the rationale for the PhD, and the main conclusions of each chapter. Some wider implications of those conclusions are then discussed, followed by suggestions for future work.*

## **6.1. Rationale**

The purpose of this thesis was to provide new insight and understanding of sediment transport processes, using acoustic signals. Such work is important due to a number of different factors, the first of which is the lack of understanding around the mechanisms of sediment transport (Margalit, 2017; Cook and Dietze, 2022). The second factor is that some types of sediment transport event are challenging to measure in action (e.g. seafloor turbidity currents) and thus poorly understood (Mohrig and Marr, 2003; Talling *et al.* 2012). Indeed, turbidity current events are still challenging to measure, even with methods such as ADCPs and repeat multibeam swath bathymetry surveys (Smith *et al.* 2005; Paull *et al.* 2010,2011; Andrieux *et al.* 2013; Talling *et al.* 2015, 2022; Hizzett *et al.* 2018). This is because turbidity currents can badly damage or flush away equipment moored in their paths, as these flows tend to break the mooring's anchor line. In addition, ADCP and other active sensors are expensive to run and usually requires a high amount of battery power to operate, resulting in a limited operational time (Clare *et al.* 2020). A promising alternative to active sensors are passive sensors (Rigby *et al.* 2015; Gaida *et al.* 2020). These passive techniques, which can be used in tandem or separately from active methods, use passive acoustic to listen for grain-grain collisions, colloquially named sediment-generated noise (Thorne, 1985, 1986). Passive sensors potentially allow us to monitor sediment transport in new ways, at a reduced cost, for longer than previously before, with the only downside being that they come with a reduced spatial resolution (Bassett *et al.* 2013; Rigby *et al.* 2015; Talling *et al.* 2022). However, at present, there are significant research gaps that we need to fill to use acoustic signals to monitor sediment transport, including how the frequency of sediment-generated noise varies with different grain sizes, and in practical field tests (Marineau *et al.* 2015; Rigby *et al.* 2016).

This thesis seeks to understand sediment transport using a combination of active and passive acoustic techniques. The thesis is subdivided into two sections. The first section (Chapters 1 – 3) focuses on passive acoustics. It uses laboratory and field experiments to understand how different factors (e.g. grain size, flow speed, bedforms etc.) determine the basic character (e.g. strength and different frequencies) of passive acoustic signals emitted by sediment transport

processes. Chapter 2 comprises laboratory experiments with a 1 Hz – 450 kHz hydrophone and two ADCPs (600 kHz and 1.2 MHz) used in a passive manner. This chapter seeks first to understand if sediment-generated noise can be detected within a new recirculating flume setup. This is followed by a determination of the controls of sediment-generated noise.

Then in the next section (Chapters 3 – 5), a combination of passive and active acoustic methods are used to understand sediment transport processes. Chapter 3 uses 600 kHz and 1.2 MHz ADCPs to determine the extent to which both passive and active acoustic signals record sediment transport in the sandy Río Paraná in South America. Chapter 4 compares sediment-generated noise emitted by turbidity currents within three different submarine channel systems (Bute Inlet, Monterey Canyon, Congo Canyon). This chapter uses data collected passively by ADCPs to determine how sediment-generated noise varies over the duration of a turbidity current, and what controls sediment-generated noise from such flows. Chapter 5 then uses an active acoustic method (multibeam swath bathymetry) within Bute Inlet in Canada to document how turbidity currents scult the seabed, and how flows are generated. Data from Bute Inlet are compared to similar measurements from another nearby fjord-delta in British Columbia, Canada. This comparison between Bute Inlet and Squamish Delta seeks to understand fundamental controls on turbidity current initiation mechanisms and behaviour using such acoustic methods.

## 6.2. Conclusions

### 6.2.1. Chapter 2 - Laboratory analysis of passively detected acoustic signals in recirculating flume experiments

Previous laboratory experiments that analysed controls on sediment-generated noise were usually conducted with rotating drums (Thorne 1985, 1986, 1990). Chapter 2 tests whether simpler and cheaper experiments in a recirculating flume can rather be used (Rigby *et al.* 2016; Gimbert *et al.* 2019). Furthermore, most previous experiments and field studies have only considered coarse-grained (gravel) sediment, and there are few studies of acoustic signals from transport of finer-grained sand. (Wren *et al.* 2015; Le Guern *et al.* 2021). It was also proposed that bedforms may affect sediment-generated noise, but this had not been tested via controlled laboratory experiments. Finally, ADCPs are commonly used as active sensors to understand sediment flow processes, such as by measuring flow velocity. However, ADCPs also record noise that is passively emitted by sediment transport, and this could provide important extra information.

Chapter 2's recirculating flume experiments successfully established that acoustic signals from sediment transport could be measured, which exceeded background noise (e.g. from pumps).

However, experiments using a 0.4 MHz hydrophone were limited in what they show regarding the relationship between acoustic power and flow speed, as signals from sediment transport do not exceed those from background noise at slow ( $< 0.6$  m/s) flow speeds. Furthermore, due to the lack of separation between power spectral density values for different sediment grain sizes, it is not possible to determine the relationship between grain sizes and acoustic signals.

Additional experiments with a 0.4 MHz hydrophone showed that it was not possible to see significant changes in acoustic power across the profile of a bedform (for ripples to upper-stage plane bed). Comparing variations in acoustic power between types of bedform also shows an unclear trend, but with a weak trend of increasing power spectral density as bedform type changes from upper-stage plane bed into ripples. This trend is unexpected, and it could be related to issues such as a low signal-to-noise ratio and quantisation within the data.

The most significant finding from the hydrophone data is that clay may act as an acoustic dampener, and at high flow speeds it might be possible to detect suspended particle collisions within the water column using acoustic signals.

In a similar fashion to Hay *et al.* (2021), results from both 600 kHz and 1.2 MHz ADCPs exhibit strong positive correlations between sound intensity and flow speed. However, between ADCP types, the exponents vary that relate flow speed to acoustic signal power. The 600 kHz ADCP produced an exponent of between 6.2 – 6.9, broadly similar to the exponent of 7 found by Hay *et al.* (2021) in a field experiment within Squamish Delta in Canada. However, the exponent relating flow speed to sound intensity in the 1.2 MHz ADCP experiments is significantly lower (5.6 – 2.5). It is not possible to fully determine why there is such a significant difference between the exponent for the 1.2 MHz ADCP data, as compared to the exponent seen by Hatcher (2017), Hay *et al.* (2021) and in the 600 kHz ADCP data.

### **6.2.2. Chapter 3 - Can acoustic signals help to understand sediment transport in a sand-bed river?**

Chapter 3 successfully developed methods to analyse passive acoustic data from a sand-bed river, which addresses Conevski *et al.*'s (2018) request that new methods are needed to help monitor bedload transport via acoustic signals. Furthermore, the development of these new methods allow for the identification and analysis of sediment-generated noise from a moving vessel collected via an ADCP.

Not all field data analysed in Chapter 3 show a relationship between flow speed and passively detected noise generated by sediment collisions. The study area which does (2004 northern study area) show such a relationship, exhibits a weak relationship between flow speed and passively detected noise ( $R^2$  of 0.36) and a large degree of scatter. In addition, for the 2004 northern study area, the exponent (2.9) in the relationship between flow speed and passively detected noise for the Río Paraná is significantly lower than that observed by Hatcher (2017), Hay *et al.* (2021), and the labwork in this thesis (Chapter 2). The discrepancies in relationship calculated for the Río Paraná potentially resulted from a number of factors, such as attenuation and the presence of high levels of interferent noise within both the northern (2004) and southern (2011) data sets from the Río Paraná.

This fieldwork in the Parana River found no significant relationship between sediment-generated noise and friction velocity ( $u_*$ ). This is unexpected, and it differs from the proposal by Hatcher (2017) and Hay *et al.* (2021) that sound pressure is strongly related to flow speed to the power of 7, and thus friction velocity to the power of 7. The lack of the relationship could have resulted from the method used to calculate friction velocity, as the ADCP setup ensured that there were few data points for flow velocities within the lower 20% of the flow, and there were high levels of scatter within the data. More closely spaced and higher precision velocity measurements may be needed close to the bed, as it is this part of the flow's velocity profile that is used to calculate shear velocity ( $u_*$ ).

Data from the southern study area of the Parana River show no relationship between bedload transport rate and sediment-generated noise. The lack of a relationship between both bedload transport rate and sediment-generated noise is unexpected, as previous work by Le Guern *et al.* (2021) linked acoustic signal strength and bedload transport rate within the Loire River (France).

Across the profile of several bedforms within the Río Paraná, it was possible to identify a link between the presence of sediment-generated noise and flow speed. The presence of this link was seen by increases in both RSSI of sediment-generated noise and flow velocity, from the trough to the crest across multiple bedforms.

It should be noted that in the Río Paraná, there was a high degree of instrumental noise; this could help explain the weakened or obscured relationships presented within this chapter.

### **6.2.3. Chapter 4 - Passive acoustic monitoring of turbidity currents within submarine channel systems**

Owing to the findings of Chapter 2, that ADCPs can be used to passively detect sediment-generated noise. Chapter 4 sought to determine if it is possible to use passive signals recorded by ADCPs to understand turbidity currents within three submarine systems (Bute Inlet in Canada, Monterey Canyon in California, and Congo Canyon off West Africa). Such passive monitoring could have major advantages for studying turbidity currents, as passive acoustic sensors can be placed outside the flow, and out of harm's way. They can also be deployed for longer periods due to their lower power consumption.

This analysis showed that it was possible to use ADCPs to passively detect noise from turbidity currents. At these three field sites, the passive ADCP data highlighted a link between increasing mud content, and a reduction in the number of turbidity currents with sediment-generated noise. It was found that sandy flows (e.g. as in Monterey Canyon) nearly always emitted sediment-generated noise at 300 kHz. Flows with a higher mud content in Bute Inlet occasionally emitted detectable sediment-generated noise at this frequency. Finally, turbidity currents in the Congo Canyon are mud-dominated, and they did not emit any form of sediment-generated noise, at least at the frequency of the available ADCPs (75 to 600 kHz). The conclusion that muddy turbidity currents tended to emit little or no acoustic noise is consistent with laboratory experiments that show how mud tends to damp passively emitted acoustic signals (Chapter 2).

ADCPs deployed along the Monterey Canyon showed that there could be significant variance in the level and position of sediment-generated noise over the duration of a single turbidity current. These changes are possibly related to the internal character of the flow. They could result from changes in turbidity current structure, sediment type and suspended sediment concentration as turbidity currents evolve (Simmons *et al.* 2020). Observations suggest that both turbidity current structure and suspended sediment concentration play an important role in controlling the level of sediment-generated noise detected by ADCPs.

Passive acoustic data from ADCPs in Bute Inlet and Monterey Canyon show that there is a relationship between flow speed and passively detected noise. However, due to the lack of detectable sediment-generated noise within the Congo Canyon, it was impossible to identify this relationship in that canyon system. Due to the asynchronous timings of passively detected noise and flow speed within Bute Inlet and Monterey Canyon, it was not possible to directly ascertain an exponent to determine if the strength of passively detected noise was related to frontal speed to the exponent of 7, as proposed by Hay *et al.* (2021). The asynchronous nature of timings suggests that the relationship between flow speed and passively detected noise is thus more complex in turbidity currents than suggested by Hatcher (2017) or Hay *et al.* (2021).

#### **6.2.4. Chapter 5 - Initiation mechanisms of turbidity currents occurring at Bute Inlet and Squamish Delta**

Multibeam bathymetry surveys were conducted for the offshore Homathko Delta in Bute Inlet during the summer of 2022, whose aim was to determine how turbidity currents are generated

and what controls their runout distance and character. Time-lapse surveys at Bute Inlet were also compared to those from another nearby fjord delta, Squamish Delta in Howe Sound, to see if similar initiation mechanisms and flow behaviour patterns occurred in multiple settings.

No significant link was observed between river discharge and tides, and the amount of seabed change observed on the Homothko Delta. This absence of a link is potentially related to the limited time window of the study in 2022 (only 18-days).

For the Homathko Delta in Bute Inlet, numerous small turbidity current events could be generated at a similar time, most of which travelled downslope before forming into one larger turbidity current. On all occasions, the primary turbidity current was landslide initiated. Landslides were the most common initiation mechanism of turbidity currents at Bute Inlet. This contrasts with previous work at Squamish Delta (Hizzett *et al.* 2018) that found turbidity currents were mainly initiated without landslides, via sediment settling from surface (hypopycnal) river plumes.

Bathymetry data from Bute Inlet suggest turbidity currents generated by multiple landslides always rework the most amount of seabed sediment, followed by turbidity currents initiated via sediment settling from surface river plumes. Events which are entirely generated by landslides rework the smallest volume of sediment.

The volumes of seabed change per unit time are similar at Squamish Delta and Bute Inlet. Both sites have closely matching changes in seabed sediment volumes per unit time. There are also similar frequencies of turbidity currents. However, Bute Inlet does have slightly more frequent turbidity currents (0.94 flows per day), compared to 0.92 per day in Squamish Delta.

## **6.3. Wider Implications**

*The previous sections outlined the main conclusions from Chapters 2 to 5. In this section, some wider implications of that work is now outlined.*

### **6.3.1. Wider implications for flume experiments**

Findings from Chapter 2 have helped to improve understanding of how sediment transport generates acoustic signals and produced new methods for such analysis. This means that recirculating flumes could be used to study acoustic signals from sediment transport, at a relatively low cost.

Furthermore, the experiments conducted in Chapter 2 confirm that it is possible to use ADCPs to passively detect sediment-generated noise. The detection of sediment-generated noise via ADCPs adds another method to monitor sediment transport in the natural environment.

### **6.3.2. Implications for studying turbidity currents within submarine channel systems and geohazard assessment**

Chapter 4 has shown that it is possible to passively detect sediment-generated noise from turbidity currents. Thus, instruments such as hydrophones (often cheaper than ADCPs, and other active methods) could be deployed in arrays to monitor turbidity currents within submarine canyon systems. With future improvement, passive acoustics even have the potential to enhance our ability to predict where hazards posed by turbidity currents are greatest, thus helping companies route new infrastructure through areas of reduced risk.

## 6.4. Future research

*This section identifies how future work should progress, extending from results in the thesis.*

### 6.4.1. Weak relationships in Río Paraná data

A surprising result from the analysis of field data in the Paraná River (Chapter 3) was the weak relationships between flow speed (and bed shear stress and bedload transport) and passively detected noise strength. This means that further field data collection may be warranted.

Future work should aim to improve the signal-to-noise ratio of the field data and the method used to derive the friction velocity. For example, in order to improve the signal-to-noise ratio, a housing with acoustically permeable mediums over the transducer faces should be created to encompass any deployed ADCP. This housing would prevent any particle collisions against the transducer face, thus helping to reduce instrumental noise.

During the next set of field experiments, a narrower ADCP measurement bin size should be used, such that there are more closely spaced velocity measurements in the vertical direction in each profile. This will allow a greater density of velocity measurements in the part of the water column used to derive the shear velocity ( $u_*$ ) via the Law of the Wall method, which is the first 20% of the water column above the bed. In addition, to help reduce scatter within the data, averaging should be performed over adjacent ensembles.

Following past work from Le Guern *et al.* (2021), who used a hydrophone to passively determine bedload flux, it would be preferential to repeat any new field measurements with an anchored boat instead of a moving boat. Anchoring the boat would significantly reduce errors due to boat movement and enable averaging over timescales associated with the migration of bedforms. Given the successful nature of Le Guern *et al.*'s. (2021) study in passively determining bedload flux using a hydrophone, collecting passive measurements with both an ADCP and a hydrophone would provide a useful comparison to one another - before trying to collect new moving transects with an ADCP.

### 6.4.2. Passive acoustic monitoring of submarine canyons

Chapter 4 found that turbidity currents can emit acoustic signals, although it appears that only sand-dominated flows (e.g. at Bute Inlet and Monterey Canyon) generate such acoustic signals,

at least at 300 kHz. Mud-dominated flows (e.g. Congo Canyon) do not emit passive acoustic signals at such 300 kHz frequencies. Future work should build upon the knowledge developed in Chapter 4, and also test new equipment. Chapter 4 showed that there are variations between the level of acoustic power detected by ADCPs in different canyons, which may be strongly affected by dominant grain size, which in turn affects the frequency of the sound that is emitted by sediment transport. Therefore, future work may deploy ADCPs with different frequencies that are chosen to capture acoustic signals from the grain sizes found within a specific canyon.

### **6.4.3. Sediment transport assessment around offshore windfarms**

*The following section highlights why it is important to monitor wind farms and also seeks to show how sediment-generated noise can be used in the future to monitor them.*

#### *6.4.3.1. Why is it important to monitor windfarms?*

During this PhD, one of the initial aims was to seek to help improve the monitoring of structures used for offshore wind energy. The Covid-19 pandemic prevented any research into this specific aim, including new field deployments of sensors. However, this type of fieldwork could be the focus for future research that builds upon the results in this thesis.

It is important to monitor wind farms as the installation of offshore wind turbines can affect site hydrodynamics (Christie, 2014; Margalit, 2017). This can also result in changes to the marine environment (Christie, 2014; Margalit, 2017). For example, the installation of wind turbines can influence sediment movement throughout a site and alter the morphology of bedforms - such as their height and migration rate (Christie, 2014; Margalit, 2017).

Presently, the monitoring of a site is performed via side-scan sonar and multibeam bathymetric surveys from ships (Arnot *et al.* 2014; Weinert *et al.* 2015). One of the main problems with relying on vessels is that they are costly and require a high amount of manpower (Arnot *et al.* 2014; Weinert *et al.* 2015). This, in turn, reduces the number of times that surveys can be performed, giving them a low temporal resolution, usually between six months to five years (Arnot *et al.* 2014; Weinert *et al.* 2015; ABP, 2023). The low temporal resolution of such surveys means that preventative actions for potential hazards are often carried out, even when the hazard might not become an issue (Weinert *et al.* 2015). This costs money, which could be avoided.

#### 6.4.3.2. *How can sediment-generated noise be used to monitor windfarms?*

This PhD has shown that acoustic instruments can be used to monitor a number of different properties within the natural environment. At present, there has been no study into whether sediment-generated noise can be detected around wind farms, which are often a noisy environment (Betke *et al.* 2005). Therefore, a small study should be completed in the future using hydrophones and ADCPs in order to test whether acoustic signals can be detected near an offshore wind farm.

Then, on a larger scale, an array of passive instruments should be deployed to develop a standard method for using sediment-generated noise to monitor wind farms. With further investigation, sediment-generated noise data collected around an offshore wind farm could be used to measure friction velocity, which can be used to calculate shear stress, sediment transport rate and direction of the sediment transport across an entire site (Johnson and Cowen, 2017).

The development of a new monitoring method using sediment-generated noise around windfarms could allow seasonal and annual changes in sediment transport to be identified. This could help provide high temporal resolution data within the intermediate gaps between standard vessel-born methods such as multibeam surveys, thus helping to reduce costs (Wiley, 2014).

# Bibliography

---

- Acrement, G. J., & Schneider, V. R. (1989). Guide for Selecting Manning's Roughness Coefficients for Natural Channels and Flood Plains. In *U.S. Geological Survey Water-Supply* (Vol. 2339). <https://doi.org/10.3133/wsp2339>.
- Ainslie M. A., & McColm. James. G. (1998). A simplified formula for viscous and chemical absorption in sea water. *The Journal of the Acoustical Society of America*, **103**(3). 1671 – 1672, 1998.
- Akay, A., & Hodgson, T. H. (1978). Sound radiation from an accelerated or decelerated sphere. *The Journal of the Acoustical Society of America*, **63**(2), 313 – 318.
- Ali, S. Z., & Dey, S. (2017). Origin of the scaling laws of sediment transport. *Proceedings of the Royal Society A: Mathematical, Physical and Engineering Sciences*, **473**(2197). <https://doi.org/10.1098/rspa.2016.0785>.
- Allen, J. R. L. (1980). Sandwaves: A model of origin and internal structure. *Sedimentary Geology*, **26**, 281 – 328. [https://doi.org/10.1016/0037-0738\(80\)90022-6](https://doi.org/10.1016/0037-0738(80)90022-6).
- Allen, P. A., & Homewood, P. (1984). Evolution and mechanics of a Miocene tidal sandwave. *Sedimentology*, **31**(1), 63 – 81. Doi:10.1111/j.1365-3091.1984.tb00723.x.
- Allstadt, K. E., Matoza, R. S., Lockhart, A. B., Moran, S. C., Caplan-Auerbach, J., Haney, M. M., Thelen, W. A., & Malone, S. D. (2018). Seismic and acoustic signatures of surficial mass movements at volcanoes. *Journal of Volcanology and Geothermal Research*, **364**, 76 – 106. <https://doi.org/10.1016/j.jvolgeores.2018.09.007>.
- Andrieux, O., Cooper, C. K., & Wood, J. (2013). *Turbidity Current Measurements in the Congo Canyon*. <https://doi.org/10.4043/23992-ms>.
- Amos, C. L., & King, E. L. (1984). Bedforms of the Canadian eastern seaboard: A comparison with global occurrences. *Marine Geology*, **57**(1 – 4), 167 – 208. [https://doi.org/10.1016/0025-3227\(84\)90199-3](https://doi.org/10.1016/0025-3227(84)90199-3).
- Antony, A., Cittadini, L., Karrenberg, R., Kisteleki, R., Refice, T., Vest, T., and Wilhelm R. (2008). Mediterranean fiber cable cut (January-February 2008) analysis of network dynamics, Technical Report RT-DIA-124- 2008, University of Rome, Italy.
- Arnot, C., Verfuss, U., Morris, T., Sparling, C., Burton, N., Theobald, P., Pangerc, T., & Piper, R. (2014). Review of Post-Consent Offshore Wind Farm Monitoring Data Associated with Licence Conditions.

- Ashley, G. M. (1990). Classification of large-scale subaqueous bedforms: a new look at an old problem. *Journal of Sedimentary Petrology*, **60**(1), 160 – 172. <https://doi.org/10.2110/jsr.60.160>.
- Associated British Ports. (2023). Accessed at: [https://www.humber.com/Estuary\\_Information/Marine\\_Information/Hydrography\\_and\\_Hydrographic\\_Services/](https://www.humber.com/Estuary_Information/Marine_Information/Hydrography_and_Hydrographic_Services/), 28/02/2023.
- Ayala Castillo, P., Brennan, M., Almeida, F., Kroll, F., Obata, D., & Paschoalini, A. (2018). *An Investigation into the effects of signals distortion on the accuracy of the time delay estimation for leak detection in buried plastic water pipes*. 1 – 7. <https://doi.org/10.26678/ABCM.CONEM2018.CON18-0244>.
- Azpiroz-Zabala, M., Cartigny, M. J. B., Talling, P. J., Parsons, D. R., Sumner, E. J., Clare, M. A., Simmons, S. M., Cooper, C., & Pope, E. L. (2017). Newly recognized turbidity current structure can explain prolonged flushing of submarine canyons. *Science Advances*, **3**(10). <https://doi.org/10.1126/sciadv.1700200>.
- Baas, J. H., van Kesteren, W., & Postma, G. (2004). Deposits of depletive high-density turbidity currents: A flume analogue of bed geometry, structure and texture. *Sedimentology*, **51**(5), 1053 – 1088. <https://doi.org/10.1111/j.1365-3091.2004.00660.x>.
- Baas, J. H., McCaffrey, W. D., Houghton, P. D. W., & Choux, C. (2005). Coupling between suspended sediment distribution and turbulence structure in a laboratory turbidity current. *Journal of Geophysical Research: Oceans*, **110**(11), 1 – 20. <https://doi.org/10.1029/2004JC002668>.
- Baas, J. H., Best, J. L., Peakall, J., & Wang, M. (2009). A Phase Diagram for Turbulent, Transitional, and Laminar Clay Suspension Flows. *Journal of Sedimentary Research*, **79**(4), 162 – 183. <https://doi.org/10.2110/jsr.2009.025>.
- Baas, J. H., Best, J. L., & Peakall, J. (2016A). Predicting bedforms and primary current stratification in cohesive mixtures of mud and sand. *Journal of the Geological Society*, **173**(1), 12 – 45. <https://doi.org/10.1144/jgs2015-024>.
- Baas, J. H., Manica, R., Puhl, E., & de Oliveira Borges, A. L. (2016b). Thresholds of intrabed flow and other interactions of turbidity currents with soft muddy substrates. *Sedimentology*, **63**(7), 2002 – 2036. <https://doi.org/10.1111/sed.12292>.
- Baeye, M., & Fettweis, M. (2015). In situ observations of suspended particulate matter plumes at an offshore wind farm, southern North Sea. *Geo-Marine Letters*, **35**(4), 247 – 255. <https://doi.org/10.1007/s00367-015-0404-8>.
- Baas, J., Tracey, N. D., & Peakall, J. (2021). Sole marks reveal deep-marine depositional process and environment: implications for flow transformation and hybrid event bed models. *Journal of Sedimentary Research*, **91**(9), 986 – 1009. <https://doi.org/10.2110/jsr.2020.104>.

- Babonneau, N., Savoye, B., Cremer, M., & Klein, B. (2002). Morphology and architecture of the present canyon and channel system of the Zaire deep-sea fan. *Marine and Petroleum Geology*, **19**, 445 – 467. [10.1016/S0264-8172\(02\)00009-0](https://doi.org/10.1016/S0264-8172(02)00009-0).
- Babonneau, N., Cattaneo, A., Savoye, B., Barjavel, G., Déverchère, J., and Yellès, K. (2012). The Kramis Deep-Sea Fan off Western Algeria: Role of Sediment Waves in Turbiditic Levee Growth. [10.2110/pec.12.99.0293](https://doi.org/10.2110/pec.12.99.0293).
- Bagherimiyab, F., & Lemmin, U. (2013). Shear velocity estimates in rough-bed open-channel flow. *Earth Surface Processes and Landforms*, **38**(14), 1714 – 1724. <https://doi.org/10.1002/esp.3421>.
- Baker, M. L., Baas, J. H., Malarkey, J., Jacinto, R. S., Craig, M. J., Kane, I. A. N. A., & Barker, S. (2017). The Effect of Clay Type on the Properties of Cohesive Sediment Gravity Flows and Their Deposits. *Journal of Sedimentary Research*, **87**, 1176 – 1195. <https://doi.org/10.2110/jsr.2017.63>.
- Bailey, L. P., Clare, M. A., Rosenberger, K. J., Cartigny, M. J. B., Talling, P. J., Paull, C. K., Gwiazda, R., Parsons, D. R., Simmons, S. M., Xu, J., Haigh, I. D., Maier, K. L., McGann, M., & Lundsten, E. (2021). Preconditioning by sediment accumulation can produce powerful turbidity currents without major external triggers. *Earth and Planetary Science Letters*, **562**, 116845. <https://doi.org/10.1016/j.epsl.2021.116845>.
- Bailey, L. P., Clare, M. A., Pope, E. L., Haigh, I. D., Cartigny, M. J. B., Talling, P. J., Lintern, D. G., Hage, S., & Heijnen, M. (2023). Predicting turbidity current activity offshore from meltwater-fed river deltas. *Earth and Planetary Science Letters*, **604**, 117977. <https://doi.org/10.1016/j.epsl.2022.117977>.
- Ballard, M. S., & Lee, K. M. (2017). The Acoustics of Marine Sediments. *Acoust. Today*, **13**(3), 11 – 18.
- Barrière, J., Krein, A., Oth, A., & Schenkluhn, R. (2015). An advanced signal processing technique for deriving grain size information of bed-load transport from impact plate vibration measurements, *Earth Surf. Processes Landforms*, **40**, 913 – 924, [doi:10.1002/esp.3693](https://doi.org/10.1002/esp.3693).
- Barrière, J., Oth, A., Hostache, R., & Krein, A. (2015). Bed load transport monitoring using seismic observations in a low-gradient rural gravel bed stream. *Geophysical Research Letters*, **42**(7), 2294 – 2301. <https://doi.org/10.1002/2015GL063630>.
- Barton, J.S. (2006). Passive acoustic monitoring of coarse bedload in mountain streams. PhD. [PhD Thesis].
- Barton, J., Slingerland, R. R. L., Pittman, S., & Gabrielson, T. B. (2010). Monitoring coarse bedload transport with passive acoustic instrumentation: A field study. *US Geological Survey Scientific Investigations Report*, **5091**, 38 – 51.
- Bassett, C., Thomson, J., & Polagye, B. (2013). Sediment-generated noise and bed stress in a tidal channel. *Journal of Geophysical Research: Oceans*, **118**(4), 2249 – 2265. [Doi:10.1002/jgrc.20169](https://doi.org/10.1002/jgrc.20169).

- Bassetti, M. A., Jouet, G., Dufois, F., Berné, S., Rabineau, M., & Taviani, M. (2006). Sand bodies at the shelf edge in the Gulf of Lions (Western Mediterranean): Deglacial history and modern processes. *Marine Geology*, **234**(1 – 4), 93 – 109. <https://doi.org/10.1016/j.margeo.2006.09.010>.
- Basuki, B & Palupi, M. (2020). Sound Energy Approach in The Use of LRAD as A Bird Deterrent Device in Sam Ratulangi Manado International Airport, North Sulawesi, Indonesia. IOP Conference Series: Materials Science and Engineering. 943. 012053. [10.1088/1757-899X/943/1/012053](https://doi.org/10.1088/1757-899X/943/1/012053).
- Beaudoin, J. (2010). Real-time monitoring of uncertainty due to refraction in multibeam echo sounding. 3 – 13.
- Belleudy, P., Valette, A., & Graff, B. (2010). Passive hydrophone monitoring of bedload in river beds: first trials of signal spectral analyses. *U.S. Geological Survey Scientific Investigations*, **5091**, 67 – 84. <https://pubs.usgs.gov/sir/2010/5091/papers/>.
- Berner, R. A. (1982). Burial of organic carbon and pyrite sulfur in the modern ocean; its geochemical and environmental significance. *American Journal of Science*, **282**(4), 451 LP – 473. <https://doi.org/10.2475/ajs.282.4.451>.
- Berner, R. A., & Canfield, D. E. (1989). A new model for atmospheric oxygen over Phanerozoic time. *American Journal of Science*, **289**(4), 333 LP – 361. <https://doi.org/10.2475/ajs.289.4.333>.
- Bernhardt, A., & Schwanghart, W. (2021). Where and Why Do Submarine Canyons Remain Connected to the Shore During Sea-Level Rise? Insights From Global Topographic Analysis and Bayesian Regression. *Geophysical Research Letters*, **48**(10), 1 – 15. <https://doi.org/10.1029/2020GL092234>.
- Betke, K., Schultz-von-Glahn, M., & Matuschek, R. (2005). *Underwater noise emissions from offshore wind turbines*. 1 – 2.
- Biltoft, C. A., & Pardyjak, E. R. (2009). Spectral Coherence and the Statistical Significance of Turbulent Flux Computations. *Journal of Atmospheric and Oceanic Technology*, **26**(2), 403 – 409. Doi:10.1175/2008jtecha1141.1.
- Blanpain, O., Bailly, P., Cugier, P., & Lafite, R. (2007). *Dynamic Sediment Profile Imagery ( DySPI ): new field device for the study of bedload processes Dynamic Sediment Profile Imagery ( DySPI ): a new field device for the study of bedload processes*.
- Blanpain, O., Demoulin, X., Waeles, B., Ravilly, M., Garlan, T., & Guyomard, P. (2015). Passive acoustic measurement of bedload discharge features on a sandy seafloor. *Proceedings of the Institute of Acoustics*, **37**, 327 – 334.
- British Oceanographic Data Centre (BODC). (2019). Cruise Report Understanding Hazardous Seafloor Sediment Flows in the Congo Submarine Canyon, Offshore West Africa RRS James Cook – **JC187**. 1 – 282. Unpublished Report.

- Brennan, M. L., Schoellhamer, D. H., Burau, J. R., & Monismith, S. G. (2002). Tidal asymmetry and variability of bed shear stress and sediment bed flux at a site in San Francisco Bay, USA. In *Proceedings in Marine Science* (Vol. 5, Issue C). Elsevier B.V. [https://doi.org/10.1016/S1568-2692\(02\)80010-9](https://doi.org/10.1016/S1568-2692(02)80010-9).
- Briggs, K.B., Williams, K.L., Richardson, M.D. & Jackson, D.R., (2001). Effects of changing roughness on acoustic scattering, natural changes. *Proceedings-institute of acoustics*, **23**(2), 375 – 382.
- Brindley, G. W. (1952). Structural Mineralogy of Clays. *Clays and Clay Minerals*, **1**(1), 33 – 43. <https://doi.org/10.1346/ccmn.1952.0010105>.
- Britter, R. E., & Simpson, J. E. (1978). Experiments on the dynamics of a gravity current head. *Journal of Fluid Mechanics*, **88**(2). <https://doi.org/10.1017/S0022112078002074>.
- Brüel & Kjør., (2021). Accessed at: <https://www.Bksv.Com/En/Transducers/Acoustic/Microphones/Hydrophones /8103>, 10/06/2021.
- Bruschi, R., Bughi, S., Spinazzé, M., Torselletti, E., & Vitali, L. (2006). Impact of debris flows and turbidity currents on seafloor structures. *Norsk Geologisk Tidsskrift*, **86**(3), 317 – 336.
- Carpenter, W. O., Goodwiller, B. T., Chambers, J. P., Wren, D. G., & Kuhnle, R. A. (2014). Acoustic measurement of suspensions of clay and silt particles using single frequency attenuation and backscatter. *Applied Acoustics*, **85**, 123 – 129. <https://doi.org/https://doi.org/10.1016/j.apacoust.2014.04.013>.
- Carroll, D., & Starkey, H. C. (1958). Effect of Sea-Water on Clay Minerals. *Proc. Nat. Conf. Clays and Clay Minerals*, 7<sup>th</sup>, **7**(1934), 80 – 101. <https://doi.org/10.1346/CCMN.1958.0070103>.
- Carter, L., Gavey, R., Talling, P. J., & Liu, J. T. (2014). Insights into submarine geohazards from breaks in subsea telecommunication cables. *Oceanography*, **27**(2), 58 – 67. <https://doi.org/10.5670/oceanog.2014.40>.
- Chadwick, A., & Morfett, J. (1998). Hydraulics in civil and environmental engineering. *Hydraulics In Civil And Environmental Engineering*. <https://doi.org/10.4324/9780203235454>.
- Chadwick, W. W., Dziak, R. P., Haxel, J. H., Embley, R. W., & Matsumoto, H. (2012). Submarine landslide triggered by volcanic eruption recorded by in situ hydrophone. *Geology*, **40**(1), 51 – 54. <https://doi.org/10.1130/G32495.1>.
- Chen, J., Huang, G., & Benesty, J. (2015). Study of the maximum signal-to-noise-ratio filters for single- and multi-channel noise reduction. *Journal of the Acoustical Society of America*, **137**, 2238-2238. Doi:10.1121/1.4920164.

- Chen, Y., Parsons, D. R., Simmons, S. M., Williams, R., Cartigny, M. J. B., Hughes Clarke, J. E., Stacey, C. D., Hage, S., Talling, P. J., Azpiroz-Zabala, M. Clare, M. A., Hizzett, J. L., Heijnen, M. S., Hunt, J. E., Lintern, D. G., Sumner, E. J., Vellinga, A. J., & Vendettuoli, D. (2021). Knickpoints and crescentic bedform interactions in submarine channels. *Sedimentology*, **68**(4), 1358 – 1377. <https://doi.org/https://doi.org/10.1111/sed.12886>.
- Chen, C., & Tian, Y. (2021). Comprehensive Application of Multi-beam Sounding System and Side-scan Sonar in Scouring Detection of Underwater Structures in Offshore Wind Farms. IOP Conference Series: Earth and Environmental Science. **668**. 012007. 10.1088/1755-1315/668/1/012007.
- Chiang, C. S., Hsiung, K. H., Yu, H. S., & Chen, S. C. (2020). Three types of modern submarine canyons on the tectonically active continental margin offshore southwestern Taiwan. *Marine Geophysical Research*, **41**(1), 1 – 17. <https://doi.org/10.1007/s11001-020-09403-z>.
- Chiocci, F. L., Cattaneo, A., & Urgeles, R. (2011). Seafloor mapping for geohazard assessment: State of the art. *Marine Geophysical Research*, **32**(1 – 2), 1 – 11. <https://doi.org/10.1007/s11001-011-9139-8>.
- Choi, J.-H., Jun, K.-W., & Jang, C.-D. (2020). Bedload collision sound filtering through separation of pipe hydrophone frequency bands. *Water*, **12**(7), 1 – 19. <https://doi.org/10.3390/W12071875>.
- Choux, C. M. A., Baas, J. H., McCaffrey, W. D., & Haughton, P. D. W. (2005). Comparison of spatio-temporal evolution of experimental particulate gravity flows at two different initial concentrations, based on velocity, grain size and density data. *Sedimentary Geology*, **179**(1 – 2), 49 – 69. <https://doi.org/10.1016/j.sedgeo.2005.04.010>.
- Christie, E. K. (2014). Numerical modelling of morphological impacts of Offshore Wind Farms. PhD. [*PhD Thesis*], 1 – 237.
- Clare, M. A., Hughes Clarke, J. E., Talling, P. J., Cartigny, M. J. B., & Pratomo, D. G. (2016). Preconditioning and triggering of offshore slope failures and turbidity currents revealed by most detailed monitoring yet at a fjord-head delta. *Earth and Planetary Science Letters*, **450**, 208 – 220.
- Clare, M. A., Vardy, M. E., Cartigny, M. J. B., Talling, P. J., Himsforth, M. D., Dix, J. K., Harris, J. M., Whitehouse, R. J. S., & Belal, M. (2017). Direct monitoring of active geohazards: Emerging geophysical tools for deep-water assessments. *Near Surface Geophysics*, **15**(4), 427 – 444. <https://doi.org/10.3997/1873-0604.2017033>.
- Clare, M., Lintern, D. G., Rosenberger, K., Hughes Clarke, J. E., Paull, C., Gwiazda, R., Cartigny, M. J. B., Talling, P. J., Perara, D., Xu, J., Parsons, D., Jacinto, R. S. & Apprioual, R. (2020). Lessons learned from the monitoring of turbidity currents and guidance for future platform designs. *Geological Society, London, Special Publications*, SP500-2019 – 2173. <https://doi.org/10.1144/sp500-2019-173>.

- Clare, M. A., Yeo, I. A., Bricheno, L., Aksenov, Y., Brown, J., Haigh, I. D., Wahl, T., Hunt, J., Sams, C., Chaytor, J., Bett, B. J., & Carter, L. (2023). Climate change hotspots and implications for the global subsea telecommunications network. *Earth-Science Reviews*, **237**, 104296. <https://doi.org/https://doi.org/10.1016/j.earscirev.2022.104296>.
- Conevski, S. Winterscheid, A. Ruther, N. Guerrero, M. & Rennie, C. (2018). Evaluation of an acoustic Doppler technique for bedload transport measurements in sand-bed Rivers. *E3S Web of Conferences*, 40. <https://doi.org/10.1051/e3sconf/20184002053>.
- Conevski, S. Guerrero, M. Winterscheid, A. Rennie, C. D. & Ruther, N. (2020). Acoustic sampling effects on bedload quantification using acoustic Doppler current profilers. *Journal of Hydraulic Research*, **58**(6), 982 – 1000. <https://doi.org/10.1080/00221686.2019.1703047>.
- Cook, K. L., & Dietze, M. (2022). Seismic Advances in Process Geomorphology. *Annual Review of Earth and Planetary Sciences*, **50**, 183 – 204. <https://doi.org/10.1146/annurev-earth-032320-085133>.
- Couldrey, A., Whitehouse, R.J.S., & Harris, J. (2021). *Scour hole collapse at an offshore wind farm foundation*. In: 4th Virtual Geoscience Conference (VGC 2021), 29 September to 1 October 2021, Online.
- Csuka, Z., & Olšiak, R. (2016). The profile of shear stress in the liquid at turbulent flow. *AIP Conference Proceedings*, **1768**, 2 – 32. Doi:10.1063/1.4963054.
- Deane, G., & Stokes, M. (2010). Model calculations of the underwater noise of breaking waves and comparison with experiment. *The Journal of the Acoustical Society of America*. **127**, 3394 – 3410. Doi: 11.1121/1.3419774.
- Degraer, S., Brabant, R. & Rumes, B. (2012). Offshore Wind Farms in the Belgian Part of the North Sea: Heading for an Understanding of Environmental Impacts. *Report by Ghent University. Report for Royal Belgian Institute of Natural Sciences (RBINS)*, 1 – 306.
- Deines, K.L. (1999). Backscatter estimation using Broadband acoustic Doppler current profilers. *IEEE Proceedings of the IEEE Sixth Working Conference on Current Measurement (Cat. No.99CH36331)*, San Diego, CA, USA, pp. 249 – 253, doi: 10.1109/CCM.1999.755249.
- Den Boon, J., Sutherland, J., Whitehouse, R., Soulsby, R., Stam, C.-J., Verhoeven, K., Høgedal, M., & Hald, T. (2004). *Scour behaviour and scour protection for monopile foundations of offshore wind turbines*. 1 – 14.
- Dennielou, B., Droz, L., Babonneau, N., Jacq, C., Bonnel, C., Picot, M., Le Saout, M., Saout, Y., Bez, M., Savoye, B., Olu, K., and Rabouille, C. (2017). Morphology, structure, composition and build-up processes of the active channel-mouth lobe complex of the Congo deep-sea fan with inputs from remotely operated underwater vehicle (ROV) multibeam and video surveys. *Deep-Sea Research Part II: Topical Studies in Oceanography*, **142**, 25 – 49. <https://doi.org/10.1016/j.dsr2.2017.03.010>.

- De Rooij, F., & Dalziel, S.B. (2001). Time- and Space-Resolved Measurements of Deposition under Turbidity Currents. <https://doi.org/10.1002/9781444304275.ch15>.
- Desanto, J., & Sandwell, D. (2022). Physical Principles of Multibeam Sonar for Mapping of the Seafloor. 10.13140/RG.2.2.27027.96805.
- Dorfman, J. & van Beijeren, H. (1977). Kinetic Theory of Gases. Doi:10.1007/978-1-4615-7906-9\_3.
- Down Under GeoSolutions (DUG). (2023). Accessed at: <https://help.dugeo.com/m/Insight/1/438778-how-it-works-time-depth-conversion>, 17/11/2023.
- Duguid, L. (2017). Offshore Wind Farm Substructure Monitoring and Inspection Operations and Maintenance.
- Eça, L., Saraiva, G., Vaz, G., & Abreu, H. (2015). The Pros and Cons of Wall Functions. *Proceedings of the ASME 2015 34<sup>th</sup> International Conference on Ocean, Offshore and Arctic Engineering OMAE2015 May 31 – June 5, 2015, St. John's, Newfoundland, Canada*, **2**, 1 – 11. <https://doi.org/doi:10.1115/OMAE2015-41518>.
- Etminan, V., Conde-Frias, M., Abdolahpour, M., Ghisalberti, M., & Lowe, R. (2018). Shear stresses on beds with large roughness elements. *Proceedings of the 21<sup>st</sup> Australasian Fluid Mechanics Conference, AFMC 2018, December*, 2 – 5.
- Fan, W., McGuire, J. J., & Shearer, P. M. (2020). Abundant Spontaneous and Dynamically Triggered Submarine Landslides in the Gulf of Mexico. *Geophysical Research Letters*, **47**(12), 1 – 16. <https://doi.org/10.1029/2020GL087213>.
- Fang, H., Cheng, W., Fazeli, M., & Dey, S. (2017). Bedforms and Flow Resistance of Cohesive Beds with and without Biofilm Coating. *Journal of Hydraulic Engineering*, **143**(8), 06017010-1-11. [https://doi.org/10.1061/\(asce\)hy.1943-7900.0001313](https://doi.org/10.1061/(asce)hy.1943-7900.0001313).
- Fisher, F. H., & Simmons, V. P. (1977). Sound absorption in sea water. *Journal of the Acoustical Society of America*, **62**(3), 558 – 564. <https://doi.org/10.1121/1.381574>.
- Flemming, B. (1988). On the classification of subaquatic flow-transverse bedforms. *Conference Paper*, **29**, 44 – 47.
- Flemming, B. (2000). The role of grain size, water depth and flow velocity as scaling factors controlling the size of subaqueous dunes. *Proc. MARID*. 55 – 61.
- Francois, R. E., & Garrison, G. R. (1982a). Sound absorption based on ocean measurements: Part I: Pure water and magnesium sulfate contributions. *The Journal of the Acoustical Society of America*, **72**(3), 896 – 907. <https://doi.org/10.1121/1.388170>.
- Francois, R. E., & Garrison, G. R. (1982b). Sound absorption based on ocean measurements. Part II: Boric acid contribution and equation for total absorption. *Journal of the Acoustical Society of America*, **72**, 1879 – 1890. <https://api.semanticscholar.org/CorpusID:121003964>.

- Fredsøe, J., & Deigaard, R. (1992). Mechanics of Coastal Sediment Transport. In *Advanced Series on Ocean Engineering: Vol. Volume 3*. World Scientific. <https://doi.org/doi:10.1142/1546>.
- Gaeuman, D., & Jacobson, R. (2006). Acoustic bed velocity and bed load dynamics in a large sand bed river. *Journal of Geophysical Research*, **111**. <https://doi.org/10.1029/2005JF000411>.
- Gaeuman, D., & Jacobson, R. (2007). Field Assessment of Alternative Bed-Load Transport Estimators. *Journal of Hydraulic Engineering-Asce - J HYDRAUL ENG-ASCE*, **133**. [https://doi.org/10.1061/\(ASCE\)0733-9429\(2007\)133:12\(1319\)](https://doi.org/10.1061/(ASCE)0733-9429(2007)133:12(1319)).
- Gaida, T. C., van Dijk, T. A. G. P., Snellen, M., Vermaas, T., Mesdag, C., & Simons, D. G. (2020). Monitoring underwater nourishments using multibeam bathymetric and backscatter time series. *Coastal Engineering*, **158**, 103666. <https://doi.org/10.1016/j.coastaleng.2020.103666>.
- Galy, V., France-Lanord, C., Beyssac, O., Faure, P., Kudrass, H., and Palhol, F. (2007). Efficient organic carbon burial in the Bengal fan sustained by the Himalayan erosional system. *Nature*, **450**(7168), 407 – 410. <https://doi.org/10.1038/nature06273>.
- Gani, M. (2004). From Turbid to Lucid: A Straightforward Approach to Sediment Gravity Flows and Their Deposits. *The Sedimentary Record*, **2**(3). <https://doi.org/10.2110/sedred.2004.3.4>.
- Garde, R. J., & Rang Raju, K. G. (1985). Mechanics of sediment transportation and alluvial stream problems. *Second edition*.
- Gavey, R., Carter, L., Liu, J. T., Talling, P. J., Hsu, R., Pope, E., & Evans, G. (2017). Frequent sediment density flows during 2006 to 2015, triggered by competing seismic and weather events: Observations from subsea cable breaks off southern Taiwan. *Marine Geology*, **384**, 147 – 158. Doi:10.1016/j.margeo.2016.06.001.
- Geay, T., Belleudy, P., Gervaise, C., Habersack, H., Aigner, J., Kreisler, A., Seitz, H., & Laronne, J. B. (2017a). Passive acoustic monitoring of bed load discharge in a large gravel bed river. *Journal of Geophysical Research: Earth Surface*, **122**(2), 528 – 545. <https://doi.org/10.1002/2016JF004112>.
- Geay, T., Belleudy, P., Laronne, J. B., Camenen, B., & Gervaise, C. (2017b). Spectral variations of underwater river sounds. *Earth Surface Processes and Landforms*, **42**(14), 2447 – 2456. <https://doi.org/10.1002/esp.4208>.
- Geay, T., Zanker, S., Petrut, T., & Recking, A. (2018). Measuring bedload grain-size distributions with passive acoustic measurements. *E3S Web of Conferences*, **40**, 1 – 9 <https://doi.org/10.1051/e3sconf/20184004010>.
- Geay, T., Zanker, S., Misset, C., & Recking, A. (2020). Passive Acoustic Measurement of Bedload Transport: Toward a Global Calibration Curve? *Journal of Geophysical Research: Earth Surface*, **125**(8), 1 – 19. <https://doi.org/10.1029/2019JF005242>.

- Gervaise, C., Kinda, B. G., Bonnel, J., Stéphan, Y., & Vallez, S. (2012). Passive geoacoustic inversion with a single hydrophone using broadband ship noise. *The Journal of the Acoustical Society of America*, **131**(3), 1999 – 2010. <https://doi.org/10.1121/1.3672688>.
- Gimbert, F., Fuller, B. M., Lamb, M. P., Tsai, V. C., & Johnson, J. P. L. (2019). Particle transport mechanics and induced seismic noise in steep flume experiments with accelerometer-embedded tracers. *Earth Surface Processes and Landforms*, **44**(1), 219 – 241. <https://doi.org/10.1002/esp.4495>.
- Gläscher, J. (2004). *Nanmean*. MATLAB Central File Exchange. Accessed at: <https://www.mathworks.com/matlabcentral/mlc-downloads/downloads/submissions/52976/versions/2/previews/nanmean.m/index.html>, 9/03/2021.
- Gostiaux, L., & van Haren, H. (2010). Extracting meaningful information from uncalibrated backscattered echo intensity data. *Journal of Atmospheric and Oceanic Technology*, **27**(5), 943 – 949. <https://doi.org/10.1175/2009JTECHO704.1>.
- Gourvenec, S., & Sykes, R. (2021). Accessed at: <https://theconversation.com/offshore-wind-turbines-could-number-30-000-by-2030-new-ideas-in-ocean-engineering-are-needed-to-install-them-162618#:~:ext=Current%20projections%20indicate%20234%20gigawatts,electricity%20than%20their%20onshore%20equivalents>, 07/10/2021.
- Government of Canada (GC). (2022). Accessed at: <https://www.tides.gc.ca/en/stations/8069>, 30/08/2022.
- Gray, J. R., Laronne, J. B., & Marr, J. D. G. (2010). *Bedload-surrogate monitoring technologies* (Vols. **2010 – 5091**). <https://doi.org/10.3133/sir20105091>.
- Guériot, D., Chèdru, J., Daniel, S & Maillard, E. (2000). The patch test: a comprehensive calibration tool for multibeam echosounders. **3**, 1655 – 1661 vol.3. [10.1109/OCEANS.2000.882178](https://doi.org/10.1109/OCEANS.2000.882178).
- Guerrero, Q. (2019). Bedforms and associated sediment dynamics on the inner shelves at different spatio-temporal scales. [*PhD Thesis*], 1 – 162.
- Günther, R., Klemperer, S., & Goodliffe, A. (2006). Modeling sideswipe in 2D oceanic seismic surveys from sonar data: Application to the Mariana arc. *Tectonophysics*, **420**, 333 – 343. Doi:10.1016/j.tecto.2006.01.027.
- Hackney, C. R., Darby, S. E., Parsons, D. R., Leyland, J., Aalto, R., Nicholas, A. P., & Best, J. L. (2018). The influence of flow discharge variations on the morphodynamics of a diffuence – confluence unit on a large river. *Earth Surface Processes and Landforms*, **43**(2), 349 – 362. <https://doi.org/10.1002/esp.4204>.

- Hage, S., Cartigny, M. J. B., Sumner, E. J., Clare, M. A., Hughes Clarke, J. E., Talling, P. J., Lintern, D. G., Simmons, S. M., Silva Jacinto, R., Vellinga, A. J., Allin, J. R., Azpiroz- Zabala, M., Gales, J. A., Hizzett, J. L., Hunt, J. E., Mozzato, A., Parsons, D. R., Pope, E. L., Stacey, C. D., Symons, W. O., Vardy, M. E., & Watts, C. (2019). Direct Monitoring Reveals Initiation of Turbidity Currents From Extremely Dilute River Plumes. *Geophysical Research Letters*, **46**(20), 11310 – 11320. <https://doi.org/10.1029/2019GL084526>.
- Hage, S., Galy, V. V., Cartigny, M. J. B., Acikalin, S., Clare, M. A., Gröcke, D. R., Hilton, R. G., Hunt, J. E., Lintern, D. G., McGhee, C. A., Parsons, D. R., Stacey, C. D., Sumner, E. J., & Talling, P. J. (2020). Efficient preservation of young terrestrial organic carbon in sandy turbidity-current deposits. *Geology*, **48**(9), 882 – 887. <https://doi.org/10.1130/G47320.1>.
- Hage, S., Galy, V. V., Cartigny, M. J. B., Heerema, C., Heijnen, M. S., Acikalin, S., Clare, M. A., Giesbrecht, I., Gröcke, D. R., Hendry, A., Hilton, R. G., Hubbard, S. M., Hunt, J. E., Lintern, D. G., McGhee, C., Parsons, D. R., Pope, E. L., Stacey, C. D., Sumner, E. J., Tank, S., & Talling, P. J. (2022). Turbidity Currents Can Dictate Organic Carbon Fluxes Across River-Fed Fjords: An Example From Bute Inlet (BC, Canada). *Journal of Geophysical Research: Biogeosciences*, **127**(6), e2022JG006824. <https://doi.org/https://doi.org/10.1029/2022JG006824>.
- Hatcher, M. G. (2017). Ambient Noise From Turbidity Currents In Howe Sound. In *[Msc Thesis]*. Dalhousie University.
- Haught, D., Venditti, J. G., & Wright, S. A. (2017). Calculation of in situ acoustic sediment attenuation using off-the-shelf horizontal ADCPs in low concentration settings. *Water Resources Research*, **53**(6), 5017 – 5037. <https://doi.org/10.1002/2016WR019695>.
- Haughton, P., Davis, C., McCaffrey, W. & Barker, S. (2009). Hybrid sediment gravity flow deposits - Classification, origin and significance. *Marine and Petroleum Geology*, **26**(10), 1900 – 1918.
- Hay, A. E., Hatcher, M. G., & Hughes Clarke, J. E. (2021). Underwater noise from submarine turbidity currents. *JASA Express Letters*, **1**(7), 070801. <https://doi.org/10.1121/10.0005668>.
- Heathershaw, A., & Thorne, P. (1985). Sea-bed noises reveal role of turbulent bursting phenomenon in sediment transport by tidal currents. *Nature*, **316**, 339 – 342.
- Hedrick, L. B. Anderson, J. T. Welsh, S. A. & Lin, L.-S. (2013). Sedimentation in Mountain Streams: A Review of Methods of Measurement. *Natural Resources*, **4**(01), 92 – 104. <https://doi.org/10.4236/nr.2013.41011>.

- Heerema, C. J., Talling, P. J., Cartigny, M. J., Paull, C. K., Bailey, L., Simmons, S. M., Parsons, D. R., Clare, M. A., Gwiazda, R., Lundsten, E., Anderson, K., Maier, K. L., Xu, J. P., Sumner, E. J., Rosenberger, K., Gales, J., McGann, M., Carter, L., & Pope, E. (2020). What determines the downstream evolution of turbidity currents? *Earth and Planetary Science Letters*, **532**, 116023. <https://doi.org/10.1016/j.epsl.2019.116023>.
- Heezen, B. C., & Hollister, C. (1964). Deep-sea current evidence from abyssal sediments. *Marine Geology*, **1**(2), 141 – 174. [https://doi.org/https://doi.org/10.1016/0025-3227\(64\)90012-X](https://doi.org/https://doi.org/10.1016/0025-3227(64)90012-X).
- Heijnen, M. S., Clare, M. A., Cartigny, M. J. B., Talling, P. J., Hage, S., Lintern, D. G., Stacey, C. Parsons, D. R., Simmons, S. M., Chen, Y., Sumner, E. J., Dix, J. K., & Hughes Clarke, J. E. (2020). Rapidly-migrating and internally-generated knickpoints can control submarine channel evolution. *Nature Communications*, **11**(1), 3129. <https://doi.org/10.1038/s41467-020-16861-x>.
- Heijnen, M. S., Clare, M. A., Cartigny, M. J. B., Talling, P. J., Hage, S., Pope, E. L., Bailey, L., Sumner, E., Gwyn Lintern, D., Stacey, C., Parsons, D. R., Simmons, S. M., Chen, Y., Hubbard, S. M., Eggenhuisen, J. T., Kane, I., & Hughes Clarke, J. E. (2022). Fill, flush or shuffle: How is sediment carried through submarine channels to build lobes? *Earth and Planetary Science Letters*, **584**, 117481. <https://doi.org/10.1016/j.epsl.2022.117481>.
- Hizzett, J. L., Hughes Clarke, J. E., Sumner, E. J., Cartigny, M. J. B., Talling, P. J., & Clare, M. A. (2018). Which Triggers Produce the Most Erosive, Frequent, and Longest Runout Turbidity Currents on Deltas? *Geophysical Research Letters*, **45**(2), 855 – 863. <https://doi.org/10.1002/2017GL075751>.
- Hossein, A. & Rennie, C.D. (2009). Determination Of Bed Shear Stress In Gravel-Bed Rivers Using Boundary-Layer Parameters, *Hydrological Sciences Journal*, **54**(1), 147-159, Doi: 10.1623/Hysj.54.1.147.
- Hoyal, D. C. J. D., Bursik, M. I., & Atkinson, J. F. (1999a). Settling-driven convection: A mechanism of sedimentation from stratified fluids. *Journal of Geophysical Research*, **104**, 7952 – 7966.
- Hoyal, D. C. J. D., Bursik, M. I., & Atkinson, J. F. (1999b). The influence of diffusive convection on sedimentation from buoyant plumes. *Marine Geology*, **159**(1 – 4), 205 – 220.
- Hsu, S.K., Kuo, J., Lo, C.L., Tsai, C.H., Doo, W.B., Ku, C.Y., & Sibuet, J.C. (2008). Turbidity currents, submarine landslides and the 2006 Pingtung earthquake off SW Taiwan. *Terrestrial Atmos. Oceanic Sci.*, **19**, 767 – 772.
- Huang, C. J., Shieh, C. -L., & Yin, H. -Y. (2004). Laboratory study of the underground sound generated by debris flows. *Journal of Geophysical Research: Earth Surface*, **109**(F1). Doi:10.1029/2003jf000048.

- Huang, C., Bian, G., Lu, X., Wang, M., Huang, X., & Wang, K. (2017). The Analysis of Error Sources and Quality Assessment for Multibeam Sounding Products. *The International Hydrographic Review*, **18 SE-Articles**.
- Huang, H. (2019). The importance of ADCP alignment with GPS in moving-boat streamflow measurements. *Flow Measurement and Instrumentation*, **67**, 33 – 40. <https://doi.org/10.1016/j.flowmeasinst.2019.04.002>.
- Huggett W.S., & Woodward. M. J. (1981). Tidal Currents in Johnstone Strait. Pacific Marine Science Report 81 – 22. Institute of Ocean Sciences, Sidney, B.C., Canada. p.44.
- Hughes Clarke, J. E., Brucker, S., Muggah, J., Hamilton, T., Cartwright, D., Church, I., & Kuus, P. (2012). Temporal progression and spatial extent of mass wasting events on the Squamish prodelta slope. In *Landslides and engineered slopes: Protecting society through improved understanding* (Vol. **122**, (pp. 1091 – 1096). London: Taylor and Francis Group.
- Hughes Clarke, J. E., Marques, C. R. V., & Pratomo, D. (2014). Imaging active mass-wasting and sediment flows on a fjord delta (pp. 249 – 260). Squamish, British Columbia: Springer International Publishing. [https://doi.org/10.1007/978-3-319-00972-8\\_22](https://doi.org/10.1007/978-3-319-00972-8_22).
- Hughes Clarke, J. E. (2016). First wide-angle view of channelised turbidity currents links migrating cyclic steps to flow characteristics. *Nature Communications*, **7**, 11896. <https://doi.org/10.1038/ncomms11896>.
- Hughes Clarke, J (2018). The Impact of Acoustic Imaging Geometry on the Fidelity of Seabed Bathymetric Models. *Geosciences*, **8**(4), 109 – .doi:10.3390/geosciences 8040109.
- International Council on Large Electric Systems (CIGRE). (2009). Third-party damage to underground and submarine cables. *Brochure 398*, WG B1.21.
- Iwen, D. (2017). Horizontal Accuracy Issues During MBES Surveys. *Annual of Navigation*, **24**. <https://doi.org/10.1515/aon-2017-0005>.
- International Hydrographic Office (IHO). (2005). *Manual on Hydrography*. 1 – 501.
- Jakobsson, M., Gyllencreutz, R., Mayer, L., Dowdeswell, J., Canals, M., & Todd, B., Dowdeswell, E., & Hogan, K.A., & Larter, R. (2016). Mapping submarine glacial landforms using acoustic methods. *Geological Society, London, Memoirs*. **46**, 17-40. 10.1144/M46.182.
- Jamieson, E., Rennie, C., & Jacobson, R. (2011). Evaluation of ADCP Apparent Bed Load Velocity in a Large Sand-Bed River: Moving versus Stationary Boat Conditions. *Journal of Hydraulic Engineering*, **137**, 1064 – 1071. [https://doi.org/10.1061/\(ASCE\)HY.1943-7900.0000373](https://doi.org/10.1061/(ASCE)HY.1943-7900.0000373).
- Jazi, S. D., & Wells, M. G. (2016). Enhanced sedimentation beneath particle-laden flows in lakes and the ocean due to double-diffusive convection. *Geophysical Research Letters*, **43**, **1**(10), 10,883 – 810,890. Doi:10.1002/ 2016GL069547.

- Johnson, E. D., & Cowen, E. A. (2017). Estimating bed shear stress from remotely measured surface turbulent dissipation fields in open channel flows. *Water Resources Research*, **53**(3), 1982 – 1996. <https://doi.org/10.1002/2016WR018898>
- Johnstone, M. A. (2013). Aristotle on Sounds. *British Journal for the History of Philosophy*, **21**(5), 631 – 48.
- Jones, F. R. H., & Mitson, R. B. (1982). The movement of noisy sandwaves in the Strait of Dover. *ICES J. Mar. Sci.*, **40**(1), 53 – 61.
- Katsnelson, B. G., Godin, O. A., & Zhang, Q. (2021). Observations of acoustic noise bursts accompanying nonlinear internal gravity waves on the continental shelf off New Jersey. *J. Acoust. Soc. Am.*, **149**(3), 1609 – 1622.
- Kennedy, J. F. (1969). The Formation of Sediment Ripples, Dunes, and Antidunes. *Annual Review of Fluid Mechanics*, **1**, 147 – 168. <https://doi.org/10.1146/annurev.fl.01.010169.001051>.
- Kerman, B. (1988). Sea Surface Sound: Natural Mechanisms of Surface Generated Noise in the Ocean. Doi:10.1007/978-94-009-3017-9.
- Khripounoff, A., Crassous, P., Lo Bue, N., Dennielou, B., & Silva Jacinto, R. (2012). Different types of sediment gravity flows detected in the Var submarine canyon (northwestern Mediterranean Sea). *Progress in Oceanography*, **106**, 138 – 153. <https://doi.org/10.1016/j.pocean.2012.09.001>.
- Kim, H. Y., Gutierrez, B., Nelson, T., Dumars, A., Maza, M., Perales, H., & Voulgaris, G. (2004). Using the acoustic Doppler current profiler (ADCP) to estimate suspended sediment concentration. University of South Carolina, 04 – 01.
- Klaucke, I., Masson, D., Kenyon, N., & Gardner, J. (2004). Sedimentary processes of the lower Monterey Fan channel and channel-mouth lobe. *Marine Geology*. **206**. 181 – 198. [10.1016/j.margeo.2004.02.006](https://doi.org/10.1016/j.margeo.2004.02.006).
- Knaapen, M. A. F. (2005). Sandwave migration predictor based on shape information. *Journal of Geophysical Research: Earth Surface*, **110**(4), 1 – 9. <https://doi.org/10.1029/2004JF000195>.
- Kneller, B., & Buckee, C. (2000). The structure and fluid mechanics of turbidity currents: A review of some recent studies and their geological implications. *Sedimentology*, **47**, 62 – 94. <https://doi.org/10.1046/j.1365-3091.2000.047s1062.x>.
- Knott, S. T., & Hersey, J. B. (1957). Interpretation of high-resolution echo-sounding techniques and their use in bathymetry, marine geophysics, and biology. *Deep Sea Research (1953)*, **4**, 36 – 44. Doi:10.1016/0146-6313(56)90030-2.
- Kogelnig, A., Hübl, J., Suriñach, E., Vilajosana, I., & McArdell, B. W. (2014). Infrasound produced by debris flow: Propagation and frequency content evolution. *Natural Hazards*, **70**(3), 1713 – 1733. <https://doi.org/10.1007/s11069-011-9741-8>.

- Kok, J. F. (2010). Analytical calculation of the minimum wind speed required to sustain wind-blown sand on Earth and Mars. *ArXiv Preprint ArXiv:1001.4840*.
- Kongsberg. (2023). Accessed at: <https://www.kongsberg.com/maritime/products/ocean-science/mapping-systems/multibeam-echo-sounders/>, 01/03/2023.
- Konsoer, K., Zinger, J., & Parker, G. (2013). Bankfull hydraulic geometry of submarine channels created by turbidity currents: Relations between bankfull channel characteristics and formative flow discharge. *J. Geophys. Res. Earth* **118**, 216 – 228.
- Koss, L. L., & Alfredson, R. J. (1973). Transient sound radiated by spheres undergoing an elastic collision. *Journal of Sound and Vibration*, **27**(1), 59 – 75. Doi:10.1016/0022-460x(73)90035-7.
- Kostaschuk, R. Villard, P. & Best, J. (2004). Measuring Velocity and Shear Stress over Dunes with Acoustic Doppler Profiler. *Journal of Hydraulic Engineering*, **130**(9), 932 – 936. [https://doi.org/10.1061/\(asce\)0733-9429\(2004\)130:9\(932\)](https://doi.org/10.1061/(asce)0733-9429(2004)130:9(932)).
- Kostaschuk, R., Best, J., Villard, P., Peakall, J., & Franklin, M. (2005). Measuring flow velocity and sediment transport with an acoustic Doppler current profiler. *Geomorphology*, **68**(1), 25 – 37. <https://doi.org/10.1016/j.geomorph.2004.07.012>.
- Krein, A., Klinck, H., Eiden, M., Symader, W., Bierl, R., Hoffmann, L., & Pfister L., (2008), Investigating the transport dynamics and the properties of bedload material with a hydro-acoustic measuring system, *Earth Surf. Processes Landforms*, **33**, 152 – 163, doi:10.1002/esp.1576.
- Kuenen, P. H., & Migliorini, C. I. (1950). Turbidity Currents as a Cause of Graded Bedding. *The Journal of Geology*, **58**(2), 91 – 127. <https://doi.org/10.1086/625710>.
- Kuenen, P. H. (1952). Estimated size of the Grand Banks [Newfoundland] turbidity current. *Am. J. Sci.* **250**, 874 – 884.
- Kuryanov, B.F. (1993). The Theory of Low-Frequency Noise Generated by Turbulence Near the Atmosphere-Ocean Interface. In: Kerman, B.R. (eds) *Natural Physical Sources of Underwater Sound*. Springer, Dordrecht. [https://doi.org/10.1007/978-94-011-1626-8\\_20](https://doi.org/10.1007/978-94-011-1626-8_20).
- Lai, H., Fang, H., Huang, L., He, G., & Reible, D. (2018). A review on sediment bioflocculation: Dynamics, influencing factors and modelling. *Science of the Total Environment*, **642**, 1184 – 1200. <https://doi.org/10.1016/j.scitotenv.2018.06.101>.
- Landsat. (2008). Accessed at: <https://earthexplorer.usgs.gov>, 04/10/2021.
- Larner, K., Chambers, R., Yang, M., Lynn, W., & Wai, W. (1983). Coherent noise in marine seismic data. *Geophysics*, **48** (7), 854 – 886.

- Latosinski, F. G., Szupiany, R. N., Guerrero, M., Amsler, L., & Vionnet, C. (2017). The ADCP 's bottom track capability for bedload prediction: Evidence on method reliability from sandy river applications. *Flow Measurement and Instrumentation*, **54**(June 2016), 124 – 135. <https://doi.org/10.1016/j.flowmeasinst.2017.01.005>.
- Latosinski, F. G., Amsler, M. L., Vionnet, C. A., Heredia, A. I., Szupiany, R. N., Lozada, J. M. D., García, C. M., García, M. H., Latosinski, F. G., Amsler, M. L., Vionnet, C. A., Ana, I., Ligorria, H., Szupiany, R. N., Lozada, J. M. D., García, C. M., & Marcelo, H. (2022). The role of dunes in flow resistance in a large and a small river . The case of the Paraná and Tercero. *Journal of Hydraulic Research*, **60**(3), 389 – 407. <https://doi.org/10.1080/00221686.2021.2001588s>.
- Leary, K. C. P., & Buscombe, D. (2020). Estimating sand bedload in rivers by tracking dunes: A comparison of methods based on bed elevation time series. *Earth Surface Dynamics*, **8**(1), 161 – 172. <https://doi.org/10.5194/esurf-8-161-2020>.
- Le Guern, J. Rodrigues, S. Geay, T. Zanker, S. & Hauet, A. (2020). *Relevance of acoustic methods to quantify bedload transport and bedform dynamics in a large sandy-gravel bed river*. October, 1 – 34. <https://doi.org/10.5194/esurf-2020-77>.
- Le Guern, J., Rodrigues, S., Geay, T., Zanker, S., Hauet, A., Tassi, P., Claude, N., Jugé, P., Duperray, A., & Vervynck, L. (2021). Relevance of acoustic methods to quantify bedload transport and bedform dynamics in large sandy-gravel bed river. *Earth Surface Dynamics Discussions*, 1 – 34. <https://doi.org/10.5194/esurf-2020-77>.
- Lefter, J. (1993). Instrumentation For Measuring Scour At Bridge Piers And Abutments. NCHRP Research Results Digest, Transportation Research Board, **No. 189**, 8 pp.
- Lepper, P., Robinson, S., Humphrey, V., & Butler, M. (2014). Underwater acoustic monitoring at wave and tidal energy sites: guidance notes for regulators, 1 – 20.
- Li, M. Z., & King, E. L. (2007). Multibeam bathymetric investigations of the morphology of sand ridges and associated bedforms and their relation to storm processes, Sable Island Bank, Scotian Shelf. *Marine Geology*, **243**(1 – 4), 200 – 228. <https://doi.org/10.1016/j.margeo.2007.05.004>.
- Lichte, H. (1919). On the influence of horizontal temperature layers in seawater on the range of underwater sound signals. *Physikalische Zeitschrift*, **17**, (385 – 389).
- Liu, J., Tian, J., & Yi, P. (2015). Impact forces of submarine landslides on offshore pipelines. *Ocean Engineering*, **95**, 116 – 127. <https://doi.org/10.1016/j.oceaneng.2014.12.003>.
- Liu, H., Yang, F., Zheng, S., Li, Q., Li, D., & Zhu, H. (2019). A method of sidelobe effect suppression for multibeam water column images based on an adaptive soft threshold. *Applied Acoustics*, **148**, 467 – 475. [Doi:10.1016/j.apacoust.2019.01.006](https://doi.org/10.1016/j.apacoust.2019.01.006).
- Liu, H., Zhou, R., Pan, Qi., Dong, L., Ma, Q., Cheng, Z., & Wang, X., (2022). Noise spectrum characteristics of marine pump units induced by different excitation sources. *Scientific Reports*. **12**. 8678. [10.1038/s41598-022-12755-8](https://doi.org/10.1038/s41598-022-12755-8).

- Liu, X., Sun, J., Lu, Y., & Guo, X. (2023). Control of ambient fluid on turbidity current evolution: Mechanisms, feedbacks and influencing factors. *Geosystems and Geoenvironment*, **2**(4), 100214. <https://doi.org/10.1016/j.geogeo.2023.100214>.
- Lowe, D. R. (1982). Sediment gravity flows: II. Depositional models with special reference to the deposits of high-density turbidity currents. *Journal of Sedimentary Petrology*, **52**(1), 279 – 297. <https://doi.org/10.1306/212f7f31-2b24-11d7-8648000102c1865d>
- Lurton, X & Jackson, D. (2004). An Introduction to Underwater Acoustics. *Journal of The Acoustical Society of America - J ACOUST SOC AMER.* **115**. 443 – 443. [10.1121/1.1639324](https://doi.org/10.1121/1.1639324).
- Malarkey, J., Baas, J. H., Hope, J. A., Aspden, R. J., Parsons, D. R., Peakall, J., Paterson, D. M., Schindler, R. J., Ye, L., Lichtman, I. D., Bass, S. J., Davies, A. G., Manning, A. J., & Thorne, P. D. (2015). The pervasive role of biological cohesion in bedform development. *Nature Communications*, **6**, 1 – 6. <https://doi.org/10.1038/ncomms7257>.
- Maier, K. L., Gales, J. A., Paull, C. K., Rosenberger, K., Talling, P. J., Simmons, S. M., Gwiazda, R., McGann, M., Cartigny, M. J. B., Lundsten, E., Anderson, K., Clare, M. A., Xu, J., Parsons, D., Barry, J. P., Wolfson-Schwehr, M., Nieminski, N. M., & Sumner, E. J. (2019). Linking direct measurements of turbidity currents to submarine canyon-floor deposits. *Frontiers in Earth Science*, **7**. <https://doi.org/10.3389/feart.2019.00144>.
- Manica, R. (2000). Sediment Gravity Flows: Study Based on Experimental Simulations. In: Schulz, (ed) *Hydrodynamics - Natural Water Bodies*. Available at: <http://www.intechopen.com/books/hydrodynamics-natural-water-bodies/sediment-gravity-flows-study-based-on-experimental-simulations>.
- Manica, R. (2012). Sediment Gravity Flows: Study Based on Experimental Simulations. *Hydrodynamics – Natural Water Bodies*. <https://doi.org/10.5772/28794>.
- Margalit, J. (2017). Development of natural seabed forms and their interaction with offshore wind farms. Technical University of Denmark. DCAMM Special Report, 1-183. [*PhD Thesis*].
- Marineau, M. D., Minear, J. T., & Wright, S. A. (2015). Using hydrophones as a surrogate monitoring technique to detect temporal and spatial variability in bedload transport. *10<sup>th</sup> Federal Interagency Sedimentation Conference*, April, 12.
- Marineau, M. D., Wright, S. A., & Gaeuman, D. (2016). Calibration of sediment-generated noise measured using hydrophones to bedload transport in the Trinity River, California, USA. *River Flow. Proceedings of the International Conference on Fluvial Hydraulics, River Flow*, 1519 – 1526. <https://doi.org/10.1201/9781315644479-239>.

- Masselink, G., Kroon, A., & Davidson-Arnott, R. G. D. (2006). Morphodynamics of intertidal bars in wave-dominated coastal settings – A review. *Geomorphology*, **73**, 33 – 49. <https://doi.org/10.1016/j.geomorph.2005.06.007>.
- McClelland, S., J. (2019). *Standard Operating Procedures (SOP) Content Guidance Note Draft 3* (pp. 1 – 12). (Unpublished).
- McNaught, A. D., & Wilkinson, A. (1997). *IUPAC. Compendium of Chemical Terminology, 2<sup>nd</sup> ed. (the “Gold Book”)*, **Vol. 1669**, Blackwell Scientific Publications.
- Meral, R., Kaya, S., doğan demir, A., & Demir, Y. (2017). Water Quality Limitation For Turbidity Based Sediment Measurement In Rivers. *The Eurasia Proceedings of Science, Technology, Engineering & Mathematics (EPSTEM) ISSN: 2602 – 3199*, **1**, 383 – 387.
- Melo, I., Llusia, D., Bastos, R. P., & Signorelli, L. (2021). Active or passive acoustic monitoring? Assessing methods to track anuran communities in tropical savanna wetlands. *Ecological Indicators*, **132**, 108305. <https://doi.org/https://doi.org/10.1016/j.ecolind.2021.108305>.
- Melville, B. W., & Sutherland, A. J. (1989). Design Method for Local Scour at Bridge Piers. *Journal of Hydraulic Engineering. Journal of Hydraulic Engineering*, **114**(10), 1210 – 1226. [https://doi.org/doi:10.1061/\(asce\)0733-9429\(1988\)114:10\(1210\)](https://doi.org/doi:10.1061/(asce)0733-9429(1988)114:10(1210)).
- Middleton, G. V. (1966). Experiments on density and turbidity currents: II. Uniform flow of density currents. *Can. J. Earth Sci.* **3**, 627 – 637.
- Middleton, G. V. (1993). Sediment deposition from turbidity currents. *Annual Review of Earth & Planetary Sciences*, **21**(1), 89 – 114. <https://doi.org/10.1146/annurev.ea.21.050193.000513>.
- Millard, N.W. (1976). Noise Generated By Moving Sediments, In: Proceedings Of The Conference On Recent Developments In Underwater Acoustics 31 March-1 April 1976, London, U.K.: Institute Of Acoustics.
- Miller, M. C., McCave, I. N., & Komar, P. D. (1977). Threshold of sediment motion under unidirectional currents. *Sedimentology*, **24**(4), 507 – 527.
- Mizuyama, T., Hirasawa, R., Kosugi, K., Tsutsumi, D., & Nonaka, M. (2011). Sediment monitoring with a hydrophone in mountain torrents. *International Journal of Erosion Control Engineering*, **4**(2), 43 – 47. <https://doi.org/10.13101/ijece.4.43>.
- Mondol, N., & Bjørlykke, K. (2010). Seismic Exploration. [10.1007/978-3-642-02332-3\\_17](https://doi.org/10.1007/978-3-642-02332-3_17).
- Monteale-Gavazzi, G., Roche, M., Degrendele, K., Lurton, X., Terseleer, N., Baeye, M., Francken, F., & Van Lancker, V. (2019). Insights into the short-term tidal variability of multibeam backscatter from field experiments on different seafloor types. *Geosciences (Switzerland)*, **9**(1). <https://doi.org/10.3390/geosciences9010034>.

- Mosher, D. C., Piper, D., Xu, Z., Campbell, D., Cunningham, J., & Desroches, K. (2006). The 1929 Grand Banks Landslide and Tsunami Revisited. *AGU Fall Meeting Abstracts*.1.05.
- Mulder, T., & Syvitski, J. P. M. (1995). Turbidity currents generated at river mouths during exceptional discharges to the world oceans. *The Journal of Geology*, **103**(3), 285 – 299. <https://doi.org/10.1086/629747>.
- Mulder, T., Syvitski, J. P. M., & Skene, K. I. (1998). Modeling of erosion and deposition by turbidity currents generated at river mouths. *J. Sediment. Res.* **68**, 124 – 137.
- Mulder, T., Syvitski, J. P. M., Migeon, S., Faugères, J.-C., & Savoye, B. (2003). Marine hyperpycnal flows: Initiation, behavior and related deposits. A review. *Marine and Petroleum Geology*, **20**(6-8), 861 – 882. <https://doi.org/10.1016/j.marpetgeo.2003.01.003>.
- National Oceanic and Atmospheric Administration (NOAA). (2018). What is eutrophication? National Ocean Service website. Accessed at: <https://oceanservice.noaa.gov/facts/hydrophone.html>, 20/07/2020.
- National Physical Laboratory (NPL). (2023). Accessed at: <http://resource.npl.co.uk/acoustics/techguides/seaabsorption/>, 14/09/2023.
- Newman, P. (1984). Seismic response to sea-floor diffractors. *First Break*, **2** (2), 9 – 19.
- Normandeau, A., Campbell, D. C., Piper, D. J. W., & Jenner, K. A. (2019). Are submarine landslides an underestimated hazard on the western North Atlantic passive margin? *Geology*, **47**(9), 848 – 852. <https://doi.org/10.1130/G46201.1>.
- Nortek. (2018). *The Comprehensive Manual for Velocimeters*. 1 – 119.
- Nortek. (2022). *The Comprehensive Manual – ADCP*. 1 – 147.
- Novo, E. M. M., Hansom, J. D., & Curran P. J. (1989). The effect of sediment type on the relationship between reflectance and suspended sediment concentration, *International Journal of Remote Sensing*, **10**(7), 1283 – 1289, doi: 10.1080/01431168908903967.
- Obelcz, J., Xu, K., Georgiou, I. Y., Maloney, J., Bentley, S. J., & Miner, M. D. (2017). Sub-decadal submarine landslides are important drivers of deltaic sediment flux: Insights from the Mississippi River Delta front. *Geology*, **45**(7), 703 – 706. <https://doi.org/10.1130/G38688.1>.
- O'Brien, P. N. S. (1983). Aspects of seismic reflection prospecting for oil and gas, *Geophysical Journal International*, **Volume 74**, Issue 1, July, Pages 97 – 127, <https://doi.org/10.1111/j.1365-246X.1983.tb01872.x>.
- Open University (OU). (1999). *Waves, Tides and Shallow-Water Processes* (J. Wright, A. Colling, & D. Park (eds.)). Gulf Professional Publishing. <https://books.google.co.uk/books?id=vrUpJeDKUgEC>.

- Ortiz, J., & Klompmaker, A. (2015). Turbidity Currents: Comparing Theory and Observation in the Lab. *Oceanography (Washington D.C.)*, **28**, 220 – 227. <https://doi.org/10.5670/oceanog.2015.73>.
- Parker, G., Fukushima, Y., & Pantin, H. M. (1986). Self-accelerating turbidity currents. *Journal of Fluid Mechanics*, **171**, 145 – 181. <https://doi.org/DOI:10.1017/S0022112086001404>.
- Parsons, J. R., Bush, J. W. M., & Syvitski, J. P. M. (2001). Hyperpycnal plume formation from riverine outflows with small sediment concentrations. *Sedimentology*, **48**, 465 – 478.
- Parsons, D. R., Best, J. L., Orfeo, O., Hardy, R. J., Kostaschuk, R., & Lane, S. N. (2005). Morphology and flow fields of three-dimensional dunes, Rio Paraná, Argentina: Results from simultaneous multibeam echo sounding and acoustic Doppler current profiling. *Journal of Geophysical Research: Earth Surface*, **110**(4), 1 – 9. <https://doi.org/10.1029/2004JF000231>.
- Parsons, J. D., Friedrichs, C. T., Traykovski, P. A., Mohrig, D., Imran, J., Syvitski, J. P. M., Parker, G., Puig, P., Buttles, J. L., and Garca, M. H. (2009). The Mechanics of Marine Sediment Gravity Flows. In *Continental Margin Sedimentation*. <https://doi.org/10.1002/9781444304398.ch6>
- Paull, C. K., Ussler, W., Caress, D. W., Lundsten, E., Covault, J. A., Maier, K. L., Xu, J., & Augenstein, S. (2010). Origins of large crescent-shaped bedforms within the axial channel of Monterey Canyon, Offshore California. *Geosphere*, **6**(6), 755 – 774. <https://doi.org/10.1130/GES00527.1>.
- Paull, C. K., Caress, D. W., Ussler, W., Lundsten, E., & Meiner-Johnson, M. (2011). High-resolution bathymetry of the axial channels within Monterey and Soquel submarine canyons, offshore central California. *Geosphere*, **7**(5), 1077 – 1101. <https://doi.org/10.1130/GES00636.1>.
- Paull, C. K., Talling, P. J., Maier, K. L., Parsons, D., Xu, J., Caress, D. W., Gwiazda, R., Lundsten, E. M., Anderson, K., Barry, J. P., Chaffey, M., O'Reilly, T., Rosenberger, K. J., Gales, J. A., Kieft, B., McGann, M., Simmons, S. M., McCann, M., Sumner, E. J., Clare, M. A., & Cartigny, M. J. (2018). Powerful turbidity currents driven by dense basal layers. *Nature Communications*, **9**(1), 1 – 9. <https://doi.org/10.1038/s41467-018-06254-6>.
- Peng, Y., Yu, Q., Wang, Y., Zhu, Q., & Wang, Y. P. (2020). Sensitivities of bottom stress estimation to sediment stratification in a tidal coastal bottom boundary layer. *Journal of Marine Science and Engineering*, **8**(4), 1 – 13. <https://doi.org/10.3390/JMSE8040256>.
- Pensieri, S., & Bozzano, R. (2017). *Active and Passive Acoustic Methods for In-situ Monitoring of the Ocean Status* (A. Zak (ed.); p. Ch. 5). IntechOpen. <https://doi.org/10.5772/intechopen.68998>.

- Petersen, T. U. (2014). Scour around Offshore Wind Turbine Foundations Scour around Offshore Wind Turbine Foundations Department of Mechanical Engineering Technical University of Denmark. [*PhD Thesis*].
- Petrut, T., Geay, T., Gervaise, C., Belleudy, P., & Zanker, S. (2018). Passive acoustic measurement of bedload grain size distribution using self-generated noise. *Hydrology and Earth System Sciences*, **22**(1), 767 – 787. <https://doi.org/10.5194/hess-22-767-2018>.
- Piper, D. J. W., Cochonat, P., & Morrison, M. L. (1999). The sequence of events around the epicentre of the 1929 Grand Banks earthquake: Initiation of debris flows and turbidity current inferred from side-scan sonar. *Sedimentology*, **46**(1), 79 – 97. <https://doi.org/10.1046/j.1365-3091.1999.00204.x>.
- Piper, D., & Normark, W. (2009). Processes That Initiate Turbidity Currents and Their Influence on Turbidites: A Marine Geology Perspective. *Journal of Sedimentary Research - J SEDIMENT RES.* **79**, 347-362. 10.2110/jsr.2009.046.
- Placidi, M. (2015). On the effect of surface morphology on wall turbulence. *University of Southampton, Engineering and the Environment*, PhD. [*PhD Thesis*], 1 – 162.
- Pope, E. L., Cartigny, M. J. B., Clare, M. A., Talling, P. J., Lintern, D. G., Vellinga, A., Hage, S., Açikalin, S., Bailey, L., Chapplow, N., Chen, Y., Eggenhuisen, J. T., Hendry, A., Heerema, C. J., Heijnen, M. S., Hubbard, S. M., Hunt, J. E., McGhee, C., Parsons, D. R., Simmons S. M., Stacey, C. D., & Vendettuoli, D. (2022). First source-to-sink monitoring shows dense head controls sediment flux and runout in turbidity currents. *Science Advances*, **8**(20). <https://doi.org/10.1126/sciadv.abj3220>.
- Porcile, G., Bolla Pittaluga, M., Frascati, A., & Sequeiros, O. E. (2020). Typhoon-induced megarips as triggers of turbidity currents offshore tropical river deltas. *Communications Earth & Environment*, **1**(1), 2. <https://doi.org/10.1038/s43247-020-0002-1>.
- Priego-Hernandez, G. A., Rubio-Arias, H., & Rivera Trejo, F. (2019). ADCP, Multi-frequency analysis for flow measurements in rivers. *Acta Scientiarum Polonorum Formatio Circumiectus.* **18**, 101 – 112. 10.15576/ASP.FC/2019.18.1.101.
- Prendergast, L. J., Gavin, K., & Doherty, P. (2015). An investigation into the effect of scour on the natural frequency of an offshore wind turbine. *Ocean Engineering*, **101**, 1 – 11. <https://doi.org/10.1016/j.oceaneng.2015.04.017>.
- Prior, D. B., Wiseman, W. J., & Gilbert, R. (1981). Submarine slope processes on a fan delta, Howe Sound, British Columbia. *Geo-Marine Letters*, **1**(2), 85 – 90. <https://doi.org/10.1007/BF02463323>.
- Prior, D.B. Bornhold, B.D. Wiseman Jr. W.J. & Lowe, D.R. (1987). Turbidity current activity in a British Columbia fjord. *Science*, **237**, 1330 – 1333.

- Reesink, A. J. H., Ashworth, P. J., Sambrook Smith, G. H., Best, J. L., Parsons, D. R., Amsler, M. L., Hardy, R. J., Lane, S. N., Nicholas, A. P., Orfeo, O., Sandback, S. D., Simpson, C., & Szupiany, R. N. (2014). Scales and causes of heterogeneity in bars in a large multi-channel river: Rio Parana, Argentina. *Sedimentology*, **61**(4), 1055 – 108. <https://doi.org/10.1111/sed.12092>.
- Rennie, C. D., & Millar, R. G. (2002). Spatial distribution of bedload transport velocity using an acoustic Doppler current profiler. *Hydraulic Measurements and Experimental Methods*, **128**(5), 430 – 439. [https://doi.org/10.1061/40655\(2002\)66](https://doi.org/10.1061/40655(2002)66).
- Rennie, C., Millar, R., & Church, M. (2002). Measurement of Bed Load Velocity Using an Acoustic Doppler Current Profiler. *Journal of Hydraulic Engineering-Asce - J HYDRAUL ENG-ASCE*, **128**. [https://doi.org/10.1061/\(ASCE\)0733-9429\(2002\)128:5\(473\)](https://doi.org/10.1061/(ASCE)0733-9429(2002)128:5(473)).
- Rennie, C. D., & Villard, P. V. (2004). Site specificity of bed load measurement using an acoustic Doppler current profiler. *Journal of Geophysical Research: Earth Surface*, **109**(F3). <https://doi.org/https://doi.org/10.1029/2003JF000106>.
- Rennie, C. D., & Millar, R. G. (2004). Measurement of the spatial distribution of fluvial bedload transport velocity in both sand and gravel. *Earth Surface Processes and Landforms*, **29**(10), 1173 – 1193. <https://doi.org/https://doi.org/10.1002/esp.1074>.
- Rezar, R., & Lavoie, D. L. (1993). *Carbonate microfibrils*. New York (Springer-Verlag), 121pp.
- Riccobene, G. (2009). Long-term measurements of acoustic background noise in very deep sea. *Nuclear Instruments and Methods in Physics Research Section A: Accelerators, Spectrometers, Detectors and Associated Equipment*, **604**(1 – 2), 149 – 157. <https://doi.org/https://doi.org/10.1016/j.nima.2009.03.195>.
- Richards, S. Heathershaw, A. D., & Thorne, P. (1996). The effect of suspended particulate matter on sound attenuation in seawater. *Journal of the Acoustical Society of America*, **100**, 1447-1450. Doi:10.1121/1.415991.
- Richardson, E. V., & Davis, S. R. (2001). Evaluating Scour At Bridges-Fourth Edition. *Hydraulic Engineering Circular*, **18**, 378.
- Rickenmann, D., Turowski, J. M., Fritschi, B., Klaiber, A., & Ludwig, A. (2012). Bedload transport measurements at the Erlenbach stream with geophones and automated basket samplers. *Earth Surface Processes and Landforms*, **37**(9), 1000 – 1011. <https://doi.org/10.1002/esp.3225>.
- Rigby, J. R., Kuhnle, R. A., Goodwiller, B. T., Nichols, M. H., Carpenter, W. O., Wren, D. G., & Chambers, J. P. (2015). Sediment-generated noise (SGN): Comparison with physical bed load measurements in a small semi – arid watershed, Paper presented at the 2015 SEDHYD Conference, Reno, Nevada, USA, available at: <http://www.sedhyd.org/2015/>, last access: 13 05 2022.

- Rigby, J. R., Wren, D. G., & Kuhnle, R. A. (2016). Passive Acoustic Monitoring of Bed Load for Fluvial Applications. *Journal of Hydraulic Engineering*, **142**(9), 02516003. Doi:10.1061/(asce)hy.1943-7900.0001122.
- Rinaldi, G., Thies, P. R., & Johannng, L. (2021). Current status and future trends in the operation and maintenance of offshore wind turbines: A review. *Energies*, **14**(9). <https://doi.org/10.3390/en14092484>.
- Ross, D. S., Wemple, B. C., Willson, L. J., Balling, C. M., Underwood, K. L., & Hamshaw, S. D. (2019). Impact of an Extreme Storm Event on River Corridor Bank Erosion and Phosphorus Mobilization in a Mountainous Watershed in the Northeastern United States. *Journal of Geophysical Research: Biogeosciences*, **124**(1), 18 – 32. <https://doi.org/10.1029/2018JG004497>.
- Rouse, H.L. (1994), Measurement of bedload gravel transport: The calibration of a self-generated noise system. *Earth Surf. Process. Landforms*, **19**, 789 – 800. <https://doi.org/10.1002/esp.3290190905>.
- Salinas, J. S., Cantero, M. I., Shringarpure, M., & Balachandar, S. (2019). Properties of the body of a turbidity current at near-normal conditions: 1. Effect of bed slope. *Journal of Geophysical Research: Oceans*, **124**, 7989 – 8016. <https://doi.org/10.1029/2019JC015332>.
- Sandbach, S. D., Hardy, R. J., Lane, S. N., Parsons, D. R., Best, J. L., Ashworth, P. J., Reesink, A. J. H., Amsler, M. L., Szupiany, R. N., Nicholas, A. P., Orfeo, O., & Sambrook-Smith, G. H. (2010). Three-dimensional modelling of a very large river, the Rio Parana. *Proceedings of the IAHR River Flow 2010 Conference, 2008*, 409 – 417.
- Schimmel, A.C.G., Ierodiaconou, D., Hulands, L., & Kennedy, D.M. (2015). Accounting for uncertainty in volumes of seabed change measured with repeat multibeam sonar surveys. *Continental Shelf Research*, **111**, 52 – 68. Doi:10.1016/j.csr.2015.10.019.
- Schmitt, T., Mitchell, N. C. A., & Ramsay, T S. (2008). Characterising uncertainties for quantifying bathymetry change between time-separated multibeam echo-sounder surveys. **28**(9), 0 – 1176. Doi:10.1016/j.csr.2008.03.001.
- Sea Beam. (2000). Multibeam Sonar Theory of Operation. *L-3 Communications Sea Beam Instruments*. 107pp.
- Sebastian, S. M. & Caruthers, J. W. (2001). “Effects of naturally occurring bubbles on multibeam sonar operations,” *MTS/IEEE Oceans 2001. An Ocean Odyssey. Conference Proceedings (IEEE Cat. No.01CH37295)*, **2**, 1241 – 1247 doi: 0.1109/OCEANS.2001.968288.
- Secomandi, M., Jones, E., Terente, V., Comrie, R., & Owen, M. (2017). Application of the Bathymetric Position Index Method (BPI) for the Purpose of Defining a Reference Seabed Level for Cable Burial. *Offshore Site Investigation Geotechnics 8<sup>th</sup> International Conference Proceedings*, 904 – 913. <https://doi.org/10.3723/osig17.904>.

- Sequeiros, O. E., Bolla Pittaluga, M., Frascati, A., Pirmez, C., Masson, D. G., Weaver, P., Crosby, A. R., Lazzaro, G., Botter, G., & Rimmer, J. G. (2019). How typhoons trigger turbidity currents in submarine canyons. *Scientific Reports*, **9**(1), 9220. <https://doi.org/10.1038/s41598-019-45615-z>.
- Shanmugam, G. (2022). 150 Years (1872 – 2022) of research on deep–water processes, deposits, settings, triggers, and deformation: A difficult domain of progress, dichotomy, diversion, omission, and groupthink. *Journal of Palaeogeography*, **11**(4), 469 – 564. <https://doi.org/https://doi.org/10.1016/j.jop.2022.08.004>.
- Sharifuzzaman, M. D., Lemckert, C. J. & Etemad-Shahidi, A. (2017). Dynamics of lock-release crystalline gravity currents. *Geology, Ecology, and Landscapes*, **1**(4), 213 – 218.
- Sher, D., & Woods, A. W. (2015). Gravity currents: entrainment, stratification and self-similarity. *Journal of Fluid Mechanics*, **784**, 130 – 162. <https://doi.org/DOI:10.1017/jfm.2015.576>.
- Sime, L. C., Ferguson, R. I., & Church, M. (2007). Estimating shear stress from moving boat acoustic Doppler velocity measurements in a large gravel bed river. *Water Resources Research*, **43**(3), 1 – 12. <https://doi.org/10.1029/2006WR005069>.
- Simmons, S. M., Azpiroz-Zabala, M., Cartigny, M. J. . B., Clare, M. A., Cooper, C., Parsons, D. R., Pope, E. L., Sumner, E. J., & Talling, P. J. (2020). Novel Acoustic Method Provides First Detailed Measurements of Sediment Concentration Structure Within Submarine Turbidity Currents. *Journal of Geophysical Research: Oceans*, **125**, e2019JC015904. <https://doi.org/10.1029/2019jc015904>.
- Smith, D.P., Ruiz, G., Kvittek, R., & Iampietro, P J. (2005). Semiannual patterns of erosion and deposition in upper Monterey Canyon from serial multibeam bathymetry. *Geological Society of America Bulletin*, **117**(9), 1123 – .doi:10.1130/B25510.1.
- Smith, G. H. S. Ashworth, P. J. Best, J. L. Lunt, I. A. Orfeo, O. & Parsons, D. R. (2009). The sedimentology and alluvial architecture of a large braid bar, río paraná, argentina. *Journal of Sedimentary Research*, **79**(8), 629 – 642. <https://doi.org/10.2110/jsr.2009.066>.
- Song, Y. H., Joo, J. G., Lee, J. H., & Yoo, D. G. (2020). Numerical assessment of shear boundary layer formation in sewer systems with fluid-sediment phases. *Water (Switzerland)*, **12**(5). <https://doi.org/10.3390/W12051332>.
- Soni, S., (2017). A Review Paper on Hydrophones. *International Journal of Engineering Research & Technology*, Conference proceedings (Special issue).
- SonTEK, (2000). Acoustic Doppler Profiler Principles of Operation. 2 – 28.
- Soulsby, R. (1997). *Dynamics of marine sands: a manual for practical applications*. Telford. <http://site.ebrary.com/id/10868638>.

- Southall, B. L., Scholik-Schlomer, A. R., Hatch, L., Bergmann, T., Jasny, M., Metcalf, K., Weilgart, L., & Wright, A. J. (2017). Underwater Noise from Large Commercial Ships- International Collaboration for Noise Reduction. *Encyclopedia of Maritime and Offshore Engineering*, 1 – 9. <https://doi.org/10.1002/9781118476406.emoe056>.
- Soutter, E., Bell, D., Cumberpatch, Z., Ferguson, R., Spsychala, Y., Kane, I., & Eggenhuisen, J. (2021). The Influence of Confining Topography Orientation on Experimental Turbidity Currents and Geological Implications. *Frontiers in Earth Science*, 8. <https://doi.org/10.3389/feart.2020.540633>.
- Stevenson, C. J., Jackson, C. A. -L., Hodgson, D. M., Hubbard, S. M., & Eggenhuisen, J. T. (2015). Deep-Water Sediment Bypass. *Journal of Sedimentary Research*, 85(9), 1058 – 1081. <https://doi.org/10.2110/jsr.2015.63>.
- Strasberg, M. (1984), Adaptive Methods in Underwater Acoustics, 125 – 143, Reidel, Boston, MA.
- Strasberg, M. (1988), Dimensional analysis of windscreen noise, *J. Acoust. Soc. Am.*, 83(2), 544 – 548, doi:10.1121/1.396148. 2264.
- Strasberg, N. (1979), Nonacoustic noise interference in measurements of infrasonic ambient noise, *J. Acoust. Soc. Am.*, 66(5), 1487 – 1493, doi: 10.1121/1.383543.
- Sutherland, B. R., Barrett, K. J., & Gingras, M. K. (2014). Clay settling in fresh and salt water. *Environmental Fluid Mechanics*, 15(1), 147 – 160. <https://doi.org/10.1007/s10652-014-9365-0>.
- Sutherland, B. R., Gingras, M. K., Knudson, C., & Steverango, L. Surma, C. (2018). Particle-bearing currents in uniform density and two-layer fluids. *Physical Review Fluids*, 3(023801).
- Symons, W. O., Sumner, E. J., Paull, C. K., Cartigny, M. J. B., Xu, J. P., Maier, K. L., Lorenson, T. D., and Talling, P. J. (2017). A new model for turbidity current behavior based on integration of flow monitoring and precision coring in a submarine canyon. *Geology*, 45(4), 367 – 370. <https://doi.org/10.1130/G38764.1>.
- Syvitski, J. P. M., Asprey, K. W., Clattenburg, D. A., & Hodge, G. D. (1985). The prodelta environment of a fjord: suspended particle dynamics. *Sedimentology*, 32(1), 83 – 107. <https://doi.org/https://doi.org/10.1111/j.1365-3091.1985.tb00494.x>.
- Syvitski, J. P. M., & Farrow, G. E. (1983). Structures and processes in bayhead deltas: Knight and bute inlet, British Columbia. *Sedimentary Geology*, 36(2), 217 – 244. [https://doi.org/https://doi.org/10.1016/0037-0738\(83\)90010-6](https://doi.org/https://doi.org/10.1016/0037-0738(83)90010-6).
- Tajallibakhsh, T., Monim, M., Simpson, K., Lapierre, T., Dahl, J., Rowe, J., Spaulding, M., & Miller, J. (2020). *Potential Earthquake, Landslide, Tsunami and Geo-Hazards for the U.S. Offshore Pacific Wind Farms*.

- Talling P. J., Wynn, R.B., Masson, D.G., Frenz, M., Cronin, B.T., Schiebel, R., Akhmetzhanov, A.M., Dallmeier-Tiessen, S., Benetti, S., Weaver, P.P.E., Georgiopoulou, A., Zühlsdorff, C., and Amy, L.A. (2007). Onset of submarine debris flow deposition far from original giant landslide, *Nature*, **450**, 541 – 544.
- Talling, P. J., Masson, D. G., Sumner, E. J., & Malgesini, G. (2012). Subaqueous sediment density flows: Depositional processes and deposit types. *Sedimentology*, **59**(7), 1937 – 2003. <https://doi.org/10.1111/j.1365-3091.2012.01353.x>.
- Talling, P. J. (2013). Hybrid submarine flows comprising turbidity current and cohesive debris flow: Deposits, theoretical and experimental analyses, and generalised models. *Geosphere*, **9**(3), 460 – 488.
- Talling, P. J., Paull, C. K., & Piper, D. J. W. (2014). How are subaqueous sediment density flows triggered, what is their internal structure and how does it evolve? Direct observations from monitoring of active flows. *Earth-Science Reviews*, **125**, 244 – 287. <https://doi.org/10.1016/j.earscirev.2013.07.005>.
- Talling, P. J., Allin, J., Armitage, D. A., Arnott, R. W. C., Cartigny, M. J. B., Clare, M. A., Felletti, F., Covault, J. A., Girardclos, S., Hansen, E., Hill, P. R., Hiscott, R. N., Hogg, A. J., Clarke, J. H., Jobe, Z. R., Malgesini, G., Mozzato, A., Naruse, H., Parkinson, S., Peel, F. J., Piper, D. J. W., Postma, G., Rowley, P., Sguazzini, A., Stevenson, C. J., Sumner, E. J., Sylvester, Z., Watts, C., & Xu, J. (2015). Key Future Directions For Research On Turbidity Currents and Their Deposits. *Journal of Sedimentary Research*, **85**(2), 153 – 169. <https://doi.org/10.2110/jsr.2015.03>.
- Talling, P. J., Baker, M. L., Pope, E. L., Ruffell, S. C., Jacinto, R. S., Heijnen, M. S., Hage, S., Simmons, S. M., Hasenhündl, M., Heerema, C. J., Mcghee, C., Apprioual, R., Ferrant, A., Cartigny, M. J. B., Parsons, D. R., Clare, M. A., Tshimanga, R. M., Trigg, M. A., Cula, C. A., Faria, R., Gaillot, A., Bola, G., Wallace, D., Griff, A., & Nunny, R. (2022). Longest sediment flows yet measured show how major rivers connect efficiently to deep sea. *Nat Commun*, **13**, 4193. <https://doi.org/10.1038/s41467-022-31689-3>.
- Talling, P. J., Cartigny, M. J. B., Pope, E., Baker, M., Clare, M. A., Heijnen, M., Hage, S., Parsons, D. R., Simmons, S. M., Paull, C. K., Gwiazda, R., Lintern, G., Hughes Clarke, J. E., Xu, J., Silva Jacinto, R., & Maier, K. L. (2023). Detailed monitoring reveals the nature of submarine turbidity currents. *Nature Reviews Earth & Environment*, **4**(9), 642–658. <https://doi.org/10.1038/s43017-023-00458-1>.
- Tan, X., Hu, L., Reed, A. H., Furukawa, Y., & Zhang, G. (2014). Flocculation and particle size analysis of expansive clay sediments affected by biological, chemical, and hydrodynamic factors Topical Collection on the 11th International Conference on Cohesive Sediment Transport. *Ocean Dynamics*, **64**(1), 143 – 157. <https://doi.org/10.1007/s10236-013-0664-7>.
- Teledyne RDI. (2001). Workhorse commands and output data format. RD Instruments Tech. Rep. 957-6156-00, 158 pp.

- Teledyne RDI. (2011). Acoustic Doppler Current Profiler Principles of Operation A Practical Primer. (Jan). 1 – 62.
- Tesei, A., Canepa, G., & Zampelli, M. (2009). Measurements and modelling of high-frequency acoustic scattering by a rough seafloor and sea surface. Proceedings of the 3rd International Conference and Exhibition on Underwater Acoustic Measurements: Technologies and Results, 21 – 26.
- Thorne, P. D. (1985). The measurement of acoustic noise generated by moving artificial sediments, *The Journal of the Acoustical Society of America*, **78**, 1013 – 1023.
- Thorne, P. D. (1986). Laboratory and marine measurements on the acoustic detection of sediment transport. *The Journal of the Acoustical Society of America*, **80**(3), 899 – 910. Doi:10.1121/1.393913.
- Thorne, P. D., & Foden, D. J. (1988). Generation of underwater sound by colliding spheres. *The Journal of the Acoustical Society of America*, **84**(6), 2144 – 2152. Doi:10.1121/1.397060.
- Thorne, P. D. (1990). Seabed generation of ambient noise. *Journal of the Acoustical Society of America*, **87**(1), 149 – 153. <https://doi.org/10.1121/1.399307>.
- Thorne, P. D. (2014). An overview of underwater sound generated by interparticle collisions and its application to the measurements of coarse sediment bedload transport. *Earth Surface Dynamics*, 2. Doi:10.5194/esurf-2-531-2014.
- Thorne, P. D., MacDonald, I. T., & Vincent, C. E. (2014). Modelling acoustic scattering by suspended flocculating sediments. *Continental Shelf Research*, **88**, 81 – 91. doi:10.1016/j.csr.2014.07.003.
- Thorne, Peter & Lichtman, Ian Dougal & Hurther, David. (2020). Acoustic scattering characteristics and inversions for suspended concentration and particle size above mixed sand and mud beds. *Continental Shelf Research*. **214**. 104320. 10.1016/j.csr.2020.104320.
- Tolhurst, T. J., Gust, G., & Paterson, D. M. (2002). The influence of an extracellular polymeric substance (EPS) on cohesive sediment stability. *Proceedings in Marine Science*, **5**, 409 – 425. [https://doi.org/10.1016/S1568-2692\(02\)80030-4](https://doi.org/10.1016/S1568-2692(02)80030-4).
- University of Brighton, (2022). Accessed at: <https://www.brighton.ac.uk/aquatic/what-we-do/research-projects/paran%C3%A1.aspx>, 17/06/2022.
- Urban, P., Köser, K., & Greinert, J. (2017), Processing of multibeam water column image data for automated bubble/seep detection and repeated mapping. *Limnol. Oceanogr. Methods*, **15**, 1 – 21. <https://doi.org/10.1002/lom3.10138>.
- Van Rijn, L. C. (1984). Sediment Transport, Part III: Bed forms and Alluvial Roughness. *Journal of Hydraulic Engineering*, **110**(12), 1733 – 1754. [https://doi.org/10.1061/\(ASCE\)0733-9429\(1984\)110:12\(1733\)](https://doi.org/10.1061/(ASCE)0733-9429(1984)110:12(1733)).

- Veeraiyan, V. B., & Rajendran, V. (2020). Underwater Ambient Noise. [10.5772/intechopen.93057](https://doi.org/10.5772/intechopen.93057).
- Vendettuoli, D., Clare, M. A., Hughes Clarke, J. E., Vellinga, A., Hizzet, J., Hage, S., Cartigny, M. J. B., Talling, P. J., Waltham, D., Hubbard, S. M., Stacey, C., & Lintern, D. G. (2019). Daily bathymetric surveys document how stratigraphy is built and its extreme incompleteness in submarine channels. *Earth and Planetary Science Letters*, **515**, 231 – 247. [https://doi.org/https://doi.org/10.1016/j.epsl.2019.03.033](https://doi.org/10.1016/j.epsl.2019.03.033).
- Venditti, J. G. (2013). Bedforms in Sand-Bedded Rivers. *Treatise on Geomorphology*. 137-162. <https://doi.org/10.1016/B978-0-12-374739-6.00235-9>.
- Villard, P., Church, M., & Kostaschuk, R. (2005). Estimating bedload in sand-bed channels using bottom tracking from an acoustic Doppler profiler (**Vol. 35**, pp. 197 – 209).
- Voulgaris, G., Wilkin, M. P., & Collins, M. B. (1995). The in situ passive acoustic measurement of shingle movement under waves and currents: instrument (TOSCA) development and preliminary results. *Continental Shelf Research*, **15**(10), 1195 – 1211. [https://doi.org/10.1016/0278-4343\(94\)00074-W](https://doi.org/10.1016/0278-4343(94)00074-W).
- Von Kármán, T. (1930). Mechanische Ähnlichkeit und Turbulenz, Nachrichten von der Gesellschaft der Wissenschaften zu Göttingen. *Fachgruppe I (Mathematik)*, **5**, 58 – 76.
- Water Survey of Canada (WSC). (2022). Accessed at: [https://wateroffice.ec.gc.ca/report/real\\_time\\_e.html?stn=08GD004&mode=Graph&startDate=2022-08-01&endDate=2022-09-30&prm1=47&y1Max=&y1Min=&max1=1&min1=1&mean1=1&prm2=-1&y2Max=&y2Min=, 09/12/2022](https://wateroffice.ec.gc.ca/report/real_time_e.html?stn=08GD004&mode=Graph&startDate=2022-08-01&endDate=2022-09-30&prm1=47&y1Max=&y1Min=&max1=1&min1=1&mean1=1&prm2=-1&y2Max=&y2Min=, 09/12/2022).
- Walter, T. R., Haghshenas Haghighi, M., Schneider, F. M., Coppola, D., Motagh, M., Saul, J., Babeyko, A., Dahm, T., Troll, V. R., Tilmann, F., Heimann, S., Valade, S., Triyono, R., Khomarudin, R., Kartadinata, N., Laiolo, M., Massimetti, F., & Gaebler, P. (2019). Complex hazard cascade culminating in the Anak Krakatau sector collapse. *Nature Communications*, **10**(1). <https://doi.org/10.1038/s41467-019-12284-5>.
- Ward, S. L., Neill, S. P., Van Landeghem, K. J. J., & Scourse, J. D. (2015). Classifying seabed sediment type using simulated tidal-induced bed shear stress. *Marine Geology*, **367**, 94 – 104. <https://doi.org/10.1016/j.margeo.2015.05.010>.
- Watkins, R. K., & Moser, A. P. (1971). Response of corrugated steel pipe to external soil pressures. *Highw Res Rec*.
- Weinert, J., Smolka, U., Schümann, B., & Cheng, P. W. (2015). Detecting critical scour developments at monopile foundations under operating conditions. *European Wind Energy Association Annual Conference and Exhibition 2015, EWEA 2015 - Scientific Proceedings*, 135 – 139.
- Wenz, G. M. (1962). Acoustic Ambient Noise in the Ocean: Spectra and Sources. *The Journal of the Acoustical Society of America*, **34**(12), 1936 – 1956. <https://doi.org/10.1121/1.1909155>.

- Wheaton J. M., Brasington, J., Darby, S. E., & Sear D. A. (2010). Accounting for uncertainty in DEMs from repeat topographic surveys: improved sediment budgets. *35*(2), 0 – 0. doi:10.1002/esp.1886.
- Whitehouse, R. J. S., Harris, J. M., Sutherland, J., & Rees, J. (2011). The nature of scour development and scour protection at offshore windfarm foundations. *Marine Pollution Bulletin*, *62*(1), 73 – 88. <https://doi.org/10.1016/j.marpolbul.2010.09.007>.
- Wilcock, P. R. (1996). Estimating local bed shear stress from velocity observations. *Water Resources Research*, *32*(11), 3361 – 3366. <https://doi.org/10.1029/96WR02277>.
- Wilcock, P. R., & Kenworthy, S. T. (2002). A Two-Fraction Model for the Transport of Sand / Gravel Mixtures A two-fraction model for the transport of sand / gravel mixtures. *Water Resources Research*, *38*(10), 1194. <https://doi.org/10.1029/2001WR000684>.
- Wiley, M. (2014). *Estuarine Processes: Circulation, Sediments, and Transfer of Material in the Estuary*. Academic Press. <https://books.google.co.uk/books?id=TUGoBQAAQBAJ>.
- Williams, J. J., Thorne, P. D., & Heathershaw, A. D. (1989). Comparisons between acoustic measurements and predictions of the bedload transport of marine gravels. *Sedimentology*, *36*(6), 973 – 979. <https://doi.org/10.1111/j.1365-3091.1989.tb01534.x>.
- Winterwerp, J. C., & van Kesteren, W. G. M. (2004). Introduction to the Physics of Cohesive Sediment Dynamics in the Marine Environment. *Developments in sedimentology*.
- Wood, M., Fosness, R., Pachman, G., Lorang, M., & Tonolla, D. (2015). Evaluation of Multiple-Frequency, Active and Passive Acoustics as Surrogates for Bedload Transport. *SEDHYD 2015, 10th Federal Interagency Sedimentation Conference*, 19-23.
- Wren, D. G., Goodwiller, B. T., Rigby, J. R., Carpenter, W. O., Kuhnle, R. A., & Chambers, J. P. (2015). *Sediment-Generated Noise (SGN): laboratory determination of measurement volume. Proc. 3rd Jt. Fed. Interag. Conf., 10th Fed. Interag. Sediment. Conf. 5th Fed. Interag. Hydrol. Model. Conf, Reno, Nevada*, 19 – 23.
- Wright, L. D., Friedrichs, C. T., Kim, S. C., & Scully, M. E. (2001). Effects of ambient currents and waves on gravity-driven sediment transport on continental shelves. *Marine Geology*, *175*(1 – 4), 25 – 45. [https://doi.org/10.1016/S0025-3227\(01\)00140-2](https://doi.org/10.1016/S0025-3227(01)00140-2).
- Wright, L. D., & Friedrichs, C. T. (2006). Gravity-driven sediment transport on continental shelves: A status report. *Continental Shelf Research*, *26*(17 – 18), 2092 – 2107. <https://doi.org/10.1016/j.csr.2006.07.008>.
- Wyss, C. R., Rickenmann, D., Fritschi, B., Turowski, J. M., & Weitbrecht, V. (2016). Laboratory flume experiments with the Swiss plate geophone bed load monitoring system: 1. Impulse counts and particle size identification. *Journal of the American Water Resources Association*, *52*, 7744 – 7759. <https://doi.org/10.1111/j.1752-1688.1969.tb04897.x>.

- Xu, J. P., Noble, M. A., & Rosenfeld, L. K. (2004). In-situ measurements of velocity structure within turbidity currents. *Geophysical Research Letters*, **31**(9). <https://doi.org/10.1029/2004GL019718>.
- Xu, J. P. (2011). Measuring currents in submarine canyons: Technological and scientific progress in the past 30 years. *Geosphere*, **7**(4), 868 – 876. <https://doi.org/10.1130/GES00640.1>.
- Yan, Z. -L., Qin, L. -L., Wang, R., Li, J., Wang, X. -M., Tang, X. -L., & An, R. (2018). The Application of a Multi-Beam Echo-Sounder in the Analysis of the Sedimentation Situation of a Large Reservoir after an Earthquake. *Water*, **10**, 557. [10.3390/w10050557](https://doi.org/10.3390/w10050557).
- Yoo, M.W., Kim, Y.D., Lyu, S., & Seo, I.W. (2009). Flowrate and Velocity Measurement in Nakdong River Using ADCP. In: *Advances in Water Resources and Hydraulic Engineering*. Springer, Berlin, Heidelberg. [https://doi.org/10.1007/978-3-540-89465-0\\_333](https://doi.org/10.1007/978-3-540-89465-0_333).
- Zakeri A. (2008). A potentially devastating offshore geohazard - submarine debris flow impact on pipelines. *Explor. Prod. Oil Gas. Rev.* **6**, 118 – 121.
- Zeng, J.J., Lowe, D.R. Prior, D.B. Wiseman, W.J. & Bornhold, B.D. (1991). Flow properties of turbidity currents in Bute Inlet, British Columbia. *Sedimentology*, **38**, 975 – 996.
- Zeng, J.J., & Lowe, D.R. (1997). Numerical simulation of turbidity current flow and sedimentation. 2. Results and geological applications. *Sedimentology*, **44**, 85 – 104.
- Zhang, M., & Yu, G. (2017). Critical conditions of incipient motion of cohesive sediments. *Water Resources Research*, **53**(9), 7798 – 7815. <https://doi.org/10.1002/2017WR021066>.
- Zhang, J., Dai, S., Ma, C., Di, J., & Zhao, J. (2017). Common-path digital holographic microscopy for near-field phase imaging based on surface plasmon resonance. *Applied Optics*, **56**, 3223. [10.1364/AO.56.003223](https://doi.org/10.1364/AO.56.003223).
- Zhang, L., Zhang, F., Cai, A., Song, Z., & Tong, S. (2020). Comparison of methods for bed shear stress estimation in complex flow field of bend. *Water (Switzerland)*, **12**(10), 1 – 16. <https://doi.org/10.3390/w12102753>.
- Zhang, M., Liu, Y., Xu, J., & Zhao, H. (2021). Analysis on the influence of water concentration on ADCP current measurement. *E3S Web Conf.*, **290**. <https://doi.org/10.1051/e3sconf/202129001006>.
- Zwolak, K. (2015). Underwater objects' detection system choice for harbor surveillance purposes. *Zeszyty Naukowe Akademii Marynarki Wojennej*, **200**, 1 – 1. [10.5604/0860889X.1161261](https://doi.org/10.5604/0860889X.1161261).

# Appendices

## Appendix A

Survey days	Runout distance (m)	Location of event along delta-lip	Type of initiation mechanism	Volume (m <sup>3</sup> )	Full extent of event known
29/08 – 30/08	129	Middle	Landslide	12	Yes
29/08 – 30/08	59	Middle	Landslide	17	Yes
30/08 – 31/08	1170	Multiple	Both	44732	No
31/08 – 01/09	1045	Middle	Both	11994	No
31/08 – 01/09	29	East	Landslide	19	Yes
01/09 – 02/09	820	Multiple	Both	9740	No
01/09 – 02/09	251	Middle	Both	3516	No
01/09 – 02/09	40	East	Landslide	250	Yes
01/09 – 02/09	25	East	Landslide	113	Yes
01/09 – 02/09	18	East	Landslide	95	Yes
02/09 – 03/09	615	Multiple	Both	3231	No
02/09 – 03/09	228	West	Settling plume	228	No
02/09 – 03/09	84	East	Landslide	94	Yes
02/09 – 03/09	69	Middle	Landslide	19	Yes
02/09 – 03/09	34	East	Landslide	20	Yes
03/09 – 04/09	832	Multiple	Both	17712	Yes
03/09 – 04/09	670	West	Both	6926	No
03/09 – 04/09	574	West	Settling plume	6781	Yes
03/09 – 04/09	74	East	Landslide	343	Yes
03/09 – 04/09	60	Middle	Landslide	9	Yes
03/09 – 04/09	54	Middle	Landslide	32	Yes
04/09 – 05/09	2387	Multiple	Both	76063	No
05/09 – 06/09	2255	Multiple	Both	6331	No
05/09 – 06/09	212	Middle	Settling plume	87	Yes
05/09 – 06/09	47	Middle	Landslide	26	Yes
06/09 – 07/09	2297	Multiple	Both	7517	No
06/09 – 07/09	1225	West	Settling plume	2324	Yes
07/09 – 09/09	623	Middle	Landslide	7129	Yes
07/09 – 09/09	31	East	Landslide	29	Yes
08/09 – 09/09	20	Middle	Landslide	83	Yes
09/09 – 10/09	614	Middle	Settling plume	3928	Yes

Appendix 8.1. Summary of all events recorded during the Bute Inlet study 2022 (29/08/2022 – 14/09/2022). “Multiple” indicates the event originated from multiple regions of the delta-lip. “Both” denotes that the event was generated by multiple initiation mechanisms comprising both landslide and settling plume.